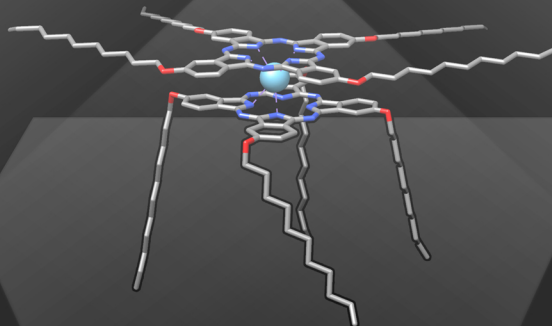


Università degli Studi di Parma

# Multifunctional Nanomaterials: Theranostic Nanoparticles and SMM-decorated Surfaces



**Federico Bertani**

**XXVII cycle**

UNIVERSITÀ DEGLI STUDI DI PARMA

Dottorato di ricerca in Scienza e Tecnologia dei  
Materiali Innovativi

Ciclo XXVII (2012-2014)

**Multifunctional Nanomaterials:  
Theranostic Nanoparticles and  
SMM-decorated Surfaces**

Coordinatore:  
Prof. Enrico Dalcanale

Tutor:  
Prof. Enrico Dalcanale

Dottorando: Federico Bertani

2015

This PhD Thesis has been supported by the Spinner Project "Sistemi molecolari e materiali fotoresponsivi per applicazioni nano e biotecnologiche e in oncologia"



"As a Magician, I try to show things to people that seem impossible. And I think magic whether I'm holding my breath or shuffling a deck of cards is pretty simple: it's practice, it's training and it's experimenting while pushing through the pain to be the best that I can be. And that's what magic is to me."

David Blaine, TedTalks, October 2009.





# Contents

CHAPTER 1.....	1
<b>Cavitands as Supramolecular Receptors</b>	
1.1 Supramolecular Chemistry.....	2
1.2 Molecular Receptors.....	3
1.2.1 Tetraphosphonate Cavitands.....	3
1.2.2 Tetraquinoxaline Bridged-cavitands.....	7
1.3 References.....	11
CHAPTER 2.....	15
<b>Functionalization of PEGylated Fe<sub>3</sub>O<sub>4</sub> Magnetic Nanoparticles with Tetraphosphonate Cavitand for Biomedical Application</b>	
2.1 Introduction.....	16
2.2 Results and Discussion.....	18
2.2.1 Bare MNPs.....	18
2.2.2 Synthesis and Characterization of Functionalized MNPs.....	18
2.2.3 Drug Load/release.....	26
2.3 Conclusions.....	28
2.4 Acknowledgements.....	29
2.5 Experimental Section.....	30
2.6 References.....	33
CHAPTER 3.....	37
<b>Multifunctional Magnetic Nanoparticles for Enhanced Intracellular Drug Transport</b>	
3.1 Introduction.....	38
3.2 Results and Discussion.....	40
3.2.1 Synthesis of Functionalized Nanoparticles.....	40

3.2.2 Magnetic Properties.....	44
3.2.3 Intracellular Uptake.....	45
3.2.4 Drug Load/release.....	47
3.2.5 Intra-cellular Transport.....	48
3.3 Conclusions.....	50
3.4 Acknowledgements.....	51
3.5 Experimental Section.....	52
3.6 Supplementary Information.....	56
3.7 References.....	59
CHAPTER 4.....	63
<b>Trypticene Quinoxaline-bridged Cavitands</b>	
4.1 Introduction.....	64
4.2 Results and Discussion.....	65
4.2.1 Design of Tripty-QxCav.....	65
4.2.2 Synthesis of the Triptycene-quinoxaline Bridging Unit.....	66
4.2.3 Synthesis of Tripty-QxCav <b>9</b> .....	67
4.2.4 <sup>1</sup> H NMR Characterization of <b>9</b> .....	69
4.2.5 Synthesis of Tripty-QxCav <b>11</b> .....	73
4.2.6 Thermo Gravimetric Analysis of <b>9</b> and <b>11</b> .....	75
4.2.7 SPME Analysis.....	77
4.3 Conclusions.....	82
4.4 Acknowledgements.....	83
4.5 Experimental Section.....	84
4.6 References.....	92
CHAPTER 5.....	93
<b>Molecular Magnetism</b>	
5.1 Nanotechnology.....	94
5.2 Molecular Magnetism.....	94
5.3 Single-Molecule Magnets.....	96

5.3.1 Design and Synthesis of SMMs.....	101
5.3.2 Lanthanide Phthalocyanines Double Decker.....	103
5.3.3 SMMs on Surface.....	106
5.4 References.....	110
CHAPTER 6.....	115
<b>Magnetic Behaviour of TbPc<sub>2</sub> Single-Molecule Magnets Chemically Grafted on Silicon Surface</b>	
6.1 Introduction.....	116
6.2 Results and Discussion.....	117
6.2.1 Synthesis of the TbPc <sub>2</sub> (OC <sub>11</sub> H <sub>21</sub> ) <sub>8</sub> Complex.....	117
6.2.2 Magnetic Characterization of Bulk TbPc <sub>2</sub> (OC <sub>11</sub> H <sub>21</sub> ) <sub>8</sub> .....	119
6.2.3 Monolayer Preparation and Chemical Characterization.....	121
6.2.4 Structural Characterization of the TbPc <sub>2</sub> (OC <sub>11</sub> H <sub>21</sub> ) <sub>8</sub> @Si Monolayer...	123
6.2.5 Magnetic Characterization of the TbPc <sub>2</sub> (OC <sub>11</sub> H <sub>21</sub> ) <sub>8</sub> @Si Monolayer....	125
6.3 Conclusions.....	127
6.4 Acknowledgements.....	128
6.5 Experimental Section.....	129
6.6 References.....	132
CHAPTER 7.....	137
<b>Oriented Grafting of SMMs on Silicon Surface</b>	
7.1 Introduction.....	138
7.1.1 TbPc <sub>2</sub> Synthetic Remarks.....	138
7.2 Results and Discussion.....	140
7.2.1 Synthesis of TbPc <sub>2</sub> for Oriented Grafting on Silicon.....	141
7.2.2 Magnetic Characterization of Bulk.....	152
7.2.3 Covalent Grafting on Silicon.....	153
7.2.4 X-Ray Natural Linear Dichroism (XNLD).....	154
7.2.4 X-ray Absorption Characterization of the 11@Si Monolayer.....	156
7.3 Conclusions.....	159

7.4 Acknowledgements.....	159
7.5 Experimental Section.....	160
7.6 References.....	165

CHAPTER 8..... 167

**Synthesis and Magnetic Properties of Novel Functionalized TbPc<sub>2</sub>**

8.1 Introduction.....	168
8.1.1 Phosphonate TbPc <sub>2</sub> .....	170
8.1.2 Clamshell TbPc <sub>2</sub> .....	171
8.1.3 Iodinated TbPc <sub>2</sub> .....	173
8.2 Results and Discussion.....	173
8.2.1 Synthesis of Phosphonate TbPc <sub>2</sub> .....	173
8.2.2 Synthesis of Clamshell TbPc <sub>2</sub> .....	179
8.2.3 Synthesis of Iodinated TbPc <sub>2</sub> .....	181
8.2.4 Magnetic Characterization.....	187
8.2.5 Sonogashira@TbPc <sub>2</sub> .....	190
8.3 Conclusions.....	194
8.4 Acknowledgements.....	194
8.5 Experimental Section.....	195
8.6 References.....	200

CHAPTER 9..... 203

**In Situ Metalation of Free Base Phthalocyanine Covalently Bonded to Silicon Surfaces**

9.1 Introduction.....	204
9.2 Results and Discussion.....	205
9.2.1 Synthesis of 1-Pc.....	205
9.2.2 XPS Characterization of Si-bonded Phthalocyanine.....	206
9.2.3 Metalation of SAM.....	209
9.3 Conclusions.....	212

9.4 Acknowledgements.....	212
9.5 Experimental Section.....	213
9.6 References.....	215
<b>Appendix A</b> .....	219
Materials and Methods.....	220
Acknowledgments.....	221
The Author.....	223



# Chapter 1

## Cavitands as Supramolecular Receptors



## 1.1 Supramolecular Chemistry

Beyond the molecules, supramolecular chemistry aims at developing highly complex chemical systems from different molecular components held together by non-covalent intermolecular forces.<sup>1</sup> Based on the principles of molecular recognition<sup>2</sup> and self-assembly,<sup>3</sup> the multidisciplinary domain of supramolecular chemistry is intrinsically dynamic, which allows the spontaneous but information-directed generation of organized structures under equilibrium conditions. The molecular recognition phenomena in biological systems started to be an interesting topic in the early seventies, after the accidental discovery of crown ethers by C. Pedersen.<sup>4</sup> In fact, in 1974 Lehn<sup>1</sup> and Cram<sup>5</sup> began to work on molecular receptors for small charged and neutral molecules. For their studies they were awarded with the Nobel Prize in 1987. In the 1990s, supramolecular chemistry became even more sophisticated, with researchers such as James Fraser Stoddart and Vincenzo Balzani developing molecular machinery and highly complex self-assembled structures.<sup>6</sup> 30 years of researches in this field have highlighted how the weak interactions are the glue and the key issue for the construction of chemical structures with higher and higher degree of complexity.

Nature offers the best source of inspiration for researchers, since self-assembly processes occur in everyday life and are optimized to a high degree by evolution.<sup>7</sup> Thanks to a constant and continuous development, supramolecular chemistry has expanded the playground of the researchers in the material science field. In this regard, thanks to its capability to manipulate the non-covalent intermolecular forces that hold together different constituents, supramolecular chemistry is a powerful strategy for the creation of new materials with outstanding properties. In fact, by mastering molecular recognition processes, chemists can impart and finely tune new active functions leading to advanced functional materials that are hardly achievable with other methods. Simple system are replaced by even more complex ones, building blocks become more intricate, with respect to both structure and function. Nowadays supramolecular chemistry is even more an application oriented science,<sup>8</sup> because it has a central role in the generation of structures capable of advanced tasks.

## 1.2 Molecular receptors

Molecular recognition is a key task of supramolecular chemistry: it has been defined as the process involving both binding and selection of a substrate (guest) by a given receptor molecule (host), as well as possibly a specific function. It implies a structurally well defined pattern of intermolecular interactions.<sup>9</sup> The selective binding of a substrate by a molecular receptor to form a complex is based on shape complementarity and the presence of specific weak interactions such as hydrogen bonding,<sup>10</sup>  $\pi$ - $\pi$  stacking,<sup>11</sup> and CH- $\pi$  interactions.<sup>12</sup> Design of molecular receptors has been made extending the "lock and key" theory (enunciated by Emil Fischer in 1894)<sup>13</sup> over energetical (electronic) as well as geometrical features. Indeed, as for biological systems, the concepts of size, shape and chemical complementarity are crucial for successful molecular recognition processes in artificial host-guest systems.

### 1.2.1 Tetraphosphonate Cavitands

Considerable attention has been paid to molecular receptors named cavitands. According to Cram, they are synthetic organic compounds having enforced cavities large enough to complex complementary organic molecules or ions.<sup>14</sup> They can be easily prepared by the acid-catalyzed condensation between resorcinol and either aliphatic or aromatic aldehydes (Figure 1.1).<sup>15</sup>

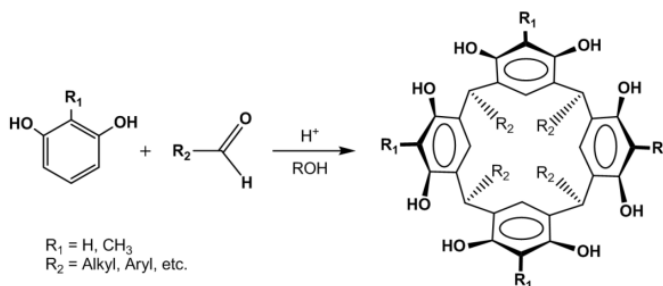


**Figure 1.1** *Synthesis of resorcin[4]arene.*

The choice of a different R group in the resorcinol or in the aldehyde ( $\text{R}_1$  or  $\text{R}_2$ ) provides different entry points for derivatization both at the upper and at the lower rim, that can be exploited in the molecular recognition process and in the design of the cavitand receptor. However, the resorcinarene scaffold is too flexible to be used in host-guest chemistry, whereas bridging the phenolic

groups with a proper functionality leads to a rigid cavity, improving complexation capability. The choice of the bridging groups is pivotal to determine shape, dimensions and complexation properties of the final cavitand. Among the possible bridging groups, phosphonate moieties impart special recognition features toward positively charged species such as alkaline-earth cations,<sup>16</sup> *N*-methylammonium or *N*-methylpyridinium species.<sup>17</sup> The presence of four stereogenic centers in the tetraphosphonate cavitands gives rise to six possible diastereomeric isomers, differing from each other for the orientation of the P=O moieties, inward (i) or outward (o) the cavity (Figure 1.2).<sup>18</sup>

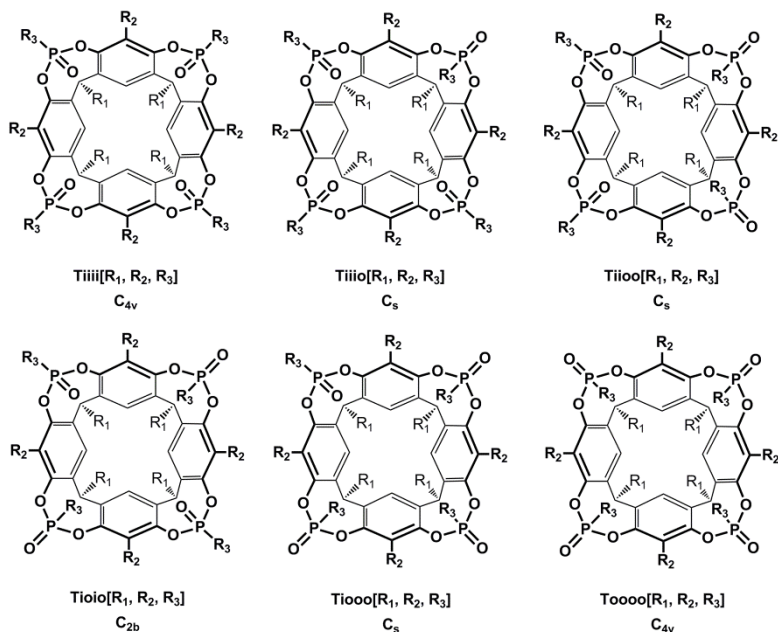


**Figure 1.2** Isomers of tetraphosphonate bridged cavitands.

The complexing capability is determined by stereochemistry: as shown in previous works,<sup>16,18,19</sup> increasing the number of P=O groups pointing inward the cavity leads to an enhancement of the molecular recognition properties. Therefore the cavitand that presents the best recognition properties is the one with all the four P=O moieties oriented inward with respect to the cavity (Tiiii). Considering the methyl-ammonium salts class as target guests, the main specific interactions responsible for its complexation ability, which can be activated either individually or in combination, are: (i) multiple ion-dipole interactions between the inward facing P=O and the positively charged species, (ii) single or multiple H-bonding involving the P=O groups and the nitrogen protons, and (iii) CH<sub>3</sub>- $\pi$  interactions between an acidic *N*-methyl group of the

guest and the  $\pi$ -basic cavity of the host. Figure 1.3 shows the complexation mode of tetraphosphonate cavitand towards *N*-methylpyridinium (left) and *N*-alkylammonium salts (right). In the first case the recognition process is driven by cation-dipole and CH- $\pi$  interactions, while in the second case all the three interactions operate in a synergistic fashion, causing the higher affinity of the *N*-methylammonium towards the cavity.<sup>20</sup>

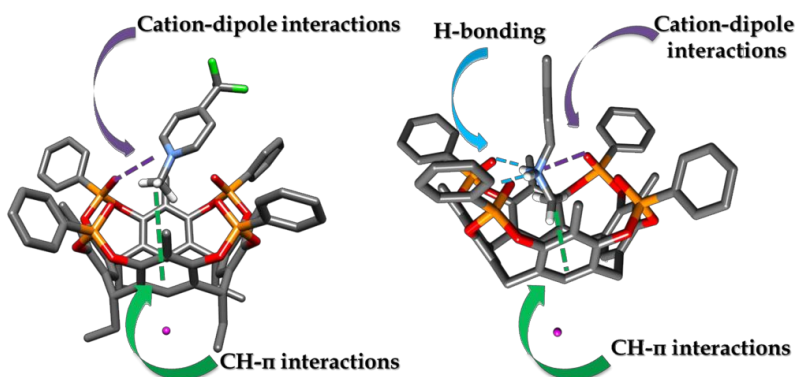


**Figure 1.3** Complexation mode of tetraphosphonate cavitands towards *N*-methylpyridinium salts (left) and *N*-methylammonium salts (right).

As already discussed, the complexation ability of tetraphosphonate cavitand is determined by its stereochemistry: from here the demand of an appropriate synthetic path leading to the phosphonate cavitand with all  $\text{P}=\text{O}$  groups oriented inward the cavity (**Tiiii**) as the major product. A two step reaction to synthesize the **Tiiii** stereoisomers in high yield (up to 90%) has been developed:<sup>21</sup> the reactions proceeds through the bridging of the resorcinarene scaffold with dichlorophenylphosphine in pyridine to form four P(III) units, followed by oxidation in situ with hydrogen peroxide (Figure 1.4). The stereospecificity of the reaction is related to the formation of an intermediate based on P(III), where all the electrons lone pairs point inside the cavity.<sup>22</sup>

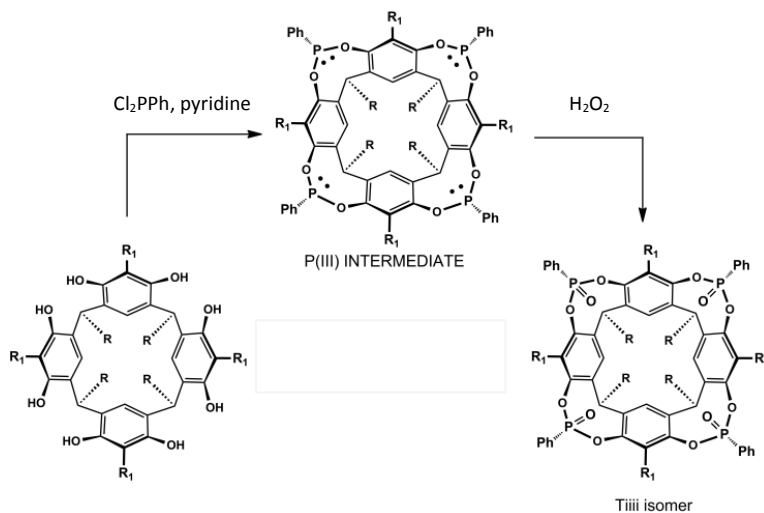


**Figure 1.4** *Tiiii* isomer synthesis via P(III) intermediate.

In our group we extensively studied the complexation properties of phosphonate cavitands toward organic guests in the solid state,<sup>19b,17</sup> in solution,<sup>23</sup> and in the gas phase.<sup>24</sup>

In 2012 we fruitfully exploited the molecular recognition properties of **Tiiii** cavitand to selectively detect sarcosine ( $K_a = 6.8 \pm 0.5 \times 10^4 \text{ M}^{-1}$  in MeOH, by ITC measurements), a methylated form of glycine, recently linked to the occurrence of aggressive prostate cancer forms,<sup>25</sup> in water and urine. The decisive step in this work was grafting the receptor on a silicon wafer (**Tiiii-Si**), hence transferring the complexation features of **Tiiii** onto the surface. The functionalized surface was tested in urine with XPS and fluorescence guest displacement tests that demonstrated the selectivity of **Tiiii-Si** towards sarcosine. In the same year we covalently functionalized single-walled carbon nanotubes (SWCNT's) with a tetraphosphonate cavitand receptor.<sup>26</sup> The resulting hybrid material was shown to function as chemiresistive sensor for the detection of sarcosine and its ethyl ester hydrochloride in water with high selectivity at concentrations as low as 0.02 mM. Exposure to sarcosine and its derivative resulted in an increased conductance, in contrast to a decreased conductance response observed for potential interferents such as the structurally related glycine ethyl ester hydrochloride. In a more recent work we developed a nanomechanical device able to detect the whole class of methamphetamine drugs independently of the type of residue attached to the  $^+\text{NH}_2\text{-CH}_3$  moiety.<sup>27</sup> The sensor showed extremely high selectivity in water, and it was successfully tested on a street sample.

In this Thesis, in Chapter 2, we exploit the ability of cavitand receptor **Tiii** to selectively recognize *N*-methylammonium hydrochloride group to realize multifunctional nanoparticles (MNPs) possessing magnetic, biocompatibility and drug load/release capabilities.

In Chapter 3 the tetraphosphonate cavitand-based MNPs system will be further improved by introducing new functionalities, making it suitable for multifunctional theranostic treatments.

## 1.2.2 Tetraquinoxaline Bridged-cavitands

Tetraquinoxaline cavitands (**QxCav**) are formed by bridging resorcinarene phenolic oxydryl groups in a nucleophilic aromatic substitution with dichloroquinoxaline moiety.<sup>28</sup> This kind of resorcinarene scaffold functionalization leads to a deep, hydrophobic and electron rich cavity, thanks to the presence of electron rich quinoxaline units. The quinoxaline spacers can occupy either axial or equatorial positions: thus the system is able to perform reversible switching between a closed “vase” conformation with a deep cavity, capable to guest complexation, and an open “kite” conformation with a flat extended surface (Figure 1.5) capable of inducing dimerization.<sup>29</sup>

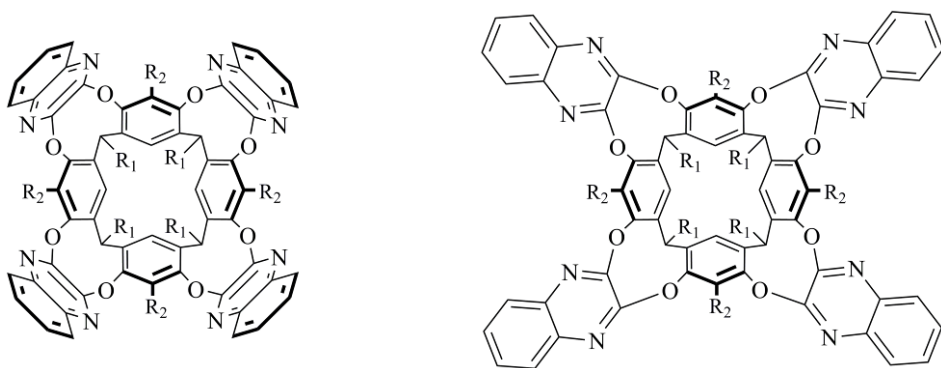


**Figure 1.5** Structure of quinoxaline cavitand vase conformer (left) and kite conformer (right).

Several factors influence the equilibrium between the two conformations: in compounds without methyl groups in apical position of the resorcinarene for instance, the vase and kite forms are equilibrating. At room temperature, in apolar solvents, only the close vase conformation can be detected by the <sup>1</sup>H NMR. Upon cooling, the population of the open and less symmetric kite form increases, until all cavitands are fully transformed at ≈ 230 K. This behavior is

due to the different solvation of the cavitand in its two geometrically conformations.<sup>30</sup> In the open kite form, the solvent-accessible surface is much larger than in the close one, so that much more solvent molecules can stabilize this molecule by non-covalent interactions. This kind of stabilization is effective only at low temperature, while at high temperature the less strained vase form dominates. In fact, interactions between solvent and cavitand result in a reduced solvent translational freedom, which determines an entropic loss that becomes too unfavourable at higher temperatures ( $\Delta G = \Delta H - T\Delta S$ ). Changing the pH is another effective method to exert dynamic control over the kite-vase equilibrium.<sup>31</sup> Since the quinoxaline nitrogen atoms are weakly basic ( $pK_a$  293 K = 0.56),<sup>32</sup> addition of a strong acid, such as  $CF_3COOH$  ( $pK_a$  at 293 K = 0.52) protonates them, inducing repulsive forces that lead the cavitand to assume the kite conformation, where the positive charges are moved apart from each other (Figure 1.6).

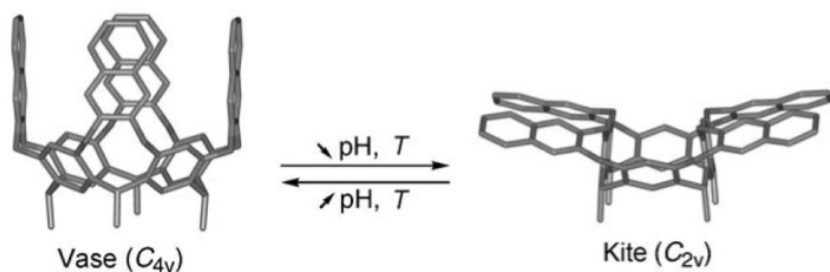
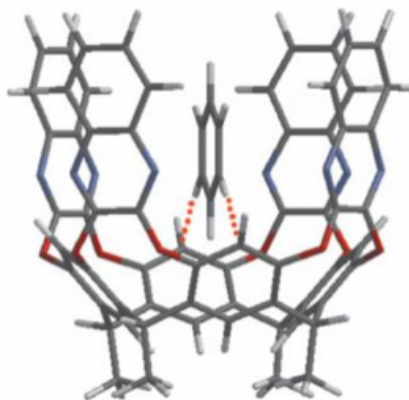


Figure 1.6 Kite-vase equilibrium for quinoxaline cavitand.

In the vase conformer the spacers touch each other via their  $\alpha$ -hydrogens while forming a box like cavity with  $C_{4v}$  symmetry which is approximately 7 Å wide and 8 Å deep.<sup>33</sup> The cavity is open at the top and closed at the bottom by the cavitand itself. In the kite conformer, the spacers are more or less in the same plane.

Tetraquinoxaline cavitands in the vase conformation present strong affinity toward aromatic guests inclusion. Theoretical calculations evidenced the presence of multiple electrostatic and  $CH-\pi$  interactions as the driving force for the complexation of aromatic guests (Figure 1.7).<sup>34</sup> In particular the complexation properties of **QxCav** toward aromatic compounds have been demonstrated both in solution<sup>35</sup> and in the gas phase.<sup>36</sup>



**Figure 1.7** Geometry-optimized structure of QxCav–benzene complex.

Our group developed several applications based on quinoxaline cavitands to detect benzene and other aromatic hydrocarbons in air at trace level, even in presence of other airborne pollutants.<sup>34,37</sup> In particular, in collaboration with Dr. Stefano Zampolli from CNR-Bologna, we realized a portable, stand-alone mini GC device that was successfully employed for real-world sub-ppb level monitoring of aromatic volatile organic compounds concentrations (Figure 1.8).<sup>38</sup>



**Figure 1.8** Photograph of the complete monitoring system with a pencil for size comparison.



Moreover we demonstrated that the functionalization at the upper rim of **QxCav** cavity can be exploited in order to enhance selectivity towards included guests.<sup>35e,36</sup> In particular, by employing a **QxCav** functionalized with a carboxylic group at the upper rim, we developed a selective cavitand-based solid-phase microextraction coating for the determination of nitroaromatic explosives and explosive taggants at trace levels in air and soil.<sup>39</sup>

In this Thesis, the enhanced selectivity and sensitivity of a triptycene-functionalized **QxCav** towards benzene and other aromatic hydrocarbons will be investigated in Chapter 4.

### 1.3 References

- <sup>1</sup> J. M. Lehn, *Angew Chem. Int. Ed.* **1988**, 27, 89-112.
- <sup>2</sup> J. M. Lehn, *Science* **2002**, 295, 2400-2403.
- <sup>3</sup> a) G. M. Whitesides, J. P. Mathias, C. T. Seto, *Science* **1991**, 254, 1312-1319; b) G. M. Whitesides, M. Boncheva, *Proc. Natl. Acad. Sci. U.S.A.* **2002**, 99, 4796-4774.
- <sup>4</sup> a) C. J. Pedersen, *J. Am. Chem. Soc.* **1967**, 89, 7017-7036; b) C. J. Pedersen, *Angew. Chem. Int. Ed.* **1988**, 1021-1027.
- <sup>5</sup> D. J. Cram, *Angew. Chem. Int. Ed.* **1988**, 27, 1009-1020.
- <sup>6</sup> V. Balzani, M. Gómez-López, J. F. Stoddart, *Acc. Chem. Res.* **1998**, 31, 405-414.
- <sup>7</sup> L. Stryer, *Biochemistry 4th Ed.* **1995**, W.H. Freeman & Company, New York.
- <sup>8</sup> a) X. Yan, F. Wang, B. Zheng, F. Huang, *Chem. Soc. Rev.* **2012**, 41, 6042-6065; b) K. Liu, Y. Kang, Z. Wang, X. Zhang, *Adv. Mater.* **2013**, 25, 5530-5548.
- <sup>9</sup> J. M. Lehn, *Nobel lecture* **1987**.
- <sup>10</sup> J. Rebek, *Angew. Chem. Int.* **1990**, 29, 245-255.
- <sup>11</sup> C. H. Hunter, K. R. Lawson, J. Perkins, C. J. Urch, *J. Chem. Soc., Perkin Trans.* **2001**, 2, 651-669.
- <sup>12</sup> M. Nishio, M. Hirota, Y. Umezawa, *The CH- $\pi$  Interactions* **1998**, Wiley-VCH, New York.
- <sup>13</sup> E. Fischer, *Ber. Dtsch. Chem. Ges.* **1894**, 27, 2985-2993.
- <sup>14</sup> D. J. Cram, J. M. Cram, *In Container Molecules and Their Guests* **1994**, The Royal Society of Chemistry, Cambridge, Chapter 5.

- <sup>15</sup> L. M. Tunstad, J. A. Tucker, E. Dalcanale, J. Weiser, J. A. Bryant, J. C. Sherman, R. C. Helgeson, C. B. Knobler, D. J. Cram, *J. Org. Chem.* **1989**, *54*, 1305-1312.
- <sup>16</sup> a) P. Delangle, J.-C. Mulatier, B. Tinant, J.-P. Declercq, J.-P. Dutasta, *Eur. J. Org. Chem.* **2001**, 3695-3704; b) J.-P. Dutasta, *Top. Curr. Chem.* **2004**, *232*, 55-91.
- <sup>17</sup> E. Biavardi, M. Favazza, A. Motta, I. L. Fragalà, C. Massera, L. Prodi, M. Montalti, M. Melegari, G. C. Condorelli, E. Dalcanale, *J. Am. Chem. Soc.* **2009**, *131*, 7447-7455.
- <sup>18</sup> R. Pinalli, M. Suman, E. Dalcanale, *Eur. J. Org. Chem.* **2004**, 451-462.
- <sup>19</sup> a) R. Pinalli, F. F. Nachtigall, F. Ugozzoli, E. Dalcanale, *Angew. Chem., Int. Ed.* **1999**, *38*, 2377-2380; b) M. Melegari, M. Suman, L. Pirondini, D. Moiani, C. Massera, F. Ugozzoli, E. Kalenius, P. Vainiotalo, J.-C. Mulatier, J.-P. Dutasta, E. Dalcanale, *Chem. Eur. J.* **2008**, *14*, 5772-5779.
- <sup>20</sup> D. Menozzi, E. Biavardi, C. Massera, F. P. Schmidtchen, A. Cornia, E. Dalcanale, *Supramol. Chem.* **2010**, *22*, 768-775
- <sup>21</sup> E. E. Nifant'ev, V. I. Maslennikova, R. V. Merkulov, *Acc. Chem. Res.* **2005**, *38*, 108-116.
- <sup>22</sup> W. Xu, J. P. Rourke, R. J. Puddephatt, *J. Chem. Soc., Chem. Commun.* **1993**, 145-147.
- <sup>23</sup> E. Biavardi, G. Battistini, M. Montalti, R. M. Yebeutchou, L. Prodi, E. Dalcanale, *Chem. Commun.* **2008**, 1638-1640.
- <sup>24</sup> E. Kalenius, D. Moiani, E. Dalcanale, P. Vainiotalo, *Chem. Commun.* **2007**, 3865-3867.
- <sup>25</sup> A. Sreekumar, L. M. Poisson, T. M. Rajendiran, A. P. Khan, Q. Cao, J. Yu, B. Laxman, R. Mehra, R. J. Lonigro, Y. Li, M. K. Nyati, A. Ahsan, S. Kalyana-Sundaram, B. Han, X. Cao, J. Byun, G. S. Omenn, D. Ghosh, S. Pennathur, D. C.

Alexander, A. Berger, J. R. Shuster, J. T. Wei, S. Varambally, C. Beeche, A. M. Chinnaiyan, *Nature* **2009**, 457, 910-914.

<sup>26</sup> M. Dionisio, J. M. Schnorr, V. K. Michaelis, R. G. Griffin, T. M. Swager, E. Dalcanale, *J. Am. Chem. Soc.* **2012**, 134, 6540-6543.

<sup>27</sup> E. Biavardi, S. Federici, C. Tudisco, D. Menozzi, C. Massera, A. Sottini, G. G. Condorelli, P. Bergese, E. Dalcanale, *Angew. Chem. Int. Ed.* **2014**, 53, 1-7.

<sup>28</sup> a) J. R. Moran, S. Karbach, D. J. Cram, *J. Am. Chem. Soc.* **1982**, 104, 5826-5828; b) J. A. Bryant, J. L. Ericson, D. J. Cram, *J. Am. Chem. Soc.* **1990**, 112, 1255-1256; c) D. J. Cram, H. J. Choi, J. A. Bryant, C. B. Knobler, *J. Am. Chem. Soc.* **1992**, 114, 7748-7765.

<sup>29</sup> P. Roncucci, L. Pirondini, G. Paderni, C. Massera, E. Dalcanale, V. A. Azov, F. Diederich, *Chem. Eur. J.* **2006**, 12, 4775-4784.

<sup>30</sup> V. A. Azov, B. Jaun, F. Diederich, *Helv. Chim. Acta* **2004**, 87, 449-462.

<sup>31</sup> P. J. Skinner, A. G. Cheetham, A. Beeby, V. Gramlich, F. Diederich, *Helv. Chim. Acta* **2001**, 84, 2146-2153.

<sup>32</sup> *CRC Handbook of Chemistry and Physics* (Ed. D. R. Lide) **2005**, Taylor & Francis, Boca Raton, FL, USA.

<sup>33</sup> E. Dalcanale, P. Soncini, G. Bacchilega, F. Uguzzoli *J. Chem. Soc., Chem. Commun.* **1989**, 500-502.

<sup>34</sup> F. Bianchi, R. Pinalli, F. Uguzzoli, S. Spera, M. Careri, E. Dalcanale, *New J. Chem.* **2003**, 27, 502-509.

<sup>35</sup> a) D. J. Cram, S. Karbach, H. E. Kim, C. B. Knobler, E. F. Maverick, J. L. Ericson, R. C. Helgeson, *J. Am. Chem. Soc.* **1988**, 110, 2229-2237; b) J. A. Tucker, C. B. Knobler, K. N. Trueblood, D. J. Cram, *J. Am. Chem. Soc.* **1989**, 111, 3688-3689; d) J. R. Moran, J. L. Ericson, E. Dalcanale, J. A. Bryant, C. B. Knobler and D. J. Cram, *J. Am. Chem. Soc.* **1991**, 113, 5707-5714; e) P. Soncini, S. Bonsignore, E. Dalcanale and F. Uguzzoli, *J. Org. Chem.* **1992**, 57, 4608-4612.

<sup>36</sup> a) M. Vincenti, E. Dalcanale, P. Soncini, G. Guglielmetti, *J. Am. Chem. Soc.* **1990**, *112*, 445-447; b) M. Vincenti, E. Pelizzetti, E. Dalcanale, P. Soncini, *Pure Appl. Chem.* **1993**, *65*, 1507-1512; c) M. Vincenti, E. Dalcanale, *J. Chem. Soc., Perkin Trans.* **1995**, *2*, 1069-1076; d) M. Vincenti, A. Irico E. Dalcanale, *Advances in Mass Spectrometry* **1998**, Elsevier Science Publishers B. V., Amsterdam, vol. 14, p. 129.

<sup>37</sup> a) G. G. Condorelli, A. Motta, M. Favazza, E. Gurrieri, P. Betti, E. Dalcanale *Chem. Commun.* **2010**, *46*, 288-290; b) F. Bianchi, M. Mattarozzi, P. Betti, F. Bisceglie, M. Careri, A. Mangia, L. Sidisky, S. Ongarato, E. Dalcanale, *Analytical Chemistry* **2008**, *80*, 6423-6430.

<sup>38</sup> a) S. Zampolli, I. Elmi, F. Mancarella, P. Betti, E. Dalcanale, G. C. Cardinali, M. Severi, *Sens. Actuators B* **2009**, *141*, 322-328; b) S. Zampolli, P. Betti, I. Elmi, E. Dalcanale, *Chem. Commun.* **2007**, 2790-2792.

<sup>39</sup> F. Bianchi, A. Bedini, N. Riboni, R. Pinalli, A. Gregori, L. Sidisky, E. Dalcanale, M. Careri, *Anal. Chem.* **2014**, *86*, 10646-10652.

# Chapter 2

## Functionalization of PEGylated Fe<sub>3</sub>O<sub>4</sub> Magnetic Nanoparticles with Tetraphosphonate Cavitanol for Biomedical Application<sup>\*</sup>

<sup>\*</sup> This chapter has been published in *Nanoscale*: C. Tudisco, F. Bertani, M. T. Cambria, F. Sinatra, E. Fantechi, C. Innocenti, C. Sangregorio, E. Dalcanale, G. G. Condorelli, *Nanoscale* **2013**, *5*, 11438-11446.

## 2.1 Introduction

Magnetic nanoparticles (MNPs) have attracted enormous attention for their potential use in the biomedical field for both diagnostic and therapeutic applications<sup>1</sup> such as controlled drug delivery,<sup>2</sup> cell separation,<sup>3</sup> magnetic resonance imaging (MRI),<sup>4</sup> localized hyperthermia for cancer therapy (MFH),<sup>5</sup> biosensing<sup>6</sup> and detoxification of biological fluids.<sup>7</sup> The intrinsic multifunctionality due to the combination of superparamagnetic properties with biocompatibility and biological activity provided by the specific coatings of the superparamagnetic core is the most attractive aspect of MNPs. The search of new MNPs pointed to two objectives: the improvement of the efficiency of the superparamagnetic core<sup>8</sup> and the development of versatile, active and stable coatings which represent the functional interface between MNPs and the biological environment.<sup>9</sup> Since surface plays a pivotal role in determining the interaction between the MNP and its biological target, the quality of the functionalization of MNPs surface is crucial to a successful application in the biological field. For this reason, the present decade has seen a surge of interest in functionalization studies of magnetic metal oxides with biocompatible coatings such as PEG,<sup>10</sup> cyclodextrins,<sup>11</sup> and dextrane<sup>12</sup> based on polymeric films or on covalently bonded molecular monolayers<sup>13</sup> usually acting as linker between the surface and the activemolecules.

In this context, we describe the synthesis of new multifunctional organic-inorganic MNPs, which possess suitable biocompatibility and hyperthermic capability, and are designed to load, carry and release of *N*-methylated drugs and biomolecules. The synthesized MNPs consist of a Fe<sub>3</sub>O<sub>4</sub> core covalently coated with a mixed monolayer of PEG and tetraphosphonate cavitand. The key strength of the new system lies in the highly selective recognition properties of the tetraphosphonatecavitands (Ti<sub>iiii</sub>), towards *N*-methyl ammonium salts. Cavitands, synthetic organic compounds with resorcinarene-based cavities of molecular dimensions, are well-known molecular receptors,<sup>14</sup> and, in particular, the complexation properties of Ti<sub>iiii</sub>,<sup>15</sup> in which four P=O bridging groups connect the phenolic hydroxyls of the resorcinarene scaffold, have been extensively studied in the solid state,<sup>16</sup> in solution,<sup>17</sup> and in the gas phase.<sup>18</sup> The main specific interactions responsible for the recognition of methyl ammonium salts evidenced by these studies are H-bonding, cation-dipole and CH<sub>3</sub>- $\pi$  interactions. The removal of the last two interactions upon deprotonation leads to the complete release of the guests as free bases. The potential of cavitand receptors is fully exploited through their surface grafting<sup>19</sup> since the solid surface allows the occurrence of recognition events to otherwise

inaccessible solvents, precluded by Tiii insolubility in them. Tiii surface grafting on silicon slides recently allowed the use of this hydrophobic receptor in the detection of sarcosine, the *N*-methylated analogue of glycine which was indicated as prostate cancer biomarker,<sup>20</sup> directly in biological fluids (urine).<sup>21</sup> In the present work, Fe<sub>3</sub>O<sub>4</sub> MNPs have been synthesized through coprecipitation method, and then functionalized with Tiii and polyethylene glycol (PEG). The aim was to introduce Tiii recognition properties in a system suited for “*in vivo*” applications (drug delivery) made of superparamagnetic and biocompatible PEGylated MNPs, through an efficient synthetic route. The synthetic approach is based on MNPs pre-functionalization with the alkynylphosphonic monolayer formed by 10-undecynylphosphonic acid (alkyne), followed by the surface reaction *via* “click-chemistry” of the alkyne termination of the monolayer with the tetraphosphonatecavitand (Tiii-N<sub>3</sub>) and a PEG (PEG-N<sub>3</sub>), both bearing an azide moiety. The copper(I) catalysed azide-alkyne cycloaddition (CuAAC), known as “click chemistry”,<sup>22</sup> involves 1,3-dipolar cycloaddition between azides and terminal alkynes to form 1,2,3-triazoles. This reaction has several advantages for surface functionalization:<sup>23</sup> (1) high chemoselectivity; (2) high yield; (3) no requirement of temperature or pressure control; (4) easy accessibility of the two active functional groups (azide and alkyne groups) and (5) an irreversible nature that results in a stable linkage, because of the formation of a 1,2,3-triazole ring. Two different types of MNPs functionalized with Tiii and PEG (Tiii-PEG-Alkyne@MNPs), were obtained using PEG oligomers with molecular weight (MW) either of 1000 or 5000 Dalton. PEG was introduced onto MNPs to overcome water solubility problems of Tiii-coated MNPs due to the Tiii hydrophobic cavity. In addition, PEG coatings reduce reticuloendothelial system (RES) clearance, reduce toxicity, decrease enzymatic degradation, and can thereby increase the stability of nanoparticles, prolonging their circulation half-life *in vivo*.<sup>10,24</sup> The obtained Tiii and PEG (1000 or 5000 Da) decorated MNPs (Tiii-PEG-Alkyne@MNPs), were characterized by X-ray photoelectron spectroscopy (XPS) and FTIR spectroscopy. Biocompatibility of Tiii-PEG-Alkyne@MNPs was measured and compared using two different cell lines, LoVo (Human colon adenocarcinoma cell line) and BM18 (mesenchyme cell line). The ability of Tiii-functionalized nanoparticles to carry *N*-methylated drugs as salts and slowly release them as free bases has been tested adopting procarbazine hydrochloride (PCZ·HCl), a useful anti-neoplastic agent in the treatment of several malignancies,<sup>25</sup> and epinephrine hydrochloride (EPN·HCl), a catecholamine neurotransmitter (known as adrenaline) in mammalian central nervous systems, which is also used to treat various pathologic conditions.<sup>26</sup>



## 2.2 Results and Discussion

### 2.2.1 Bare MNPs

The structure and cristallinity of the bare MNPs (see Experimental Section for the synthesis) were investigated by Powder X-ray diffractometry (Figure 2.1). The position and relative intensity of all diffraction peaks ( $2\theta$  reflections: 30.1, 35.5, 43.1, 57.0, 62.7°) well matched those of the standard PDF card for magnetite (19-0629), maghemite (39-1346) or any intermediate composition between the two phases, and could be indexed as (220), (311), (400), (511) and (440), respectively. The lattice constant,  $a$ , was found to be 8.378 Å, close to the lattice parameter of bulk magnetite (8.396 Å). The small discrepancy can be ascribed to a slight oxidation of surface ferrous ions. The crystallite size has been evaluated at the full-width at half maximum of the strongest reflection of the (311) peak, using the Debye-Scherrer equation ( $D = 0.9\lambda/\beta \cos\theta$ ), where  $D$  is the average crystallite size (nm),  $\lambda$  is the X-ray wavelength (nm),  $\theta$  and  $\beta$  are the Bragg angle (radians) and the excess line broadening (radians), respectively. The average particle size for bare MNPs is about 12 nm.

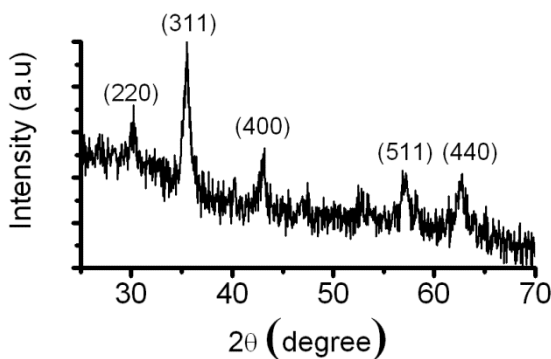
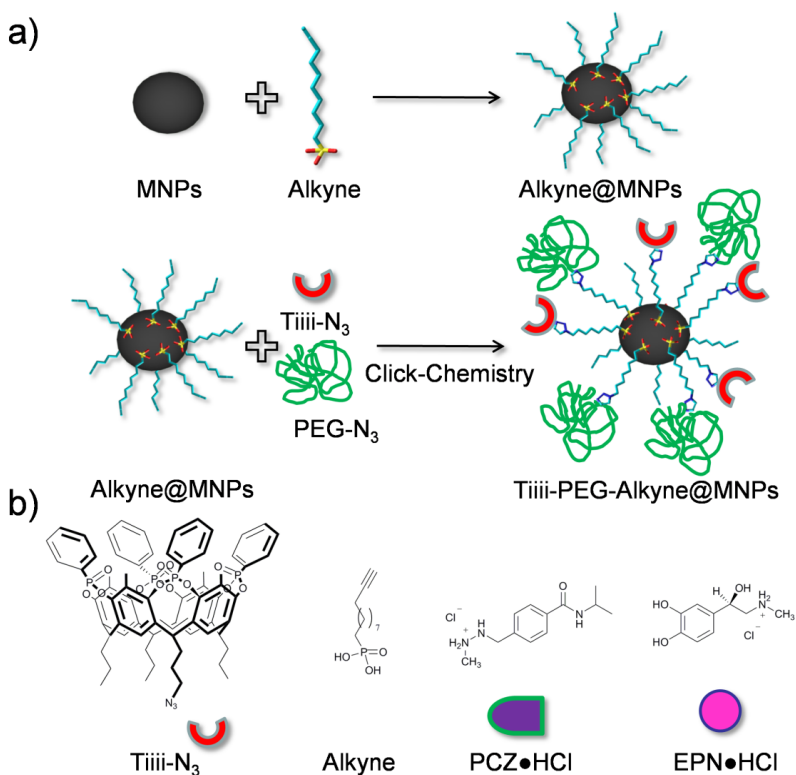


Figure 2.1 XRD pattern of bare MNPs.

### 2.2.2 Synthesis and Characterization of Functionalized MNPs

The two-step synthetic route to obtain Tiiii-PEG-Alkyne@MNPs is illustrated in Scheme 2.1. In order to covalently immobilize the Tiiii cavitand and PEG on the MNPs surface through CuAAC reaction, MNPs functionalized with monolayers having terminal acetylenic groups have been firstly prepared.

Therefore a phosphonic acid, able to covalently anchoring on MNPs surface through P-O-Fe bonds and bearing a terminal acetylene group was grafted on MNPs (Alkyne@MNPs) in the first step. Tiii and PEG molecules (either with MW. 1000 or 5000 Da) bearing an azide group were bonded on alkyne pre-functionalized MNPs using Cu(I)-catalyzed 1,3-dipolar cycloaddition reaction. All MNPs obtained in the first and second step, Alkyne@MNPs and Tiii-PEG-Alkyne@MNPs, have been characterized by XPS and FTIR. Note, however, that since characterizations of MNPs obtained adopting either PEG 1000 Da or PEG 5000 Da are similar, only XPS and FTIR spectra of Tiii-PEG(1000 Da)-Alkyne@MNPs are reported, although results are valid for both PEG 1000 Da and 5000 Da.



**Scheme 2.1** (a) Reaction steps for the preparation of functionalized-MNPs; (b) structure of cavitand, phosphonic acid grafting agent and the drugs used in their complexed salt form.

Figure 2.2 shows the FT-IR spectra in the 750-1300 cm<sup>-1</sup> (right) and in the 2200-2000 cm<sup>-1</sup> region (left) of bare MNPs, Alkyne@MNPs, Tiii-PEG-Alkyne@MNPs,

and the powders of Tiii-N<sub>3</sub> and PEG-N<sub>3</sub>. In the FT-IR spectrum of Alkyne@MNPs, the absence of the P=O stretches (1254 cm<sup>-1</sup>) and P-O-H stretches (920 cm<sup>-1</sup>) typical of phosphonic acid powders<sup>11,15b,27</sup> and the presence of a single broad and strong band at *ca.* 1040 cm<sup>-1</sup> due to the phosphate bonding group indicate that the phosphonic acids anchor through multidentate bonding with the surface,<sup>11</sup> which involves both P=O and P-O-terminations. FT-IR spectra of Tiii-PEG-Alkyne@MNPs show the increase of a broad band between 1150 and 950 cm<sup>-1</sup> due to presence of P-O-C of the cavitand and the overlapped C-O-C stretching of PEG. In addition, we can observe the presence of new features at 1256 cm<sup>-1</sup> and 803 cm<sup>-1</sup> due to the free P=O stretches and to O-P-O vibrations of the Tiii cavitand, respectively.

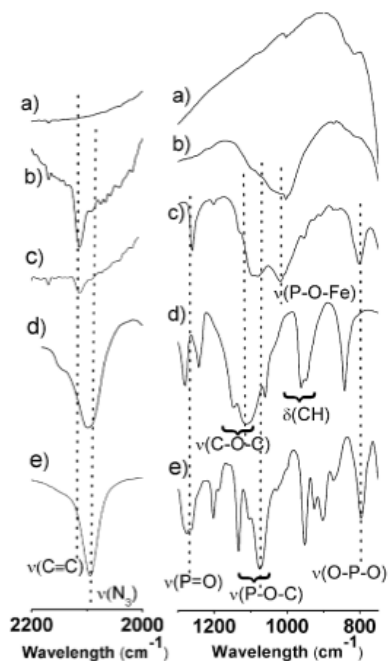


**Figure 2.2** FT-IR spectral regions in the 2000–2200 cm<sup>-1</sup> (left) and 750–1300 cm<sup>-1</sup> (right) ranges of (a) bare MNPs, (b) Alkyne@MNPs, (c) Tiii-PEG-Alkyne@MNPs, (d) PEG-N<sub>3</sub>, and (e) Tiii-N<sub>3</sub>.

In the FT-IR spectra of Alkyne@MNPs the presence of the characteristic absorption peak of alkyne group at 2108 cm<sup>-1</sup>, which is absent in the spectra of bare MNPs, suggests that anchoring process preserves the active alkyne terminated groups.<sup>28</sup> After the subsequent click chemistry reaction, in Tiii-

PEG-Alkyne@MNPs spectra, the decrease of this alkyne characteristic band indicates the successful proceeding of “click reaction”. Furthermore, the absence of stretching vibration of azido groups at 2075 cm<sup>-1</sup> in the spectrum of Tiiii-PEG-Alkyne@MNPs ruled out any possible physisorption of Tiiii-N<sub>3</sub> or PEG-N<sub>3</sub> on MNPs surface.

XPS P 2p, N 1s, C 1s and O 1s spectral regions of (a) Alkyne@MNPs and (b) Tiiii-PEG-Alkyne@MNPs are shown in Figure 2.3.

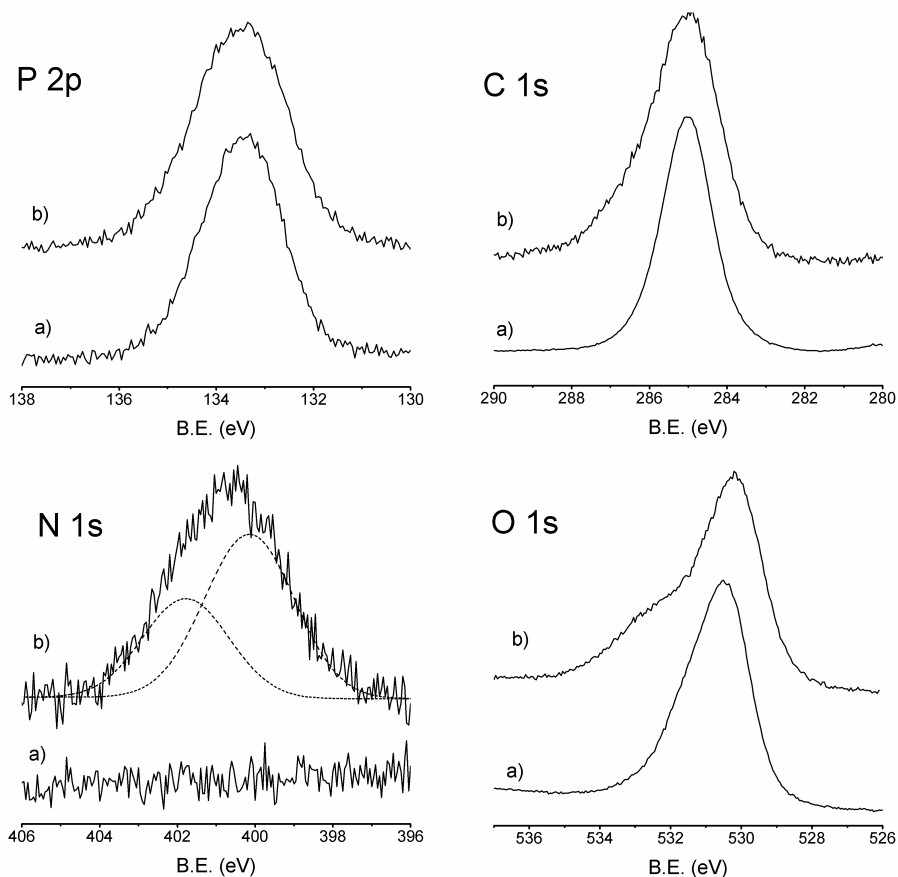


**Figure 2.3** High resolution P 2p, N 1s, C 1s and O 1s XPS spectral regions of a) Alkyne@MNPs and b) Tiiii-PEG-Alkyne@MNPs.

The presence and the position of the P 2p band is a reliable indicator to evaluate the grafting process of the phosphonic acid. P 2p peak of Alkyne@MNPs is observed at 133.2 eV. This value, which is about 0.9 eV lower than the value observed for undissociated -PO<sub>3</sub>H<sub>2</sub> groups, is associated with the deprotonation of -POH terminations, which leads to the occurrence of two P-O-

Fe bonds. After Tiii and PEG grafting, P 2p band of Tiii-PEG-Alkyne@MNPs is still centered at 133.2 eV, thus indicating that the anchored phosphonic acid is not removed by the click reaction. However, the band shape shows a broadening towards higher B.E. which can be explained by the presence of the expected component around 134 eV due to tetraphosphonic bridge of Tiii. The N 1s spectral regions of Alkyne@MNPs and Tiii-PEG-Alkyne@MNPs are shown in Figure 2.2. As expected, no N 1s signal is present on Alkyne@MNPs, whilst a N 1s peak centred at 401 eV is observed after click reaction. The band shape is broad, suggesting the presence of different nitrogen atoms consistently with the formation of a triazole moiety from the fusion of azido species with the acetylene-decorated surface. The N 1s signal can be deconvoluted into two peaks due to N-N\*=N\*(N\* at 400.2 eV) and N\*-N=N(N\* at 401.7 eV) with a 2:1 intensity ratio.<sup>29</sup> No signal was present at 405 eV, corresponding to the central, electron deficient N atom of the azido group, thus indicating that no physisorption of Tiii-N<sub>3</sub> or PEG-N<sub>3</sub> occurs. In the high-resolution C 1s region of Alkyne@MNPs is present a single contribution at 285.0 eV, assigned only to aliphatic carbons. In the spectra of Tiii-PEG-Alkyne@MNPs beside the main peak at 285.0 eV due to aliphatic and aromatic carbons, there is an evident shoulder around 286 eV due to the presence of the oxygen-bonded carbons of Tiii and PEG.<sup>30</sup> In addition, quantitative XPS analysis indicates a significant increase of C amount on the surface in Tiii-PEG-Alkyne@MNPs. O 1s XPS spectra of Alkyne@MNPs mainly consist of a component at 530.2 eV due to the iron oxide cores. After the addition of Tiii and PEG a new component at 532.2 eV becomes evident due to the PEG oxygens.

On the basis of the overall XPS and FTIR results, it could be concluded that Tiii-N<sub>3</sub> and PEG-N<sub>3</sub> have been successfully grafted on Alkyne@MNPs through click chemistry reaction.

In Figure 2.4 a typical TEM micrograph of the Tiii-PEG-Alkyne@MNPs is shown. The sample is composed of almost spherical nanoparticles with a mean diameter of  $10.8 \pm 3.5$  nm. The diameter size distribution obtained from a statistical analysis over *ca.* 400 nanoparticles, reported in the inset of Figure 2.4, can be nicely fitted to a log-normal function, as commonly observed for nanoparticles prepared with wet-chemical techniques. The best fit parameters gives a mean diameter of 10.3 nm ( $\sigma = 0.32$ ), which is in agreement with the value obtained from direct statistics.

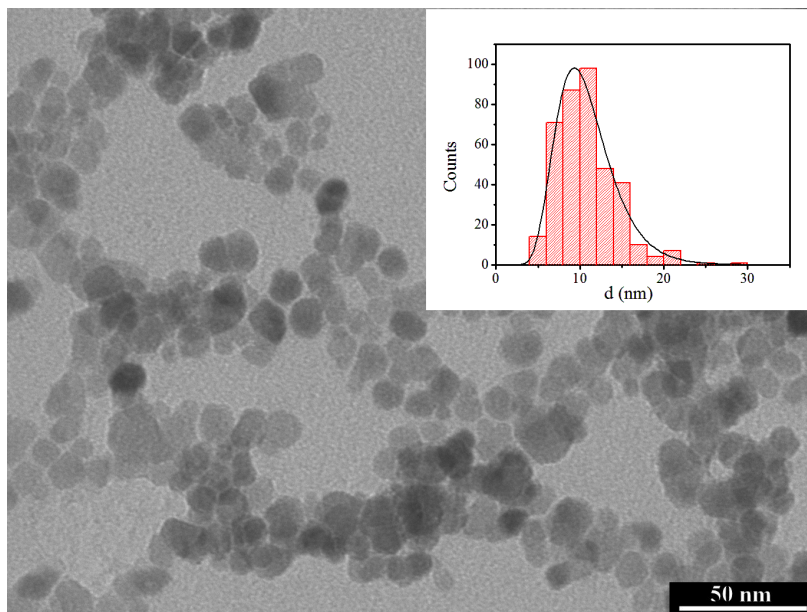


**Figure 2.4** TEM image of Tiii-PEG-Alkyne@MNPs. In the inset, the size distribution over ca. 400 nanoparticles is reported; the continuous line represents the best fit curve to a log-normal distribution.

The magnetic properties of Tiii-PEG-Alkyne@MNPs were investigated both as a function of temperature and magnetic field. In Figure 2.5a are reported the zero-field cooled (ZFC) and field-cooled (FC) magnetizations as a function of temperature: the sample shows thermal irreversibility characteristic of an ensemble of single domain MNPs of few tens of nanometers. However, the blocking temperature,  $T_B$ , commonly identified as the maximum of the ZFC curve, is higher than room temperature and is clearly not reached in the investigated temperature range.

In Figure 2.5b are reported the  $M$  vs.  $H$  curves recorded at low temperature (2.5 K) and at room temperature (300 K). At low temperature, the magnetization curve shows hysteresis (see magnification in the inset of Figure 5b) with a

coercive field of  $\mu_0 H_C = 26.7$  mT and a remnant magnetization,  $M_R = \frac{M_{0T}}{M_{5T}}$ ,

0.39. This value is slightly lower than the one expected for a set of isolated uniaxial nanoparticles whose easy axis are isotropically orientated (0.5), a behaviour that is commonly observed in iron oxides NPs and can be also influenced by the presence of magnetic interparticle interactions.<sup>31</sup> At room temperature (300 K), neither hysteresis nor coercivity was observed. The

saturation magnetization values,  $M_s$ , estimated by fitting the curve to the empirical law,<sup>32</sup>  $M = M_s + \frac{a}{H} + \frac{b}{H^2}$ , at high fields, are 75 and 67 emu/g<sup>-1</sup>, for 2.5 and 300 K, respectively, which are *ca.* 25% smaller than those observed for bulk magnetite,<sup>33</sup> although quite large if compared to the data reported in the literature for nanosized iron oxides. The reduction of  $M_s$  in nanosized magnetic materials can be attributed to the presence of a dead spin layer on the surface,<sup>34</sup> whose contribution become more and more significant with size reduction.

The magnetic anisotropy constant,  $K_{eff}$ , evaluated from the low temperature magnetization curve as  $K_{eff} = \frac{H_C M_s}{0.96}$ , is 9.6 kJ/m<sup>3</sup> which is in good agreement with the value of bulk magnetite (11.0 kJ/m<sup>3</sup>).<sup>34</sup>

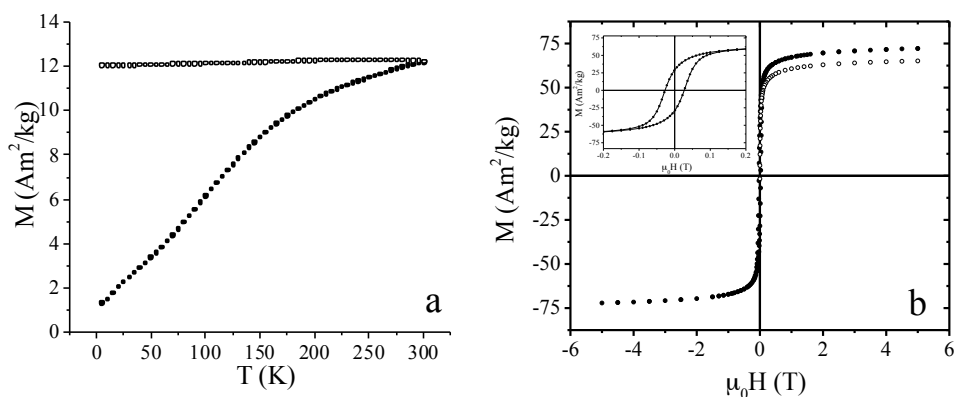


**Figure 2.5** a) Temperature dependence of the ZFC (full circles) and FC (open circles) magnetizations of Tiii-PEG-Alkyne@MNPs, measured under the field of 5 mT; b)  $M$  vs.  $H$  curves of Tiii-PEG-Alkyne@MNPs, measured at 2.5 K (full circles) and 300 K (open circles). In the inset of b) is reported the low temperature curve magnification in the low field region.

The mean hydrodynamic sizes of functionalized MNPs were determined by DLS in PBS (pH 6.8) (Fig. 2.6a). The hydrodynamic size distributions of Tiii-PEG-Alkyne@MNPs coated with PEG 1000 or 5000 Da were centered at 70 nm and 80 nm, respectively. However, the broadening of the size distribution towards larger values in Tiii-PEG(1000)-Alkyne@MNPs suggests the occurrence of some aggregations for low MW coating. Note that a comparison with the hydrodynamic size of naked Fe<sub>3</sub>O<sub>4</sub> NPs in PBS was not possible since severe aggregation was observed at pH = 6.8, which is very close to the Fe<sub>3</sub>O<sub>4</sub>

isoelectric point (pH = 6.2). The hydrodynamic size of naked MNPs obtained in alkaline solution (pH = 11) was 70 nm. The zeta potential of both Tiiii-PEG-Alkyne@MNPs coated with PEG 1000 or 5000 Da was determined as a function of the pH (Fig. 2.6b). Zeta potential vs. pH trends are similar for the two PEGs with different lengths (1000 or 5000 Da), with close isoelectric points (at pH = 2.4 and 2.9 for PEG 5000 and 1000 Da, respectively) and a zeta potential in the physiologic pH range around -30 mV. The low values on the isoelectric points and, therefore, the negative values of the zeta potential in the physiological pH range, are mainly due to the negatively charged core and the effect of the phosphonic acid prefunctionalization which further shifts the isoelectric point to lower values.<sup>13c</sup>

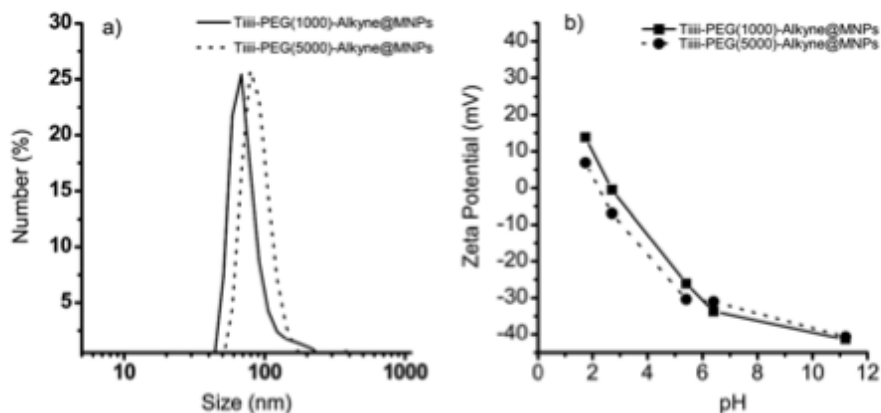


**Figure 2.6** a) Size distribution in PBS and b) zeta potential as a function of pH of Tiiii-PEG-Alkyne@MNPs coated with PEG 1000 (solid line) or 5000 Da (dashed line).

The evaluation of cell viability of Tiiii-PEG-Alkyne@MNPs coated with PEG (5000 or 1000 Da) is reported in Figure 2.7. The values obtained at 72 h showed a different reduction of MTT depending on the nanoparticles coating and on the type of cell line used. The cell viability of mesenchymal cells was unchanged for all investigated concentrations of nanoparticles. Conversely, in LoVo cells, a slight decrease compared to the control was observed. The decrease was similar for all three concentrations and it was more evident using Tiiii-PEG(1000)-Alkyne@MNPs. Therefore, both nanocarriers were shown to be biocompatible with hMSCs at all concentrations, while they showed a lower biocompatibility in LoVo cells to which they caused a slowdown in proliferative activity.



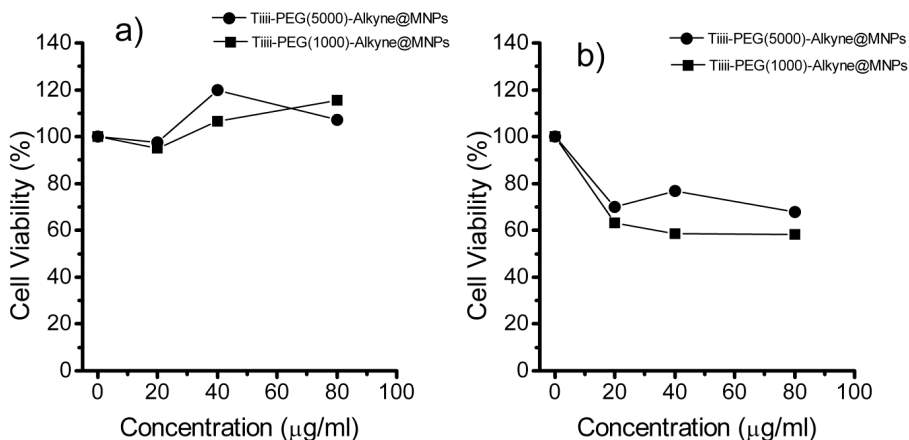
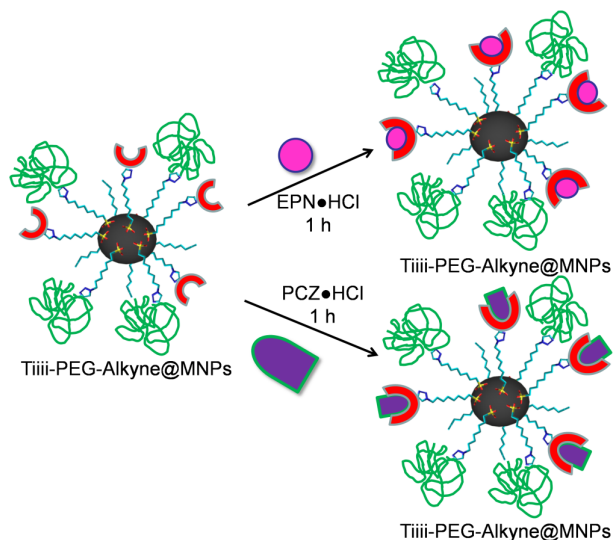


**Figure 2.7** a) Cell viability of hMSC cells with TiIII-PEG-Alkyne@MNPs coated with PEG (1000 or 5000 Da) and b) cell viability of LoVo cells with TiIII-PEG-Alkyne@MNPs coated with PEG (1000 or 5000 Da).

### 2.2.3 Drug Load/release

Drug loading and release experiments were performed by adopting two *N*-methylated molecules: the antitumor drug PCZ which is an alkylating agent and the neurotransmitter EPN. Molecule loading was performed in PBS (1 h of treatment) from their hydrochloride solutions (1 mM) which allows enough amounts of protonated guests suitable for TiIII complexation (Scheme 2.2). Drug loading/release of TiIII receptors is in fact mainly affected by the protonation/deprotonation equilibrium of the guest.<sup>16,17</sup>

The amounts of loaded drugs were  $5.4 \mu\text{g mg}^{-1}$  ( $21 \mu\text{mol g}^{-1}$ ) and  $8.3 \mu\text{g mg}^{-1}$  ( $38 \mu\text{mol g}^{-1}$ ) for PCZ and EPN, respectively. These values are comparable to other drug loads such as doxorubicin ( $15\text{-}150 \mu\text{mol g}^{-1}$ )<sup>35</sup> and 5-fluorouracil ( $6\text{-}90 \mu\text{mol g}^{-1}$ ).<sup>36</sup>



**Scheme 2.2** Drugs-loading of Tiiii-PEG-Alkyne@MNPs.

For release experiments, drug-loaded MNPs are first magnetically separated and then re-dispersed in fresh PBS water solution, loaded drugs are released from the Tiiii cavity through guest deprotonation equilibrium.<sup>16,17</sup> Figure 2.8 shows the release profile of PCZ and EPN from Tiiii-PEG-Alkyne@MNPs. It was evident after 36 hours that almost 96% of PCZ loaded was released, while EPN release is around 80%, both as free bases. The release profile of PCZ is much faster than EPN, with almost 50% of release after 2 h of experiment; at the same time the EPN release is around 35%. The great amount and the fast release profile of PCZ, with respect to the EPN release profile, can be justified considering the medium where the experiment was performed. PCZ is freely soluble in water and the release is improved, while EPN is sparingly soluble in water and the release is slower and not complete. Although the interaction between the Tiiii cavity and the  $^+NH_2-CH_3$  group is the same irrespective of the R group attached,<sup>17b,21</sup> it is solvent dependent. In this case the higher solubility of PCZ in PBS is responsible for faster release.

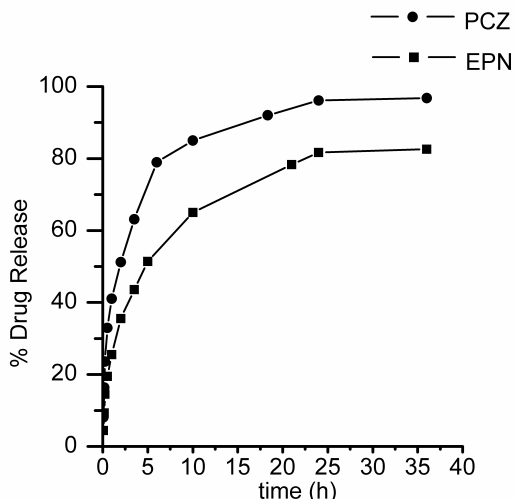


**Figure 2.8** PCZ and EPN release profile from Tiii-PEG-Alkyne@MNPs.

## 2.3 Conclusions

In this work we reported on the synthesis of new multifunctional nanoparticles possessing magnetic, biocompatibility and drug load/release capabilities. The developed synthetic approach is based on MNPs pre-functionalization with a phosphonic linker followed by covalent anchoring of biocompatible PEG chains and Tiii receptors. Overall FT-IR and XPS characterizations demonstrated the success of the adopted synthetic route. Obtained MNPs (mean diameter 10 nm) show the typical magnetic behavior of an ensemble of single domain magnetite nanoparticles, with magnetic irreversibility at low temperature and no coercivity at 300 K. The main magnetic parameters are consistent with those of magnetite nanoparticles of a few tens of nanometers with a broad size distribution, even if narrower than those of most commonly used commercial ones. Due to their good crystallinity level, the obtained values of saturation magnetization are high, making this nanomaterial suitable for the most common biomedical applications such as contrast agents for MRI or heat mediators for MFH. Moreover, cytotoxicity tests indicate that the functional MNPs could be applied in biomedical or bioengineering field. In addition, the presence of hydrophilic PEG chains allowed overcoming water solution problems associated with the hydrophobic Tiii receptors. Although both Tiii-PEG-Alkyne@MNPs with 1000 Da or 5000 Da PEG were biocompatible, better properties were observed adopting 5000 Da PEG. Despite the presence of the long PEG chains, the Tiii receptors anchored on the MNP surface retain their

peculiar complexation properties. Drug release experiments showed that both Tiiii-PEG-Alkyne@MNPs with 5000 and 1000 Da PEG can be loaded with *N*-methylated molecules of interest in the biomedical fields. In particular, the anti-tumoral drug PCZ and the neurotransmitter EPN have been used as tested molecules, but the applications of these MNPs can be extended to the loading and recognition of several *N*-methylated salts, such as *N*-methylated aminoacids, due to the specific recognition properties of Tiiii receptors.

## **2.4 Acknowledgements**

The authors thank Ministero dell'Istruzione, dell'Università e della Ricerca (MIUR) for financial support through FIRB "RINAME Rete Integrata per la NAnoMedicina" (RBAP114AMK). The authors also thank Prof. G. Vecchio for DLS facilities.

## 2.5 Experimental Section

**Materials.** Ferrous chloride tetrahydrate ( $\text{FeCl}_2 \cdot 4\text{H}_2\text{O}$ ), Ferrous chloride hexahydrate ( $\text{FeCl}_3 \cdot 6\text{H}_2\text{O}$ ), Ammonium hydroxide ( $\text{NH}_4\text{OH}$ ), *N,N*-Dimethylformamide (DMF), ethanol, (+)-sodium L-ascorbate, Copper sulphate ( $\text{CuSO}_4$ ), Methoxypolyethylene glycol azides (PEG- $\text{N}_3$ ) of molecular weight (MW) 1000 and 5000 Da, PCZ-HCl and EPN were purchased from Sigma-Aldrich Chemicals and were used without further purification. 10-Undecynylphosphonic acid (Alkyne) was obtained from SiKÉMIA, Montpellier, France. The water was of Milli-Q grade (18.2 M $\Omega$ cm) and was filtered through a 0.22  $\mu\text{m}$  filter.

**Synthesis of Tiii-N<sub>3</sub>.** Tiii-N<sub>3</sub> was prepared following a published procedure.<sup>37</sup>

**Synthesis of magnetic nanoparticles.** Bare magnetite nanoparticles were synthesized by alkaline coprecipitation of  $\text{Fe}^{3+}$  and  $\text{Fe}^{2+}$  according to the protocol described in literature.<sup>38</sup> Briefly,  $\text{FeCl}_2 \cdot 4\text{H}_2\text{O}$  and  $\text{FeCl}_3 \cdot 6\text{H}_2\text{O}$  (molar ratio 1:2) were dissolved in water (50 mL) under a  $\text{N}_2$  atmosphere with vigorous stirring.  $\text{NH}_4\text{OH}$  (5 mL, 25%) was added to the solution at 80°, and the reaction was continued for 30 min. The resulting suspension was cooled to room temperature and washed with ultrapure water. The obtained bare magnetic nanoparticles (bare MNPs) were isolated from the solvent by magnetic decantation.

**Alkyne-Functionalized MNPs.** MNPs (200 mg) were dispersed in DMF (25mL) using an ultrasonic bath for 30 min. An excess of 10-undecynyl phosphonic acid (200 mg) was added and the suspension was agitated for 6 h at room temperature. The particles were separated magnetically and washed four times with DMF followed by ethanol and dried under air.

**Tiii-N<sub>3</sub> and PEG-N<sub>3</sub> “click reaction” on MNPs.** Alkyne@MNPs (100 mg), Tiii-N<sub>3</sub> (0.02 mmol) and PEG-N<sub>3</sub> (0.02 mmol) were dispersed in DMF (20 mL), then  $\text{CuSO}_4$  and (+)-sodium L-ascorbate (0.05 mmol) were added in sequence. The mixture was vibrated with an orbital shaker at 25°C for 24 hours. Afterwards, Tiii-PEG-Alkyne@MNPs were separated with the help of a magnet and washed with DMF three times and ethanol once, then dried overnight at 25°C. The possible presence of residual copper physisorbed on the MNP surface was ruled out by XPS analysis, since spectra of functionalized MNPs did not show any significant signal in the Cu 2p region (925–960 eV).

## Characterization

**Chemical characterization.** X-Ray powder diffraction (XRD) measurements were performed with a  $\theta$ - $\theta$  5005 Bruker-AXS diffractometer (Zeiss, Oberkochen, Germany) using Cu K $\alpha$  radiation operating at 40 kV and 30 mA .

XPS spectra were recorded with a PHI 5600 multi-technique ESCA-Auger spectrometer with a standard Mg-K $\alpha$  X-ray source. Analyses were carried out with a photoelectron angle of 45° (relative to the sample surface) with an acceptance angle of  $\pm 7^\circ$ . The XPS binding energy (B. E.) scale was calibrated by centring the C 1s peak due to hydrocarbon moieties and adventitious carbon at 285.0 eV. Transmission FT-IR measurements were recorded with a JASCO FTIR 430 spectrometer, using the KBr pellet technique, with 100 scans collected per spectrum (scan range 560–4000 cm<sup>-1</sup>, resolution 4 cm<sup>-1</sup>).

**TEM characterization.** Average nanoparticle diameter and size distribution of Tiii-PEG-Alkyne@MNPs were determined by Transmission Electron Microscopy (TEM), using a CM12 PHILIPS microscope operating at 100kV. Samples were prepared by drop drying an aqueous diluted suspension of MNPs onto 200 mesh carbon-coated copper grids. Recorded images were further analysed with the Image Pro-Plus© software. The mean diameter and size distribution of each sample were obtained from a statistical analysis over 400 nanoparticles.

**Magnetic characterization.** Magnetic measurements were carried out by a SQUID magnetometer (Quantum Design MPMS) operating in the 1.8 K - 300 K temperature range with applied field up to 5 T. Measurements were performed on dried powder, hosted in a Teflon sample holder and then pressed in a pellet in order to prevent preferential orientation of the nano-crystallites under the magnetic field action. All data were corrected for the diamagnetic contribution of the sample holder. ZFC/FC curves were obtained by cooling the sample in the absence/presence of a small magnetic field from room temperature to 5 K, then measuring the magnetic moment on warming the sample to 300 K with a controlled rate with a small probe field applied (5 mT).

**Cytotoxicity of Tiii-PEG-Alkyne@MNPs.** Human mesenchymal stem cells (hMSCs), obtained from human bone marrow of healthy donor, and human colon adenocarcinoma (LoVo), were cultivated, respectively, in  $\alpha$ -Minimum Essential Medium ( $\alpha$ MEM) and RPMI 1640 supplemented with L-Glutamine, Nucleosides, Fungizon (Penicillin 10.000 U/mL, Streptomycin 1000  $\mu$ g/mL),

10% fetal bovine serum (FBS), 100  $\mu$ M ascorbic acid and maintained in 37°C incubator, in humidified atmosphere of 5% CO<sub>2</sub> /95% air. All products used were purchased from GIBCO (Life technologies).

Both cell lines were detached by Trypsin/EDTA4Na (0.05% / 1x) and used for experiments. From a 10<sup>4</sup> cells ml<sup>-1</sup> cell suspension, 200  $\mu$ l was seeded into each well of a 96-well tissue culture plate and incubated for 24h followed by a medium change with fresh medium containing Tiii-PEG-Alkyne@MNPs at concentration of 20, 40, 80  $\mu$ g/mL. After incubation for 24, 48 and 72 h, cytotoxicity assay was performed using MTT test, based on reduction of tetrazolium salts to formazan by mitochondrial dehydrogenase. The optical density (OD) values at 550 nm of the wells, with background subtraction of OD at 655 nm, were measured by a microliter plate reader. The cell viability were expressed in values % respect to the control. All experiments were performed in triplicates.

**Drug loading and release Study.** Stock solutions of PCZ (1 mM) and EPN hydrochlorides (1 mM) were prepared by dissolving the drugs in Phosphate Buffered Saline (PBS) water solution (pH 6.8, 10 mM). Drugs loading was performed by dispersing MNPs (5 mg, Tiii-PEG-Alkyne@MNPs) in PCZ-HCl solution (4 mL) or EPN-HCl solution (4 mL). The solution was sonicated for 1 h in an ultrasonic bath, and the MNPs were isolated from the solution by magnetic separation. The PCZ-loaded and EPN-loaded MNPs were suspended in PBS and were transferred into dialysis tubing (MW cutoff 3.0 kDa) and dialyzed against PBS (50 mL) for 36 h. Samples (2 mL) were periodically removed and assayed. The withdrawn volume of each sample was replaced by the same volume of fresh medium. The amount of released PCZ and EPN were analysed with a JASCO V-560 UV/Vis spectrophotometer equipped with a 1 cm path length cell at 230 nm and 300 nm respectively. The drug release study was performed in duplicate.

## 2.6 References

- <sup>1</sup> a) M. Colombo, S. Carregal-Romero, M. F. Casula, L. Gutiérrez, M. P. Morales, I. B. Böhm, J. T. Heverhagen, D. Prospero, W. J. Parak, *Chem. Soc. Rev.* **2012**, *41*, 4306-4334; b) G. Mistlberger, K. Koran, E. Scheucher, D. Aigner, S. M. Borisov, A. Zankel, P. Polt, I. Klimant, *Adv. Funct. Mater.* **2010**, *20*, 1842-1851.
- <sup>2</sup> J. Nicolas, S. Mura, D. Brambilla, N. Mackiewicz, P. Couvreur, *Chem. Soc. Rev.* **2013**, *42*, 1147-1235.
- <sup>3</sup> Y. Pan, X. Du, F. Zhao, B. Xu, *Chem. Soc. Rev.* **2012**, *41*, 2912-2942.
- <sup>4</sup> a) N. Lee, T. Hyeon, *Chem. Soc. Rev.* **2012**, *41*, 2575-2589; b) F. Hu, Y. S. Zhao, *Nanoscale* **2012**, *4*, 6235-6243.
- <sup>5</sup> Y. Huang, S. He, W. Cao, K. Cai, X.-J. Liang, *Nanoscale* **2012**, *4*, 6135-6149.
- <sup>6</sup> S. Jiang, K. Y. Win, S. Liu, C. P. Teng, Y. Zheng, M.-Y. Han, *Nanoscale* **2013**, *5*, 3127-3148.
- <sup>7</sup> a) N. Erathodiyil, J. Y. Ying, *Acc. Chem. Res.* **2011**, *44*, 925-935; b) S. Laurent, D. Forge, M. Port, A. Roch, C. Robic, L. V. Elst, R. N. Muller, *Chem. Rev.* **2008**, *108*, 2064-2110.
- <sup>8</sup> W. Wang, V. Pacheco, H.-J. Krause, Y. Zhang, H. Dong, R. Hartmann, D. Willbold, A. Offenhäusser, Z. Gu, *J. Phys. Chem. C* **2012**, *116*, 17880-17884.
- <sup>9</sup> a) S. T. Selvan, T. T. Y. Tan, D. K. Yi, N. R. Jana, *Langmuir*, **2010**, *26*, 11631-11641; b) A. K. Gupta, M. Gupta, *Biomaterials* **2005**, *26*, 3995-4021; c) M. Mazur, A. Barras, V. Kuncser, A. Galatanu, V. Zaitzev, K. V. Turcheniuk, P. Woisel, J. Lyskawa, W. Laure, A. Siriwardena, R. Boukherroub, S. Szunerits, *Nanoscale* **2013**, *5*, 2692-2702.
- <sup>10</sup> E. K. U. Larsen, T. Nielsen, T. Wittenborn, L. M. Rydtoft, A. R. Lokanathan, L. Hansen, L. Østergaard, P. Kingshott, K. A. Howard, F. Besenbacher, N. C. Nielsen, J. Kjems, *Nanoscale* **2012**, *4*, 2352-2361.



- <sup>11</sup> C. Tudisco, V. Oliveri, M. Cantarella, G. Vecchio, G.G. Condorelli, *Eur. J. Inorg. Chem.* **2012**, 32, 5323-5331.
- <sup>12</sup> C. Tassa, S. Y. Shaw, R. Weissleder, *Acc. Chem Res.* **2011**, 44, 842-852.
- <sup>13</sup> a) I. J. Bruce, T. Sen, *Langmuir* **2005**, 21, 7029-7035; b) C. Yee, G. Kataby, A. Ulman, T. Prozorov, H. White, A. King, M. Rafailovich, J. Sokolov, A. Gedanken, *Langmuir* **1999**, 15, 7111-7115; c) S. Mohapatra, P. Pramanik, *Colloids and Surfaces A: Physicochem. Eng. Aspects* **2009**, 339, 35-42; d) K. V. P. M. Shafi, A. Ulman, X. Yan, N.-L. Yang, C. Estournès, H. White, M. Rafailovich, *Langmuir* **2001**, 17, 5093-5097; e) B. Basly, G. Popa, S. Fleutot, B. P. Pichon, A. Garofalo, C. Ghobril, C. Bilotey, A. Berniard, P. Bonazza, H. Martinez, D. Felder-Flesch, S. Begin-Colin, *Dalton Trans.* **2013**, 42, 2146-2157.
- <sup>14</sup> D. J. Cram, J. M. Cram, *Container Molecules and Their Guests* **1994**, ed. J. F. Stoddart, The Royal Society of Chemistry, Cambridge.
- <sup>15</sup> a) R. Pinalli, M. Suman, E. Dalcanale, *Eur. J. Org. Chem.* **2004**, 3, 451-462; b) R. Pinalli, E. Dalcanale, *Acc. Chem. Res.* **2013**, 46, 399-411.
- <sup>16</sup> E. Biavardi, M. Favazza, A. Motta, I. L. Fragalà, C. Massera, L. Prodi, M. Montalti, M. Melegari, G. G. Condorelli, E. Dalcanale, *J. Am. Chem. Soc.* **2009**, 131, 7447-7455.
- <sup>17</sup> E. Biavardi, G. Battistini, M. Montalti, R. M. Yebeutchou, L. Prodi, E. Dalcanale, *Chem. Commun.* **2008**, 1638-1640; b) R. M. Yebeutchou, E. Dalcanale, *J. Am. Chem. Soc.* **2009**, 131, 2452-2453.
- <sup>18</sup> E. Kalenius, D. Moiani, E. Dalcanale, P. Vainiotalo, *Chem. Commun.* **2007**, 3865-3867.
- <sup>19</sup> G. G. Condorelli, A. Motta, M. Favazza, I. L. Fragalà, M. Busi, E. Menozzi, E. Dalcanale, *Langmuir* **2006**, 22, 11126-11133.
- <sup>20</sup> A. Sreekumar, L. M. Poisson, T. M. Rajendiran, A. P. Khan, Q. Cao, J. Yu, B. Laxman, R. Mehra, R. J. Lonigro, Y. Li, M. K. Nyati, A. Ahsan, S. Kalyana-

Sundaram, B. Han, X. Cao, J. Byun, G. S. Omenn, D. Ghosh, S. Pennathur, D. C. Alexander, A. Berger, J. R. Shuster, J. T. Wei, S. Varambally, C. Beecher, A. M. Chinnaiyan, *Nature* **2009**, 457, 910-915.

<sup>21</sup> E. Biavardi, C. Tudisco, F. Maffei, A. Motta, C. Massera, G. G. Condorelli, E. Dalcanale, *Proc. Natl. Acad. Sci. USA* **2012**, 109, 2263-2268.

<sup>22</sup> H. C. Kolb, M. G. Finn, K. B. Sharpless, *Angew. Chem., Int. Ed.* **2001**, 40, 2004-2021.

<sup>23</sup> H. Koichiro, M. Makoto, S. Wataru, Y. Toshinobu, *Chem. Mater.* **2009**, 21, 1318-1325.

<sup>24</sup> J.-B. Qu, H.-H. Shao, G.-L. Jing, F. Huang, *Colloids and Surfaces B: Biointerfaces* **2013**, 102, 37-44.

<sup>25</sup> C. A. Graham, T. F. Cloughesy, *Semin. Oncol. Nurs* **2004**, 20, 260-272.

<sup>26</sup> Y. Yamanaka, T. Mammoto, T. Kirita, M. Mukai, T. Mashimo, M. Sugimurac, Y. Kishi, H. Nakamura, *Cancer Lett.* **2002**, 176, 143-148.

<sup>27</sup> E. Smecca, A. Motta, M. E. Fragalà, Y. Aleeva, G. G. Condorelli, *J. Phys. Chem. C* **2013**, 117, 5364-5372.

<sup>28</sup> W. Zhang, Y. Zhang, X. Shi, C. Liang, Y. Xian, *J. Mater. Chem.* **2011**, 21, 16177-16183.

<sup>29</sup> A. C. Cardiel, M. C. Benson, L. M. Bishop, K. M. Louis, J. C. Yeager, Y. Tan, R. J. Hamers, *ACS Nano* **2012**, 6, 310-318.

<sup>30</sup> R. Tedja, A. H. Soeriyadi, M. R. Whittaker, M. Lim, C. Marquis, C. Boyer, T. P. Davisband, R. Amal, *Polym. Chem.* **2012**, 3, 2743-2751.

<sup>31</sup> M. El-Hilo, R. W. Chantrell, K. O'Grady, *J. Appl. Phys.* **1998**, 9, 5114-5122.

<sup>32</sup> J. I. Gittlemann, B. Abeles, S. Bosowski, *Phys. Rev. B* **1974**, 9, 3891-3897.

- <sup>33</sup> M. M. Schieber, *Experimental Magnetochemistry* **1967**, ed. E. P. Wohlfarth, North-Holland Publishing Company, Amsterdam.
- <sup>34</sup> A. Millan, A. Urtizberea, N. J. O. Silva, F. Palacio, V. S. Amaral, V. Snoeck, V. Serin, *J. Magn. Magn. Mater.* **2007**, 312, L5-L9.
- <sup>35</sup> a) M. K. Yu, Y. Y. Jeong, J. Park, S. Park, J. W. Kim, J. J. Min, K. Kim, S. Jon, *Angew. Chem. Int. Ed.* **2008**, 47, 53–62; b) T. K. Jain, M. A. Morales, S. K. Sahoo, D. L. Leslie-Pelecky, V. Labhasetwar, *Mol. Pharmaceutics* **2005**, 2, 194–205.
- <sup>36</sup> J. L. Arias, F. Linares-Molinero, V. Gallardo, A. V. Delgado, *Eur. J. Pharm. Sci.* **2008**, 33, 252–261.
- <sup>37</sup> M. Dionisio, J. M. Schnorr, V. K. Michaelis, R. G. Griffin, T. M. Swager, E. Dalcanale, *J. Am. Chem. Soc.* **2012**, 134, 6540–6543.
- <sup>38</sup> Y. S. Kang, S. Risbud, J. F. Rabolt, P. Stroeve, *Chem. Mater.* **1996**, 8, 2209–2211.

# Chapter 3

## Multifunctional Magnetic Nanoparticles for Enhanced Intracellular Drug Transport<sup>\*</sup>

<sup>\*</sup> This chapter has been submitted to Journal of Materials Chemistry B: C. Tudisco, M. T. Cambria, F. Bertani, F. Sinatra, A. Alba, S. Saccone, E. Fantechi, C. Innocenti, C. Sangregorio, E. Dalcanale, G. G. Condorelli, *J. Mater. Chem. B* 2015, under revision.

### 3.1 Introduction

Nanotechnology, and magnetic nanoparticles (MNPs) in particular, play an increasing role in molecular diagnostics, in vivo imaging, and improved treatment of diseases.<sup>1</sup> In this field, iron oxide nanoparticles are attracting considerable interest, mainly because the specific magnetic properties of the core and the versatile functionalization of the surface are here combined in a small-sized object.<sup>2</sup> MNPs are therefore under investigation, and in some cases already in use, for several biomedical applications such as protein and cell sorting and manipulation,<sup>3</sup> cell labelling,<sup>4</sup> magnetic dialysis,<sup>5</sup> magnetically controlled drug delivery,<sup>6</sup> Magnetic Resonance Imaging (MRI),<sup>7</sup> and magnetic thermotherapy.<sup>8</sup> The ability to functionalize the surface with targeting ligands as well as with imaging and therapeutic moieties allows the creation of multimodal, multifunctional nanoagents.<sup>9</sup> These new materials pave the way towards a novel theranostics in cancer treatment aimed at providing monitoring/diagnosis and therapy tools, simultaneously.<sup>10</sup> In this context, we describe the synthesis of novel multicomponent biocompatible organic-inorganic MNPs, which possess magnetic and optical properties, targeting capability and are designed to load, carry and release *N*-methylated drugs. The synthesized MNPs consist of a Fe<sub>3</sub>O<sub>4</sub> core covalently coated with a mixed monolayer of carboxy-*X*-rhodamine (Rhod), Folic Acid (FA), PEG and tetraphosphonate cavitand (Tiiii from now onward). The outstanding molecular recognition properties of Tiiii receptors<sup>11</sup> towards various *N*-methylated guests<sup>12</sup> was demonstrated for bio-markers,<sup>13</sup> neurotransmitters<sup>14</sup> and drugs.<sup>15</sup> Tiiii complexation properties were also exploited in biological medium by their anchoring on water dispersible and biocompatible PEGylated MNPs. This behavior is due to the high binding affinity of Tiiii receptors towards *N*-methylated guest, which is the result of the combination of three interaction modes: i) multiple ion-dipole interactions between the inward facing P=O groups and the positively charged CH<sub>3</sub>-NH<sub>2</sub>- group; ii) single or dual H bonding involving the P=O groups; and iii) CH- $\pi$  interactions between a methyl group present on the guest and the cavity of the host.<sup>11-15</sup>

In this work, the synthesis of a multifunctional system allowed us to fully exploit the potentiality of cavitand-based MNPs as intracellular vector able to load specific antitumor drugs from the intercellular medium and to transport them inside the intracellular region thus enhancing their antitumor efficiency. The fluorescent Rhod probe covalently bonded to the MNPs surface was embedded in the multifunctional system, in order to monitor the uptake into the target cells by confocal microscopy. From a therapeutic point of view, the

use of MNPs for drug delivery is significantly improved by the introduction of a specific targeting moiety able to increase cellular uptake by internalization through receptor-mediated endocytosis. Many works point to FA,<sup>16</sup> a biomolecule fundamental for cell survival and required in numerous biochemical processes,<sup>17</sup> as an important targeting moiety for tumor cells. In fact, FA receptors (FAR) are over-expressed in several human carcinomas and thus provide highly selective binding sites onto tumor cells.<sup>18</sup> The functionalization with FA, was, therefore, proposed to promote cellular uptake through FAR mediated internalization and, at the same time, to improve the biocompatibility of the overall nanosystem. On the other side, for diagnostic purpose, the synthesis of a highly biocompatible bi-modal magnetic/fluorescent nanostructure offers the capability to perform both MRI and fluorescence microscopy, which are complementary techniques in biomedical research.<sup>19</sup> The success of the proposed multistep synthetic route for the preparation of an efficient multifunctional system was proved through the evaluation of the functional properties, namely biocompatibility, magnetic/hyperthermic properties, drug loading and cell uptake. The potential of the synthesized nanosystem as intracellular vector for *N*-methylated drugs was evaluated through specifically designed drug delivery experiments adopting the procarbazine hydrochloride (PCZ·HCl), an anti-neoplastic agent used in the treatment of several malignancies.<sup>20</sup> In particular, these experiments aimed at evaluating if the presence of cavitand-functionalized MNPs improves the PCZ efficacy in a colon adenocarcinoma cell line. To definitively prove the role of the nanosystem as intracellular shuttle, control experiments were also performed with a specifically designed inactive transport reference made by a MNP system possessing the same PEG, Rhod and FA functionalities but without the cavitand receptor. Experimental results showed that the key strength of the new system lies in the recognition properties of the surface bonded tetraphosphonate cavitands towards the PCZ drug which allows to reversible and selective drug loading directly from the intercellular medium and to release it in the intracellular medium thus increasing drug cytotoxicity.

## 3.2 Results and Discussion

### 3.2.1 Synthesis of Functionalized Nanoparticles

The overall approach for the synthesis of active (**1-PA@MNPs**) and inactive (**2-PA@MNPs**) nanosystems is reported in Figure 3.1.

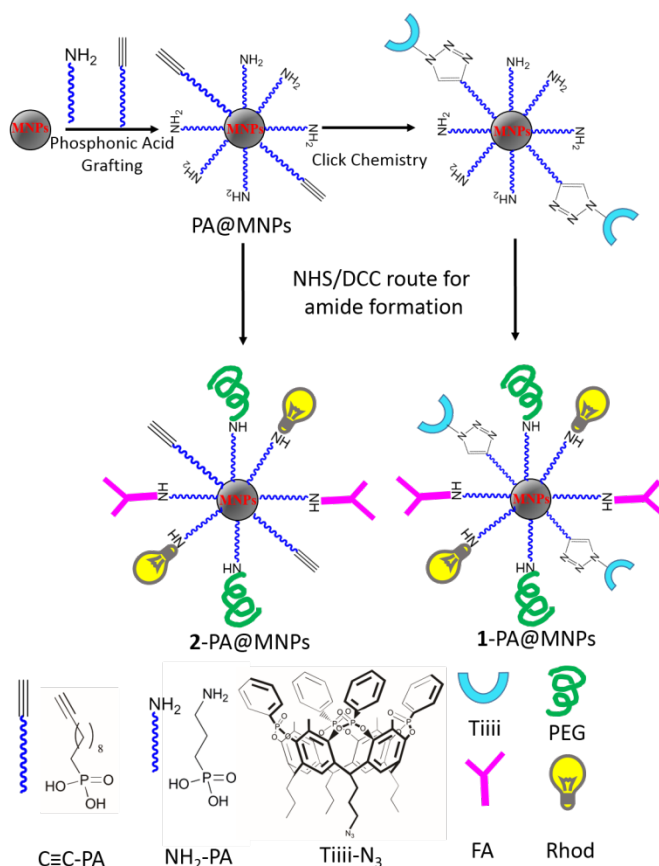


**Figure 3.1** Synthesis of active (**1-PA@MNPs**) and inactive (**2-PA@MNPs**) nanosystems.

As a first step, iron oxide MNPs were synthesized by a co-precipitation method<sup>21</sup> and characterized by XRD and TEM. As reported in the previous Chapter, the position and relative intensity of all diffraction peaks (Supplementary Information, Figure S1) matched well those of the standard PDF card for magnetite (19-0629) maghemite (39-1346) or any intermediate composition between the two phases. TEM micrographs (SI, Figure S2) indicate a particle mean diameter of about  $11 \pm 4$  nm. Afterwards, MNPs were

functionalized with two phosphonic acids (10-undecynylphosphonic acid and aminopropylphosphonic acid), having terminal acetylenic and amino groups (PA@MNPs) able to provide an active platform for further functionalization with organic molecules. Tiii receptors were then reacted with the alkyne moieties of PA@MNPs through a copper(I) catalysed azide-alkyne cycloaddition (CuAAC) according to a previously reported synthetic approach.<sup>14</sup> Finally, *N*-hydroxysuccinimide-activated forms of PEG, FA and Rhod were chemically coupled to the free amine moieties of PA@MNPs through the formation of an amide bond. In addition, to evaluate the specific role of Tiii receptor as drug-carrier, an analogous system without Tiii was prepared (2-PA@MNPs). Both active and inactive MNPs were characterized by FTIR and XPS spectroscopy.

Comparison of FT-IR spectra of PA@MNPs, 1-PA@MNPs and 2-PA@MNPs in the 850-1900  $\text{cm}^{-1}$  (right) and 2000-2200  $\text{cm}^{-1}$  regions (left) are shown in Figure 3.2.

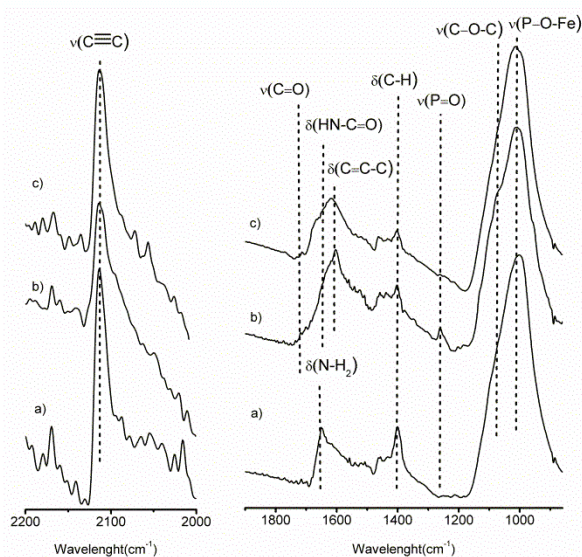


**Figure 3.2** FT-IR spectral regions in the 2000–2200  $\text{cm}^{-1}$  (left) and 850–1900  $\text{cm}^{-1}$  (right) ranges of a) PA@MNPs, b) 1-PA@MNPs, c) 2-PA@MNPs.

In the FT-IR spectra of PA@MNPs, the presence of a single broad and strong band at ca. 1040  $\text{cm}^{-1}$  due to the phosphate bonding group and the absence of the P=O stretches (1254  $\text{cm}^{-1}$ ) and P-O-H stretches (920  $\text{cm}^{-1}$ ) typical of phosphonic acid powders are indications of the phosphonic acids bonding to the surface.<sup>14,22</sup> In addition, spectra show also two characteristic bands at 1650



$\text{cm}^{-1}$  and  $2121 \text{ cm}^{-1}$ . The first one is associated to the bending vibrations of  $-\text{NH}_2$  groups of the amino propyl phosphonic component<sup>23</sup> of the mixed monolayer present, whilst the second one is due to the acetylenic group of the alkyne-PA molecule.<sup>14</sup> This observation indicates that the nanosystems preserve both the amino and alkyne terminated groups needed for the subsequent coupling reactions. FT-IR spectra of **1-PA@MNPs** show a feature at  $1250 \text{ cm}^{-1}$  due to the presence of free  $\text{P}=\text{O}$  moiety of Tiiii,<sup>14</sup> while this component is absent in the spectra of **2-PA@MNPs** where this receptor is not present. The band convolution around  $1630\text{--}1600 \text{ cm}^{-1}$  is due to the vibrations of the amide groups and benzene rings of FA.<sup>24</sup> The shoulder at  $1695 \text{ cm}^{-1}$  is assigned to the  $\text{C}=\text{O}$  stretching of the carbonyl groups of FA and Rhod.<sup>25</sup> These peaks indicate the presence of FA and Rhod on both **1-PA@MNPs** and **2-PA@MNPs** nanosystems. The broad band in the  $1150\text{--}870 \text{ cm}^{-1}$  range is a convolution of the characteristic  $\text{C}-\text{O}-\text{C}$  antisymmetric and symmetric stretches of PEG with the strong peak due to the phosphate binding group (ca.  $1040 \text{ cm}^{-1}$ ) of the monolayer. Note that in the case of **1-PA@MNPs** a decrease of the characteristic absorption peak of the alkyne group at  $2108 \text{ cm}^{-1}$  compared to **2-PA@MNPs** and **PA@MNPs** is consistent with the occurrence of “click-reaction” between the alkyne moiety and the azide terminations of Tiiii.

The N 1s and C 1s XPS spectral regions of **PA@MNPs**, **1-PA@MNPs** and **2-PA@MNPs** are shown in Figure 3.3.

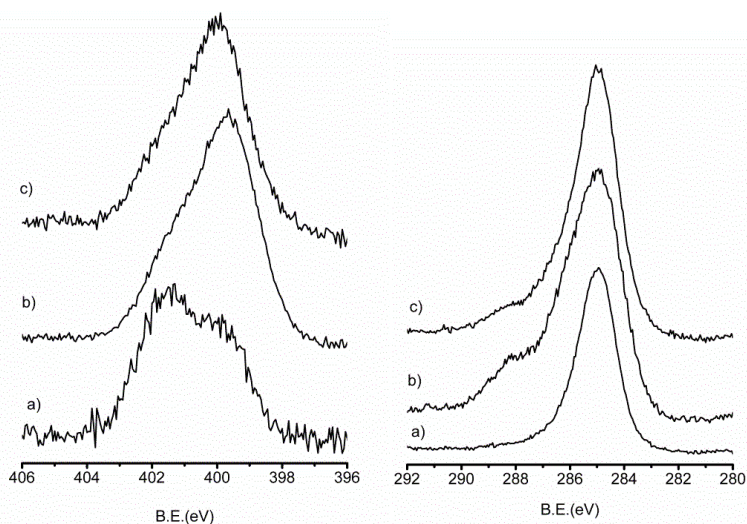


**Figure 3.3** High resolution N 1s (left) and C 1s (right) XPS spectral regions of a) **PA@MNPs**, b) **2-PA@MNPs** and c) **1-PA@MNPs**. Intensities were normalized to the Fe  $2p_{3/2}$  signal.

N 1s band of PA@MNPs (Figure 3.3 left) consists of two components of comparable intensity. The component at 399.9 eV is associated to the  $-NH_2$  groups of the anchored aminopropylphosphate, whilst the component centered at 401.5 eV, is due to the amino groups interacting with  $Fe_3O_4$  surface through protonation or formation of  $-H$  bonds.<sup>22b</sup> N 1s band of **1-PA@MNPs** shows a rich structure, due to the presence of nitrogens with different chemical environment. These new contributions include N atoms of triazole moiety ( $\sim 401.0$  eV) formed after the click reaction, the nitrogen atoms involved in the amidic bond (400.2 eV) between the anchored aminopropylphosphate and the FA, PEG and Rhod molecules and N atoms of FA and Rhod (at 399.1 eV and 400.6 eV).<sup>26</sup> The N 1s shape of **2-PA@MNPs** does not change significantly compared to that of **1-PA@MNPs** since the contribution of the triazole moiety of **1-PA@MNPs** is overlapped with that of the N of the other functional molecules ( $NH_2$ -PA, FA, Rhod and PEG). The C 1s band (Figure 3.3 right) of PA@MNPs consists of a single peak at 285.0 eV, assigned to aliphatic carbons. Spectra of **1-PA@MNPs** and **2-PA@MNPs** show, beside the main peak at 285.0 eV due to aliphatic and aromatic carbons, a shoulder around 286 eV arising from the oxygen-bonded carbons of Tiii and PEG and a component around 288.6 due to carboxylic and amidic groups of FA and Rhod. Note that these last components are more evident on **2-PA@MNPs** sample since in the absence of the large Tiii molecules and the steric hindrance on the surface is reduced a higher amounts of PEG, FA and Rhod molecules can be grafted on the MNPs. The presence of slightly higher amounts of FA and Rhod molecules on **2-PA@MNPs** sample is also supported by the higher intensity of the N 1s signal compared to the analogous signal of **1-PA@MNPs**.

The total amount of organic coating was determined by thermogravimetric measurements. The change of sample mass with the increasing temperature allows the deconvolution of inorganic and organic content. Thermogravimetric curves in the 100-600°C range (SI, Figure S3) showed a weight loss of about 8% in the 270-410°C temperature range.

The mean hydrodynamic size of **1-PA@MNPs** was determined by DLS in water. The size distribution (SI, Figure S4) consists of a monomodal curve with a polydispersity index of 0.125 and an hydrodynamic average size of 60 nm. A zeta potential of -23 mV was also determined. The negative value of the zeta potential is mainly due to the negatively charged core and to the effect of the presence of phosphonic acid monolayer.<sup>14,27</sup>

MNPs cytotoxicity of **1-PA@MNPs** and **2-PA@MNPs** was evaluated using human mesenchymal stem cells (hMSCs) from healthy adipose tissue and human colon adenocarcinoma cells (LoVo). Cell viability was measured using

MTT test after 72h of incubation in the presence of different concentrations of MNPs (20, 40 and 80  $\mu\text{g}/\text{ml}$ ) (SI, Figure S5 and S6). Results indicate that cell viability is poorly affected by the presence of MNPs thus indicating that both synthesized systems are biocompatible.

### 3.2.2 Magnetic Properties

The field dependence of 1-PA@MNPs magnetization was recorded at low (2.5 K) and room (300 K) temperature (Figure 3.4). The low temperature  $M$  vs.  $H$  curve shows hysteresis (see magnification in the inset of Figure 3.4a) with a coercive field of  $\mu_0 H_C = 29.7\text{mT}$  and a remnant magnetization  $M_R = \frac{M_{0T}}{M_{5T}} = 0.39$ .

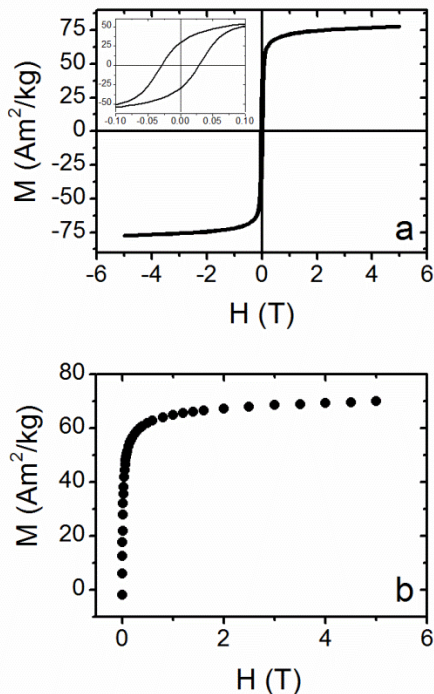


**Figure 3.4** a) Hysteresis loop of 1-PA@MNPs measured at 2.5 K. In the inset the magnification of the low field region is reported. b)  $M$  vs.  $H$  curve of 1-PA@MNPs at 300 K.

This value is slightly lower than the one foreseen for a set of isolated uniaxial nanoparticles whose easy axes are isotropically oriented ( $M_R=0.5$ ). A lower magnetic remanence, however, is commonly observed in iron oxides MNPs and

can be also influenced by the presence of magnetic interparticle interactions.<sup>28</sup> At 300 K, no hysteresis nor coercivity were observed, suggesting that the particles are in the superparamagnetic regime at this temperature. The saturation magnetization values,  $M_s$ , were estimated 83 and 75 emu/g<sup>-1</sup>, for 2.5 and 300 K, respectively, by fitting the curve to the empirical law,<sup>29</sup>

$$M = M_s + \frac{a}{H} + \frac{b}{H^2}, \text{ in the high field region.}$$

The temperature kinetic curve of an aqueous dispersion of 1-PA@MNPs (0.09% w/w of iron oxide) exposed to an alternating magnetic field of 17 kA/m amplitude and 183 kHz frequency (Figure 3.5) shows a temperature increase of about 4.2°C after a 5 minutes exposition to the field. The Specific Absorption Rate (SAR), i.e. the power absorbed per unit of mass, was evaluated from the initial slope of the kinetic curve and was found to be  $62.7 \pm 11.0$  [W]/[grams of iron]. It should be also noted that the hyperthermic efficiency is considerably high particularly considering that it was estimated using field parameters below the physiological limit.<sup>30</sup>

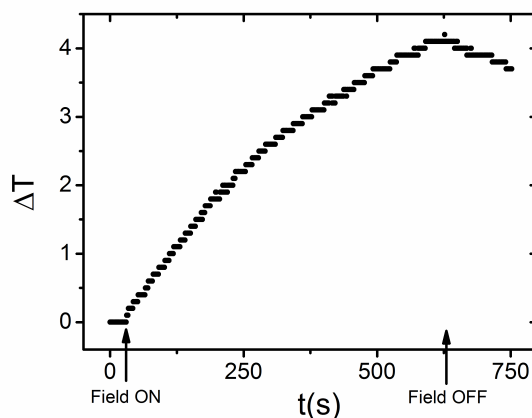


**Figure 3.5** Temperature kinetics of a dispersion of 1-PA@MNPs under the application of an alternating magnetic field (17 kA/m, 183 kHz, 5 min). The temperature measured when the field was switched on was about 37 °C.

### 3.2.3 Intracellular Uptake

The intracellular uptake of functionalized MNPs was evaluated after 1, 6, 48, and 72 h of incubation of 1-PA@MNPs at the lower concentration (20 μg mL<sup>-1</sup>) in LoVo cells using confocal laser scanning fluorescence microscopy (Figure 3.6). The obtained results show that the uptake of functionalized MNPs

occurs after 1 h of incubation and continues up to 6 h of incubation when an increased amount of internalized MNPs is present.

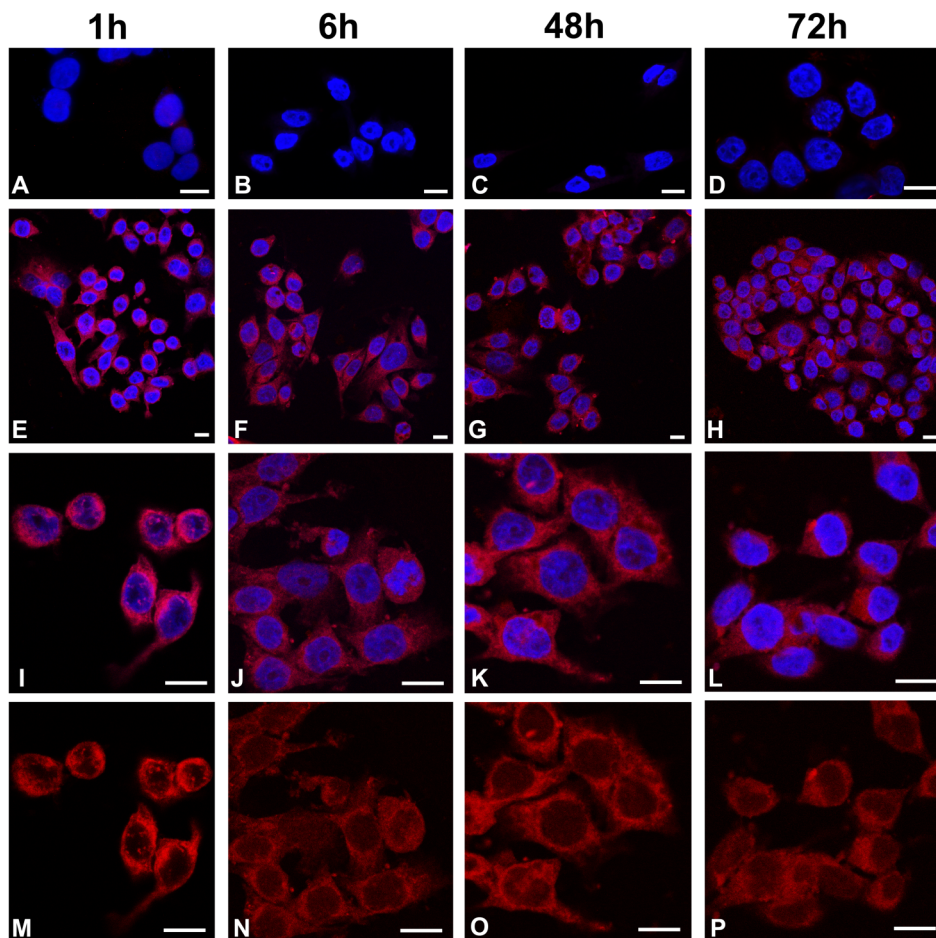


**Figure 3.6** Intracellular uptake of 1-PA@MNPs in LoVo cells. After incubation for 1, 6, 48, and 72 cells were analyzed using a confocal laser scanning microscopy. The signal associated with functionalized MNPs is displayed in red, due to the covalently linked rhodamine. Cell nuclei were stained with DAPI (blue stain). A, B, C, and D: control LoVo cells without nanoparticles. E, F, G, H and their enlargements I, J, K, L: LoVo cells incubated with 1-PA@MNPs for the indicated hours. M, N, O, P: the same images in I, J, K, L, respectively, showing only the fluorescence due to the 1-PA@MNPs. Scale bars: 10  $\mu\text{m}$ .

Moreover, an intense fluorescent signal related to 1-PA@MNPs can be observed in the cytoplasmic compartment of the cells while a low level signal is localized in the nuclei even after 72 hours of incubation. These data indicate that 1-

PA@MNPs were fast internalized into cells with a prevalent location in the cytoplasm.

### 3.2.4 Drug Load/release

The complexation properties of 1-PA@MNPs were investigated adopting the antitumor drug PCZ. Molecule loading was performed in water (2 h of treatment) from their hydrochloride solutions (300  $\mu\text{g}/\text{ml}$ ) by forming a host-guest inclusion complex with the drug protonated form. Similar loading experiments were performed using the complexation inactive 2-PA@MNPs as blank reference. Figure 3.7 compares the release profile (as  $\mu\text{g}$  of PCZ per mg of MNPs) of 1-PA@MNPs and 2-PA@MNPs in PBS solution. The two profiles are significantly different. 1-PA@MNPs shows an initial rapid release during the first 5 min followed by a continuous release with lower rate in the next 12 h while 2-PA@MNPs release is much lower, very fast and almost complete after 5 minutes.

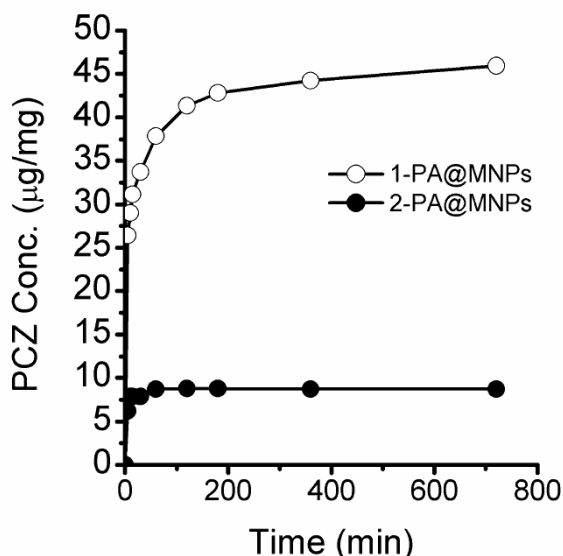


Figure 3.7 PCZ release profile from 1-PA@MNPs and 2-PA@MNPs.

This different behavior can be explained by considering the amount of the loaded drug as well as the different nature of the drug-coating interactions. The amount of PCZ loaded on 2-PA@MNPs surface does not possess suitable receptors and the loaded drug is physisorbed on the surface. By contrast, the

presence of the cavitand on **1-PA@MNPs** surface allows a more efficient loading (about five times higher than **2-PA@MNPs**) with a sustained release for longer time, thus indicating that the combination of the supramolecular interactions between Tiii cavity and *N*-methylated guest is a key step in determining load-release properties.

### 3.2.5 Intra-cellular Transport

The recognition potentialities of cavitand-functionalized surface and their fast cell uptake, demonstrated in the previous experiments, are therefore combined in a single multifunctional object which appears as an ideal candidate to recognize *in-situ* a specific drug and promote its cellular internalization for improving the therapeutic efficacy. Specific experiments were thus designed to verify the capability of the cavitand-activated **1-PA@MNPs** as intracellular vectors for *N*-methylated drugs (Figure 3.8). In the experiments controlled amounts of free PCZ and cavitand-functionalized MNPs were added simultaneously to LoVo cell cultures.

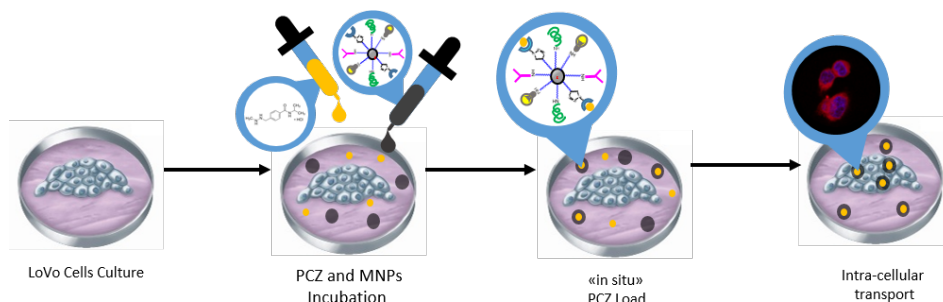


**Figure 3.8** Scheme of the proposed experiment. A PCZ solution and a MNPs suspension were added simultaneously to the LoVo cells. The expected result consists in the load of the drug followed by the internalization of the drug loaded MNPs.

The enhancement of the anticancer effect of PCZ due to the larger loading granted by the efficient cell uptake of **1-PA@MNPs**, was evaluated by measuring the cell viability at different concentrations of drug and magnetic carriers. Figure 3.9a and 3.9c compare the cytotoxicity of PCZ at two concentrations (30 and 300  $\mu\text{g}/\text{ml}$ ) with the cytotoxicity observed by the addition of various concentration of **1-PA@MNPs** (20, 40 and 80  $\mu\text{g}/\text{ml}$ ). Plots indicate that the simultaneous presence of **1-PA@MNPs** and PCZ in the cell culture increase the drug efficacy.

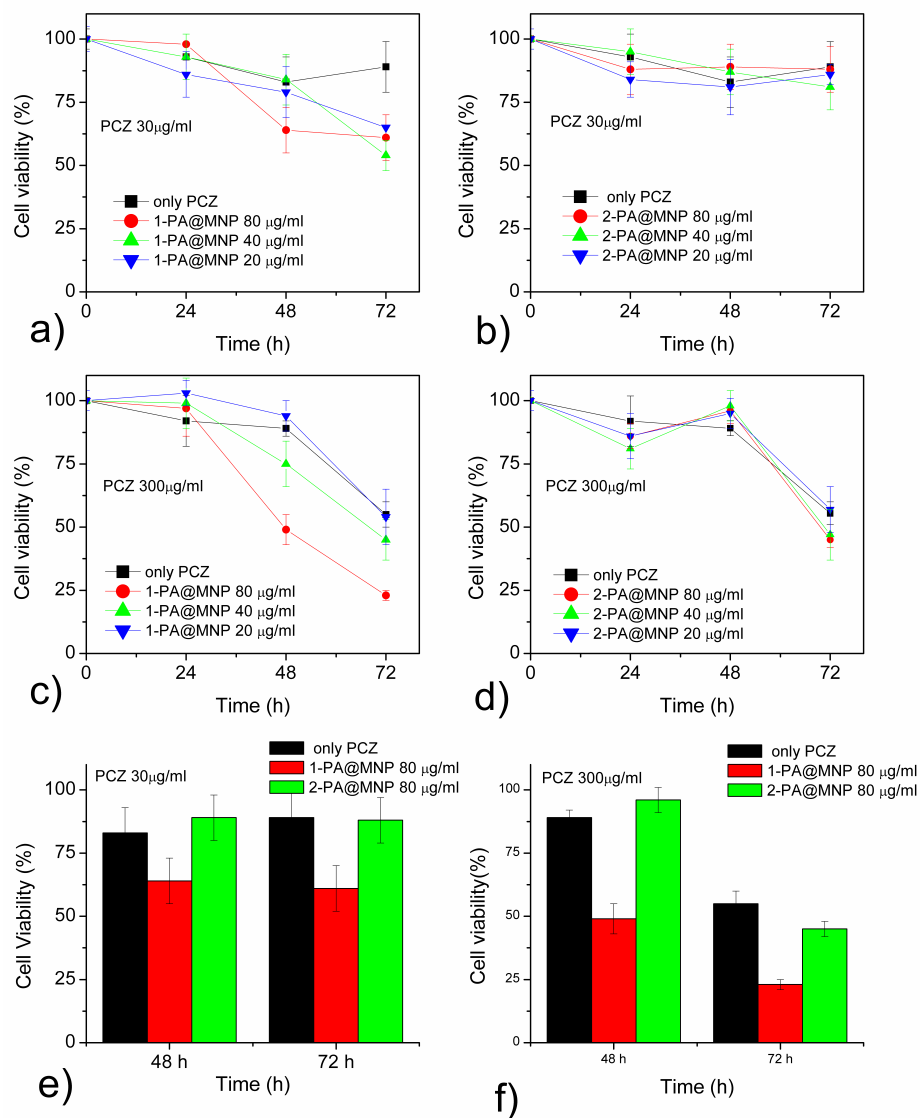


**Figure 3.9** Cytotoxicity test of PCZ incubated in LoVo cells for 24, 48 and 72 h either alone or in the presence of three concentrations of MNPs (20 µg/ml, 40 µg/ml and 80 µg/ml): (a-b) 30 µg/ml and (c-d) 300 µg/ml PCZ solutions used alone or in the presence of (a and c) 1-PA@MNPs or (b and d) 2-PA@MNPs; comparison of cytotoxicity after 48 h and 72 h incubation of (e) 30 µg/ml and (f) 300 µg/ml PCZ solutions used alone (black bar) or in the presence of 80 µg/ml of 1-PA@MNPs (red bar) or 2-PA@MNPs (green bar).



At low PCZ concentrations (30  $\mu\text{g}/\text{ml}$ ) and 80  $\mu\text{g}/\text{ml}$  of **1-PA@MNPs**, cell viability is reduced to about 60% after 48 h, while with the same concentration of PCZ alone cell viability remain at 80%. After 72 h cell viability is reduced down to about 50% for all **1-PA@MNPs** concentrations, while in the absence of MNPs it is in the 80-90% range (Figure 3.9a).

For higher concentration of PCZ (300  $\mu\text{g}/\text{ml}$ ), the presence of 80  $\mu\text{g}/\text{ml}$  of **1-PA@MNPs** produces an evident enhancement of PCZ efficiency, reducing cell viability down to 20% after 72 h. Lower **1-PA@MNPs** concentration (20  $\mu\text{g}/\text{ml}$ ) does not induce a significant enhancement of PCZ efficiency (Figure 3.9c). In order to elucidate the role of the cavitand-functionalized MNPs in PCZ transport and delivery, the same cytotoxicity experiments in LoVo cells were performed adopting **2-PA@MNPs**, which is structurally analogous to **1-PA@MNPs** but inactive with respect to drug transport. Figure 3.9b and 3.9d compare the cytotoxicity of PCZ with that obtained by the addition of **2-PA@MNPs** (20, 40 and 80  $\text{mg}/\text{ml}$ ). Plots show no difference among the effects obtained by PCZ alone and in combination with **2-PA@MNPs** for all the concentrations. This result confirms that the absence of cavitand receptors precludes an effective PCZ loading on the MNPs surface (see figure 3.7) and, in turn, the MNPs-mediated internalization of the PCZ drug. The different behaviour between cavitand functionalized **1-PA@MNPs** and transport inactive **2-PA@MNPs** (summarized in Figure 3.9e-f for the highest concentration) when incubated with *N*-methylated drugs such as PCZ points out the importance of the combination of the cavitand complexation properties with the internalization capability of MNPs.

### 3.3 Conclusions

In this Chapter we reported the synthesis of new biocompatible MNPs possessing hyperthermic, luminescent and recognition properties, suited for multifunctional theranostic applications. This new system is based on a mixed phosphonic monolayer having two different terminal moieties ( $-\text{C}\equiv\text{CH}$ ,  $-\text{NH}_2$ ) which allow the anchoring of various functional molecules (Ti<sup>iii</sup>, PEG, FA and Rhod) through orthogonal azide-alkyne cycloaddition and amide bond formation, thus improving the versatility and the multi-functionality of the system. The magnetic characterization showed the typical magnetic behaviour of an ensemble of single domain magnetite nanoparticles, with magnetic irreversibility at low temperature and absence of coercivity at 300 K. Hyperthermic measurements, performed within the tolerance limits for clinical

applications, showed a significant SAR value (62.7 W/g), conferring to this material also the capability to act as heat mediator for Magnetic Fluid Hyperthermia, MFH. This nanomaterial is, therefore, suitable for the most common biomedical applications employing superparamagnetic nanoparticles, such as contrast agents for MRI or heat mediators for MFH. In addition, the rhodamine moieties anchored on the magnetic core makes it a luminescent probe for optical imaging applications. The synthesized new system thus possesses various complementary potentialities suited for both diagnostic and therapeutic applications ranging from bi-modal optical and magnetic imaging to hyperthermia and intracellular drug delivery. In this work, in particular, the luminescent properties were exploited to evaluate the internalization of functionalized MNPs after incubation in a LoVo cell culture by confocal microscopy, showing that internalization is very fast as it already occurs after 1 h of incubation. It must be noted that, despite the presence of the hydrophobic Tiii receptor and the rhodamine probe, **1-PA@MNPs** proved to be biocompatible, thanks to the presence of the hydrophilic PEG and FA. The potential of this new multi-functional system as enhanced intracellular drug carrier were evidenced by comparing the drug delivery properties of the cavitand-decorated nanoparticles **1-PA@MNPs** with the analogous transport inactive system **2-PA@MNPs**. The new synthesized cavitand-decorated **1-PA@MNPs**, indeed, are able to recognize and load PCZ, *in-situ*, acting as a shuttle which promotes the cellular internalization of the drug. These results not only confirmed a better loading capability of **1-PA@MNPs** compared to **2-PA@MNPs**, but also showed that the combined use of **1-PA@MNPs** with PCZ strongly increases the cytotoxicity of the drug towards tumoral cells. In conclusion, the proposed experiment demonstrates that the difference between success or failure in cancer therapy is often not only due to the used drug, but also how the drug is used.

### 3.4 Acknowledgments

The authors thank Ministero dell'Istruzione, dell'Università e della Ricerca (MIUR) for financial support through FIRB "RINAME Rete Integrata per la NAnoMedicina" (RBAP114AMK). The authors also thank Prof. G. Vecchio for DLS facilities.

### 3.5 Experimental Section

**Materials.** Iron(II) chloride tetrahydrate ( $\text{FeCl}_2 \cdot 4\text{H}_2\text{O}$ ), Iron (III) chloride hexahydrate ( $\text{FeCl}_3 \cdot 6\text{H}_2\text{O}$ ), Ammonium hydroxide ( $\text{NH}_4\text{OH}$ ), *N,N*-Dimethylformamide (DMF), ethanol, (+)-sodium L-ascorbate, Copper sulphate ( $\text{CuSO}_4$ ), Procarbazine hydrochloride ( $\text{PCZ} \cdot \text{HCl}$ ), 3-Aminopropylphosphonic acid ( $\text{NH}_2\text{-PA}$ ), 5(6)-Carboxy-X-rhodamine N-succinimidyl ester (Rhod), Methoxypolyethylene glycol acetic acid N-succinimidyl ester (PEG) of molecular weight (MW) 5000 Da, Folic acid (FA), N-Hydroxysuccinimide (NHS), *N,N'*-Dicyclohexylcarbodiimide (DCC), triethylamine, Dimethyl sulfoxide (DMSO) were purchased from Sigma-Aldrich Chemicals and were used without further purification. 10-Undecynylphosphonic acid ( $\text{C}\equiv\text{C-PA}$ ) were obtained from SiKÉMIA, Montpellier, France. The water was of Milli-Q grade (18.2 M $\Omega$ cm) and was filtered through a 0.22  $\mu\text{m}$  filter.

**Synthesis of Tiii-N<sub>3</sub>.** Tiii-N<sub>3</sub> was prepared following a published procedure.<sup>31</sup>

**Synthesis of magnetic nanoparticles.** Bare MNPs were prepared following the procedure reported in Chapter 2.

#### **Synthesis of N-Hydroxysuccinimide ester of folic acid (FA-NHS)**

FA-NHS was prepared by the following published method.<sup>32</sup> FA (500 mg) was dissolved in 10 ml of DMSO with 240  $\mu\text{l}$  of triethylamine. NHS (260 mg) and DCC (470 mg) were added and the mixture was reacted overnight at room temperature in the dark. The by-product, dicyclohexylurea, was removed by filtration. The DMSO solution was then concentrated under reduced pressure and FA-NHS was precipitated in diethyl ether. The product was washed several times with anhydrous ether and dried in air.

**Synthesis of PA@MNPs.** MNPs (200 mg) were dispersed in DMF (25 ml) using an ultrasonic bath for 30 min.  $\text{C}\equiv\text{C-PA}$  (100 mg) and  $\text{NH}_2\text{-PA}$  (180 mg) were added and the suspension was agitated for 6 h at room temperature. The particles were separated magnetically and washed four times with DMF followed by ethanol and dried under air.

**Synthesis of 1-PA@MNPs.** PA@MNPs (0.1 g) and Tiii-N<sub>3</sub> (0.02 mmol) were dispersed in DMF (20 mL), then  $\text{CuSO}_4$  (0.01 mmol) and (+)-sodium L-ascorbate (0.05 mmol) were added in sequence. The mixture was

vibrated with an orbital shaker at 25 °C for 24 hours. Afterwards, Tiiii functionalized PA@MNPs were separated magnetically washed three times with DMF and once with ethanol, then dried overnight at 25°C. Then, Tiiii functionalized PA@MNPs were re-dispersed in DMSO (20 ml) and FA-NHS (3 mg) Rhod-NHS (1.5 mg) and PEG-NHS (50 mg) were added. The solution was mixed overnight at 25°C. The obtained particles were separated magnetically, washed with DMSO, H<sub>2</sub>O, ethanol and dried under air.

**Synthesis of 2-PA@MNPs.** 2-PA@MNPs were obtained with a similar procedure as described above, but leaving out the “click-reaction” required to attach the Tiiii cavitand. PA@MNPs (0.1 g), were dispersed in DMSO (20 ml) and FA-NHS (3 mg) Rhod-NHS (1.5 mg) and PEG-NHS (50 mg) were added. The solution was mixed overnight at 25 °C. The obtained particles were separated magnetically, washed with DMSO, H<sub>2</sub>O, ethanol and dried under air.

## **Characterization**

**Functionalized MNPs Characterization.** XPS spectra were recorded with a PHI 5600 multi-technique ESCA-Auger spectrometer with a standard Mg-K $\alpha$  X-ray source. Analyses were carried out with a photoelectron take off angle of 45° (relative to the sample surface) with an acceptance angle of  $\pm 7^\circ$ . The XPS binding energy (B.E.) scale was calibrated by centring the C 1s peak due to hydrocarbon moieties and adventitious carbon at 285.0 eV. Transmission FT-IR measurements were recorded with a JASCO FTIR 430 spectrometer, using the KBr pellet technique, with 100 scans collected per spectrum (scan range 560–4000 cm<sup>-1</sup>, resolution 4 cm<sup>-1</sup>).

Experimental details of XRD, TEM, TGA and DLS characterization are reported in the Supplementary Information.

The magnetic properties of 1-PA@MNPs were investigated using a Quantum Design MPMS SQUID magnetometer, operating in the 1.8 K - 350 K temperature range and with applied magnetic field up to 5 T. The powder sample was hosted into a Teflon sample holder, whose diamagnetic contribution was found to be negligible. The recorded data were normalized for the effective amount of magnetic material obtained by TGA analysis.

The investigation of the hyperthermic properties of 1-PA@MNPs was performed through calorimetric measurements. Temperature kinetics of a

water dispersion of the sample exposed to an alternating magnetic field were recorded using an experimental set-up composed of a 6 kW Fives Celes® power supply, a water-cooled induction coil, a series of variable capacitors (420 nF - 4.8 mF) and an optical fiber thermometer. This system is able to produce an alternating magnetic field with frequency range of 50–400 kHz and field amplitude up to 19.1 kA/m. The field parameters used in this work (183 kHz, 17.0 kA/m) are within the physiological limit,  $H \cdot n < 5 \cdot 10^9 \text{ Am}^{-1}\text{s}^{-1}$ , beyond which deleterious responses of living tissues were observed. Error! Bookmark not defined. About 600ml of sample water dispersion (0.09% w/w of iron oxide) was placed in the middle of the induction coil, inside a sample holder thermostated at 37°C. The Specific Absorption Rate (SAR) value was evaluated using the formula

$$SAR = \frac{\sum_i m_i c_{pi}}{m_{Me}} \Delta T / \Delta t$$
, where  $DT$  is the temperature increase in the interval of time  $Dt$ ,  $m_{Me}$  is the total mass of metal,  $m_i$  is the mass of the  $i$ -species present in the sample and  $C_{pi}$  its specific heat. Since the measurements are carried out in non adiabatic conditions, the  $\Delta T / \Delta t$  values were extrapolated from the initial slope ( $t \rightarrow 0$ ) of the temperature kinetic curves. Moreover, the time elapse  $\Delta t$  is chosen much shorter than the time constant of the external thermalization circuit.

**Drug loading and release experiments.** Stock solution of PCZ (1 mM) was prepared by dissolving the drugs in Phosphate Buffered Saline (PBS) water solution (pH 6.8, 10 mM). Drug loading was performed by dispersing 1-PA@MNPs or 2-PA@MNPs (5 mg) in PCZ solution (4 mL). The solution was sonicated for 1 h in an ultrasonic bath and the MNPs were isolated from the solution by magnetic separation. The PCZ-loaded MNPs were suspended in PBS and were transferred into dialysis tubing (MW cutoff 3.0 kDa) and dialyzed against PBS (50 mL) for 12 h. Samples (2 mL) were periodically removed and assayed. The withdrawn volume of each sample was replaced by the same volume of fresh medium. The amounts of released PCZ was analysed with a JASCO V-560 UV/Vis spectrophotometer equipped with a 1 cm path length cell at 230 nm. The drug release study was performed in duplicate.

**Cell Culture.** Human mesenchymal stem cells (hMSCs) from adipose tissue and human colon adenocarcinoma cells (LoVo) were cultivated, respectively, in  $\alpha$ -Minimum Essential Medium ( $\alpha$ MEM) and RPMI 1640,

both supplemented with L-glutamine, nucleosides, Fungizon (penicillin 10 000 U mL<sup>-1</sup>, streptomycin 1000 µg/mL), 10% fetal bovine serum (FBS), and 100 mM ascorbic acid and maintained in a 37°C incubator, in a humidified atmosphere of 5% CO<sub>2</sub> /95% air. All products used were purchased from GIBCO (Life technologies). Both cell lines were detached by Trypsin/EDTA-4Na (0.05%/0.02% w/v) and used for experiments.

**Cytotoxicity assay.** From a 10<sup>4</sup> cells per mL<sup>-1</sup> cell suspension, 200 µL was seeded into each well of a 96-well tissue culture plate and maintained for 24 h in incubator. After this pre-adhesion time, medium was changed with fresh medium containing **1-PA@MNPs** and **2-PA@MNPs** at concentrations of 20, 40, and 80 µg/mL an PCZ at different concentrations (30 and 300 µg/mL). After 24, 48 and 72 h of incubation, cytotoxicity assay was performed using an MTT test, based on the reduction of yellow 3-(4,5-dimethylthiazol-2-yl)-2,5-diphenyl tetrazolium bromide (MTT) by mitochondrial succinate dehydrogenase. The optical density (OD) values at 550 nm of the wells, with background subtraction of OD at 655 nm, were measured by a microtiter plate reader. The cell viability was expressed in values % with respect to the control. All experiments were performed in triplicate.

**Confocal microscopy.** LoVo cells were cultured on glass coverslips and after 24 h of pre-adhesion were incubated with **1-PA@MNPs** (20 mg/ml) for 1, 6, 48 and 72 h. Samples were fixed in 4% para-formaldehyde (PFA) in PBS (15' at room temperature) and mounted with Vectashield containing DAPI (Vector Laboratories, Inc., Burlingame, CA). Localization of **1-PA@MNPs** was performed by using a Confocal Laser Scanning Microscopy (CLSM) (Zeiss LSM700).

### 3.6 Supplementary Information

#### Methods

X-Ray powder diffraction (XRD) measurements was performed with a  $\theta$ - $\theta$  5005 Bruker-AXS diffractometer (Zeiss, Oberkochen, Germany) using Cu  $K\alpha$  radiation operating at 40 kV and 30 mA.

The average diameter and size distribution were determined by Transmission Electron Microscopy (TEM), using a CM12 PHILIPS microscope operating at 100 kV. A dilute suspension of MNPs in water was drop dried onto 200 mesh carbon-coated copper grids. The statistics of MNPs diameter and size distribution was obtained considering about 400 particles, analyzing the recorded images with the Image Prop plus © software.

Thermogravimetric analysis (TGA) was performed on a Mettler Toledo TGA/SDTA 851<sup>e</sup> under air atmosphere. A 5-10 mg portion of nanoparticles was heated to 90 °C at 10 °C/min and kept at 90°C for 30 min to remove all adsorbed solvent. The sample was then heated to 600°C at 20°C/min to determine the amount of organic coating on the nanoparticle surface.

Dinamic Light scattering (DLS) and zeta-potential measurements of MNPs were performed with a Nano Zetasizer (Malvern Instruments, Malvern, UK).

#### XRD pattern of bare MNPs

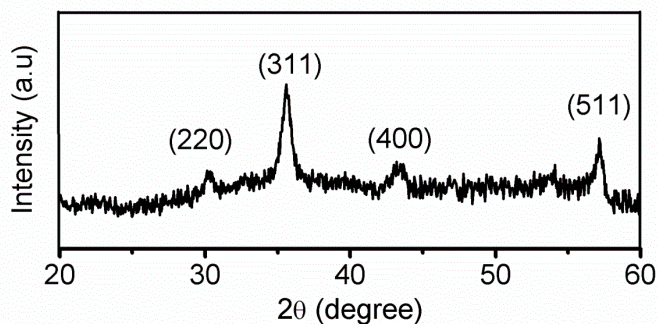
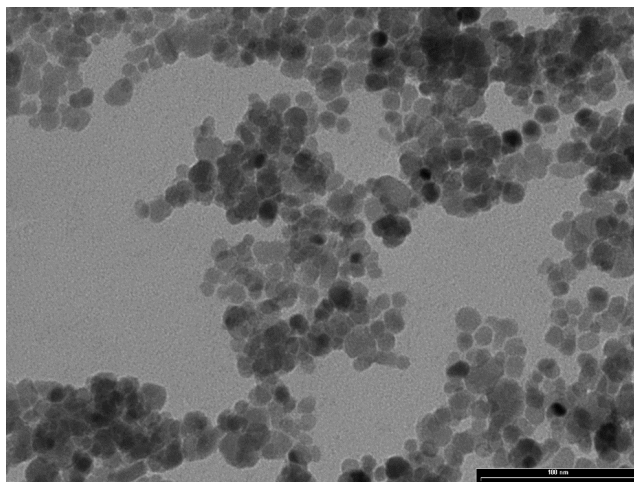


Figure S1 XRD pattern of bare MNPs.

### TEM images of bare MNPs



**Figure S2** Selected low magnification TEM image of bare MNPs.

### Thermogravimetric measurements

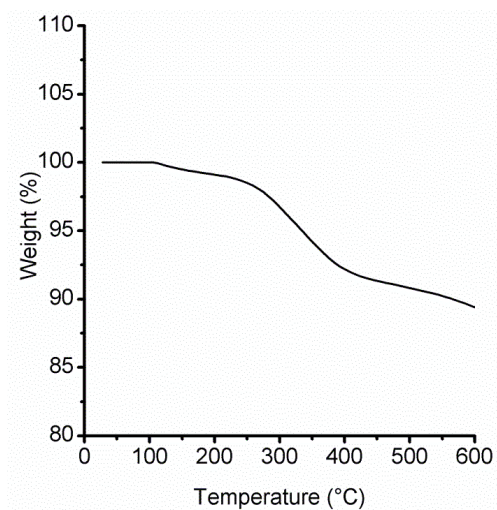


**Figure S3** Thermogram of 1-PA@MNPs.



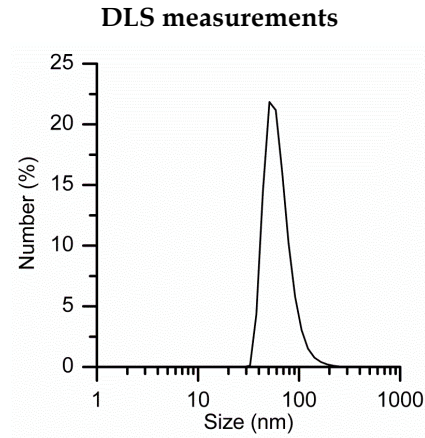


**Figure S4** Size distribution in water of 1-PA@MNPs.

### Cell Viability

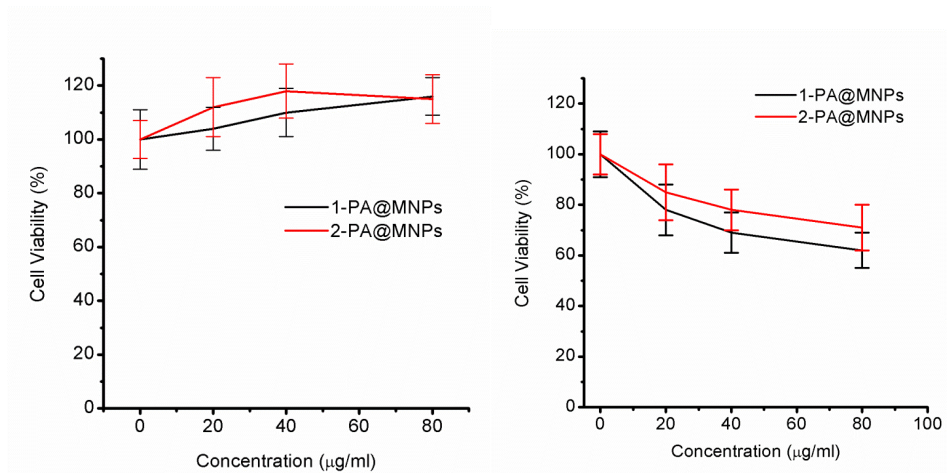


**Figure S5** Cell viability of a) hMSCs and b) LoVo cells evaluated by MTT after 72 h of incubation with 1-PA@MNPs and 2-PA@MNPs at different concentrations.

### 3.7 References

- <sup>1</sup> a) N. Erathodiyil, J. Y. Ying, *Acc. Chem. Res.* **2011**, *44*, 925–935; b) S. T. Selvan, T. T. Y. Tan, D. K. Yi, N. R. Jana, *Langmuir* **2010**, *26*, 11631–11641; c) L. K. Bogart, G. Pourroy, C. J. Murphy, V. Puentes, T. Pellegrino, D. Rosenblum, D. Peer, R. Lévy, *ACS Nano* **2014**, *8*, 3107–3122.
- <sup>2</sup> a) A. K. Gupta, M. Gupta, *Biomaterials* **2005**, *26*, 3995–4021; b) A. J. Cole, A. E. David, J. Wang, C. J. Galbán, H. L. Hill, V. C. Yang, *Biomaterials* **2011**, *32*, 2183–2193.
- <sup>3</sup> a) Y. Pan, X. Du, F. Zhao, B. Xu, *Chem. Soc. Rev.* **2012**, *41*, 2912–2942; b) Z. Huang, N. Pei, Y. Wang, X. Xie, A. Sun, Li Shen, S. Zhang, X. Liu, Y. Zou, J. Qian, J. Ge, *Biomaterials* **2010**, *31*, 2130–2140.
- <sup>4</sup> a) C. Wilhelm, F. Gazeau, *Biomaterials* **2008**, *29*, 3161–3174; b) K. Gee Neoh, E. T. Kang, *Soft Matter* **2012**, *8*, 2057–2069.
- <sup>5</sup> I. K. Herrmann, R. E. Bernabei, M. Urner, R. N. Grass, B. Beck-Schimmer, W. J. Stark, *Nephrol. Dial. Transplant* **2011**, *26*, 2948–2954.
- <sup>6</sup> a) T. T. T. N'Guyen, H. T. T. Duong, J. Basuki, V. Montembault, S. Pascual, C. Guibert, J. Fresnais, C. Boyer, M. R. Whittaker, T. P. Davis, L. Fontaine, *Angew. Chem. Int. Ed.* **2013**, *52*, 14152 – 14156; b) V. V. Mody, A. Cox, S. Shah, A. Singh, W. Bevins, H. Parihar, *Appl. Nanosci.* **2014**, *4*, 385–392.
- <sup>7</sup> a) P. Arosio, J. Thévenot, T. Orlando, F. Orsini, M. Corti, M. Mariani, L. Bordonali, C. Innocenti, C. Sangregorio, H. Oliveira, S. Lecommandoux, A. Lascialfari, O. Sandre, *J. Mater. Chem. B* **2013**, *1*, 5317–5328; b) C. Tassa, S. Y. Shaw, R. Weissleder, *Acc. Chem. Res.* **2011**, *44*, 842–852.
- <sup>8</sup> a) D. L. Troyer, S. H. Bossman, Utilization of magnetic nanoparticles for cancer therapy in *Nanomedicine and Cancer* **2012**, R. P. Srirajaskanthan, R. Victor, Eds. Science Publisher and CRC Press Taylor & Francis Group; b) M. Creixell, A. C. Bohòrquez, M. Torres-Lugo, Carlos Rinaldi, *ACS Nano* **2011**, *5*, 7124–7129; c) D. Yoo, H. Jeong, S.-H. Noh, J.-H. Lee, J. Cheon, *Angew. Chem. Int. Ed.* **2013**,

52, 13047–13051; d) E. Fantechi, C. Innocenti, M. Zanardelli, M. Fittipaldi, E. Falvo, M. Carbo, V. Shullani, L. Di Cesare Mannelli, C. Ghelardini, A. M. Ferretti, A. Ponti, C. Sangregorio, P. Ceci, *ACS Nano* **2014**, *8*, 4705–4719.

<sup>9</sup> K. Turcheniuk, A. V. Tarasevych, V. P. Kukhar, R. Boukherroub, S. Szunerits, *Nanoscale* **2013**, *5*, 10729–10752.

<sup>10</sup> a) P. Budime Santhosh, N. P. Ulrih, *Cancer Lett.* **2013**, *336*, 8–17; b) L. Lartigue, C. Innocenti, T. Kalaivani, A. Awwad, M. del Mar Sanchez Duque, Y. Guari, J. Larionova, C. Guérin, J.-L. G. Montero, V. Barragan-Montero, P. Arosio, A. Lascialfari, D. Gatteschi, C. Sangregorio, *J. Am. Chem. Soc.* **2011**, *133*, 10459–10472; c) D. Maggioni, P. Arosio, F. Orsini, A. M. Ferretti, T. Orlando, A. Manfredi, E. Ranucci, P. Ferruti, G. D'Alfonso, A. Lascialfari, *Dalton Trans.* **2014**, *43*, 1172–1183.

<sup>11</sup> R. Pinalli, E. Dalcanale, *Acc. Chem. Res.* **2013**, *46*, 399–411.

<sup>12</sup> E. Biavardi, M. Favazza, A. Motta, I. L. Fragalà, C. Massera, L. Prodi, M. Montalti, M. Melegari, G. G. Condorelli, E. Dalcanale, *J. Am. Chem. Soc.* **2009**, *131*, 7447–7455.

<sup>13</sup> E. Biavardi, C. Tudisco, F. Maffei, A. Motta, C. Massera, G. G. Condorelli, E. Dalcanale, *Proc. Natl. Acad. Sci. USA* **2012**, *109*, 2263–2268.

<sup>14</sup> C. Tudisco, F. Bertani, M. T. Cambria, F. Sinatra, E. Fantechi, C. Innocenti, C. Sangregorio, E. Dalcanale, G. G. Condorelli, *Nanoscale* **2013**, *5*, 11438–11446.

<sup>15</sup> E. Biavardi, S. Federici, C. Tudisco, D. Menozzi, C. Massera, A. Sottini, G. G. Condorelli, P. Bergese, E. Dalcanale, *Angew. Chem. Int. Ed.* **2014**, *53*, 9183–9188.

<sup>16</sup> a) K. Hayashi, M. Moriya, W. Sakamoto, T. Yogo, *Chem. Mater.* **2009**, *21*, 1318–1325; b) C. P. Leamon, A. L. Jackman, *Vitam. Horm.* **2008**, *79*, 203–233; c) Y. Lu, P. S. Low, *Adv. Drug Deliv. Rev.* **2002**, *54*, 675–693; d) S. Rijnboutt, G. Jansen, G. Postuma, J. B. Hynes, J. H. Schornagel, G. J. Strous, *J. Cell Biol.* **1999**, *132*, 35–47.

<sup>17</sup> a) G. B. Henderson, *Annu. Rev. Nutr.* **1990**, *10*, 319–335; b) A. C. Antony, *Annu. Rev. Nutr.* **1996**, *16*, 501–521.

- <sup>18</sup> a) J. Sudimack, R. J. Lee, *Adv. Drug Deliv. Rev.* **2000**, *41*, 147-162; b) J. Li, L. Zheng, H. Cai, W. Sun, M. Shen, G. Zhang, X. Shi, *Biomaterials* **2013**, *34*, 8382-8392.
- <sup>19</sup> J. J. Gallagher, R. Tekoriute, J.-A. O'Reilly, C. Kerskens, Y. K. Gun'ko, M. Lynch, *J. Mater. Chem.* **2009**, *19*, 4081-4084.
- <sup>20</sup> C. A. Graham, T. F. Cloughesy, *Semin. Oncol. Nurs.* **2004**, *20*, 260-272.
- <sup>21</sup> Y. S. Kang, S. Risbud, J. F. Rabolt, P. Stroeve, *Chem. Mater.* **1996**, *8*, 2209-2211.
- <sup>22</sup> a) E. Smecca, A. Motta, M. E. Fragalà, Y. Aleeva, G. G. Condorelli, *J. Phys. Chem. C* **2013**, *117*, 5364-5372; b) C. Tudisco, V. Oliveri, M. Cantarella, G. Vecchio, G. G. Condorelli, *Eur. J. Inorg. Chem.* **2012**, *32*, 5323-5331.
- <sup>23</sup> S. Manju, C. P. Sharma, K. Sreenivasan, *J. Mater. Chem.* **2011**, *21*, 15708-15717.
- <sup>24</sup> a) Y. Zhang, N. Kohler, M. Zhang, *Biomaterials* **2002**, *23*, 1553-1561; b) C. Lu, L. R. Bhatt, H. Y. Jun, S. H. Park, K. Y. Chai, *J. Mater. Chem.* **2012**, *22*, 19806-19811.
- <sup>25</sup> J. Coates, *Interpretation of Infrared Spectra, A Practical Approach in Encyclopedia of Analytical Chemistry* **2000**, R. A. Meyers Ed., John Wiley & Sons Ltd.
- <sup>26</sup> K. Hayashi, K. Ono, H. Suzuki, M. Sawada, M. Moriya, W. Sakamoto, T. Yogo, *ACS Appl. Mater. Interfaces* **2010**, *2*, 1903-1911.
- <sup>27</sup> S. Mohapatra, P. Pramanik, *Colloids Surf. A* **2009**, *339*, 35-42.
- <sup>28</sup> M. El-Hilo, R. W. Chantrell, K. O'Grady, *J. Appl. Phys.* **1998**, *9*, 5114-5122.
- <sup>29</sup> J. I. Gittlemann, B. Abeles, S. Bosowski, *Phys. Rev. B* **1974**, *9*, 3891-3897.
- <sup>30</sup> R. Hergt, S. Dutz, *J. Magn. Magn. Mater.* **2007**, *311*, 187-192.

<sup>31</sup> M. Dionisio, J. M. Schnorr, V. K. Michaelis, R. G. Griffin, T. M. Swager, E. Dalcanale, *J. Am. Chem. Soc.* **2012**, *134*, 6540–6543.

<sup>32</sup> R. J. Lee, P. S. Low, *J. Biological Chem.* **1994**, *5*, 3198–3204.

# Chapter 4

## Trypticene Quinoxaline- bridged Cavitands<sup>\*</sup>

<sup>\*</sup> This work has been carried out in the group of Prof. Timothy M. Swager at Massachusetts Institute of Technology (MIT), Cambridge (USA).

## 4.1 Introduction

The air pollution in vast urban and industrial areas entails the design of new air quality control systems capable to monitor the most dangerous pollutants at very low concentration. The detection of airborne aromatic hydrocarbons BTEX (benzene, ethylbenzene, toluene, xylenes) constitutes a long standing problem, due to the need of measuring them with high precision at extremely low concentrations in the presence of overwhelming amounts of aliphatic hydrocarbons: the European Union established in 2010 a stricter limit for benzene of  $5 \mu\text{g}/\text{m}^3$  ( $\sim 1.44$  ppb).<sup>1</sup> Benzene is a proven carcinogen: inhalation of high levels of benzene could be fatal and long-term exposure to lower concentrations can cause leukemia. Nowadays, the real-time air quality control measurements are done by bulky, expensive, high-end systems based on advanced laboratory equipment.

The complexation properties of tetraquinoxaline cavitands (QxCav) towards aromatic hydrocarbons have been recently exploited in our group to fabricate a low-cost system based on selective detection of harmful Volatile Organic Compounds (VOCs), exploiting molecular recognition.<sup>2</sup> The prototype is equipped with a pre-concentrator unit filled with QxCav molecules. The receptor cavity is able to discriminate aromatic from aliphatic hydrocarbons due to the formation of specific interactions like CH- $\pi$ ,  $\pi$ - $\pi$  interactions and H-bonds (see Chapter 1). The cavitand action in this device is twofold (Figure 4.1): in the adsorption phase the aromatic components are selectively retained at the ppb level in the presence of all the other pollutants and interferents present in air. Afterwards, the pre-concentrator is heated in order to release the entrapped analytes, which are consequently separated in the mini-GC column and detected by the MOX sensor.

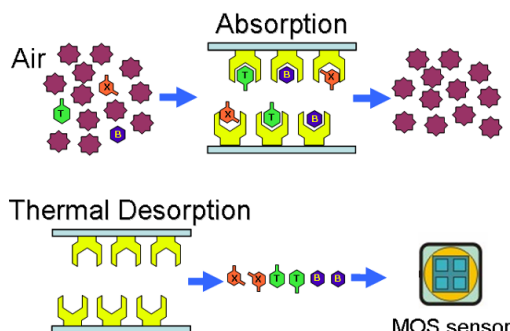


**Figure 4.1** The schematic sensing protocol of the mini-GC system.

The pre-concentrating unit shows excellent performances in terms of absorption efficiency, desorption kinetics and reproducibility. Furthermore, QxCav sampling and desorption are not influenced by relative humidity, making the system suitable for direct environmental sampling of aromatic hydrocarbons. However, the discrimination among BTEX class is impossible to achieve in this first unit: indeed the device is equipped with a GC system after the pre-concentrator for VOCs separation. Selective release of benzene before the other aromatics is an intriguing challenge for our group: to reach this target, new tetraquinoxaline cavitanths with enhanced toluene versus benzene affinity are required.

Herein we report the synthesis of a new class of tetraquinoxaline cavitanths functionalized with triptycene units at the upper rim (Figure 4.2): affinity of cavitanths **9** and **11** toward benzene was measured by  $^1\text{H}$  NMR and TGA. SPME fibers coated with **9** were tested to evaluate the selectivity in the benzene uptake over TEX.

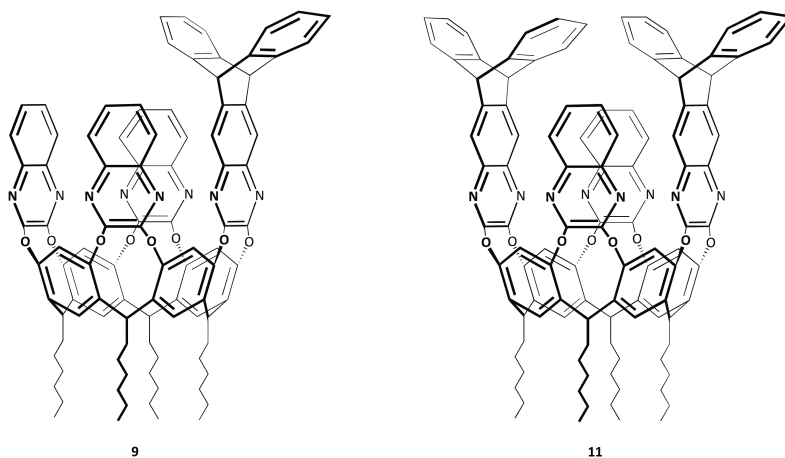


**Figure 4.2** Triptycene-functionalized quinoxaline cavitanths **9** and **11**.

## 4.2 Results and discussion

### 4.2.1 Design of Tripty-QxCav

The design of a molecular receptor requires both electronic and shape complementarity with the guest. In our case, due to its lack of dipole moment, the benzene recognition process is driven mainly by size complementarity and

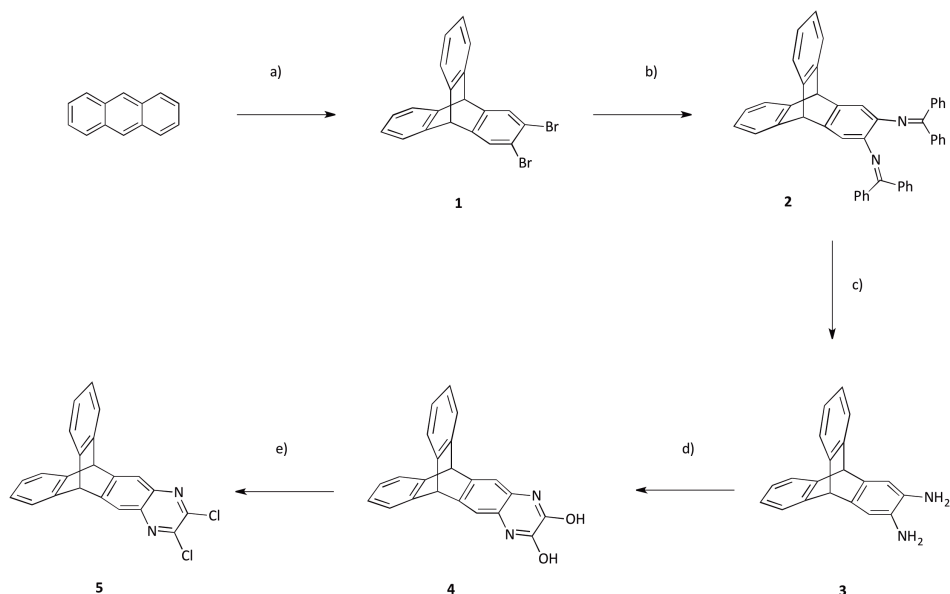


CH- $\pi$  interactions with the deep, electron rich cavity. While the electronic properties among the BTEX class are more or less invariant, their steric hindrance is different. By introducing a steric element on the host structure able to modify the shape complementarity in the host-guest complex formation, different analytes could be discriminated in the recognition processes. It is well known that structural changes introduced in the cavitand molecule have a great influence on the hosting properties of the receptor.<sup>3</sup>

Thus we designed and synthesized the QxCav **9** and **11**, single and double-functionalized respectively at the upper rim with triptycene moieties. The introduction of the bulky triptycene unit at the upper rim led to a tighter cavity mouth: the idea was to achieve a selective recognition of benzene, by an improved benzene over TEX affinity in either adsorption phase or in the desorption one. The receptors were prepared via convergent synthetic approach: 1) synthesis of the triptycene-functionalized quinoxaline bridging unit **5**; 2) synthesis of the cavitand scaffold. The last synthetic step was the bridging reaction to yield QxCav **9** and **11**.

## 4.2.2 Synthesis of the Triptycene-quinoxaline Bridging Unit

Triptycene-functionalized bridging reagent **5** was prepared in five steps and 43% overall yield (Scheme 4.1). The multistep synthesis started with the Diels-Alder addition reaction of anthracene with benzyne, *in situ* generated from the reaction of *n*-BuLi, with 1,2,4,5-tetrabromobenzene to afford dibromotriptycene **1**.<sup>4</sup> The next step was the palladium-catalyzed Buchwald-Hartwig amination with benzophenone imine in refluxing toluene: this reaction allowed the insertion of two imines to obtain compound **4** in 83% yield after chromatographic purification. The amino protecting groups were then removed at room temperature with hydrochloric acid, followed by neutralization with sodium hydroxide to afford diaminotriptycene **3** after filtration.



**Scheme 4.1** Synthesis of **5**: a) 1,2,4,5-tetrabromobenzene, *n*-BuLi, toluene, r.t., 12 h, 62%; b) benzophenone imine, Pd<sub>2</sub>(dba)<sub>3</sub>, *rac*-BINAP, NaOtBu, toluene, reflux, 12 h, 83%; c) 1) HCl 2 N, THF, r.t., 0.5 h; 2) NaOH 2 N, THF, r.t., 0.5 h, 97% (over two steps); d) oxalic acid, HCl 4 N, 12 h, reflux, 89%; e) thionyl chloride, DMF cat, 1,2-dichloroethane, reflux, 12 h, 87%.

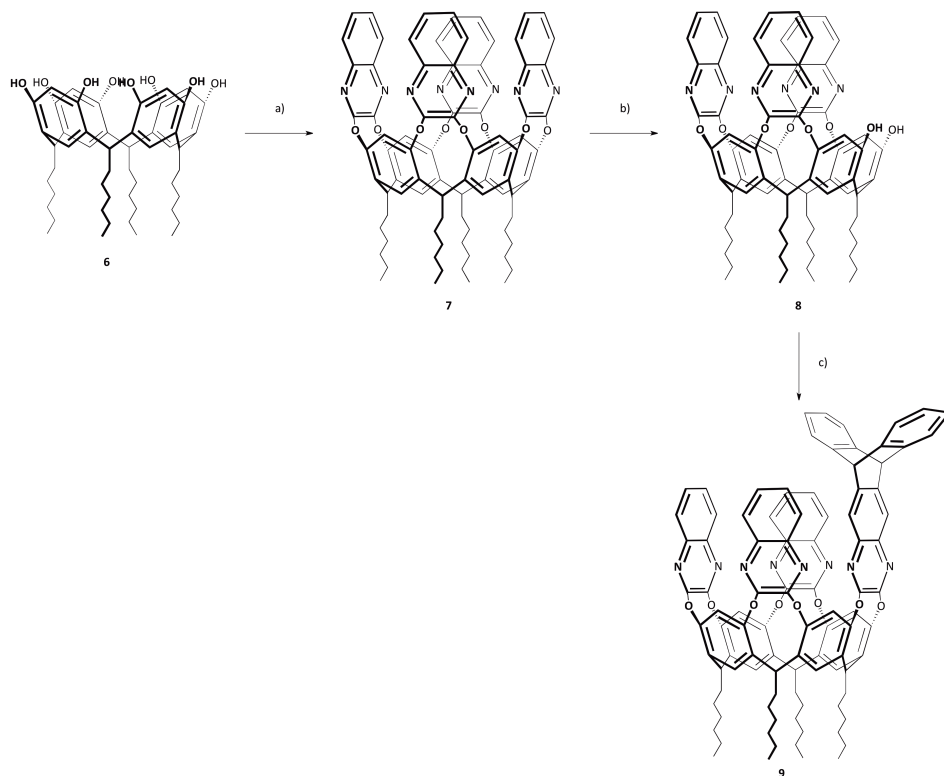
The synthetic pathway reported in literature for the synthesis derivative **3**,<sup>5</sup> a very useful building block for triptycene chemistry, proceeds through 5 synthetic steps and tedious purifications, to afford **3** in low overall yield. With this new protocol, inspired by a synthetic pathway developed for hexaamino-triptycene in 2012,<sup>6</sup> diamino-triptycene is synthesized in 3 steps with 50% yield and two only chromatographic purifications. Due to the high reactivity of amino groups, compound **3** was used without any further purification for a condensation reaction with oxalic acid under acidic conditions to give **4** in 89% yield. Target 2,3-dihydroxy-6,7-triptycenequinoxaline **5** was prepared by chlorination of **4** with thionyl chloride catalyzed by DMF in refluxing 1,2-dichloroethane. The crude was purified by flash chromatography to afford pure compound **5** as a white solid in 87% yield.

#### 4.2.3 Synthesis of Tripty-QxCav **9**

Resorcinarene **6** with hexyl feet was chosen as resorcinarene scaffold for both TriptyQxCav **9** and **11**: the length of the alkyl chains is a good compromise

between solubility and easy of crystallization. Solubility helps in purification of intermediates and final products.

The preparation of monofunctionalized QxCav **9** required the synthesis of a triquinoxaline cavitand, followed by the bringing reaction with **5** (Scheme 4.2). The most convenient route to synthesize triquinoxaline cavitands in good yield is the selective removal of one quinoxaline unit from the easily prepared tetraquinoxaline cavitand **7**.<sup>7</sup>



**Scheme 4.2** Synthesis of **9**: a) 2,3-dichloroquinoxaline,  $K_2CO_3$ , DMF,  $80^\circ C$ , 12 h, 59%; b) catechol, CsF,  $80^\circ C$ , 1 h, 70%; c) **5**,  $K_2CO_3$ , DMF,  $120^\circ C$  under microwave irradiation (300 W), 1 h, 65%.

Tetraquinoxaline cavitand **7** was obtained by reaction of **6** (see experimental section for synthesis of **6**) with 2,3-dichloroquinoxaline in presence of potassium carbonate. QxCav **7** was isolated in 65% yield after recrystallization from ethyl acetate. The selective removal of one quinoxaline unit was performed by reaction of **7** with 1.1 equivalents of catechol, in presence of cesium fluoride as base.

Purification by flash chromatography afforded trifunctionalized QxCav **8** in 70% yield.

Finally we performed the bridging reaction between **8** and **5** in presence of potassium carbonate in DMF as solvent. We found that the use of microwave, in this case, offered higher yield, cleaner reaction mixture and faster reaction. Tripty-QxCav **9** was isolated as a white solid after chromatographic purification in 65% yield. The product was characterized by MALDI-TOF (Figure 4.3) and  $^1\text{H-NMR}$ .

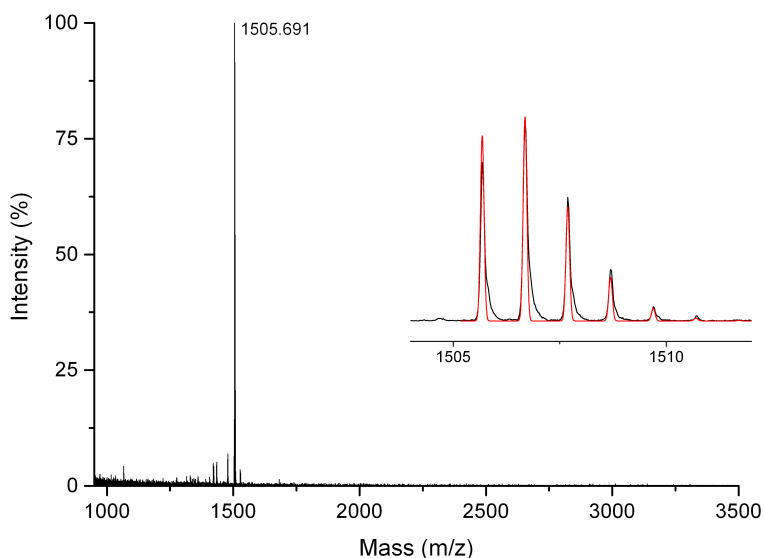


**Figure 4.3** High-resolution MALDI-TOF spectrum of **9**, with experimental (black lines) versus theoretical (red) isotopic distribution pattern in the inset.

The MALDI spectrum showed the protonated molecular ion as the major peak: the experimental isotopic distribution was in agreement with the calculated one.

#### 4.2.4 $^1\text{H}$ NMR Characterization of **9**

As already reported in Chapter 1, quinoxaline bridged-cavitands are able to perform reversible switching between a closed “vase” conformation with a deep cavity, capable to guest complexation, and an open “kite” conformation with a flat extended surface (Figure 4.4).

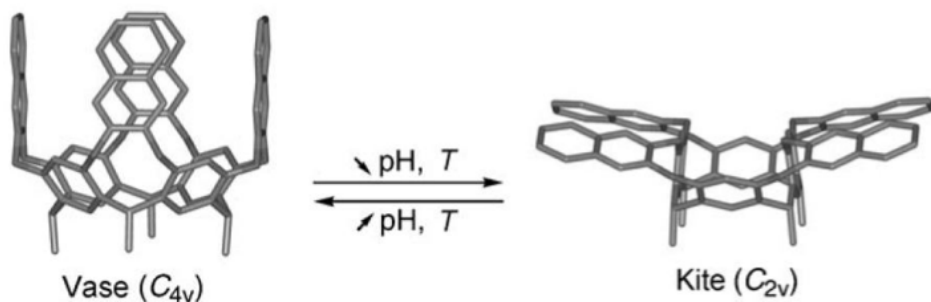


**Figure 4.4** Kite-vase equilibrium for quinoxaline bridged-cavitands.

Tetraquinoxaline cavitands in the vase conformation present strong affinity toward aromatic guests inclusion: however the presence of a bulky group at the upper rim, like the triptycene unit, could destabilize the vase conformation in favor of the kite one. The conformation adopted by a QxCav under given solvent or temperature conditions and its dynamics can be revealed by  $^1\text{H}$  NMR spectroscopy.<sup>8</sup> In particular it's crucial the analysis of the chemical shifts of the resorcinarene methine protons, as their chemical shifts are diagnostic of the conformation adopted by the cavitand.

We first investigated the conformation adopted by **9** in  $\text{CDCl}_3$  (Figure 4.5): the  $^1\text{H}$  NMR spectrum shows all the diagnostic signals. In the low ppm region are present all signals belonging to the hexyl feet; the singlet at 5.44 ppm integrating two protons corresponds to the methine protons of the triptycene moiety, while the high ppm region, from 7.0 to 8.1 ppm, is relative to the aromatic signals. The broad signal of the methine proton of the resorcinarene scaffold (red dot in Figure 4.5) at 5.34 ppm integrating 4 protons indicates the vase conformation of the cavitand. The broadness is obviously caused by the asymmetry of the molecules. At the opposite, for the kite conformation the signal would be up-field shifted to ca. 4 ppm.

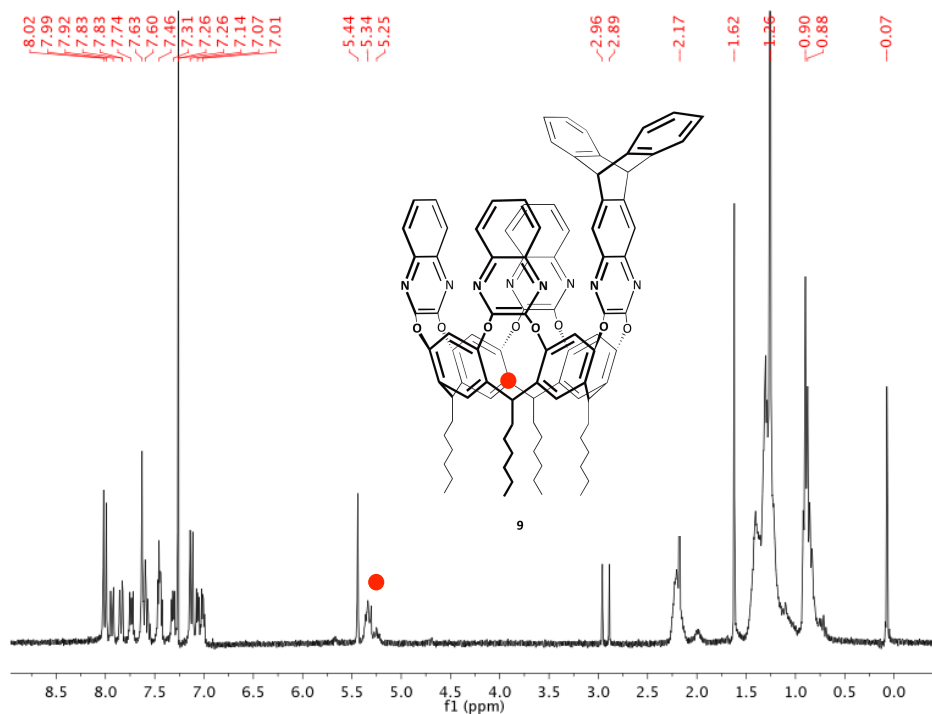


**Figure 4.5**  $^1\text{H}$  NMR spectrum of **9** in  $\text{CDCl}_3$ .

Thus we demonstrated that the introduction of the trypticene moiety at the upper rim does not prevent the vase conformation in chloroform. We then recorded the  $^1\text{H}$  NMR spectrum in  $\text{C}_6\text{D}_6$  (Figure 4.6): the diagnostic signal observed in  $\text{CDCl}_3$  at 5.34 ppm relative to methine proton was further down-field shifted to 6.0 ppm. Moreover instead of a broad signal, three different overlapped sharper triplets integrating for 4 protons total were present.

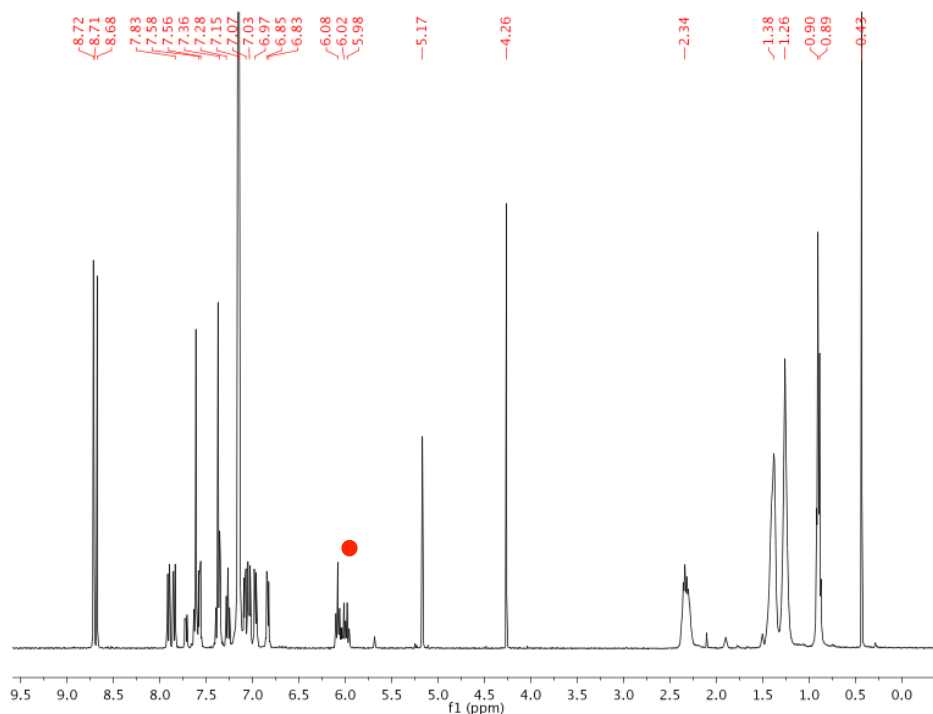


**Figure 4.6**  $^1\text{H}$ -NMR spectrum of **9** in  $\text{C}_6\text{D}_6$ .

The remarkable down-field shift observed for the CH proton in deuterated benzene along with the sharpness of the peaks are consistent with a high affinity toward the aromatic guest: in fact the benzene molecules, complexed inside the cavity, stabilize the vase conformation through CH- $\pi$  interactions with the surrounding walls of the cavitand. Vase conformation was found in all of the deuterated solvents tested (Table 4.1):

Deuterated Solvent	Chemical shift (ppm)
$\text{CDCl}_3$	5.3
$\text{C}_6\text{D}_6$	6.0
Acetone	5.7
DMSO	5.3

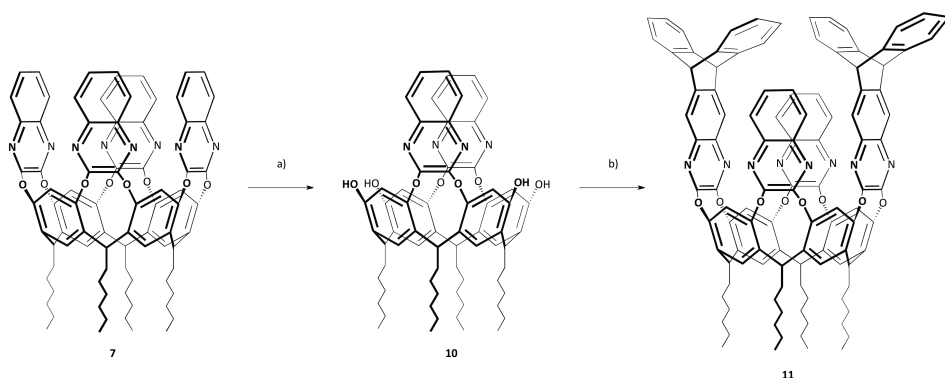
**Table 4.1**  $^1\text{H}$  NMR chemical shift of methine proton for **9** in different deuterated solvents.

Thus we proved that, despite the introduction of the triptycene unit at the upper rim, the vase conformation is still favored in solution, an essential feature to exploit TriptyQxCav **9** for benzene sensing.

#### 4.2.5 Synthesis of Tripty-QxCav **11**

As we found that vase conformation was the favorable form for Tripty-QxCav **9**, we decided to synthesize the corresponding double functionalized AC derivative **11**: the idea was to evaluate if the increased steric hindrance at the upper rim would preclude the vase conformation, and, if not, to use **11** as well as **9** for benzene complexation.

Synthesis of **11** started with the selective excision of two quinoxaline units from **7**, using 3.3 equivalents of catechol and cesium fluoride, to afford the AC cavitand **10** after purification by flash chromatography in 55% yield (Scheme 4.3).<sup>7</sup>



**Scheme 4.2** Synthesis of **9**: a) catechol, CsF, 80°C, 1 h, 55%; c) **5**, K<sub>2</sub>CO<sub>3</sub>, DMF, 120°C under microwave irradiation (300 W), 1 h, 46%.

At this point we performed the bridging reaction on **10** with **5**, in presence of potassium carbonate in DMF as solvent, under microwaves irradiation. Tripty-QxCav **11** was isolated as a white solid after chromatographic purification in 46% yield. The product was characterized by MALDI-TOF and <sup>1</sup>H NMR.



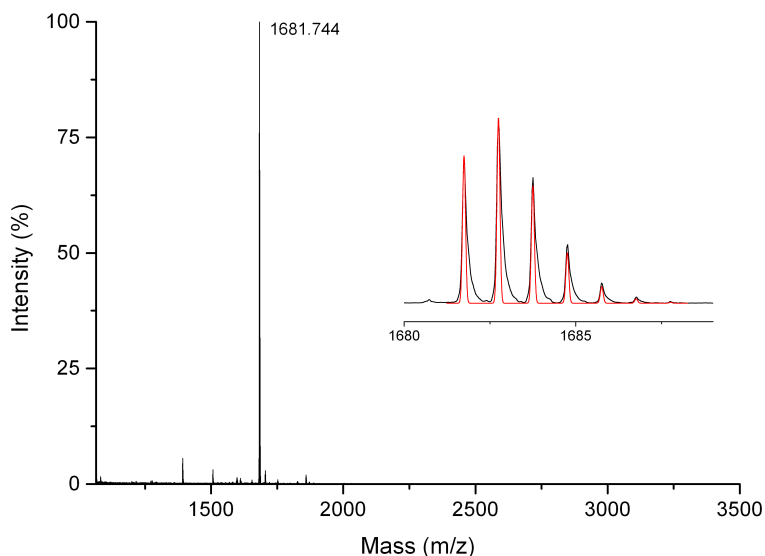


**Figure 4.7** High-resolution MALDI-TOF spectrum of **11**, with experimental (black lines) versus theoretical (red) isotopic distribution pattern in the inset.

The MALDI-TOF spectrum showed the protonated molecular ion as the major peak, and its isotopic distribution was in agreement with the theoretical one.

$^1\text{H}$  NMR spectrum recorded in  $\text{CDCl}_3$  showed the diagnostic methine proton as a broad signal at 4.86 ppm, 0.48 ppm down-field shifted with respect to analogue proton for **9**. The shift was consistent with a more open conformation, due to the presence of two triptycene units at the upper rim, hampering the vase conformation. However the cavitand molecules were not completely open: they were in fluxional situation between vase and kite forms. On the contrary, the  $^1\text{H}$  NMR spectrum of **11** recorded in  $\text{C}_6\text{D}_6$  showed two sharp triplets integrating two protons each at 6.19 and 5.86 ppm. The first one is relative to the two CH protons below the triptycene quinoxalines, while the second triplet corresponds to the methine protons below the quinoxalines. The chemical shift clearly indicated that **11** was fully in the vase conformation. Once again the guest molecules of benzene, complexed inside the cavity, stabilized the vase conformation through CH- $\pi$  interactions with the surrounding walls of the cavitand: these attractive forces were stronger than the steric repulsion.

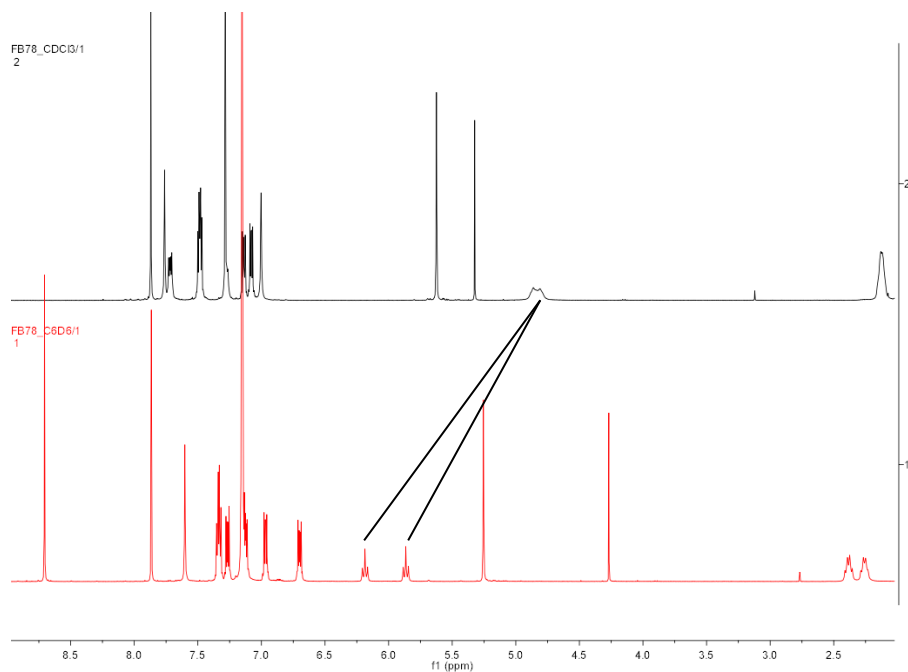
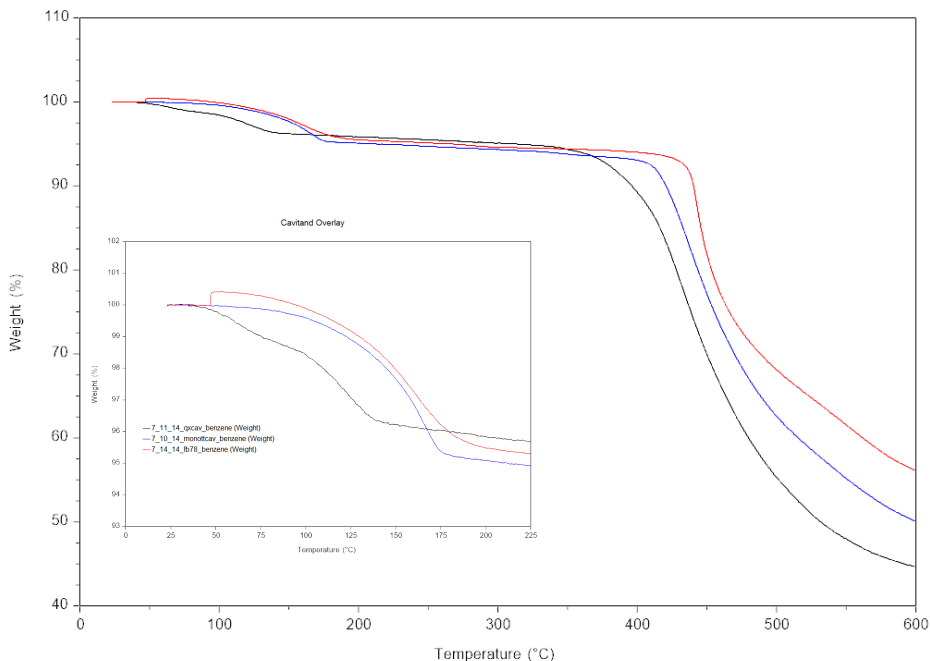


Figure 4.8 Enlarged  $^1\text{H}$  NMR spectra of **11** in  $\text{CDCl}_3$  (top) and  $\text{C}_6\text{D}_6$  (below).

#### 4.2.6 Thermo Gravimetric Analysis of **9** and **11**

The thermal stabilities of TriptyQxCavs **9** and **11** were measured by thermo gravimetric analysis and compared with the tetraquinoxaline cavitand. The three samples were completely solubilized in benzene and the solvent was removed by low pressure evaporation with a rotavapor. It is known that that entrapped guest inside the quinoxaline cavitands are released well above the boiling points of the guest component.<sup>9</sup> The release temperature is important to evaluate the forces involved in benzene complexation: the higher is the value, the stronger is the host-guest complex.

The thermal decomposition of the cavitands was measured under nitrogen atmosphere using temperature cycles spanning range from 20°C to 600°C at 5 deg/min.



**Figure 4.9** TGA analysis of QxCav (black line), **9** (blue line) and **11** (red line) cavitands under nitrogen, with enlargement in the inset.

The three samples are characterized by two different slopes: the first one, starting at ca. 40-50°C and finishing at ca. 200°C can be considered as the thermal decomplexation of the entrapped guest inside the cavity (inset figure 4.9). The second slope, from ca. 350-450°C is due to the thermal degradation of the receptors. All of the cavitands show good thermal stability up to 350°C and even higher for the TriptyQxCavs **9** and **11**.

As reported in the table below, the release temperature increases by 45°C for **9** and 55°C for **11** compared to the tetraQxCav.

Cavitand	Desorption T (°C)
QxCav	135
MonoTriptyQxCav <b>9</b>	<b>179</b>
DiTriptyQxCav <b>11</b>	<b>189</b>

**Table 4.2** Desorption temperatures for QxCav, **9** and **11**.

The increase of temperature at which the aromatic guest is desorbed in **9** and **11** compared to tetraquinoxaline cavitand is relevant, indicating higher complexation forces inside the host molecule. The introduction of a single bulky triptycene unit at the upper rim hampers the release of entrapped benzene guest inside the cavity. The introduction of a second triptycene moiety causes a smaller 10°C enhancement in the release temperature for **11**. This indicates that the major "roof" effect is obtained by a single triptycene unit.

#### 4.2.7 SPME Analysis

Solid Phase Micro Extraction (SPME) was performed in order to evaluate the properties of the new TriptyQxCav receptor **9** towards the entrapment of volatile aromatic hydrocarbons (BTEX). The general procedure is showed in Figure 4.10: the sample to be analyzed is closed in a sealed vial and the fiber is introduced in the headspace of the vial.

The fiber for the analysis was prepared coating the commercial silicon fiber with the fine powdered **9** receptor with the help of epoxy glue. In this way, the cavitand is only physisorbed on the polymeric surface and not covalently linked to the resin. The incubation was performed for 15 minutes at 25°C, followed by thermal desorption at 300°C in the GC inlet. The fiber was tested towards benzene, toluene, ethylbenzene, *o*-xylene, *m*-+*p*-xylene and styrene. A fiber coated with tetraQxCav was also prepared as an initial reference.

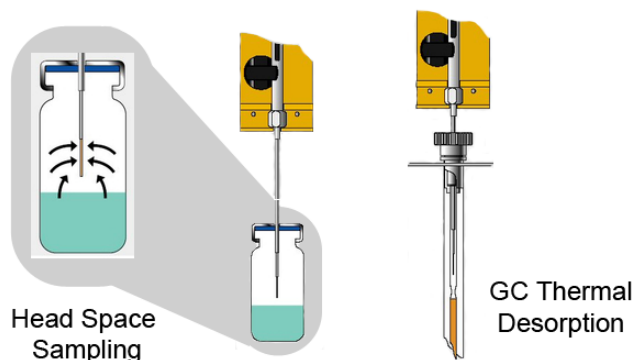


**Figure 4.10** SPME setup and procedure.

The fiber showed a good linearity range for all the tested analytes:

Benzene: 0.4-9.8  $\mu\text{g}/\text{m}^3$

Toluene: 0.4-8.8  $\mu\text{g}/\text{m}^3$

Ethylbenzene: 0.4-7.3  $\mu\text{g}/\text{m}^3$

*m*-+*p*-xylene: 0.7-13.7  $\mu\text{g}/\text{m}^3$

Styrene: 0.9-19.6  $\mu\text{g}/\text{m}^3$

*p*-xylene: 1.4-28.2  $\mu\text{g}/\text{m}^3$

In particular, limit of detection for benzene (LOD = 0.001-0.08  $\mu\text{g}/\text{m}^3$ ) was lower than the limit established by the European Union (5  $\mu\text{g}/\text{m}^3$ ),<sup>1</sup> indicating that this method is suitable for monitoring air pollution.

The comparison of **9** with the fiber coated with tetraQxCav revealed that the new receptor was by far more efficient, making the comparison even pointless. This indicated that, coherently with the TGA data, the introduction of the bulky group at the upper rim promotes a significantly higher complexation capability of the cavitand, favoring the entrapment of aromatic guest inside the cavity. We then compared receptor **9** with a functionalized quinoxaline cavitand (**QxBox**) prepared in our laboratories, which has already been integrated in a device and successfully tested for aromatic hydrocarbons detection in air (patent pending).<sup>10</sup> Selectivity tests were performed by incubation of the fibers in the headspace of a vial containing a BTEX mixture, with ratio reported in Table 4.3, at 25°C for 15 minutes.

Complex	Concentration [ $\mu\text{g}/\text{m}^3$ ]
Benzene	0.49
Toluene	0.44
Ethylbenzene	0.37
<i>m</i> -, <i>p</i> -Xylene	0.69
<i>o</i> -Xylene	0.98
Styrene	1.4

**Table 4.3** The BTEX concentration used for the selectivity tests.

The fibers were introduced into the inlet of the GC-MS system and thermal desorption was performed. The response factors of the individual analytes were calculated with respect to the actual amount of the substance that reaches the detector. Using the response factors, it was possible to correct the data, obtaining the selectivity of the materials. Due to the strong complexation, BTEX desorption was performed at 300°C. The normalized responses are reported in Figure 4.11.

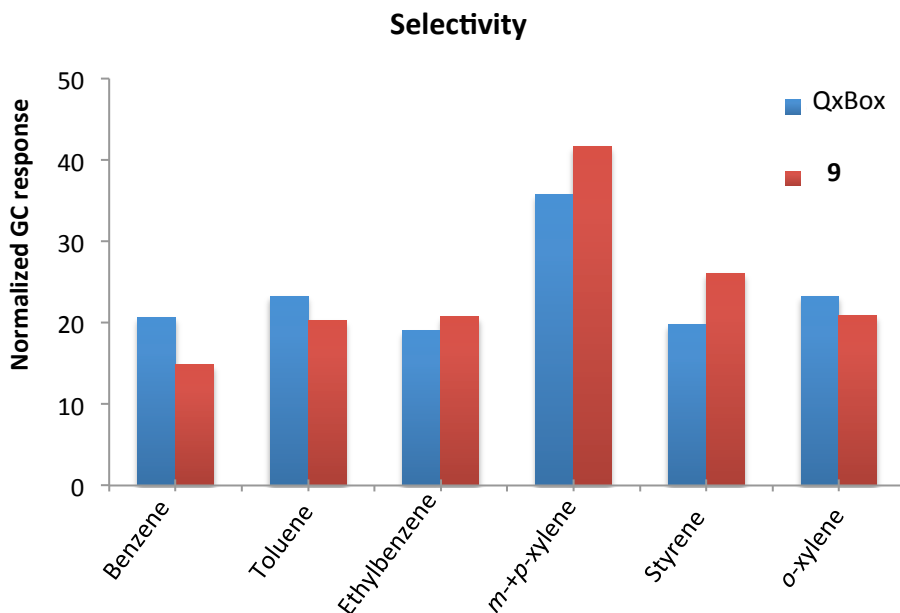


**Figure 4.11** Normalized desorption profile of **9** (red bar) and **QxBox** (blue line) SPME fibers performed at 300°C.

Both fibers bind all BTEX compounds from the gas phase, showing the best selectivity towards *m*-+*p*-xylene. **QxBox** shows slightly higher selectivity towards benzene, toluene, and *o*-xylene, while TriptyQxCav receptor **9** is more selective towards *m*-+*p*-xylene and styrene. Moreover **9** presents a slightly higher selectivity towards toluene with respect to benzene, showing that a single CH<sub>3</sub> group influences the desorption of the entrapped analyte. Overall, the performances of the two materials are comparable.

The enrichment factor of the two fibers was also evaluated (Figure 4.12). No significant differences were observed between the two fibers.

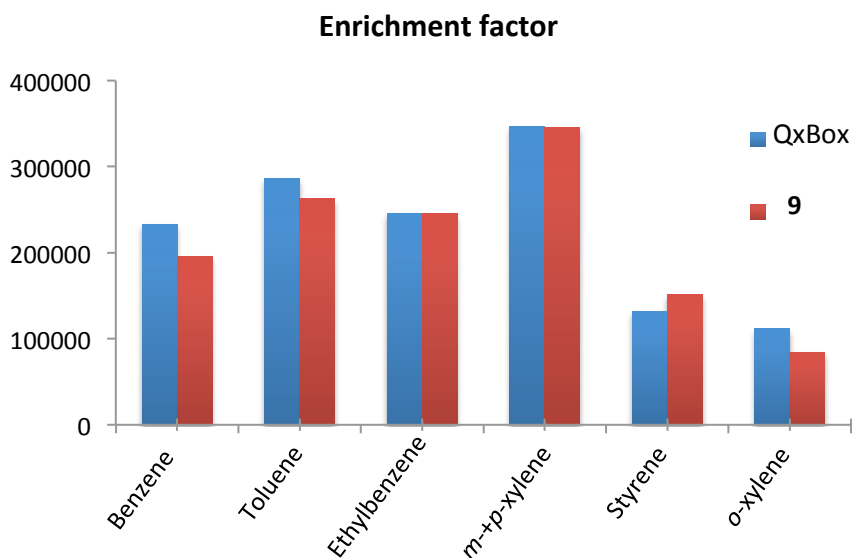


**Figure 4.12** Enrichment factors for **9** (red bar) and **QxBox** (blue line) SPME fibers performed at 300°C.

In order to mimic the real environment, the test using aliphatic hydrocarbons in superior concentration with comparison to the BTEX has been performed. The aliphatic hydrocarbon composition was used in large excess in order to examine **9** performance in environment containing large amounts of interferents. The fiber coated with **9** was incubated in the head-space of the vial containing BTEX mixture (Table 4.3) together with aliphatic hydrocarbons (5 ppb concentrations) for 15 minutes. The analysis were performed in various desorption temperatures in order to obtain full desorption profile of the system (Figure 4.13).



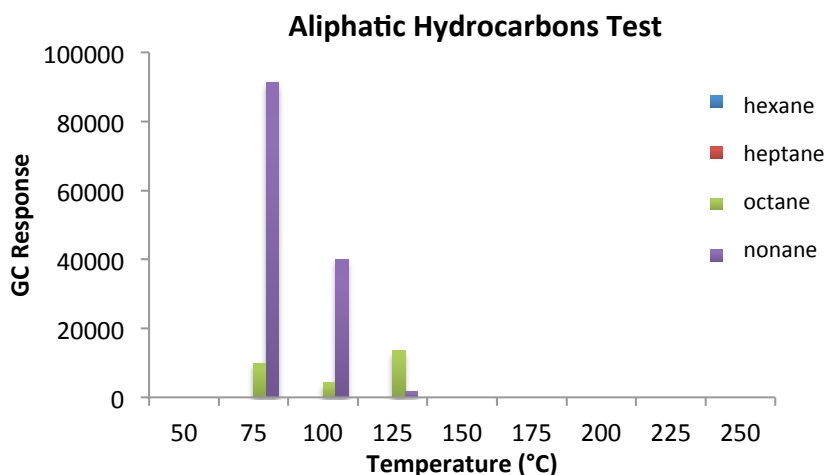


**Figure 4.13** The desorption profile of **9** cavitand upon aliphatic and aromatic hydrocarbons exposure.

Hexane and heptane were not retained at all, while nonane and traces of octane were detected in the 75-125°C range. No release above 125°C was observed, confirming that aliphatic hydrocarbons are not trapped in the cavity of **9** but are physisorbed by the matrix.

To summarize, SPME experiments indicated that the introduction of the triptycene unit led to a significant improvement in the complexation properties towards aromatic analytes of the tetraquinoxaline cavitands. The comparison of **9** with **QxB** evidenced that the TriptyQxCav receptor **9** is suitable for aromatic hydrocarbons detection in air.

### 4.3 Conclusions

In this Chapter we reported the synthesis of two novel triptycene-functionalized tetraquinoxaline cavitands. The triptycene-derivatized dichloroquinoxaline **5** has been prepared in 5 synthetic steps with 39% overall yield. The bridging reaction of **5** on triquinoxaline cavitand and diquinoxaline cavitand, has led to Tripty-QxCavs **9** and **11** in 65% and 46% yield respectively. <sup>1</sup>H NMR characterization has proved that, despite the presence of the bulky groups at the upper rim, the vase conformation is still favored in solution for both **9** and **11**, an essential feature to exploit them for benzene sensing. Thermo gravimetric analysis has evidenced a relevant increase of the desorption temperatures of the entrapped benzene for **9** and **11** with comparison to the unfunctionalized tetraQxCav. The

potential of **9** in aromatic hydrocarbons recognition has been evaluated in SPME experiments: the fiber coated with **9** has shown good linearity and low limits of detection for all the tested analytes. In particular SPME measurements have revealed that **9** is by far more efficient than the unfunctionalized tetraQxCav, with comparable behavior to the **QxBox**<sup>10</sup> in term of selectivity and enrichment factor. Although the selectivity in the benzene uptake over TEX has not been achieved, we can conclude that the introduction of single triptycene unit at the upper rim promotes a significantly higher complexation capability of the cavitand, favoring the entrapment of aromatic guest inside the cavity, making **9** suitable for aromatic hydrocarbons detection in air. The introduction of a second triptycene does not lead to significant improvements.

#### **4.4 Acknowledgments**

Special thanks to Prof. Timothy M. Swager and Dr. Elizabeth Sterner from Department of Chemistry, Massachusetts Institute of Technology, Cambridge (USA). Thanks to Dr. Federica Bianchi from Department of Chemistry, University of Parma, for SPME analysis. Thanks to Dr. Gianluca Paredi from the interdepartmental Centre SITEIA.PARMA, University of Parma, for mass spectrometry measurements.

## 4.5 Experimental section

### 2,3-Dibromotriptycene (**1**)

To a solution of anthracene (4 g, 22.4 mmol) and 1,2,4,5-tetrabromobenzene (12.4 g, 31.4 mmol) in dry toluene, *n*-BuLi 2.5 M solution in hexane (14.36 mL, 35.9 mmol) diluted in 50 mL of hexane was slowly added under argon atmosphere at 0°C. The reaction mixture was stirred overnight at room temperature. The crude was filtered and the solid was washed with dichloromethane and hexane. The organic phase was concentrated under reduced pressure. Purification by silica gel column chromatography (hexane as eluent) afforded the pure product as white solid (5.7 g, 13.9 mmol, 62%).

<sup>1</sup>H NMR (CDCl<sub>3</sub>, 400 MHz): δ (ppm) = 7.63 (s, 2H, ArH), 7.39-7.36 (m, 4H, ArH), 7.04-7.01 (m, 4H, ArH), 5.36 (s, 2H, ArCH).

### 2,3-Bis(diphenyldiiminotriptycene) (**2**)

A toluene solution of tris(dibenzylideneacetone)dipalladium(0) (0.36 g, 0.39 mmol) and (±)-BINAP (0.49 g, 0.79 mmol) was degassed 3 times with freeze pump thaw technique, purged with argon and stirred at 110°C for 1 h. The solution was cooled down to room temperature and benzophenone imine (2.13 mL, 10.9 mmol), 2,3-dibromotriptycene **1** (2 g, 4.85 mmol) and sodium *tert*-butoxide (1.22 g, 12.7 mmol) were added. The reaction mixture was stirred overnight at 110°C. The crude was filtered to remove the formed precipitate and washed with dichloromethane. The organic phase was concentrated under reduced pressure. Purification by silica gel column chromatography (hexane:ethyl acetate 9:1) afforded pure **2** as a yellow solid (2.46 g, 4.01 mmol, 83%).

<sup>1</sup>H NMR (CDCl<sub>3</sub>, 300 MHz): δ (ppm) = 7.61 (d, J=7 Hz, 4H, ArH<sub>o</sub>), 7.40-7.36 (m, 2H, ArH<sub>p</sub>), 7.32-7.30 (m, 4H, ArH<sub>m</sub>), 7.26-7.24 (m, 4H, triptycene ArH), 7.22-7.20 (m, 2H, ArH<sub>p</sub>), 7.10 (t, J=8 Hz, 4H, ArH<sub>m</sub>), 6.99-6.95 (m, 4H, triptycene ArH), 6.98 (d, J=7 Hz, 4H, ArH<sub>o</sub>), 6.55 (s, 2H, triptycene ArH), 5.07 (s, 2H, ArCH).

### 2,3-Diaminotriptycene (**3**)

2.0 M aqueous HCl solution (5.1 mL, 10.2 mmol) was added to a THF solution of **2** (2.1 g, 3.41 mmol) and the mixture was stirred at room temperature for 0.5 h. The precipitate was isolated by filtration, sonicated in dichloromethane for 0.5 h and filtered again to give the diammoniumtriptycene dichloride salt as an off-white solid. The neutralization was carried out by stirring a suspension of the salt (1.21 g, 3.39 mmol) in THF with 2.0 M aqueous NaOH solution (2.5 mL, 5.0

mmol) at room temperature for 0.5 h. Solvent was evaporated under reduced pressure to give **3** as a yellow solid (0.94 g, 3.31 mmol, 97%).

$^1\text{H NMR}$  (DMSO- $d_6$ , 400 MHz):  $\delta$  (ppm) = 7.32-7.29 (m, 4H, ArH), 6.92-6.89 (m, 4H, ArH), 6.61 (s, 2H, ArH), 5.22 (s, 2H, ArCH).

#### 2,3-dihydroxy-6,7-triptycenequinoxaline (**4**)

A solution of oxalic acid (0.3 g, 3.52 mmol) in 4N HCl (5 mL) was added to a solution of **3** (0.77 g, 2.71 mmol) in 4N HCl (15 mL), and the resulting solution was heated to reflux overnight. The reaction mixture was cooled to room temperature, and the precipitate was isolated by filtration, washed with water and dried to afford **4** as a brown solid (0.82 g, 2.41 mmol, 89%).

$^1\text{H NMR}$  (DMSO- $d_6$ , 400 MHz):  $\delta$  (ppm) = 11.88 (s, 2H, ArOH), 7.43-7.37 (m, 4H, ArH), 7.16 (s, 2H, ArH), 6.98-6.95 (m, 4H, ArH), 5.61 (s, 2H, ArCH);

#### 2,3-dihydroxy-6,7-triptycenequinoxaline (**5**)

To a suspension of **4** (0.62 g, 1.83 mmol) and thionyl chloride (0.345 mL, 4.76 mmol) in 1,2-dichloroethane few drops of DMF were added. The reaction mixture was heated to reflux overnight. Solvent was removed *in vacuo* and the crude was purified by silica flash chromatography (hexane:ethyl acetate 9:1) to give **5** as a white solid (0.6 g, 1.59 mmol, 87%).

$^1\text{H NMR}$  ( $\text{CDCl}_3$ , 400 MHz):  $\delta$  (ppm) = 7.91 (s, 2H, ArH), 7.49-7.46 (m, 4H, ArH), 7.11-7.06 (m, 4H, ArH), 5.64 (s, 2H, ArCH);  $^{13}\text{C NMR}$  ( $\text{CDCl}_3$ , 100 MHz):  $\delta$  (ppm) = 148.4, 143.5, 139.7, 126.3, 124.4, 121.9, 53.8.

#### Resorcinarene [ $\text{C}_6\text{H}_{13}$ , H] (**6**)

To a solution of resorcinol (10 g, 90.8 mmol,) and heptaldehyde (12.2 mL, 90.2 mmol) in MeOH, a 37% solution of HCl (15 mL, 180 mmol) was added dropwise over 30 min at 0°C. After the addition, the reaction mixture was stirred at 55°C for 5 days. The reaction was quenched with water, filtered, dried under vacuum and recrystallized three times from MeOH. The final product **6** was obtained as a pale yellow powder (11.2 g, 13.6 mmol, 60%).

$^1\text{H NMR}$  (Acetone- $d_6$ , 400 MHz):  $\delta$  = 8.41 (s, 8H, ArOH), 7.53 (s, 4H, ArH<sub>up</sub>), 6.20 (s, 4H, ArH<sub>down</sub>), 4.27 (t, 4H,  $J=7.8$  Hz, CHCH<sub>2</sub>CH<sub>2</sub>), 2.26 (q, 8H,  $J=7.8$  Hz, CHCH<sub>2</sub>CH<sub>2</sub>), 1.31- 1.24 (m, 32H, -CH<sub>2</sub>-), 0.85 (t, 12H,  $J=6.9$  Hz, CH<sub>2</sub>CH<sub>2</sub>CH<sub>3</sub>);

ESI-MS:  $m/z$ : 847.5 [M+Na]<sup>+</sup>.

**TetraQxCav [C<sub>6</sub>H<sub>13</sub>, H] (7)**

To a solution of resorcinarene **6** (1.0 g, 1.21 mmol) in dry DMF, 2,3-dichloroquinoxaline (1.06 g, 5.33 mmol) and K<sub>2</sub>CO<sub>3</sub> (2.51 g, 18.2 mmol) were added. The mixture was stirred overnight at 80°C. The reaction was quenched by addition of HCl 1 N and the precipitate was filtered, washed with water, and dried. The crude product was crystallized from ethyl acetate: chloroform (9:1 v/v) to afford the pure product as white solid (0.949 g, 0.72 mmol, 59%).

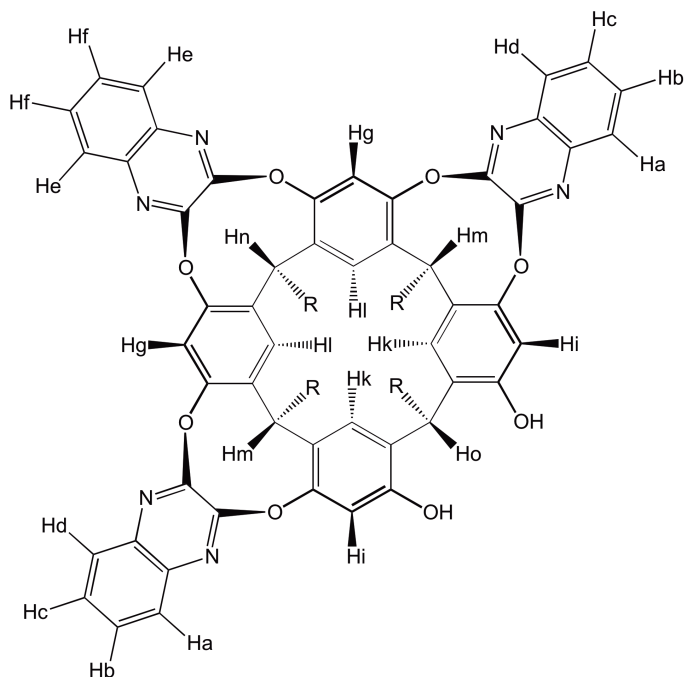
<sup>1</sup>H NMR (CDCl<sub>3</sub>, 300 MHz): δ = 8.15 (s, 4H, ArH<sub>up</sub>), 7.79 (m, 8H, ArH) 7.47 (m, 8H, ArH), 7.21 (s, 4H, ArH<sub>down</sub>), 5.56 (t, 4H, J=7.9 Hz, CHCH<sub>2</sub>CH<sub>2</sub>), 2.28 (q, 8H, J=7.8 Hz, CHCH<sub>2</sub>CH<sub>2</sub>), 1.48-1.31 (m, 32H, -CH<sub>2</sub>-), 0.93 (t, 12H, J=6.7 Hz, CH<sub>2</sub>CH<sub>2</sub>CH<sub>3</sub>);

**MALDI TOF:** calculated for C<sub>84</sub>H<sub>80</sub>N<sub>8</sub>O<sub>8</sub> [M+H]<sup>+</sup> m/z: 1329.618, found m/z= 1329.567.

**Triquinoxaline diol [C<sub>6</sub>H<sub>13</sub>, H] (8)**

A solution of tetraquinoxaline cavitand **7** (0.7 g, 0.53 mmol) and CsF (1.61 g, 10.6 mmol) in dry DMF was heated to 80°C and catechol (0.063 g, 0.58 mmol) was added. The mixture was stirred for 1 h at 80°C. The reaction was quenched by pouring into 300 mL of ice-cold brine, and the precipitate was filtered, washed with water, and dried. The crude product was purified by flash column chromatography (gradient from 100% DCM to dichloromethane:ethyl acetate 9:1) affording triquinoxaline resorcinarene **8** as a pale yellow solid (0.44 g, 0.37 mmol, 70%).

<sup>1</sup>H NMR (CDCl<sub>3</sub>, 300 MHz): δ = 8.39 (s, 2H, ArOH), 8.23 (s, 2H, Hg), 7.95-7.92 (m, 2H, Hd), 7.86-7.81 (m, 2H, He), 7.68-7.65 (m, 2H, Ha), 7.58-7.55 (m, 2H, Hc), 7.54-7.42 (m, 4H, Hb+Hf), 7.26 (s, 2H, Hi), 7.14 (s, 2H, Hl), 7.10 (s, 2H, Hk), 5.56 (t, 1H, J=8.2 Hz, Hn), 5.49 (t, 2H, J=8.1 Hz, Hm), 4.30 (t, 1H, J=8.2 Hz, Ho), 2.35-2.15 (m, 8H, CHCH<sub>2</sub>CH<sub>2</sub>), 1.53-1.18 (m, 32H, -CH<sub>2</sub>-), 0.96-0.88 (m, 12H, CH<sub>2</sub>CH<sub>2</sub>CH<sub>3</sub>);

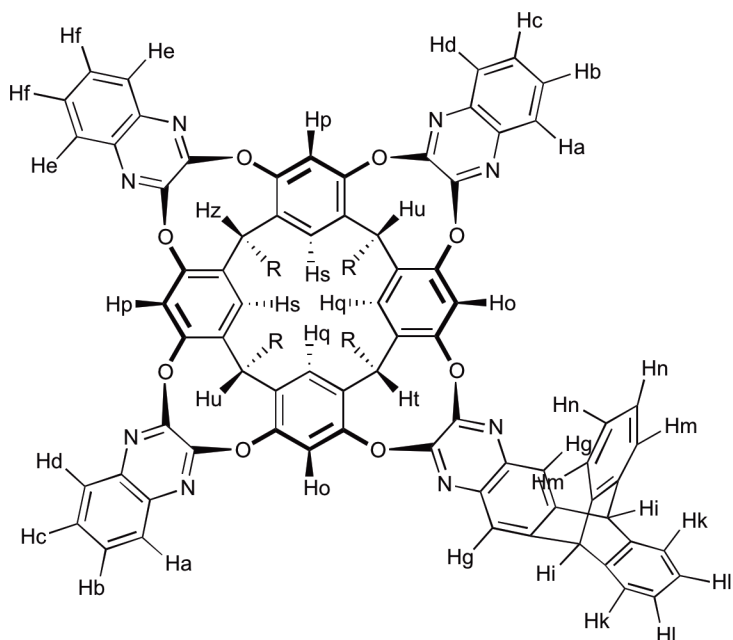


**ESI-MS:**  $m/z$  1203.6  $[M+H]^+$ ,  $m/z$  1225.6  $[M+Na]^+$ ,  $m/z$  1241.5  $[M+K]^+$ .

### MonotriptyQxCav [ $C_6H_{13}$ , H] (9)

To a solution of TriQxCav **8** (0.18 g, 0.15 mmol) in dry DMF in an oven-dried microwave vessel,  $K_2CO_3$  (0.082 g, 0.60 mmol) was added. The resulting mixture was stirred for 15 minutes at room temperature under argon atmosphere, followed by addition of **5** (0.061 g, 0.16 mmol). The mixture reaction was stirred at 120°C under microwave irradiation for 1 h. Afterwards, the reaction was quenched by addition of HCl 1 N and the precipitate was filtered, washed with water, and dried. The crude product was purified by flash column chromatography (dichloromethane as eluant) to give **9** as a white solid (0.16 g, 0.10 mmol, 65%).

$^1H$  NMR ( $CDCl_3$ , 400 MHz):  $\delta$  = 8.02 (s, 2H, Hp), 7.99 (s, 2H, Ho), 7.95 (d, 2H,  $J=7.8$  Hz, Hd), 7.86 (d, 2H,  $J=7.8$  Hz, Ha), 7.75-7.72 (m, 2H, e), 7.65 (s, 2H, Hg), 7.63-7.57 (m, 4H, Hb+Hc), 7.47 (bs, 4H, Hf+Hk), 7.33-7.30 (m, 2H, Hm), 7.15 (s, 2H, Hs), 7.13 (s, 2H, Hq), 7.08-7.05 (s, 2H, Hl), 7.03-7.00 (m, 2H, Hn), 5.43 (s, 2H, Hi), 5.34 (t, 3H,  $J=8.1$  Hz, Hu+Hz), 5.25 (t, 1H,  $J=7.9$  Hz, Ht), 2.24-2.19 (m, 8H,  $CHCH_2CH_2$ ), 1.45-1.26 (m, 32H,  $-CH_2-$ ), 0.93-0.87 (m, 12H,  $CH_2CH_2CH_3$ );



**MALDI TOF:** calculated for  $C_{98}H_{88}N_8O_8$   $[M+H]^+$   $m/z$ : 1505.680, found  $m/z$ = 1505.691.

#### Diquinoxaline tetrol AC [ $C_6H_{13}$ , H] (10)

A solution of tetraquinoxaline cavitand **8** (0.44 g, 0.33 mmol) and CsF (1.01 g, 6.62 mmol) in dry DMF was heated to 80°C and catechol (0.120 g, 1.09 mmol) was added. The mixture was stirred for 1 h at 80°C. The reaction was quenched by pouring into 300 mL of ice-cold brine, and the precipitate was filtered, washed with water, and dried. The crude product was purified by flash column chromatography (gradient from dichloromethane:ethyl acetate 95:5 to dichloromethane:ethyl acetate 85:15) affording diquinoxaline resorcinarene **9** as an off-white solid (0.19 g, 0.18 mmol, 55%).

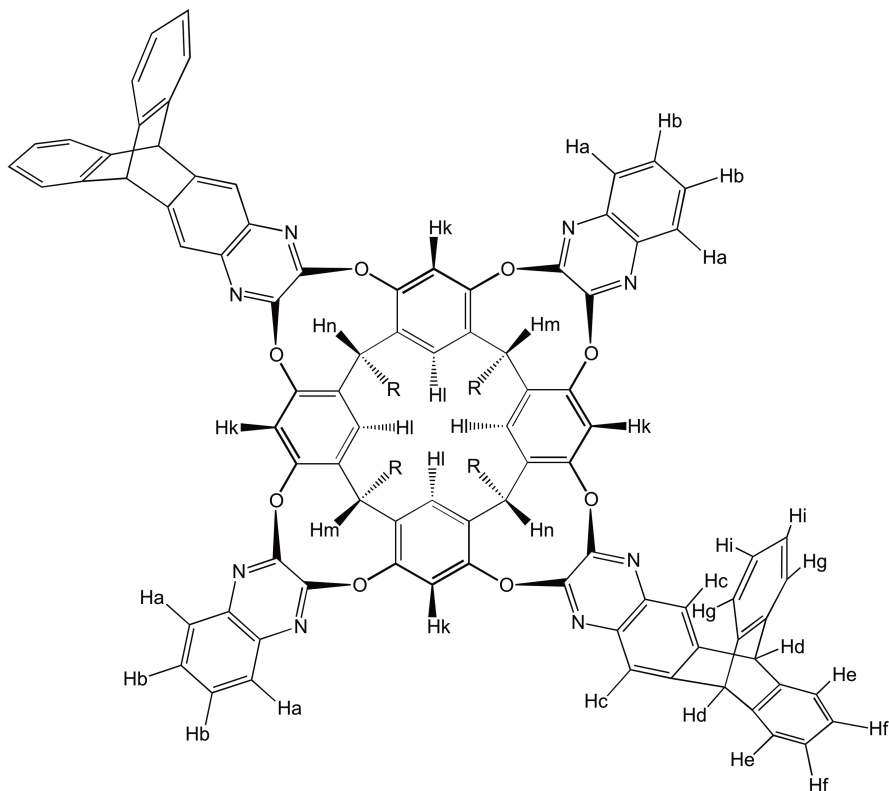
$^1H$  NMR (Acetone- $d_6$ , 400 MHz):  $\delta$  = 9.03 (bs, 4H, ArOH), 7.77 (s, 4H, ArH<sub>down</sub>), 7.54 (m, 4H, quinoxaline ArH), 7.24 (m, 4H, quinoxaline ArH), 7.16 (s, 4H, ArH<sub>up</sub>), 5.52 (t,  $J$ =8.0 Hz, 2H, CHCH<sub>2</sub>CH<sub>2</sub> below Qx), 4.47 (t,  $J$ =7.6 Hz, 2H, CHCH<sub>2</sub>CH<sub>2</sub> below OH's), 2.41 (m, 8H, CHCH<sub>2</sub>CH<sub>2</sub>), 1.47-1.26 (m, 32H, -CH<sub>2</sub>-), 0.92 (m, 12H, CH<sub>2</sub>CH<sub>2</sub>CH<sub>3</sub>), (Assignment by COSY NMR);

**ESI-MS:**  $m/z$  1077.6  $[M+H]^+$ ,  $m/z$  1099.6  $[M+Na]^+$ ,  $m/z$  1115.5  $[M+K]^+$ .

**DitriptyQxCav [C<sub>6</sub>H<sub>13</sub>, H] (11)**

To a solution of diquinoxaline tetrol **10** (0.1 g, 0.09 mmol) in dry DMF in an oven-dried microwave vessel, K<sub>2</sub>CO<sub>3</sub> (0.102 g, 0.74 mmol) was added. The resulting mixture was stirred for 15 minutes at room temperature under argon atmosphere, followed by addition of **5** (0.076 g, 0.20 mmol). The mixture reaction was stirred at 120°C under microwave irradiation for 1 h. Afterwards, the reaction was quenched by addition of HCl 1 N and the precipitate was filtered, washed with water, and dried. The crude product was purified by flash column chromatography (dichloromethane as eluant) to give **11** as a white solid (0.072 g, 0.04 mmol, 46%).

<sup>1</sup>H NMR (CDCl<sub>3</sub>, 400 MHz): δ = 7.87 (s, 4H, Hl), 7.76 (s, 4H, Hc), 7.73-7.70 (m, 4H, Ha), 7.50-7.47 (m, 8H, Hg+He), 7.28-7.26 (m, 4H, Hb), 7.15-7.13 (m, 4H, Hf), 7.09-7.07 (m, 4H, Hi), 7.00 (s, 4H, Hk), 5.62 (s, 4H, Hd), 4.86-4.81 (m, 4H, Hn+Hm), 2.20-2.04 (m, 8H, CHCH<sub>2</sub>CH<sub>2</sub>), 1.43-1.20 (m, 32H, -CH<sub>2</sub>-), 0.89-0.83 (m, 12H, CH<sub>2</sub>CH<sub>2</sub>CH<sub>3</sub>), (Assignment by COSY NMR);



**MALDI TOF:** calculated for C<sub>112</sub>H<sub>96</sub>N<sub>8</sub>O<sub>8</sub> [M+H]<sup>+</sup> m/z: 1681.743, found m/z= 1681.744.



### SPME Sampling

Preparation of the fiber: the cavitand, in the form of fine powder, was placed on a silicon support with the help of an epoxy resin resistant at high temperature.

Extraction in Headspace: a gas mixture of BTEX in  $\mu\text{g}/\text{m}^3$  range was sampled at room temperature for 15 minutes.

### GC-MS analysis

Gas-chromatograph HP 6890 Series Plus, Agilent Technologies (Milan, Italy):

- Column: MND-5S (l=30 m, i.d.=0.25 mm, d.f.=0.25  $\mu\text{m}$ ) (Supelco);
- Carrier gas: helium
- Carrier gas flux: 1 mL/min
- Carrier gas pressure: 70 KPa.
- Injector Temp: 300°C
- Injection mode: splitless
- Temperature program: 40°C for 5.5 minutes (10°C/min until 80°C) and then 30°C/min until 200°C.

Mass Spectrometer MSD 5973, Agilent Technologies:

- Source Temperature: 200°C;
- Transfer Line temperature: 200°C;
- Ionization: E.I. (70 eV);
- Voltage: 2200 V;
- Acquisition modality: Time scheduled monitoring;
- Solvent delay: 0.5 minutes;
- Dwell time: 30 ms;
- Monitored ions: Range from 40 to 150 m/z
- Monitored ions BTEX (SIM):
  - from 0.5 to 2 min: 78, m/z for benzene
  - from 2 to 4 min: 91 m/z for toluene
  - from 4 to 16 min: 91, 106 m/z for ethylbenzene and xylenes
- Monitored aliphatic hydrocarbons ions (SIM):

from 0 to 2.00 min	43, 57, 72, 86 <i>m/z</i> for hexane
from 2.00 to 3.50 min	43, 57, 71, 100 <i>m/z</i> for heptane
from 3.50 to 5.00 min	43, 57, 85, 114 <i>m/z</i> for octane
from 5.00 to 16.00 min	43, 57, 85, 128 <i>m/z</i> for nonane

The Mass Spectrometer was tuned using perfluorotributylamine and the analytes were identified by comparison with the retention time of standard solution and with the MS spectra reported in NIST Library (National Institute of Standards and Technology).

## 4.6 References

- <sup>1</sup> Directive 2000/69/EC of the European Parliament and of the Council of 16 November 2000 Relating to Limit Values for Benzene and Carbon Monoxide in Ambient Air. Official Journal L131, 13/12/2000.
- <sup>2</sup> a) S. Zampolli, P. Betti, I. Elmi, E. Dalcanale, *Chem. Commun.* **2007**, 2790-2792; b) S. Zampolli, I. Elmi, F. Mancarella, P. Betti, E. Dalcanale, G. C. Cardinali, M. Severi, *Sens. Actuators B* **2009**, *141*, 322-328.
- <sup>3</sup> P. Soncini, S. Bonsignore, E. Dalcanale, F. Ugozzoli, *J. Org. Chem.* **1992**, *57*, 4608-4612.
- <sup>4</sup> H. Hart, A. Bashir-Hashemi, J. Luo, M. A. Meador, *Tetrahedron* **1986**, *42*, 1641-1654.
- <sup>5</sup> J. H. Chong, M. J. MacLachlan, *Inorg. Chem.* **2006**, *45*, 1442-1444.
- <sup>6</sup> M. G. Rabbani, T. E. Reich, R. M. Kassab, K. T. Jackson, H. M. El-Kaderi, *Chem. Commun.* **2012**, *48*, 1141-1143.
- <sup>7</sup> P. P. Castro, G. Zhao, G. A. Masangkay, C. Hernandez, L. M. Gutierrez-Tunstad, *Org. Lett.* **2004**, *6*, 333-336.
- <sup>8</sup> a) J. R. Moran, J. L. Ericson, E. Dalcanale, J. A. Bryant, C. B. Knobler, D. J. Cram *J. Am. Chem. Soc.* **1991**, *113*, 5707-5714; b) V. A. Azov, B. Jaun, F. Diederich, *Helv. Chim. Acta.* **2004**, *87*, 449-462.
- <sup>9</sup> E. Dalcanale, G. Costantini, P. Soncini, *J. Incl. Phenom. Mol. Chem.* **1992**, *13*, 87-92.
- <sup>10</sup> J. W. Trzciński, F. Bianchi, R. Pinalli, C. Massera, E. Dalcanale, Patent Application MI2014A000523.

# Chapter 5

## Molecular Magnetism

## 5.1 Nanotechnology

Nanotechnology is based on the recognition that particles less than the size of 100 nanometers impart to the corresponding nanostructures built from them new properties and behaviors.<sup>1</sup> The laws of physics that operate on objects at the nanoscale combine classical and quantum mechanics: thus when particles become smaller than a critical size the resulting properties of the material can dramatically change and novel effect can occur. Traditionally, the origins of nanotechnology are traced back to the famous lecture given by Richard Feynman at the California Institute of Technology in December 1959 called "There's Plenty of Room at the Bottom".<sup>2</sup> Feynman considered the possibility of direct manipulation of matter at the atomic scale.

Nowadays nanotechnology can be defined as the ability to construct structures with atomic level control. Understanding the science of nanoscale interactions is extremely important to the development of nanotechnology: the study of these interactions constitutes a major research topic in the field of nanotechnology.<sup>3</sup> The research area of nanotechnology is therefore interdisciplinary, covering a wide variety of subjects: scientists and engineers from several disciplines including physics, chemistry, biology and materials science use nanoscience principles for advanced applications in energy, medicine, information storage, computing and elsewhere. Nanotechnology shows great promise for providing us in the near future with many breakthroughs that will change the direction of technological advances in a wide range of applications. Although breakthroughs in any research field are difficult to predict, the future of nanoscience will likely involve scaling up from atomic assembly and individual nanodevices to macroscopic systems and structures with evolving properties and multiple functions.

## 5.2 Molecular Magnetism

Molecular magnetism is a relatively recent scientific field which originated from the application of nanoscience principles to magnetochemistry: it's an interdisciplinary area, where chemists and physicists started to collaborate very closely with the stated goal of designing, synthesizing, and characterizing the magnetic properties of molecular based materials. The idea of using molecules, rather than the ionic and metallic lattices of typical magnets, stems from the rapid development of functional molecular materials which started in the second half of the 20th century.<sup>4</sup> What is really interesting and fascinating in

molecular magnetic materials is that, on one side, they show magnetic hysteresis as ordinary magnets and, on the other side, they are small enough to show quantum effects. This combination of classical and quantum aspects is very attractive from the theoretical point of view since it provides new challenging questions, but it can have also many technological implications, especially in the fields of data storage and quantum computation. For this reason, during the years, the attention of the scientists was turned towards the development of magnetic materials of smaller size. Not all the phenomena are scalable toward miniaturization though: this is well known in magnetism where, for instance, hysteresis loop in magnetization is observable for systems with different sizes but origins from different physical phenomena<sup>5</sup> as summarized in Figure 5.1.

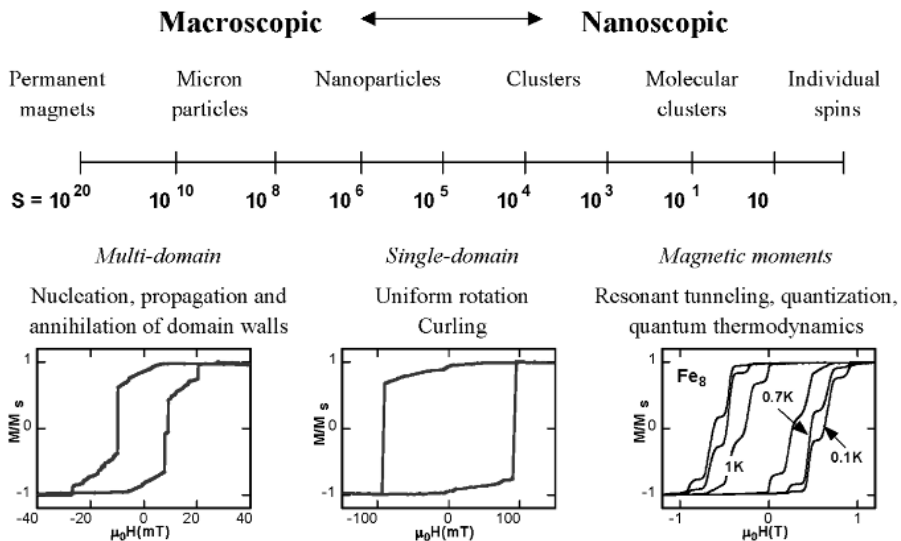


**Figure 5.1** The transition from macroscopic to microscopic magnetism. The hysteresis loops observed origin from different phenomena.

Starting from a bulk magnetic material, ideally working in a *top-down* approach decreasing the size of a magnetic object, a breakdown of the expected multi-domain model occurs when the radius of particle is comparable with the size of the domain walls.<sup>6</sup> At this point a single-domain model must be used to describe the magnetization curve of the system. The rotation of the magnetization of the particles occurs with a concerted movement of all the spins. Generally the magnetization has a preferred orientation which can be reversed by overcoming a barrier depending on the magnetic anisotropy.

Decreasing further the size of the particles also the single domain model breaks down when the energy of the barrier within the two magnetization states become comparable to thermal energy, as evidenced by the free fluctuation of the magnetization, analogously to that observed in a paramagnet. This is called the *superparamagnetic regime*, which is achieved for particles of size of a few nanometres. It marks the starting point for innovative applications for instance in bioscience<sup>7</sup> but it represents also the dead point for data storage applications,<sup>8</sup> although a technological escape to overcome this problem has been suggested and applied recently.<sup>9</sup>

An alternative approach is that of using a *bottom-up* strategy. The idea is that it should be possible to employ single molecules which are large enough to behave as bulk magnets.<sup>10</sup> These molecules were discovered in the '90s by Caneschi and co-workers<sup>11</sup> and named Single Molecule Magnets (SMMs)<sup>12</sup>. In this case the origin of the magnetism is again completely different; in fact it is bound to the slow relaxation of the magnetization of individual molecules, in other words it is due to the inner chemical structure of each molecular unit without any cooperative effects.

### 5.3 Single-Molecule Magnets

A single-molecule magnet (SMM) is a molecule that shows slow relaxation of the magnetization of purely molecular origin. Each molecule is a single-domain magnetic particle that, below its blocking temperature  $T_B$ , exhibits magnetization hysteresis, a classical property of macroscopic magnets. This is a property of the molecule itself and no interaction between the molecules is necessary for this phenomenon to occur. This makes single molecule magnets fundamentally different from traditional bulk magnets: contrary to conventional bulk magnets and molecule-based magnets, collective long-range magnetic ordering of magnetic moments is not necessary. The first identified single-molecule magnet was reported by Gatteschi and co-workers in 1991.<sup>13</sup> They measured the relaxation time of the magnetization in a dodecanuclear mixed-valent III/IV manganese oxide cluster with acetate ligands,  $Mn_{12}O_{12}(O_2CCH_3)_{16}(H_2O)_4$ . The complex (**1**), synthesized for the first time in 1980,<sup>14</sup> has eight  $Mn^{III}$  and four  $Mn^{IV}$  metal centers in a  $Mn_{12}O_{12}$  core that is surrounded by 16 acetate groups (Figure 5.2).

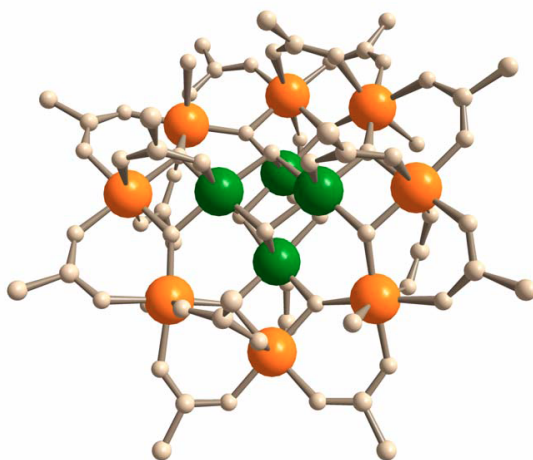


**Figure 5.2** Molecular structure of  $[\text{Mn}_{12}\text{O}_{12}(\text{OAc})_{16}(\text{H}_2\text{O})_4]$  (**1**). Color scheme:  $\text{Mn}^{\text{IV}}$ , green;  $\text{Mn}^{\text{III}}$ , orange.

This Mn complex possesses an  $S = 10$  ground state. The large spin ground state arises from antiferromagnetic interactions between the  $S = 3/2$  spins of  $\text{Mn}^{\text{IV}}$  ions and the  $S = 2$  spins of  $\text{Mn}^{\text{III}}$  ions, which do not compensate.<sup>15</sup> An axial zero-field splitting is present, and this leads to a splitting of the  $S = 10$  state into  $[2S + 1]$ , 21, levels, each characterized by a spin projection quantum number,  $m_s$ , where  $-S \leq m_s \leq S$ . Each level has an energy given as  $E(m_s) = m_s^2 D$ , where for this complex it has been found that the axial zero-field splitting parameter  $D = -0.50 \text{ cm}^{-1}$  ( $\equiv -0.70 \text{ K}$ ). The negative sign of  $D$  leads to a potential-energy barrier between the “spin-up” ( $m_s = -10$ ) and “spin-down” ( $m_s = 10$ ) orientations of the magnetic moment of an individual  $\text{Mn}_{12}$  molecule (Figure 5.3).



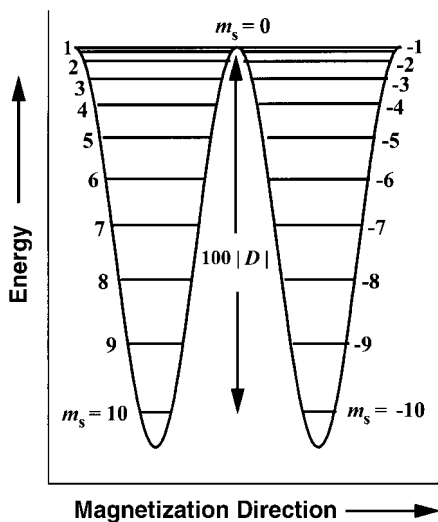


**Figure 5.3** Plot of the potential energy versus the magnetization direction for a single-molecule magnet (SMM) with an  $S=10$  ground state experiencing zero external magnetic field.

In other words, in order to flip the spin of **1** from along the  $+z$  axis to along the  $-z$  axis of the disc-like  $\text{Mn}_{12}\text{O}_{12}$  core, it takes some energy (the barrier in Figure 5.3) to reorient the spin via the perpendicular  $m_s = 0$  state. This is an easy axis type of anisotropy. If this barrier is appreciable, the spin of an SMM can be magnetized in one direction. For **1**, the barrier must be  $E(m_s = 0) - E(m_s = \pm 10) = 100D \approx 70$  K. For a thermally activated process, the time for the reorientation of the magnetization  $\tau$  depends exponentially on the height of the barrier according to Eq. 6.1:

$$\tau(T) = \tau_0 \exp(U_{\text{eff}}/k_B T) \quad \text{Eq. 6.1}$$

where  $U_{\text{eff}}$  is the energy barrier and  $k_B$  the Boltzmann constant. If complex **1** is magnetized at 2 K by applying a magnetic field and then removing the field, the relaxation of the magnetization is so slow that after two months the magnetization is still about 40% of the saturation (i.e., largest) value. At 1.5 K, the half-life for magnetization decay is hardly measurable because it is too long, although it was estimated in 50 years.<sup>16</sup>

It's clear that the slow magnetization relaxation shown by an SMM is due to an individual molecule rather than to longrange ordering as observed in nanoscale magnetic domains of bulk magnets. When a sample of **1** is exposed to a large external magnetic field parallel to  $z$  axis, the  $m_s = -10$  state is greatly stabilized in energy relative to the  $m_s = +10$  state. All of the molecules have their spins

aligned with the external field (Figure 5.4, simplified for  $S = 5$ ); all of the molecules are in the  $m_s = -S$  state, and the magnetization reaches the saturation value. Once the external field is switched off to zero, the magnetization  $M$  is frozen by the presence of the barrier and only very slowly tends to the equilibrium value ( $M = 0$ ). Thus, a remnant magnetization is observed.

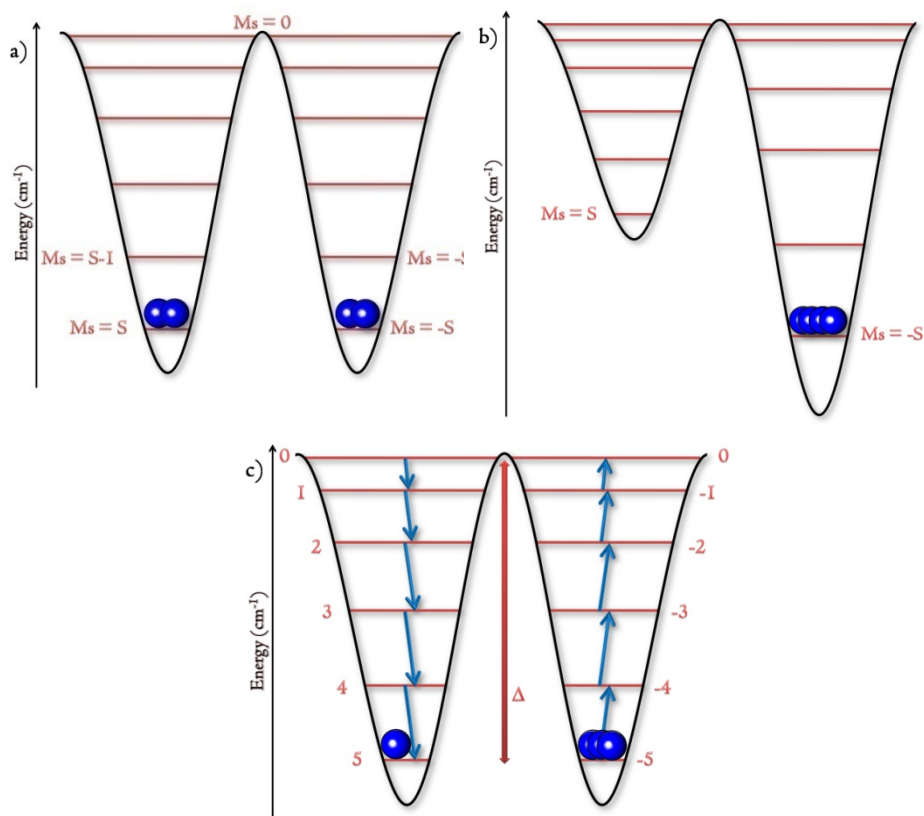


**Figure 5.4** Energy levels for a spin state  $S = 5$  with easy axis magnetic anisotropy. The  $+m_s$  levels are localized in the left well and the  $-m_s$  levels in the right well. **a)** In zero field the two wells are equally populated; **b)** the application of a magnetic field selectively populates the right well; **c)** after removing the field the return to equilibrium occurs through thermal relaxation.

A negative field reduces the height of the barrier and unfreezes the spins, thus allowing a rapid reversal of the magnetization. A hysteresis loop is therefore observed, which has a molecular and dynamical origin (Figure 5.5).

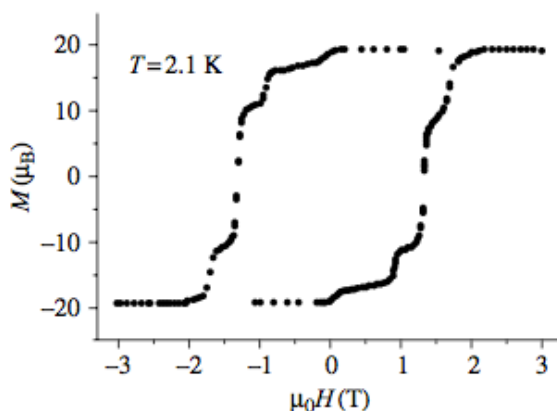


**Figure 5.5** Magnetization vs magnetic field hysteresis loop for **1**. Data were recorded on a single crystal with the magnetic field applied along the tetragonal axis of each molecule of **1**. The vertical parts of the “steps” correspond to critical values of the field where resonant magnetization tunneling is allowed.

The width of the loop (i.e., the coercive field) depends on the temperature as well as the rate of sweep of the magnetic field. Large coercive fields of several Tesla have been observed for  $\text{Mn}_{12}$  below 2 K. The important feature is that at zero field, the magnetization can be either positive or negative, depending on the history of the sample. Therefore, it is possible in principle to store information in one single, bistable molecule.

The hysteresis loop shown in Figure 5.5 is characterized by steps: the flat regions correspond to fields at which the relaxation is slow, as a result of the thermal relaxation over an anisotropy barrier; the steps correspond to fields at which a rapid increase of the relaxation rate is observed, as a result of quantum tunneling of the magnetization (QTM). In fact the magnetization can also relax through an under-barrier mechanism via quantum admixing of the “spin-up” and “spin-down” states. In a magnetic applied field, the steps occur at values of the applied field where the energies of different collective spin states of the manganese clusters coincide (Figure 5.6). At these special values of the field, relaxation from one spin to another is enhanced above the thermally activated rate by the action of resonant quantum-mechanical tunneling.<sup>17</sup>

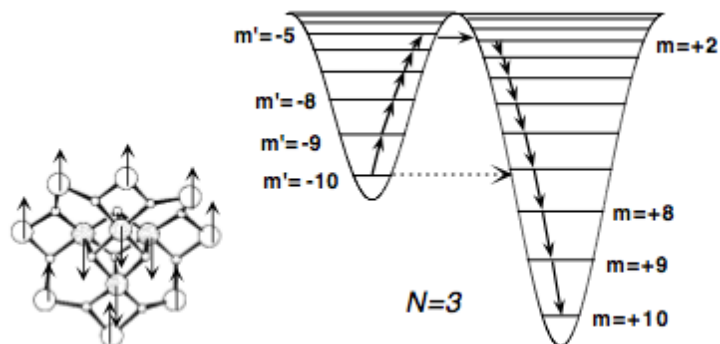


**Figure 5.6** Double-well potential in the presence of a magnetic field applied for **1**. Thermally assisted tunneling is indicated by straight-line arrows.

Thermally assisted tunneling is shown by the sequence of straight-line arrows in Fig. 5.6: the magnetization is thermally activated to a level near the top of the metastable well (e.g.,  $m_s = -5$ ), tunnels across the barrier (to  $m_s = 2$ ), and decays to the ground state ( $m_s = 10$ ) of the stable well. Thermal activation becomes exponentially more difficult as one proceeds up the ladder to higher energy levels; on the other hand, the barrier is lower and more penetrable, so that the tunneling process becomes exponentially easier. Which level (or group of adjacent levels) dominates the tunneling is determined by competition between the two effects. As the temperature is reduced and thermal activation becomes more difficult, tunneling proceeds from progressively lower energy levels deeper in the potential well.<sup>18</sup>

To summarize, the magnetic bistability of SMMs offer great potential applications: a single molecule can be trapped in one of the high-spin energy wells, thus ideally one molecule can be seen as one bit. Storage capacity of computer hard disks SMMs based would increase to unprecedented data densities. Potential applications of SMMs are vast: they are potentially useful not only in high-density magnetic storage devices, but also for sensors, quantum computing applications, and more recently spintronics.<sup>19</sup>

### 5.3.1 Design and Synthesis of SMMs

The main characteristics of a SMM are the energy barrier  $U_{eff}$  (Eq. 6.2), the blocking temperature  $T_B$  and the relaxation time  $\tau$  (Eq 6.1).

$$U_{eff} = |D|S^2 \quad \text{Eq. 6.2}$$

The height of the barrier  $U_{eff}$  scales with the square of the ground-state spin and linearly with the axial zero-field splitting parameter  $D$ . Therefore, in order to exploit magnetic properties of these molecular magnets, it is desirable to prepare SMMs with larger and larger  $S$  values and with appreciable negative  $D$  values. Since their discovery, a great number of SMMs based on various transition metal clusters, with various structures and magnetic properties, have been reported.<sup>20</sup> The first attempts to maximize the anisotropy barrier focused on maximizing  $S$  by designing systems with ferromagnetic exchange coupling. Using this approach, the largest anisotropy barrier and blocking temperature of  $U_{eff} = 86.4$  K (~12-13 K higher than that of the  $Mn_{12}$ ) and  $T_B = 4.5$  K for the dodecametallic phenolate-bridged cage  $[Mn_6O_2(sao)_6(O_2CPh)_2(EtOH)_4]$  ( $\{Mn_6\}$ ;  $saoH_2 = 2$ -hydroxybenzaldehyde oxime) were reported. This metal cluster, obtained through a deliberate structural distortion of a  $[Mn_6]$  complex, resulted in a molecule possessing an  $S = 12$  ground state with  $D = -0.43$   $cm^{-1}$ .<sup>21</sup> To date, this is the highest value observed for the energy barrier for  $3d$  metal cluster-based SMMs. This result emphasized the importance of obtaining synthetic control over SMMs, so that they can be modified in desirable ways in order to improve their magnetic properties. However, although it is possible to synthesize polymetallic complexes with very large  $S$  values, factors beyond the control of the synthetic chemist can result in an overall lack of anisotropy, compromising the SMM properties.<sup>22</sup> A recent theoretical study has even indicated that the key factor which influences  $U_{eff}$  is in fact the anisotropy and that the energy barrier may even be independent of  $S$ .<sup>23</sup>

The effort to design new SMMs with larger anisotropy barriers and more prominent hysteresis led to the discovery of several new classes of SMMs. In particular recent developments in the field have demonstrated that much larger spin reversal barriers are accessible in lanthanide-containing complexes, on account of the large single-ion magnetic anisotropy delivered by an appropriate configuration of  $4f$  electrons.<sup>24</sup>

### 5.3.2 Lanthanide Phthalocyanines Double Decker

In 2003 Ishikawa and co-workers found that a particular class of lanthanide organometallic compounds, lanthanide phthalocyanine double-decker, were able to behave as magnets at the single-molecule level.<sup>25</sup> Phthalocyanines (Pcs) compounds contain four isoindole nitrogen atoms, which are able to complex a range of metal ions: with large metal centers that favor octacoordination (e.g. rare earths), sandwich-type complexes in the form of double-deckers can be formed.<sup>26</sup> A lanthanide phthalocyanine double decker ( $\text{LnPc}_2$  hereafter) is a sandwich complex formed by two phthalocyanine ligands with a square antiprism geometry and a lanthanide ion in the middle (Figure 5.7).

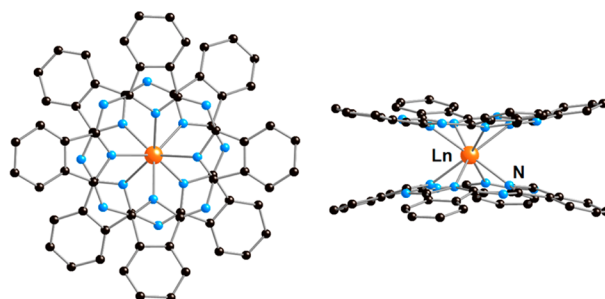


**Figure 5.7** Structure of the complex anion  $\text{LnPc}_2$ . Color scheme: Ln, orange; N, blue.

$\text{LnPc}_2$  complexes exist in three different forms, based on the oxidation state of the Pc rings. The ligands can be either oxidized or reduced while the central lanthanide ion maintains its +3 oxidation state. The anionic form  $[\text{LnPc}_2]^-$  consists of a trivalent lanthanide ion (+3) coordinated by two Pc ligands, each one bearing a formal charge of -2. Neutral  $[\text{LnPc}_2]^0$  and cationic  $[\text{LnPc}_2]^+$  forms can be easily achieved by reversible one- or two-electrons oxidation by reaction of mild oxidizing reagents or via electrochemistry.

The  $\text{LnPc}_2$  complexes showing SMM behaviors have significantly large axial magnetic anisotropy, which is given to the complexes by essentially different mechanisms than those of the well-established 3d metal cluster-based SMMs. In the 3d cluster SMMs case, the easy axis type magnetic anisotropy, which is represented by the negative zero-field-splitting constant  $D$ , is caused by the magnetic interactions among high-spin 3d metal ions in a molecule. In the lanthanide SMM case, on the other hand, such anisotropy is given by the ligand field (LF) in which the lanthanide ion is placed.<sup>27</sup> The energy terms are determined by strong coupling between the spin  $S$  and orbital angular  $L$  momenta of the lanthanide ions giving rise to a total angular momentum  $J$ , and

then split further by crystal-field effects. By analogy to giant-spin transition-metal SMMs, the  $J$  value of the ground electronic state gives rise to  $[2J + 1] m_J$  microstates, which are perturbed by a small but significant ligand field effect. Sublevel structures of the ground-state multiplets for six different lanthanide metals were determined in  $\text{LnPc}_2$  complexes in order to clarify the ligand field effect and the role of the lanthanide ion (Figure 5.8).<sup>28</sup>

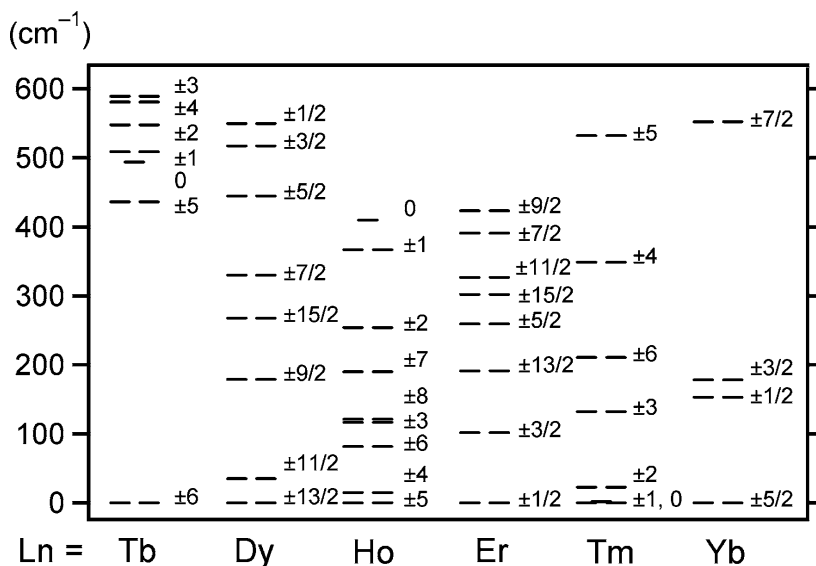


**Figure 5.8** Energy diagram for the ground multiplets of  $[\text{LnPc}_2]^-$  ( $\text{Ln} = \text{Tb}, \text{Dy}, \text{Ho}, \text{Er}, \text{Tm}, \text{or Yb}$ ).

In the Tb complex, the lowest substates are assigned to  $J_z = \pm 6$ , which are the maximum and minimum values in the  $J = 6$  ground state. The energy separation from the rest of the substates is more than  $400 \text{ cm}^{-1}$ . If the relaxation occurs through a path consisting of stepwise transitions from  $J_z$  to  $J_z \pm 1$  states, the "rate-determining step" is the first transition from  $J_z = 6$  to  $J_z = 5$  (or from  $-6$  to  $-5$ ) because of the large energy gap. In the Dy complex, the lowest substates are characterized as  $J_z = \pm 13/2$ , which are the second largest in the  $J = 15/2$  ground state. The sublevels are distributed more evenly than in the Tb case. This implies a possibility that there is no step requiring extremely high energy in the relaxation path. In Er and Tm case, the  $|J_z|$  values of the lowest substates are the smallest within the multiplet; in the Ho and Yb case,  $|J_z|$  of the lowest substates takes an intermediate value within each multiplet. Thus the use of  $\text{LnPc}_2$ , and in particular  $\text{TbPc}_2$ , allows to achieve thermal energy barriers

for the reversal of magnetization,  $U_{\text{eff}}$ , that are an order of magnitude higher than those found in d-block single-molecule magnets (SMMs).

As already shown 3d metal-cluster SMMs, the magnetization relaxation for LnPC<sub>2</sub> can occur via thermally activated quantum-mechanical tunneling. In fact the QTM process is also observed in the lanthanide-based SMMs. However the mechanism is different from those of the transition-metal cluster SMMs. In the 3d metal-cluster SMM cases, where energy separations between substates with different  $|S_z|$  values are of the order of 1–10 cm<sup>-1</sup>, QTM occurs when energy levels of two substates coincide under an appropriate magnetic field and the two states are brought to resonance. In the LnPC<sub>2</sub> case, such level coincidence cannot occur with magnetic fields below several tesla, because the lowest substates are separated from the rest of the substates by a few hundred per centimeter. Here the origin of QTM is related to the interaction between the nuclear spin term  $I$  (3/2 for Tb) and the angular momentum  $J$ .<sup>29</sup>

This different mechanism leads to the typical "butterfly-shaped" hysteresis, with an enhancement of quantum tunnelling in zero applied field region (Figure 5.9).

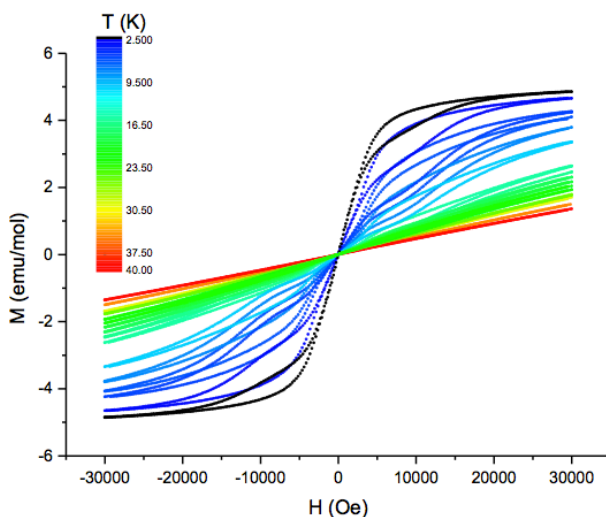


**Figure 5.9** Typical butterfly-shaped hysteresis loops recorded at different temperatures on a pure TbPC<sub>2</sub> microcrystalline powder sample.<sup>30</sup>

Different lanthanides can be readily inserted into the sandwich structure, and it is also possible to chemically modify the ligand substituents and the redox state of the ligands themselves, by one- or two-electrons oxidation to neutral [LnPC<sub>2</sub>] or to cationic [LnPC<sub>2</sub>]<sup>+</sup> forms respectively. This latter approach allows changes



in electronic structure to be investigated for the same (or very similar) molecular structures, and the impact of making such modifications can be substantial.<sup>31</sup> For instance it's been reported that single-electron oxidations cause changes in the molecular structure of the sandwich unit, which impact on the ligand field experienced by the lanthanide trications, and which result in greater energetic separation of the ground  $m_J$  sublevel from the excited states. Ishikawa reported<sup>32</sup> that two-electron oxidation of  $[\text{DyPc}_2]^-$  to give  $[\text{DyPc}_2]^+$  caused significant contraction of the sandwich structure, consistent with the removal of antibonding electrons: the two  $\text{N}_4$  planes containing the nitrogen atoms directly bonded to Dy were calculated to be closer (Figure 5.10). This structural modification resulted in drastic changes in dynamical magnetism including a doubling of the energy barrier  $U_{\text{eff}}$  and a significant rise of the blocking temperature from the original anionic form.

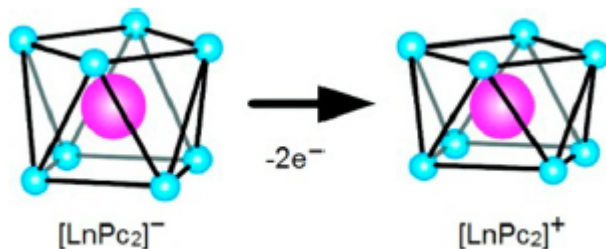


**Figure 5.10** Contraction of the square-antiprismatic coordination environment upon two-electron oxidation of  $[\text{LnPc}_2]^-$  to give  $[\text{LnPc}_2]^+$ .

To date several  $\text{LnPc}_2$  with different lanthanide ions and bearing different peripheral substituents have been synthesized, looking for the highest values of  $U_{\text{eff}}$ . At the time of writing, the record anisotropy barrier for an SMM of any kind is held by Torres and co-workers, for a  $\text{TbPc}_2$  peripherally functionalized with  $\text{OC}_6\text{H}_4\text{-}p\text{-}^t\text{Bu}$  substituents for which  $U_{\text{eff}} = 652 \text{ cm}^{-1}$  was determined.<sup>33</sup>

### 5.3.3 SMMs on Surface

Thanks to their outstanding magnetic properties, SMMs have been proposed as potential candidates for several applications such as high-density magnetic storage,<sup>34</sup> quantum computing applications<sup>35</sup> and spintronics.<sup>36</sup> However, before such applications become a reality, there is a fundamental issue that needs to be addressed, namely, the development of strategies to evolve from bulk crystals to molecules suitable to be grafted on surfaces, sensors or other

systems able to act as a device. The challenge is the definition of experimental strategies to properly assemble and integrate these molecular materials into functional devices without compromising their properties.<sup>37</sup> Transferring the magnetic properties from the bulk material to the surface is far from trivial: perturbations arising upon molecule–surface interactions can induce numerous changes, from chemical modifications (redox processes, chemical decomposition, ...) that completely alter the magnetic properties of the molecule to molecular deformations. Such deformations, though not so drastic as a chemical decomposition, can induce a modification of the magnetic exchange pathway or simply alter the easy-magnetization axes, and thus, the magnetization relaxation mechanisms and barriers. Surface effects as well as interaction with the substrate can completely change the characteristic SMM behavior observed in crystals, either increasing its magnetic anisotropy or completely removing it.

The high thermal and chemical stability of LnPc<sub>2</sub> molecules make them suitable for deposition on surface via sublimation under Ultra-High Vacuum (UHV) conditions: sub-monolayer deposition of LnPc<sub>2</sub> on different substrates has been largely investigated.<sup>38</sup> However it has been observed that peculiar magnetic behavior of the SMMs can be altered, and even suppressed, after their deposition on surface. The magnetic hysteresis is strongly affected when the environment is different from the crystalline phase: in general, the magnetization dynamics of LnPc<sub>2</sub> is severely altered in amorphous materials, where the packing of the molecules characterizing the crystalline phase is lost. In a work reported by Sessoli group,<sup>30</sup> the magnetic behavior of TbPc<sub>2</sub> was investigated in different phases (Figure 5.11).

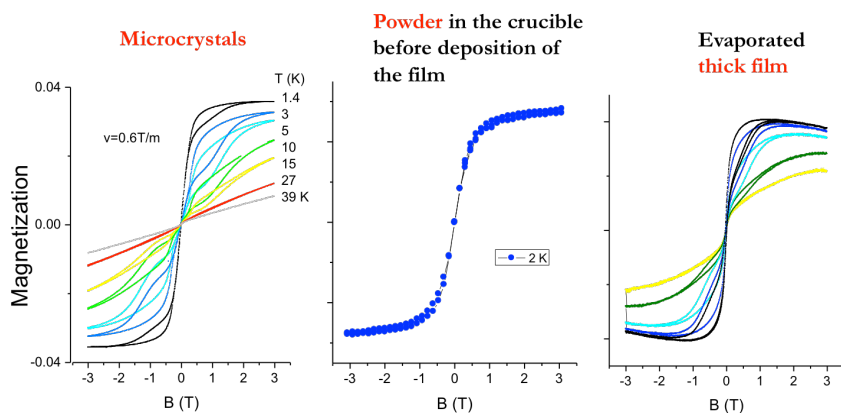


**Figure 5.11**  $TbPc_2$  magnetic hysteresis loop in **a)** microcrystals, **b)** heated powder in the crucible before the deposition of the film, **c)** sublimated film on Kapton.

Microcrystals of  $TbPc_2$  showed the typical magnetic profile of terbium double deckers, with an opening of the hysteresis at temperature as high as 15 K (Fig. 5.11a). In the deposited thick film (Fig. 5.11c) the hysteresis was retained, with the typical butterfly shaped loops opened at 10 K. Although the blocking temperature appeared to be slightly lower, the qualitative behavior remained unaltered. In contrast, the fraction of the powder sample extracted from the crucible before evaporating film did not show any comparable magnetic hysteresis over the whole investigated temperature range (Fig. 5.11b). The intactness of the complex was however confirmed by the fact that the subsequently evaporated film presents the typical magnetic hysteresis. The disappearance of the hysteresis in the heated powder and its reappearance once the treatment was extended to sublimation and reconstruction of a film with partial molecular ordering was intriguing and apparently lacks of explanation. Crystal packing could be responsible for the stabilization of a molecular structure characterized by a lower deviation of the orientation of the two phthalocyaninato rings from the exactly staggered situation ( $45^\circ$ ) (Figure 5.12). This limit case corresponds to  $D_{4d}$  symmetry of the coordination sphere of the terbium(III) ion leading to quenching of transverse anisotropy.

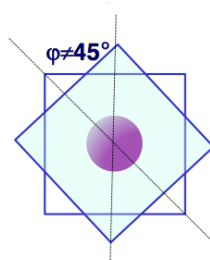


**Figure 5.12** Distortions from  $D_{4d}$  symmetry induced by intermolecular interactions.

An alternative way to assemble  $\text{LnPc}_2$  on surface is the grafting of molecules derivatized with appropriate functional groups: this approach is preferable to the unspecific deposition by thermal evaporation in the realization of durable devices due to the formation of stable bonds. Grafting offers also much more control on the orientation and the density of the components on the substrate. The possibility to chemically functionalize  $\text{LnPc}_2$  molecules makes them ideal candidates for grafting on surface. Ruben and co-workers already reported in 2009 the synthesis of a pyrene-functionalized  $\text{TbPc}_2$  and its grafting through  $\pi$ - $\pi$  interactions on carbon nanotubes<sup>39,40</sup> and on graphene.<sup>41,42</sup> In 2012 the SAM formation on gold substrate of  $\text{TbPc}_2$  functionalized with peripheral thioether substituents was reported.<sup>43</sup> However the lability of the Au-S bond<sup>44</sup> cannot guarantee the long-term stability required for the development of an SMM-based device.

Covalent grafting is preferable as it guarantees a higher stability with respect to  $\pi$ -stacking or S-Au interactions in the realization of robust and durable devices. To date, stable covalent grafting between  $\text{LnPc}_2$  molecules and surface has not been reported yet. Thus new approaches in design and synthesis of LnDD for robust integration of bistable magnetic molecules with retained magnetic behavior in electronic devices are desirable.

In this Thesis we will present our work on design and synthesis of new  $\text{TbPc}_2$  able to preserve the SMM behavior once grafted covalently on different surfaces. In particular the robust covalent grafting of  $\text{TbPc}_2$  functionalized complexes to a silicon surface yielding a partially oriented monolayer silicon surface will be presented in Chapter 6.

In Chapter 7 we will exploit the selective functionalization of one of the two Pcs forming the  $\text{TbPc}_2$  complexes in order to promote their oriented grafting on silicon surface.

In Chapter 8 we will present the synthesis and the magnetic properties of new functionalized  $\text{TbPc}_2$ .

## 5.4 References

- <sup>1</sup> C. P. Poole Jr., F. J. Owens, *Introduction to nanotechnology* **2003**, John Wiley & Sons Inc., Hoboken, New Jersey.
- <sup>2</sup> R. P. Feynman, *J. Microelectromech. Syst.* **1992**, *1*, 60–66.
- <sup>3</sup> F. Allhoff, P. Lin, D. Moore, *What is Nanotechnology and why does it Matter? From Science to Ethics* **2010**, John Wiley & Sons, Ltd.
- <sup>4</sup> W. Linert, M. Verdager, *Molecular Magnets Recent Highlights* **2003**, Springer-Verlag Wien, New York.
- <sup>5</sup> W. Wernsdorfer, *Adv. Chem. Phys.* **2001**, *118*, 99-190.
- <sup>6</sup> A. H. Morrish, *The physical principles of magnetism* **1966**, John Wiley & Sons Inc., New York.
- <sup>7</sup> Q. A. Pankhurst, J. Connolly, S. K. Jones, J. Dobson, *J.Phys. D: Appl. Phys.* **2003**, *36*, R167-R181.
- <sup>8</sup> G. E. Moore, *Electronics* **1965**, *38*, 114-117.
- <sup>9</sup> H. N., Bertram, M. Williams *IEEE Trans. Mag.* **2000**, *36*, 4-9.
- <sup>10</sup> D. Gatteschi, R. Sessoli, J. Villain, *Molecular Nanomagnets* **2006**, Oxford University Press, Oxford.
- <sup>11</sup> R. Sessoli, D. Gatteschi, A. Caneschi, M. A. Novak, *Nature* **1993**, *365*, 141-143.
- <sup>12</sup> S. M. J. Aubin, M. W. Wemple, D. M. Adams, H. L. Tsai, G. Christou, D. N. Hendrickson, *J. Am. Chem. Soc.* **1996**, *118*, 7746-7754.
- <sup>13</sup> A. Caneschi, D. Gatteschi, R. Sessoli, A. L. Barra, L. C. Brunel, M. Guillot, *J. Am. Chem. Soc.* **1991**, *113*, 5873-5874.
- <sup>14</sup> T. Lis, *Acta Cryst.* **1980**, *B36*, 2042-2046.

- <sup>15</sup> G. Christou, D. Gatteschi, D. N. Hendrickson, R. Sessoli, *MRS Bulletin* **2000**, 25, 66-71.
- <sup>16</sup> D. Gatteschi, R. Sessoli, *J. Magn. Magn. Mat.* **2004**, 272-276, 1030-1036.
- <sup>17</sup> L. Thomas, F. Lioni, R. Ballou, D. Gatteschi, R. Sessoli, B. Barbara, *Nature* **1996**, 383, 145-147.
- <sup>18</sup> K. M. Mertes, Y. Zhong, M. P. Sarachik, Y. Paltiel, H. Shtrikman, E. Zeldov, E. Rumberger, D. N. Hendrickson, G. Christou, *Europhys. Lett.* **2001**, 55, 874-879.
- <sup>19</sup> L. Ouahab, *Multifunctional Molecular Materials* **2012**, Pan Stanford Publishing Pte. Ltd., Singapore.
- <sup>20</sup> a) W. Wernsdorfer, T. Ohm, C. Sangregorio, R. Sessoli, D. Mailly, C. Paulsen, *Phys. Rev. Lett.* **1999**, 82, 3903-3906; b) A. J. Tasiopoulos, A. Vinslava, W. Wernsdorfer, K. A. Abboud, G. Christou, *Angew. Chem. Int. Ed.* **2004**, 43, 2117-2121; c) S. Wang, J. L. Zuo, S. Gao, Y. Song, H. C. Zhou, Y. Z. Zhang, X. Z. You, *J. Am. Chem. Soc.* **2004**, 126, 8900-8901; d) E. Pardo, R. Ruiz-Garcia, F. Lloret, J. Faus, M. Julve, Y. Journaux, F. Delgado, C. Ruiz-Pérez, *Adv. Mater.* **2004**, 16, 1507-1600; e) Y. Song, P. Zhang, X. M. Ren, X. F. Shen, Y. Z. Li, X. Zeng You, *J. Am. Chem. Soc.* **2005**, 127, 3708-3709; f) T. Kajiwara, M. Nakano, Y. Kaneko, S. Takaishi, T. Ito, M. Yamashita, A. Igashira-Kamiyama, H. Nojiri, Y. Ono, N. Kojima, *J. Am. Chem. Soc.* **2005**, 127, 10150-10151.
- <sup>21</sup> C. J. Milios, A. Vinslava, W. Wernsdorfer, S. Moggach, S. Parsons, S. P. Perlepes, G. Christou, E. K. Brechin, *J. Am. Chem. Soc.* **2007**, 129, 2754-2755.
- <sup>22</sup> A. M. Ako, I. J. Hewitt, V. Mereacre, R. Clérac, W. Wernsdorfer, C. E. Anson, A. K. Powell, *Angew. Chem., Int. Ed.* **2006**, 45, 4926-4929.
- <sup>23</sup> F. Neese, D. A. Pantazis, *Faraday Discuss.* **2011**, 148, 229-238.
- <sup>24</sup> S. Demir, J. M. Zadrozny, M. Nippe, J. R. Long, *J. Am. Chem. Soc.* **2012**, 134, 18546-18549.

- <sup>25</sup> N. Ishikawa, M. Sugita, T. Ishikawa, S. Koshihara, Y. Kaizu, *J. Am. Chem. Soc.* **2003**, *125*, 8694-8695.
- <sup>26</sup> J. Jiang, D. K. P. Ng, *Acc. Chem. Res.* **2009**, *42*, 79-88.
- <sup>27</sup> N. Ishikawa, *Functional Phthalocyanine Molecular Materials Structure and Bonding* **2010**, Springer Berlin Heidelberg, *135*, 211-228.
- <sup>28</sup> N. Ishikawa, M. Sugita, T. Okubo, N. Tanaka, T. Iino, Y. Kaizu, *Inorganic Chemistry* **2003**, *42*, 2440-2446.
- <sup>29</sup> N. Ishikawa, *Polyhedron* **2007**, *26*, 2147-2153.
- <sup>30</sup> L. Malavolti, M. Mannini, P. Car, G. Campo, F. Pineider, R. Sessoli, *J. Mater. Chem. C* **2013**, *1*, 2935-2942.
- <sup>31</sup> R. A. Layfield, *Organometallics* **2014**, *33*, 1084-1099.
- <sup>32</sup> N. Ishikawa, Y. Mizuno, S. Takamatsu, T. Ishikawa, S. Koshihara, *Inorg. Chem.* **2008**, *47*, 10217-10219.
- <sup>33</sup> C. R. Ganivet, B. Ballesteros, G. de la Torre, J. M. Clemente-Juan, E. Coronado, T. Torres, *Chem. Eur. J.* **2013**, *19*, 1457-1465.
- <sup>34</sup> L. Krusin-Elbaum, T. Shibauchi, B. Argyle, L. Gignac, D. Weller, *Nature* **2001**, *410*, 444-446.
- <sup>35</sup> M. N. Leuenberger, D. Loss, *Nature* **2001**, *410*, 789-793.
- <sup>36</sup> J. Camarero, E. Coronado, *J. Mater. Chem.* **2009**, *19*, 1678-1684.
- <sup>37</sup> N. Domingo, E. Bellido, D. Ruiz-Molina, *Chem. Soc. Rev.* **2012**, *41*, 258-302.
- <sup>38</sup> a) K. Katoh, Y. Yoshida, M. Yamashita, H. Miyasaka, B. K. Breedlove, T. Kajiwara, S. Takaishi, N. Ishikawa, H. Isshiki, Y. Feng Zhang, T. Komeda, M-Yamagishi, J. Takeya, *J. Am. Chem. Soc.* **2009**, *131*, 9967-9976; b) L. Margheriti, D. Chiappe, M. Mannini, P.-E. Car, P. Saintavit, M.-A. Arrio, F. B. de Mongeot, J.

C. Cezar, F. M. Piras, A. Magnani, E. Otero, A. Caneschi, R. Sessoli, *Adv. Mater.* **2010**, *22*, 5488-5493; c) A. Lodi Rizzini, C. Krull, T. Balashov, J. J. Kavich, A. Mugarza, P. S. Miedema, P. K. Thakur, V. Sessi, S. Klyatskaya, M. Ruben, S. Stepanow, and P. Gambardella, *Phys. Rev. Lett.* **2011**, *107*, 177205; d) J. Schwöbel, Y. Fu, J. Brede, A. Dilullo, G. Hoffmann, S. Klyatskaya, M. Ruben, R. Wiesendanger, *Nat. Commun.* **2012**, article number: 953.

<sup>39</sup> S. Kyatskaya, J. R. G. Mascarós, L. Bogani, F. Hennrich, M. Kappes, W. Wernsdorfer, M. Ruben, *J. Am. Chem. Soc.* **2009**, *131*, 15143–15151.

<sup>40</sup> M. Ganzhorn, S. K., M. Ruben, W. Wernsdorfer, *ACS Nano* **2013**, *7*, 6225–6236.

<sup>41</sup> M. Lopes, A. Candini, M. Urdampilleta, A. Reserbat-Plantey, V. Bellini, S. Klyatskaya, L. Marty, M. Ruben, M. Affronte, W. Wernsdorfer, N. Bendiab *ACS Nano* **2010**, *4*, 7531–7537.

<sup>42</sup> A. Candini, S. Klyatskaya, M. Ruben, W. Wernsdorfer, M. Affronte *Nano Lett.* **2011**, *11*, 2634–2639.

<sup>43</sup> U. Glebe, T. Weidner, J. E. Baio, D. Schach, C. Bruhn, A. Buchholz, W. Plass, S. Walleck, T. Glaser, U. Siemeling, *Chempluschem* **2012**, *77*, 889–897.

<sup>44</sup> J. B. Schlenoff, M. Li, H. Ly, *J. Am. Chem. Soc.* **1995**, *117*, 12528–12536.





# Chapter 6

## Magnetic Behaviour of TbPc<sub>2</sub> Single-Molecule Magnets Chemically Grafted on Silicon Surface<sup>\*</sup>

<sup>\*</sup> This chapter has been published in Nature Communications: M. Mannini, F. Bertani, C. Tudisco, L. Malavolti, L. Poggini, K. Misztal, D. Menozzi, A. Motta, E. Otero, P. Ohresser, P. Saintavit, G. G. Condorelli, E. Dalcanale, R. Sessoli, *Nat. Commun.* **2014**, *5*, article number: 4582.

## 6.1 Introduction

Molecular-based functional materials can allow the exploitation of the richness of the molecular structures to implement in technology novel and unexpected properties. Among the next-generation sensors, transistors, and memory devices, those based on spin state of molecules represent promising alternatives to traditional technologies.<sup>1</sup> In this context there is a keen interest on Single-Molecule Magnets (SMMs),<sup>2</sup> functional molecules featuring magnetic memory at the single molecule scale<sup>3</sup> as well as quantum effects.<sup>4</sup> However, beyond temperature limitations, a quick development of a *SMM-based technology* is hampered by the intrinsic chemical fragility of most polynuclear SMMs and the evanescence of the SMM behavior, which make the retention of the molecular magnetic bistability at the nanoscale far from trivial. The chemical bond between a sulphur functionalised tetrairon(III) SMM Fe<sub>4</sub> and a gold surface has been recently employed and the typical magnetic hysteresis observed through synchrotron-light based experiments.<sup>5</sup> However, the lability of the Au-S bond<sup>6</sup> cannot guarantee the long term stability required for the development of an SMM-based device. For this reason grafting of SMMs on a particularly attractive inorganic platform, such as silicon wafers, will offer the possibility to make robust and durable devices by forming stable Si-C covalent bonds. Moreover, the possibility of different doping of the silicon substrate can be used to influence the electronic properties of the grafted molecules<sup>7</sup> and the mobility of the charge carriers in the final hybrid device. Although preliminary promising results have been obtained with Fe<sub>4</sub> SMMs chemically anchored on Silicon,<sup>8</sup> the very low temperature required for the observation of magnetic bistability (i.e. below 1 K) has prompted us to another molecule, i.e. the Terbium(III) bis(phthalocyaninato) neutral complex,<sup>9</sup> TbPc<sub>2</sub> hereafter. Slow dynamics in the magnetization reversal is here due to the large activation energy barrier generated by crystal field splitting of the  $J=6$  ground multiplet of the highly anisotropic Tb<sup>III</sup> ion.<sup>10</sup> This results in one of the most promising and widely investigated SMMs,<sup>11</sup> whose insertion in single molecule transport devices has allowed to monitor the quantum dynamics of a single nuclear spin<sup>12</sup> and to observe a novel supramolecular spin valve effect.<sup>13</sup> In general, however, the magnetization dynamics of TbPc<sub>2</sub> is severely altered in amorphous materials, where the packing of the molecules characterising the crystalline phase is lost.<sup>14</sup> The origin of the phenomenon remains unclear, although it should be considered that small distortion of the two phthalocyaninato ligands from the perfectly staggered configuration, corresponding to D<sub>4d</sub> symmetry, can be very efficient in promoting the tunnel

mechanism of relaxation.<sup>14b</sup> A similar reduction of the magnetic bistability is observed at the nanoscale: by thermal evaporation of these double-deckers on clean metallic surfaces in Ultra-High Vacuum (UHV) environment, the wide opening of the magnetic hysteresis loop above liquid helium temperature vanishes.<sup>15</sup> The phthalocyaninato ligands appear to efficiently couple the magnetic moment of the Tb ion with the magnetization of substrates as recently shown for submonolayer UHV-prepared deposits of TbPc<sub>2</sub> on magnetic substrates.<sup>16</sup> The strength of the interaction can be tuned modifying the electronic characteristics of the substrate, though also in these cases no evidence of the SMM character of the pristine molecular system has been observed.

Here we report the outcome of an alternative approach aimed at the exploitation of the magnetic bistability of double-decker systems in a robust nanostructure, prerequisite to fruitfully exploit the SMM features in *ad hoc* designed molecular devices. This has been achieved by the functionalization of the original TbPc<sub>2</sub> system, resulting in a homoleptic double decker derivative bearing long aliphatic chains with terminal double bonds that allow the grafting of the molecule to the silicon surface from a diluted solution. By using X-ray Circular Magnetic Dichroism to extract the magnetic properties at the nanoscale and with the support of other parallel chemical and structural characterizations and with the support of a theoretical analysis we demonstrate that SMM behavior with enhanced hysteresis is retained on a partially ordered and chemically robust monolayer of molecules grafted on Si(100) surface through hydrosilylation reaction.

## 6.2 Results and Discussion

### 6.2.1 Synthesis of the TbPc<sub>2</sub>(OC<sub>11</sub>H<sub>21</sub>)<sub>8</sub> Complex

Silicon was chosen as surface for grafting because of its technological relevance and for the possibility to form thermally and hydrolytically stable Si-C bonds via thermal hydrosilylation.<sup>17</sup> The design of a suitable TbPc<sub>2</sub> for silicon grafting requires the introduction of  $\omega$ -functionalised alkyl chains at peripheral positions of the phthalocyanine ligands. The classical De Cian synthesis,<sup>18</sup> starting from the Terbium acetylacetonate and 1,2-dicyanobenzene derivatives, has been adopted here. The alternative option of TbPc<sub>2</sub> post-functionalization turned out to be synthetically unfeasible in this case. Moreover, the only substituents compatible with the harsh reaction conditions required for double decker formation were alkoxy derivatives, excluding most of the common

linker groups such as esters, amides, carbamates, etc. The required 4-( $\omega$ -undecenyloxy)phthalonitrile precursor<sup>19</sup> was synthesized from the commercially available 4-hydroxyphthalonitrile by the addition of 11-bromo-1-undecene in the presence of an excess of potassium carbonate in DMF in 80% yield. Homoleptic **TbPc<sub>2</sub>(OC<sub>11</sub>H<sub>21</sub>)<sub>8</sub>** was then obtained by heating Terbium(III) acetylacetonate in refluxing 1-hexanol in the presence of 4-( $\omega$ -undecenyloxy)phthalonitrile, with 1,8-diazabicyclo[5.4.0]undec-7-ene (DBU) as a basic catalyst (Fig. 6.1a). The neutral double decker compound was isolated in 35% yield as a mixture of constitutional isomers in the form of dark-green powder (see Methods and Supplementary Note 1).

The resulting **TbPc<sub>2</sub>(OC<sub>11</sub>H<sub>21</sub>)<sub>8</sub>** was characterized via high resolution MALDI-ToF mass spectrometry, X-ray Photoelectron Spectroscopy (XPS) and UV-Vis spectroscopy (see Fig.1 and Supplementary Note 2). The mass spectrometry, the most employed analytical tool for this class of compounds, revealed a unique peak centred at 2529.44 m/z that corresponds well in position and isotopic distribution to the calculated ones for the molecular ion of **TbPc<sub>2</sub>(OC<sub>11</sub>H<sub>21</sub>)<sub>8</sub>** (Fig. 6.1b and inset). The UV-VIS spectrum of **TbPc<sub>2</sub>(OC<sub>11</sub>H<sub>21</sub>)<sub>8</sub>** recorded in chloroform solution shown in Figure 6.1c, confirms the neutral  $\pi$  radical form of the molecule: the spectrum exhibits the characteristic absorption bands of double decker phthalocyaninato complexes.<sup>20</sup> The Q band at 681 nm results from the promotion of an electron from the first semi-occupied molecular orbital (SOMO) to the second LUMO and from the second fully occupied HOMO to the first LUMO. Furthermore the spectrum shows a typical split Soret band, resulting from the electronic transitions from the third occupied HOMO to the first LUMO, with maxima at 329 and 361 nm. The two weak  $\pi$ -radical bands at 469 nm and 926 nm are due to electronic transitions from the SOMO orbital to the degenerate LUMO. The multiplicity associated to the several isomers of **TbPc<sub>2</sub>(OC<sub>11</sub>H<sub>21</sub>)<sub>8</sub>** produced in the reaction does not allow the univocal attribution of all resonances by NMR (Supplementary Fig. 1). However, the strong paramagnetic upfield shifts at negative ppm are indicative of Tb complexation even if the presence of these paramagnetic units hamper a proper spectral assignment of the aromatic protons. The XPS spectra of a reference bulk phase were recorded on a thick film prepared by drop casting a diluted dichloromethane solution of the complexes on a polycrystalline gold substrate. A semi-quantitative analysis of the spectra (Supplementary Fig. 2 and Supplementary Table 1) revealed an atomic composition of the compound in agreement, within the limits of the techniques, with the proposed formula, thus confirming the mass spectrometry results.

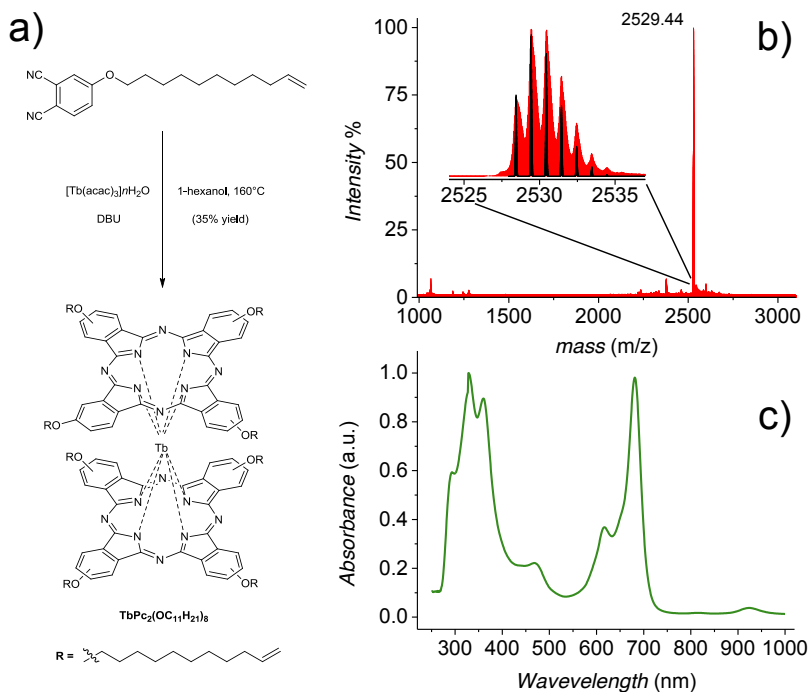


**Figure 6.1** a) Synthesis of homoleptic  $\text{TbPc}_2(\text{OC}_{11}\text{H}_{21})_8$  using 4-( $\omega$ -undecenyloxy)phthalonitrile as starting material; b) high resolution MALDI-ToF spectrum of  $\text{TbPc}_2(\text{OC}_{11}\text{H}_{21})_8$ , with experimental (red lines) versus theoretical (black) isotopic distribution pattern in the inset; c) UV/Vis absorption spectrum of  $\text{TbPc}_2(\text{OC}_{11}\text{H}_{21})_8$  in chloroform.

## 6.2.2 Magnetic Characterization of Bulk $\text{TbPc}_2(\text{OC}_{11}\text{H}_{21})_8$

Magnetic characterization, performed with standard ac and dc magnetometric techniques (Fig. 6.2, Supplementary Fig. 3) clearly indicates the SMM behavior of the complex in its bulk phase. In zero static field the ac susceptibility *vs* temperature curves are characterised by a frequency dependent peak in the out-of-phase component occurring at relatively high temperatures, e.g. the maximum in  $\chi''$  at 1 kHz is observed at 47 K, which well compares with those reported for similar homoleptic substituted TbPc<sub>2</sub> systems.<sup>21</sup> A more careful analysis of the frequency dependence of the ac susceptibility in a wide

frequency range, 0.5 Hz - 10 kHz, was performed with the extended Debye model<sup>2</sup> allowing to extract the relaxation time,  $\tau$  and its distribution width through the empirical parameter,  $\alpha$  (Supplementary Note 3). The temperature dependence of  $\tau$  is shown in Figure 6.2b. A linear behavior in the  $\ln(\tau)$  vs.  $1/T$  plot is observed at zero static field in the high temperature regime,  $T > 35$  K, providing the parameters  $\tau_0 = 5.5 \pm 0.7 \times 10^{-12}$  s and  $D/k_B = 811 \pm 5$  K for the best fit with the Arrhenius law,  $\tau = \tau_0 \exp(D/k_B T)$ . The estimated energy barrier in the thermally activated process is smaller than that found for the crystalline phase of  $\text{TbPc}_2$  (965 K)<sup>21</sup> but it is close to the value observed in similar conditions for amorphous unfunctionalized  $\text{TbPc}_2$  system (856 K),<sup>14b</sup> in agreement with the amorphous character of  $\text{TbPc}_2(\text{OC}_{11}\text{H}_{21})_8$  sample. Below 35 K the relaxation becomes temperature independent, indicating the onset of a tunnel mechanism of relaxation, with a significant increase of the width of the distribution of the relaxation times.

A better simulation of  $\chi''$  vs.  $\nu$  curves is achieved taking into account the presence of a bimodal distribution (see Supplementary Fig. 4 in SI), only the dominating one is reported in Figure 6.2b.

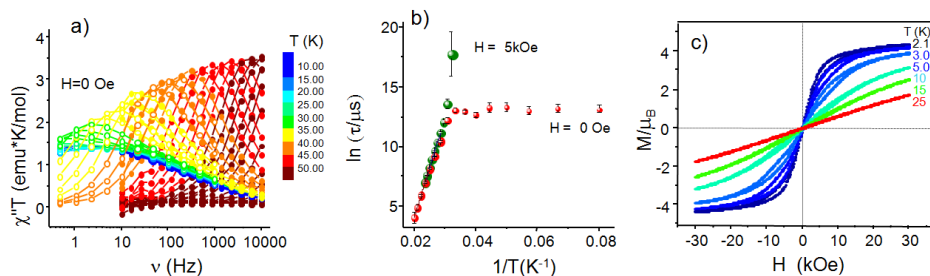


**Figure 6.2** Bulk magnetic properties of  $\text{TbPc}_2(\text{OC}_{11}\text{H}_{21})_8$ . a) ac susceptibility measurements in zero field. b) Arrhenius plot of data extracted from ac measurements in zero field and in a 5 kOe static field. c) Magnetization curves as a function of the temperature recorded at a field sweeping rate of 50 Oe  $\text{s}^{-1}$ .

The application of a static field of 5 kOe (Supplementary Fig. 3 and 5) provides comparable high temperature behavior as shown in Figure 6.2b, but significantly affects the magnetic relaxation below 35 K, suppressing the tunnelling mechanism with  $\tau$  exceeding the accessible timescale of the AC susceptometer ( $\sim 10$  s). A single distribution of  $\tau$  is observed in static field because distortions from idealised  $D_{4d}$  symmetry present in this amorphous material are less relevant when resonant quantum tunnelling is suppressed. Magnetization vs. field measurements performed at several temperatures and

scanning the field between 30 kOe and -30 kOe at 50 Oe s<sup>-1</sup> (see Fig. 6.2c) evidence an opening in the hysteresis below 15 K with the typical butterfly shape induced by the enhancement of quantum tunnelling in zero applied field.<sup>22</sup>

### 6.2.3 Monolayer Preparation and Chemical Characterization

The TbPc<sub>2</sub>(OC<sub>11</sub>H<sub>21</sub>)<sub>8</sub> complex has been anchored on a H-terminated Si(100) surface via thermal hydrosilylation of the double bonds according to published literature.<sup>23</sup> The hydrosilylation reaction leads to the formation of a robust Si-C bond and it occurs by placing the alkene functionalised molecules in a 10<sup>-3</sup> M mesitylene solution at 200°C in presence of a freshly etched H-terminated Si(100). After grafting, several cycles of cleaning (including the sonication of the sample in several solvents) guarantee the removal of all the physisorbed materials leaving on the surface only the monolayer of grafted molecules. The silicon anchored complex, TbPc<sub>2</sub>(OC<sub>11</sub>H<sub>21</sub>)<sub>8</sub>@Si hereafter, has been characterised by X-ray Photoelectron Spectroscopy (XPS) in order to verify the chemical integrity of the system (see Supplementary Note 4); only Tb 3d<sub>3/2</sub>, N 1s and C 1s signals have been included in a semiquantitative estimation of the element content on surface and are reported in Supplementary Information (see Supplementary Fig. 2 and Supplementary Table 1). Even considering the experimental error of XPS and the presence of adventitious carbon contamination in this *ex situ* prepared sample, we can assert that the procedure of grafting assures the deposition of the intact system.

Additional and more interesting information on the monolayer nature can be obtained by the analysis of the N 1s peak shape. The comparison between the spectra of the monolayer and that of the thick film, reported in Figure 6.3, evidences in fact significant differences. The drop cast film features a unique peak at 398.3 eV arising from the superposition of the contributions from the pyrrole-aza coordinating the metal and from the meso-bridging aza nitrogen atoms, as expected for a metal coordinated phthalocyanine.<sup>24</sup> On the contrary the N 1s spectral region of the monolayer presents, in addition to this signal, a more intense component at higher energy (400.3 eV), clearly indicating that a modification occurs in the chemisorbed molecules.



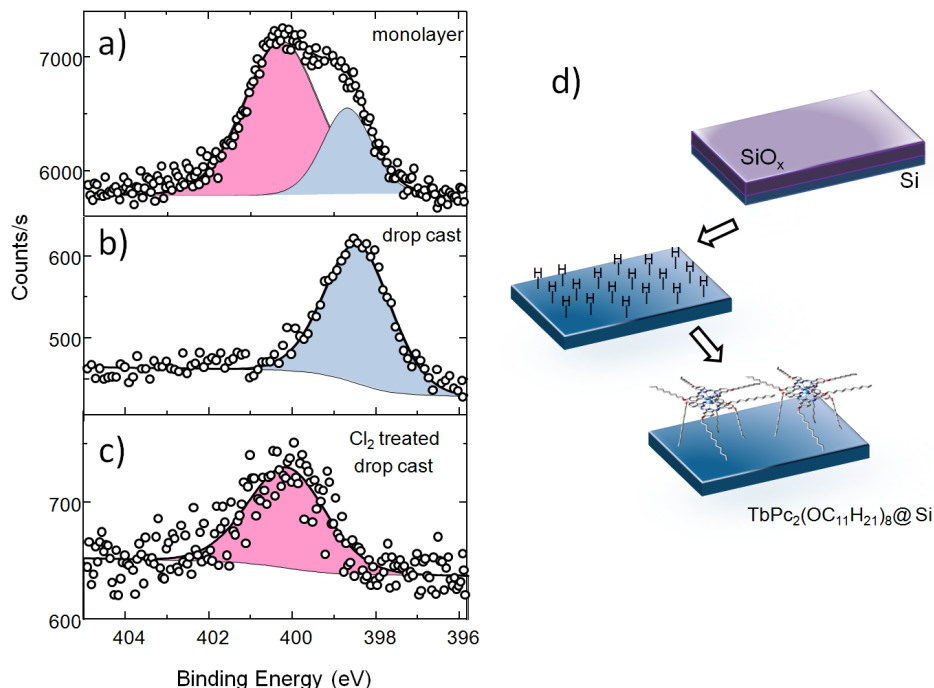


**Figure 6.3** High-resolution N 1s XPS spectra of a) the  $\text{TbPc}_2(\text{OC}_{11}\text{H}_{21})_8@Si$  monolayer, b) the drop cast deposit  $\text{TbPc}_2(\text{OC}_{11}\text{H}_{21})_8$  and c) the drop cast sample treated with chlorine. d) Sketch of the  $\text{TbPc}_2(\text{OC}_{11}\text{H}_{21})_8@Si$  grafting procedure: step 1) etching in 1% hydrofluoric acid of silicon surface; step 2) hydrosilylation at 200°C for 2 h.

Interestingly, we show in Figure 6.3c that a similar shift to higher energy of the N 1s signal can be induced also on a bulk sample of  $\text{TbPc}_2(\text{OC}_{11}\text{H}_{21})_8$  by exposing its solution to chlorine and then preparing a drop cast deposit. The treatment with chlorine, already described in literature for Lutetium(III) bis(phthalocyaninato) exposed to  $\text{Cl}_2$  under high-vacuum condition,<sup>25</sup> induces the formation of the corresponding cationic double-decker species,<sup>26</sup> that is the oxidized complex in which one of the electrons of the bis(phthalocyaninato) ligands shell has been removed. The fact that this is a surface-induced effect is evidenced by experiments where the  $\text{TbPc}_2(\text{OC}_{11}\text{H}_{21})_8$  concentration in the solution grafting was reduced to  $10^{-5}$  M. The XPS analysis (see Supplementary Fig. 6) indicates that the lower surface coverage obtained in these conditions increases the contribution of the higher energy contribution to the N 1s spectrum. On the basis of these evidences, the energy shift can be inferred to result either from stabilization effect of a cationic species formed during the grafting reaction by the silicon surface or from an electron depletion of the

molecular system induced by the interaction with the surface, in analogy to similar effects experimentally observed and discussed for various phthalocyanine monolayers adsorbed on semiconducting oxides<sup>27</sup> but never reported for double-decker complexes.

Density functional theory (DFT) calculations (see Supplementary Note 5) have been performed to clarify the effect of the oxidation of the double-decker systems on the XPS spectra as well as the perturbation caused by the silicon surface on the energy of core electrons in the complex. A non-periodic cluster approach, adopted to model the silicon surface, proved to be well suited in the perspective to obtain information on the core electron energy trend, even if a perfect reproduction of the experimental data is beyond the purposes of this paper. Results shown in Supplementary Fig. 7 evidence that nitrogen *1s* electrons are dispersed around a single energy value in the neutral double-decker species in the gas phase. Similar findings emerge on the cationic species but the mean value is significantly shifted at higher energy (+ 2.4 eV) because of the effect of the positive charge on the core electron distribution. Once the double deckers lie in contact with the silicon surface, the nitrogen *1s* electrons remain dispersed around a single energy value in both neutral and cationic species. A small energy shift (+ 0.1 eV) is observed on the neutral double decker, whereas a significant shift to lower binding energy is observed for the cationic species as a consequence of the ion pair formation between the positively charged molecule and negatively charged surface, where one oxo-termination has been introduced to respect the charge neutrality. This effect, however, decreases significantly by increasing the Si cluster size used to model the surface (Supplementary Fig. 8), and an accurate estimation of the energy difference between neutral and cationic species on surface cannot be achieved. Nevertheless, these theoretical results confirm our assignment of the observed N *1s* shift to electron-depleted TbPc<sub>2</sub> species stabilized by the silicon surface.

#### **6.2.4 Structural Characterization of the TbPc<sub>2</sub>(OC<sub>11</sub>H<sub>21</sub>)<sub>8</sub>@Si Monolayer**

Linear and circular polarization-dependent X-ray absorption experiments have been carried out on the TbPc<sub>2</sub>(OC<sub>11</sub>H<sub>21</sub>)<sub>8</sub>@Si monolayer to evaluate with the highest level of accuracy the structural and magnetic properties of the assembled nanostructure. Actually the element selectivity of this synchrotron-based technique guarantees addressing directly the properties of the anchored molecules by focusing the measurements at the Tb *M*<sub>4,5</sub> absorption edges,

whereas the surface sensitivity is warranted by the adopted detection mode, that is, the Total Electron Yield (TEY) mode.<sup>28</sup> Moreover, the DEIMOS beamline, located at Synchrotron SOLEIL, has been specifically designed to carry such measurements: very high beam stability combined with reduced photon flux guarantee measurements reproducibility without damaging the samples.<sup>29</sup>

At first, X-ray Natural Linear Dichroism (XNLD) has been measured for the  $M_{4,5}$  Tb edges. The sample has been set so that the normal to the surface  $\mathbf{n}$  and the X-ray propagation vector  $\mathbf{k}$  lie in the horizontal plane with  $(\mathbf{n}, \mathbf{k}) = 60^\circ$ . The cross-sections with horizontal linear polarization ( $\sigma_H$ ) and with vertical linear polarization ( $\sigma_V$ ) have been measured (see Fig. 6.4a and Supplementary Fig. 9).

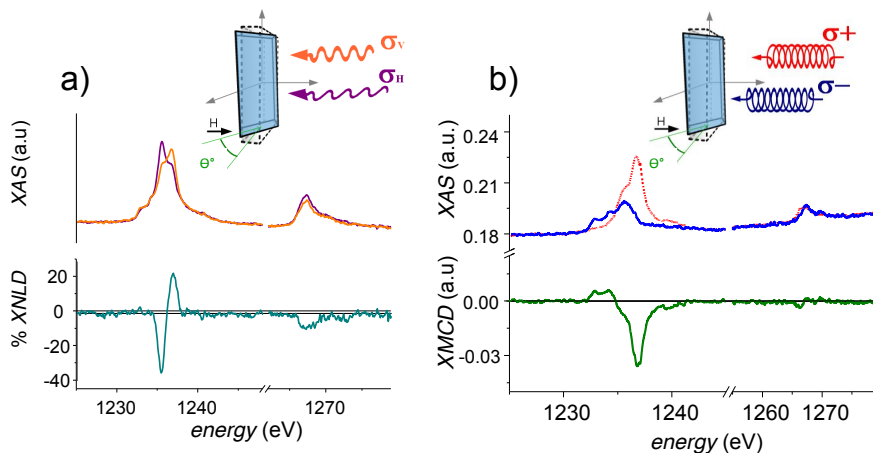


**Figure 6.4** XNLD (a) and XMCD (b) measurements at  $2.2 \pm 0.2$  K, 50 kOe, for  $(\mathbf{n}, \mathbf{k}) = 60^\circ$ . In the inset the geometry of the two experiments are presented: in a XNLD experiment vertical ( $\sigma_V$ ) and horizontally ( $\sigma_H$ ) polarised light are used and the sample is rotated by an angle  $\theta$  between the normal to the surface and the X-ray light propagation direction, an external magnetic field is used only to enhance the TEY detection capabilities; in XMCD experiment light with opposite circular polarization,  $\sigma^+$  and  $\sigma^-$ , is employed in an analogous experimental geometry, external magnetic field and  $\theta$  are varied to extract additional information.

In the ideal case where TbPc<sub>2</sub> molecules adopt a *lying down* configuration, that is, the phthalocyaninato C<sub>4</sub> axis is parallel to the surface normal, the electric field of the vertically polarized light is aligned perpendicular to the symmetry axis of the coordination square antiprism of the Tb<sup>III</sup> ion, whereas the horizontal one forms an angle of 30° with this axis. In the opposite case, where TbPc<sub>2</sub> molecules adopt a *standing* configuration with no order in the plane, the electric field of the vertically polarized light can be now aligned at any angle

with the symmetry axis of the molecules, whereas for the horizontal polarization, the electric field cannot be parallel to the molecular symmetry axis. It is thus straightforward that XNLD, evaluated as  $(\sigma_v - \sigma_H)$ , changes sign for the two configurations and can therefore be employed to extract information on the molecular arrangement in the monolayer.

By the comparison (see Supplementary Note 6) with experimental and theoretical reports from earlier literature,<sup>15a</sup> it can be straightforwardly assessed that the molecules forming the monolayer are preferentially oriented with a *lying down* configuration, with the oriented molecules accounting for about half of the sample. It is interesting to notice that a reversed XNLD signal is measured in a bulk sample obtained by drop casting a solution of **TbPc<sub>2</sub>(OC<sub>11</sub>H<sub>21</sub>)<sub>8</sub>** (see Supplementary Fig. 10). This finding is in line with the common tendency for thick bis(phthalocyaninato) films to aggregate in a standing up configuration,<sup>15a</sup> and the observed difference between the two samples confirms that our monolayer of TbPc<sub>2</sub> does not contain physisorbed aggregates.

### **6.2.5 Magnetic Characterization of the TbPc<sub>2</sub>(OC<sub>11</sub>H<sub>21</sub>)<sub>8</sub>@Si Monolayer**

X-ray absorption experiments carried out at low temperature, under a 50-kOe magnetic field parallel to the X-ray light propagation vector, using circularly polarized light allowed to extract also the X-ray Magnetic Circular Dichroism (XMCD). This is defined as the difference  $(\sigma^- - \sigma^+)$  between the absorption spectra obtained with right ( $\sigma^-$ ) and left ( $\sigma^+$ ) polarized light. The result for the monolayer is reported in Figure 6.4b: detected features and the intensity of the dichroic signal are in line with the expected ones<sup>15</sup> for a saturated Tb<sup>3+</sup> system characterized by total angular momentum  $J = L + S = 6$ .

Figure 6.5a reports the variation of the XMCD contribution at the  $M_5$  edge, normalized to the saturation value, as a function of the applied magnetic field between -50 and +50 kOe at three different temperatures. We stress here that, profiting from the fast TEY detection setup and the stability of the experimental apparatus developed in the DEIMOS beamline,<sup>29</sup> it has been possible to collect the signal as a function of the fast sweeping field, thus providing highly resolved XMCD-detected magnetization curves clearly showing hysteretic behavior already at  $4.3 \pm 0.2$  K.

The opening of the hysteresis strongly depends on the temperature and also on the speed of the scanning field (see Supplementary Fig. 11), confirming the

dynamic character of the magnetic bistability typical of TbPc<sub>2</sub> SMMs. A tiny angular dependence of the hysteresis is also detected (see Fig. 6.5b and Supplementary Fig. 11) in line with the XNLD indications of a partial orientation of the molecular film. Most important is that the comparison with the behavior of the bulk phase (see Fig. 6.2c, and Supplementary Fig. 12 for a direct comparison at the same field scan rate) reveals a significantly larger opening of the hysteresis for the monolayer. To further investigate this aspect, an analogous XMCD characterization has been carried out on the drop cast thick film of TbPc<sub>2</sub>(OC<sub>11</sub>H<sub>21</sub>)<sub>8</sub>, evidencing an opening on the hysteresis cycle significantly weaker than in the monolayer grafted to the Si surface (see Fig. 6.5b), in line with standard magnetometry experiments on the pristine compound.

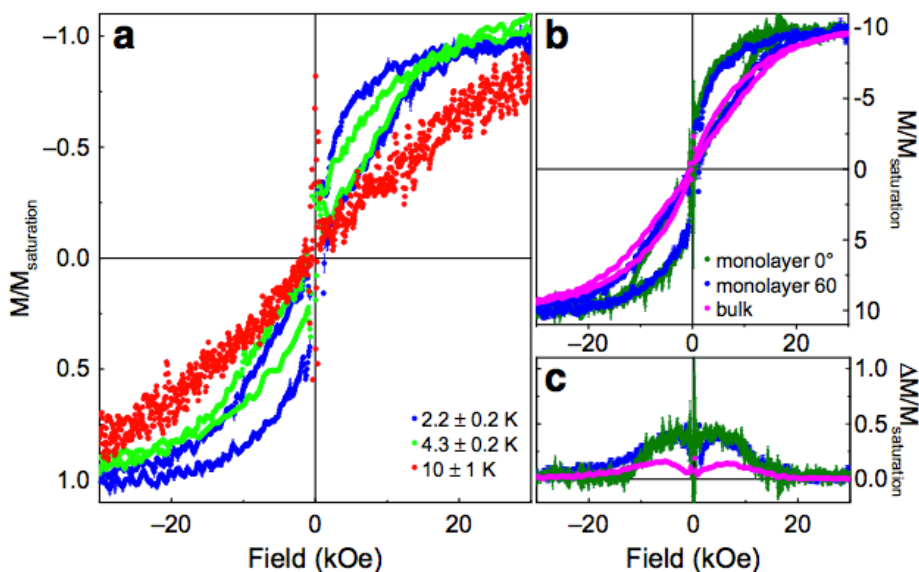


**Figure 6.5** TbPc<sub>2</sub>(OC<sub>11</sub>H<sub>21</sub>)<sub>8</sub>@Si hysteresis. a) XMCD-detected magnetization curves for  $(n,k) = 60^\circ$  as a function of the temperature in the TbPc<sub>2</sub>(OC<sub>11</sub>H<sub>21</sub>)<sub>8</sub>@Si monolayer. (b), (c) Comparison between the behavior of the thick film and the monolayer, the latter being measured for  $(n,k) = 0^\circ$  and  $60^\circ$ . These magnetization curves, measured in the same condition for all the samples ( $2.2 \pm 0.2$  K and  $500$  Oe  $s^{-1}$  scan speed) through the XMCD technique, are reported in b) with their experimental error. In c), the hysteresis opening is estimated as  $\Delta M(H)$  according to the procedure described in the text.

A better estimation of the changes in the hysteretic behavior can be achieved by plotting the difference in the magnetization obtained for increasing and decreasing field:  $\Delta M(H) = |M(H \uparrow) - M(H \downarrow)|$ . The area under these curves (Fig.

6.5c) thus corresponds to the opening of the hysteresis loop, which results to be significantly larger in the monolayer sample than in the thick film. A similar enhancement of the bistable behavior in the monolayer is also observed for hysteresis curves taken at different orientation of the substrate in respect to the magnetic field (Fig. 6.5 and Supplementary Fig. 11 for more data), thus indicating that the observed phenomenon is not due to orientation effects but has to be related to the grafting process.

### **6.3 Conclusions**

The profusion of experiments performed on the TbPc family of SMM has revealed significant changes in the magnetic bistability depending on the nature of the substrate the SMM is deposited onto. The mechanisms of these modifications remains, however, obscure. With metallic substrates, the typical butterfly hysteresis observable well above helium temperature disappears, although pyrene-functionalized TbPc<sub>2</sub> when grafted to single-wall carbon nanotubes exhibits an increase of the remnant magnetization at sub-kelvin temperatures<sup>30</sup> that is the opposite of the trend observed<sup>31</sup> when other SMM are grafted to carbon nanotubes. When ferromagnetic substrates are employed, the TbPc<sub>2</sub> hysteresis is observed at much higher temperatures<sup>16a</sup> but the bistability and coercivity are those of the substrate and cannot be considered an intrinsic property of the single molecule. We notice that an enhancement of the opening of the hysteresis has been observed<sup>26</sup> at 1.5 K in frozen solution by oxidation of the double decker to the cationic [TbPc<sub>2</sub>]<sup>+</sup> species, an effect that seems further enhanced in the monolayer investigated here.

The use of silicon, unprecedented for this type of SMMs, presents several interesting advantages. Our results show that TbPc<sub>2</sub> SMMs can be covalently and robustly anchored to a silicon substrate, with the deposited monolayer standing harsh treatments like sonication in dichloromethane. Si-C covalent bonds in fact guarantee a higher stability respect to  $\pi$ -stacking or S-Au interactions. Moreover, the pronounced magnetic bistability not only is retained at the level of the monolayer but, when quantified as the area enclosed in the hysteresis cycle, it happens to be significantly enhanced by the grafting process to silicon, even if with small remnant magnetization. More important is that this alteration correlates with changes observed in the photoelectron spectra. Although the long alkyl chains in this Tb double-decker SMM could in principle hamper a significant interaction with the substrate, their flexibility, as already observed for functionalized TbPc<sub>2</sub> molecules grafted on gold,<sup>32</sup> induces

a preferential lying down configuration that can allow a stabilization of an oxidized TbPc<sub>2</sub> system by the silicon substrate as indicated by coverage-dependent XPS results. It is well known that the oxidation of the Pc ligands reduces the height of the square-antiprism coordination polyhedron with a sensible enhancement of the effective energy barrier for the reversal of the magnetization and more pronounced hysteretic behavior.<sup>9,10,33</sup> Covalent grafting to the silicon surface appears to have a similar effect on the electron density of the phthalocyanine rings and is therefore not unreasonable that it can equally affect the magnetic anisotropy of the complex, enhancing the magnetic bistability, although not preventing tunnelling in zero field.

In conclusion, our XMCD observation of the enhanced magnetic hysteresis evidences that a careful choice of the substrate and of the grafting strategy can be exploited to tune the electronic properties of these SMMs and optimize their magnetic behavior, in contrast to what has been observed by assembling the pristine TbPc<sub>2</sub> system on solid surfaces by thermal evaporation procedures in UHV.<sup>15a,16,34</sup> The chemical robustness of these covalently grafted monolayers make them suitable for insertion in spintronic devices prepared by solution techniques, which is the emerging trend in this rapidly evolving field.<sup>35</sup>

## 6.4 Acknowledgements

We thank the staff of the DEIMOS beamline including Loic Joly, Bernard Muller and Jean-Paul Kappler for the development of the facilities available at the beamline and the interdepartmental Centre SITEIA.PARMA, University of Parma, for mass spectrometry measurements. Funding from the European Research Council through the Advanced Grant 'MolNanoMas' (2,67,746), EC through from FP7 project 'FINELUMEN' (FP7-PEOPLE-2007-1-1-ITN215399), the Italian MIUR through FIRB projects 'Nano- PlasMag' (RBFR10OAI0) and 'Nanomagneti molecolari su superfici metalliche e magnetiche per applicazioni nella spintronica molecolare' (RBAP117RWN) and the PRIN project 'RECORD' (20097X44S7) as well as the Ente Cassa di Risparmio di Firenze are acknowledged. Instrumental investments on DEIMOS have been provided by IMPMC-UMR7590 through ANR-07-BLANC-0275. A.M. acknowledges CINECA Award N. HP10C9RDDE 2013 for providing high-performance computing resources and support.

## 6.5 Experimental Section

**Supplementary Information** is available online at:

<http://www.nature.com/naturecommunications>, doi: 10.1038/ncomms5582.

### Synthesis of TbPc<sub>2</sub>(OC<sub>11</sub>H<sub>21</sub>)<sub>8</sub> (**1**)

To a stirred solution of 4-( $\omega$ -undecenyloxy)phthalonitrile (**2**) (400 mg, 1.35 mmol, see SI) in 1-hexanol (8 mL) [Tb(acac)]*n*H<sub>2</sub>O (98.6 mg, 0.216 mmol, 0.16 equiv) was added followed by 1,8-Diazabicyclo[5.4.0]undec-7-ene (DBU) (202.0  $\mu$ L, 1.35 mmol, 1 equiv). The reaction was heated to reflux and stirred for 16 h. The dark-green mixture was cooled to room temperature and the solvent removed under reduced pressure. Methanol was added to the residue until a precipitate formed. The green finely dispersed mixture was filtered off and purified by flash chromatography (CHCl<sub>3</sub> as eluant) to give **1** as a green solid (149 mg, 35% yield).

**MALDI-TOF**: calculated for C<sub>152</sub>H<sub>192</sub>N<sub>16</sub>O<sub>8</sub>Tb [M]<sup>+</sup> m/z 2529.439, found m/z = 2529.444.

**UV-Vis**:  $\lambda_{\text{max}}$  (CHCl<sub>3</sub>) 926, 681, 469, 361, 329 nm.

### Magnetic characterization of the bulk system

Quantum Design PPMS Vibrating Sample Magnetometer (VSM) set-up in the continuous measurement mode sweeping the magnetic field at 50 Oe·s<sup>-1</sup> was used to characterize a bulk TbPc<sub>2</sub>(OC<sub>11</sub>H<sub>21</sub>)<sub>8</sub> sample, pressed in a pellet, between - 50 kOe and + 50 kOe. AC magnetic susceptibility up to 10 kHz of this sample was measured with the same Quantum Design PPMS platform in zero and 5 kOe static fields. Quantum Design MPMS SQUID magnetometer was employed to extend the AC susceptibility measurements in the low frequency range (down to 0.1 Hz).

### Monolayer preparation

The TbPc<sub>2</sub>(OC<sub>11</sub>H<sub>21</sub>)<sub>8</sub> solutions in mesitylene were placed in a small, three-necked flask fitted with a nitrogen inlet and a condenser. The solutions were deoxygenated with dry nitrogen for at least 1 h. Subsequently, *p*-doped Si(100) (Boron doped, resistivity 1.5-4  $\Omega$  cm) substrates were treated in a piranha solution for 12 min, rinsed in water for 2 min, and etched in 1.0% hydrofluoric acid for 90 s, then immediately placed in the alkenes solution. The solutions were then refluxed at 200 °C for 2 h, under slow N<sub>2</sub> bubbling to prevent bumping. After cooling to RT, the samples were removed from the flask and cleaned by several rinsing cycles of ultrasonic cleaner.



### **X-ray Photoelectron Spectroscopy measurements**

XPS spectra of the monolayer of  $\text{TbPc}_2(\text{OC}_{11}\text{H}_{21})_8$  were run with a PHI 5600 multitechnique ESCA-Auger spectrometer equipped with a monochromatic Al  $K\alpha$  X-ray source. Analyses were carried out with an analyser pass energy of 23.5 eV and a photoelectron angle of  $45^\circ$  (relative to the sample surface) with an acceptance angle of  $\pm 7^\circ$ . Bulk drop cast and  $\text{Cl}_2$ -treated  $\text{TbPc}_2(\text{OC}_{11}\text{H}_{21})_8$  sample have been measured with a VSW setup equipped with non monochromatic Al  $K\alpha$  source not focalized; in this case the angle between the analyser axis and the X-ray propagation vector from the X-ray source was  $54.44^\circ$  and a pass energy of 44 eV was used. These different conditions were required to properly characterise these samples avoiding the reduction of the oxidised system by the effect of the photo-electrons and secondary electrons. In all spectra, XPS binding energy scale was calibrated by placing the C 1s peak due to hydrocarbon moieties and “adventitious” carbon at 285.0 eV. Data analysis was performed using a mixed Gaussian and Lorentzian line-shapes and background subtraction using a Shirley function. The elemental composition of the samples was evaluated by estimating the integrated area of each component corrected for the corresponding photo-ionization cross-section.<sup>36</sup> The Tb  $3d_{3/2}$  sensitivity factor was empirically verified from terbium(III)acetate hydrate powder (see Supplementary Fig. 13).

### **X-ray Absorption Spectroscopy measurements**

XAS and XMCD spectra at the Tb  $M_{4,5}$  edges were recorded at the DEIMOS beamline,<sup>28</sup> Synchrotron SOLEIL Facility in France on a UHV compatible pumped  $^4\text{He}$  cryo-magnet. Absorption spectra were measured in TEY detection mode to guarantee the optimal detection sensitivity. All the characterizations were performed using a low density of photons in order to avoid radiation damages. XNLD experiments were carried out by recording XAS with linearly polarised light (vertical and horizontal polarization) in a 50 kOe field (to enhance the TEY) placing the normal of sample surface at  $60^\circ$  with respect to the X-ray light propagation vector and extracted as  $(\sigma_V - \sigma_H)$ . Final XNLD spectrum is the result of the averaging of four scans per polarization, for both positive and negative magnetic field in order to avoid contamination from spurious X-ray Magnetic Linear Dichroism (XMLD) signal. XMCD spectra were obtained with a similar averaging procedure<sup>37</sup> from circularly polarised (left and right) absorption spectra measured at the temperature of 2 K and under an applied magnetic field of 50 kOe parallel to the X-ray propagation vector. The same set-up was used to record the XMCD dependence on the magnetic field (hysteresis curves) as a function of sample orientation and temperature, as well

as field sweeping rate. Data have been normalised with respect to the saturation value in order to be able to compare this experiment with traditional magnetometry experiments and evaluate the angular dependence.

### **DFT calculations**

Calculations were performed adopting the Perdew, Burke and Ernzerhof (PBE) formalism for both exchange and correlation functionals.<sup>38</sup> The effective core potential of Hay and Wadt<sup>39</sup> was used for the yttrium and terbium atoms. The standard all-electron 6-31G\*\* basis was used for all remaining atoms.<sup>40</sup> Closed or open shell approach are adopted depending on the charge state of the double-decker system we considered: for a + 1 charged system a closed shell is adopted, whereas for the neutral bis-phthalocyaninato system an open shell is adopted to take into account the electron multiplicity. Si(100) surface was represented by a cluster of 21 silicon atoms H-terminated with one hydroxyl termination. Moving from the gas phase to the surface-absorbed molecules, TbPc<sub>2</sub> was replaced by YPc<sub>2</sub> to avoid convergence complication due to the high multiplicity arising from *f* electrons of the terbium atom (see Supplementary Note 5 for further details). Molecular geometry optimization of stationary points was carried out without symmetry constrains and was based on an analytical gradient minimization approach. All calculations were performed using NWCHEM code<sup>41</sup> on Linux cluster systems.

## 6.6 References

- <sup>1</sup> a) A. Aviram, M. A. Ratner, *Chem. Phys. Lett.* **1974**, 29, 277–283; b) S. V. Aradhya, L. Venkataraman, *Nat. Nanotechnol.* **2013**, 8, 399–410.
- <sup>2</sup> D. Gatteschi, R. Sessoli, J. Villain, *Molecular Nanomagnets* **2006**, Oxford University Press, Oxford.
- <sup>3</sup> a) R. Sessoli, D. Gatteschi, A. Caneschi, M. A. Novak, *Nature* **1993**, 365, 141–143; b) G. Christou, D. Gatteschi, D. Hendrickson, R. Sessoli, *Mater. Res. Bull.* **2000**, 25, 66–71.
- <sup>4</sup> a) L. Thomas, F. Lioni, R. Ballou, D. Gatteschi, R. Sessoli, B. Barbara, *Nature* **1996**, 383, 145–147; b) J. R. Friedman, M. P. Sarachik, J. Tejada, R. Ziolo, *Phys. Rev. Lett.* **1996**, 76, 3830–3833; c) W. Wernsdorfer, R. Sessoli, *Science* **1999**, 284, 133–135; d) S. Takahashi, I. S. Tupitsyn, J. van Tol, C. C. Beedle, D. N. Hendrickson, P. C. E. Stamp, *Nature* **2011**, 476, 76–79.
- <sup>5</sup> a) M. Mannini, F. Pineider, P. Saintavrit, C. Danieli, E. Otero, C. Sciancalepore, A. M. Talarico, M.-A. Arrio, A. Cornia, D. Gatteschi, R. Sessoli, *Nat. Mater.* **2009**, 8, 194–197; b) M. Mannini, F. Pineider, C. Danieli, F. Totti, L. Sorace, P. Saintavrit, M.-A. Arrio, E. Otero, L. Joly, J. C. Cezar, A. Cornia, R. Sessoli, *Nature* **2010**, 468, 417–421.
- <sup>6</sup> J. B. Schlenoff, M. Li, H. Ly, *J. Am. Chem. Soc.* **1995**, 117, 12528–12536.
- <sup>7</sup> D. N. Woodruff, R. E. P. Winpenny, R. A. Layfield, *Chem. Rev.* **2013**, 113, 5110–5148.
- <sup>8</sup> G. G. Condorelli, A. Motta, I. L. Fragalà, F. Giannazzo, V. Raineri, A. Caneschi, D. Gatteschi, *Angew. Chem.Int. Ed.* **2004**, 43, 4081–4084.
- <sup>9</sup> N. Ishikawa, M. Sugita, N. Tanaka, T. Ishikawa, S. Koshihara, Y. Kaizu *Inorg. Chem.* **2004**, 43, 5498–5500.
- <sup>10</sup> N. Ishikawa, M. Sugita, T. Okubo, N. Tanaka, T. Iino, Y. Kaizu, *Inorganic Chemistry* **2003**, 42, 2440–2446.

<sup>11</sup> a) K. Katoh, Y. Yoshida, M. Yamashita, H. Miyasaka, B. K. Breedlove, T. Kajiwara, S. Takaishi, N. Ishikawa, H. Isshiki, Y. Feng Zhang, T. Komeda, M-Yamagishi, J. Takeya, *J. Am. Chem. Soc.* **2009**, *131*, 9967–9976; b) T. Komeda, H. Isshiki, J. Liu, Y.-F. Zhang, N. Lorente, K. Katoh, B. K. Breedlove, M. Yamashita, *Nat. Commun.* **2011**, *2*, article number: 217; c) L. Vitali, S. Fabris, A. Mosca Conte, S. Brink, M. Ruben, S. Baroni, K. Kern, *Nano Lett.* **2008**, *8*, 3364–3368; d) J. Schwöbel, Y. Fu, J. Brede, A. Dilullo, G. Hoffmann, S. Klyatskaya, M. Ruben, R. Wiesendanger, *Nat. Commun.* **2012**, article number: 953; e) Y.-S. Fu, J. Schwöbel, S.-W. Hla, A. Dilullo, G. Hoffmann, S. Klyatskaya, M. Ruben, R. Wiesendanger, *Nano Lett.* **2012**, *12*, 3931–3935; f) M. Gonidec, R. Biagi, V. Corradini, F. Moro, V. De Renzi, U. del Pennino, D. Summa, L. Muccioli, C. Zannoni, D. B. Amabilino, J. Veciana *J. Am. Chem. Soc.* **2011**, *133*, 6603–6612.

<sup>12</sup> R. Vincent, S. Klyatskaya, M. Ruben, W. Wernsdorfer, F. Balestro, *Nature* **2012**, *488*, 357–360.

<sup>13</sup> M. Urdampilleta, S. Klyatskaya, J.-P. Cleuziou, M. Ruben, W. Wernsdorfer, *Nat. Mater.* **2011**, *102*, 502–506.

<sup>14</sup> A. Hofmann, Z. Salman, M. Mannini, A. Amato, L. Malavolti, E. Morenzoni, T. Prokscha, R. Sessoli, A. Suter, *ACS Nano* **2012**, *6*, 8390–8396; b) L. Malavolti, M. Mannini, P. Car, G. Campo, F. Pineider, R. Sessoli, *J. Mater. Chem. C* **2013**, *1*, 2935–2942.

<sup>15</sup> a) L. Margheriti, D. Chiappe, M. Mannini, P.-E. Car, P. Saintavit, M.-A. Arrio, F. B. de Mongeot, J. C. Cezar, F. M. Piras, A. Magnani, E. Otero, A. Caneschi, R. Sessoli, *Adv. Mater.* **2010**, *22*, 5488–5493; b) R. Biagi, J. Fernandez-Rodriguez, M. Gonidec, A. Mirone, V. Corradini, F. Moro, V. De Renzi, U. del Pennino, J. C. Cezar, D. B. Amabilino, J. Veciana, *Phys. Rev. B.* **2010**, *82*, 224406.

<sup>16</sup> a) A. Lodi Rizzini, C. Krull, T. Balashov, J. J. Kavich, A. Mugarza, P. S. Miedema, P. K. Thakur, V. Sessi, S. Klyatskaya, M. Ruben, S. Stepanow, P. Gambardella, *Phys. Rev. Lett.* **2011**, *107*, 177205; b) A. Lodi Rizzini, C. Krull, T. Balashov, A. Mugarza, C. Nistor, F. Yakhov, V. Sessi, S. Klyatskaya, M. Ruben, S. Stepanow, P. Gambardella, *Nano Lett.* **2012**, *12*, 5703–5707.

- <sup>17</sup> M. R. Linford, C. E. D. Chidsey, *J. Am. Chem. Soc.* **1993**, *115*, 12631–12632.
- <sup>18</sup> A. De Cian, M. Moussavi, J. Fischer, R. Weiss, *Inorg. Chem.* **1985**, *24*, 3162–3167.
- <sup>19</sup> B. Görlach, C. Hellriegel, S. Steinbrecher, H. Yüksel, K. Albert, E. Plies, M. Hanack, *J. Mater. Chem.* **2001**, *11*, 3317–3325.
- <sup>20</sup> J. Jiang, D. K. P. Ng, *Acc. Chem. Res.* **2009**, *42*, 79–88.
- <sup>21</sup> C. R. Ganivet, B. Ballesteros, G. de la Torre, J. M. Clemente-Juan, E. Coronado, T. Torres, *Chem. Eur. J.* **2013**, *19*, 1457–1465.
- <sup>22</sup> N. Ishikawa, *Polyhedron*. **2007**, *26*, 2147–2153.
- <sup>23</sup> J. M. Buriak, *Chem. Rev.* **2002**, *102*, 1271–1308.
- <sup>24</sup> L. Lozzi, L. Ottaviano, S. Santucci, *Surf. Sci.* **2001**, *470*, 265–274.
- <sup>25</sup> J. Bufler, C. Ziegler, W. Göpel, *Synth. Met.* **1993**, *61*, 127–131.
- <sup>26</sup> M. Gonidec, E. S. Davies, J. McMaster, D. B. Amabilino, J. Veciana, *J. Am. Chem. Soc.* **2010**, *132*, 1756–1757.
- <sup>27</sup> a) P. Palmgren, K. Nilson, S. Yu, F. Hennies, T. Angot, C. I. Nlebedim, J.-M. Layet, G. Le Lay, M. Göthelid, *J. Phys. Chem. C* **2008**, *112*, 5972–5977; b) S. Yu, S. Ahmadi, C. Sun, P. Tabib Zadeh Adibi, W. Chow, A. Pietzsch, M. Göthelid, *J. Chem. Phys.* **2012**, *136*, 154703–154709; c) G. Mattioli, F. Filippone, P. Giannozzi, R. Caminiti, A. A. Bonapasta, *Chem. Mater.* **2009**, *21*, 4555–4567.
- <sup>28</sup> B. Henke, J. Liesegang, S. Smith, *Phys. Rev. B* **1979**, *19*, 3004–3021.
- <sup>29</sup> P. Ohresser, E. Otero, F. Choueikani, K. Chen, S. Stanescu, F. Deschamps, T. Moreno, F. Polack, B. Lagarde, J.-P. Daguette, F. Marteau, F. Scheurer, L. Joly, J.-P. Kappler, B. Muller, O. Bunau, P. Sainctavit, *Rev. Sci. Instrum.* **2014**, *85*, 013106.

- <sup>30</sup> S. Kyatskaya, J. R. G. Mascarós, L. Bogani, F. Hennrich, M. Kappes, W. Wernsdorfer, M. Ruben, *J. Am. Chem. Soc.* **2009**, *131*, 15143–15151.
- <sup>31</sup> A. Giusti, G. Charron, S. Mazerat, J.-D. Compain, P. Mialane, A. Dolbecq, E. Rivière, W. Wernsdorfer, R. Ngo Biboum, B. Keita, L. Nadjo, A. Filoramo, J.-P. Bourgoin, Talal Mallah, *Angew. Chem. Int. Ed.* **2009**, *48*, 4949–4952.
- <sup>32</sup> U. Glebe, T. Weidner, J. E. Baio, D. Schach, C. Bruhn, A. Buchholz, W. Plass, S. Walleck, T. Glaser, U. Siemeling, *Chempluschem* **2012**, *77*, 889–897.
- <sup>33</sup> S. Takamatsu, T. Ishikawa, S. Koshihara, N. Ishikawa, *Inorg. Chem.* **2007**, *46*, 7250–7252.
- <sup>34</sup> a) D. Klar, S. Klyatskaya, A. Candini, B. Krumme, K. Kummer, P. Ohresser, V. Corradini, V. de Renzi, R. Biagi, L. Joly, J.-P. Kappler, U. del Pennino, M. Affronte, H. Wende, M. Ruben, *Beilstein. J. Nanotechnol.* **2013**, *4*, 320–324; b) L. Malavolti, L. Poggini, L. Margheriti, D. Chiappe, P. Graziosi, B. Cortigiani, V. Lanzilotto, F. Buatier de Mongeot, P. Ohresser, E. Otero, F. Choueikani, P. Saintavit, I. Bergenti, V. A. Dediu, M. Mannini, R. Sessoli, *Chem. Commun.* **2013**, *49*, 11506–11508.
- <sup>35</sup> S. Tatay, C. Barraud, M. Galbiati, P. Seneor, R. Mattana, K. Bouzehouane, C. Deranlot, E. Jacquet, A. Forment-Aliaga, P. Jegou, A. Fert, F. Petroff, *ACS Nano* **2012**, *6*, 8753–8757.
- <sup>36</sup> C. D. Wagner, L. E. Davis, M. V. Zeller, J. A. Taylor, R. H. Raymond, L. H. Gale, *Surf. Int. Anal.* **1981**, *3*, 211–225.
- <sup>37</sup> R. Sessoli, M. Mannini, F. Pineider, A. Cornia, P. Saintavit, *Magnetism and Synchrotron Radiation: New Trends* **2010**, *133*, 279–311.
- <sup>38</sup> J. P. Perdew, K. Burke, M. Ernzerhof, *Phys. Rev. Lett.* **1996**, *77*, 3865–3868.
- <sup>39</sup> P. J. Hay, W. R. Wadt, *J. Chem. Phys.* **1985**, *82*, 299–310.
- <sup>40</sup> V. A. Rassolov, J. A. Pople, M. A. Ratner, T. L. Windus, *J. Chem. Phys.* **1998**, *109*, 1223–1229.

<sup>41</sup> M. Valiev, E. J. Bylaska, N. Govind, K. Kowalski, T. P. Straatsma, H. J. J. Van Dam, D. Wang, J. Nieplocha, E. Apra, T.L. Windus, W.A. de Jong, *Comput. Phys. Commun.* **12010**, 18, 1477–1489.

# Chapter 7

## Oriented Grafting of SMMs on Silicon Surface



## 7.1 Introduction

Magnetic anisotropy is a key ingredient for SMM behavior. Hence, controlling the orientation of the easy magnetization axes in the monolayer is essential to optimize the performance of SMM-based devices.<sup>1</sup> Investigation of SMMs orientation on surfaces needs sophisticated characterization tools, such as X-ray absorption based techniques, that became easy to perform with the development of easy to perform with the development of synchrotron-light source. In particular X-ray Natural Linear Dichroism (XNLD) has been successfully employed to extract information on the molecular arrangement of assembled LnPc<sub>2</sub> on surfaces.<sup>2</sup>

In this Chapter we present the design and synthesis of heteroleptic TbPc<sub>2</sub> for oriented grafting on silicon surface: the molecules orientation on the surface and the resulting magnetic properties of the monolayer will be investigated. Before proceeding with the design and the synthesis of the target molecule, a brief overview on the LnPc<sub>2</sub> synthetic issues is needed.

### 7.1.1 TbPc<sub>2</sub> Synthetic Remarks

The growing interest on realization of SMMs-based devices led to focus the attention to the synthesis of new TbPc<sub>2</sub> bearing different functionalities for grafting on different surfaces. However a quick development is hampered by the harsh reaction conditions required for double-decker formation and the difficulties in the purification step. Thus development of new feasible chemical approaches and reactions are highly attractive.

The synthesis of LnPc<sub>2</sub> complex has been known since the mid-1960s,<sup>3</sup> even though great attention focused starting from the early 1990s, due to their potential applications as components of electrochemical and optical sensors,<sup>4</sup> field effect transistors,<sup>5</sup> liquid crystals,<sup>6</sup> and lately single molecule magnets.<sup>7</sup>

There are different synthetic pathways to prepare LnPc<sub>2</sub>, depending on the type of the complex to synthesize. Indeed it's possible to distinguish two different types of sandwich complexes depending on the relative structures of the two phthalocyanines: if the two Pcs are identical, then the complex is named homoleptic (LnPc<sub>2</sub>), while when the two Pcs are different it's a heteroleptic LnPc'Pc" (Figure 7.1).

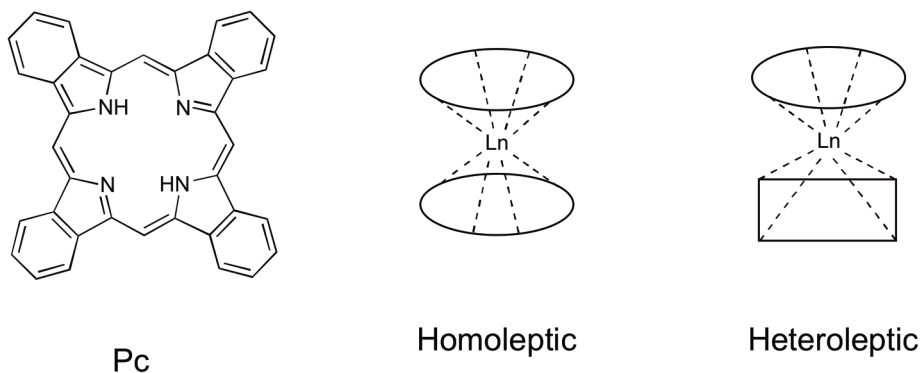


**Figure 7.1** Schematic structures of homoleptic  $\text{LnPc}_2$  and heteroleptic  $\text{LnPc}'\text{Pc}''$  sandwich complexes with Pc ligands.

Homoleptic  $\text{LnPc}_2$  are usually prepared by the classical De Cian synthesis, a cyclic tetramerization of a phthalonitrile in presence of rare earth salts and an organic base such as 1,8-diazabicyclo[5.4.0]undec-7-ene (DBU).<sup>8</sup>

Regarding the heteroleptic  $\text{LnPc}_2$ , there are three main synthetic routes for double-deckers with two different phthalocyaninato ligands. The first method involves a mixed cyclization of the two corresponding phthalonitrile precursors in the presence of a metal salt. Obviously, this method is not practically useful because of the difficulties in separating the statistical mixtures of differently substituted complexes. The second possible pathway is the treatment of a rare earth salt with the two  $\text{Pc}$ s  $\text{Pc}'$  and  $\text{Pc}''$  preformed. As expected, the reaction also produces a substantial amount of the homoleptic complexes  $\text{LnPc}'_2$  and  $\text{LnPc}''_2$  as the side products. The third and most convenient method involves the formation of an intermediate mononuclear lanthanide (III)  $\text{Pc}$  complex, starting from the free-base  $\text{Pc}$ , followed by cyclic tetramerization of the phthalonitrile around the lanthanide ion center of the preformed monophthalocyaninate. By using this method, the purification of the desired heteroleptic complexes can be greatly simplified. Purification remains though a major drawback in  $\text{LnPc}_2$  synthesis. Two main factors are responsible for difficulties in the purification step:

- poor solubility in the common organic solvents;
- strong tendency to aggregate in solution to form  $\pi$ -stacked species, due to the long  $\pi$ -electron conjugation system.

The  $\text{LnPc}_2$  molecules are generally more soluble than the corresponding  $\text{Pc}$ s, but the design and purification of functionalized  $\text{LnPc}_2$ , especially for the

asymmetric ones, is still an open challenge for the synthetic chemists. Another problematic issue in the LnPc<sub>2</sub> synthesis is related to the characterization. In fact NMR spectroscopy, the most widely spread technique in organic chemistry, is in this case useless: strong paramagnetic shifts of the signals are observed,<sup>9</sup> caused by the magnetic dipolar term, which is determined by the anisotropy of the magnetic susceptibility of the lanthanide ion. The shifts hamper a proper spectral assignment of the protons. The most employed analytical tool for this class of compounds is definitely mass spectrometry, mainly MALDI. UV-Vis spectroscopy is also a helpful technique to characterize LnPc<sub>2</sub>. The UV profiles show common features, due to the presence of typical electronic transitions (Figure 7.2):<sup>10</sup> they exhibit an intense Q-band at 650-700 nm, two broad adsorption bands characteristic of a radical Pc ligand at 450-500 and 900-950 nm and a Soret band with maxima around 300 nm. The weak shoulder attached to the Q-band (around 600 nm) has been reported to be due to the weak  $\pi$ - $\pi$  interactions occurring between the two Pc ligands.<sup>11</sup>

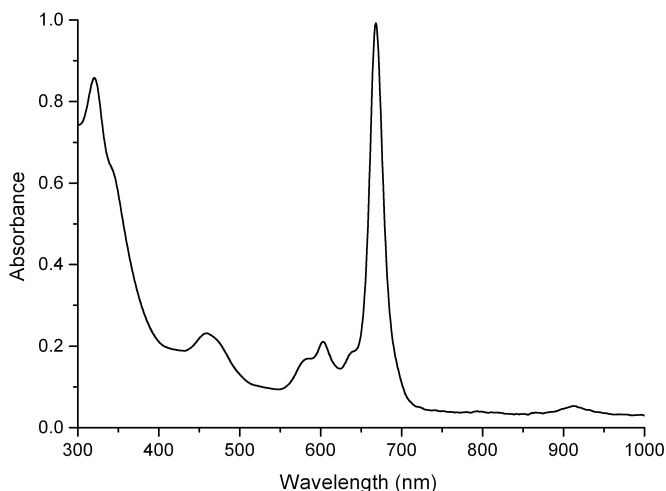


**Figure 7.2** UV-Vis absorption spectrum for unfunctionalized homoleptic TbPc<sub>2</sub> in chloroform.

## 7.2 Results and Discussion

In the previous Chapter we showed that, subsequently the covalent grafting on silicon surface, the molecules of the homoleptic TbPc<sub>2</sub>(OC<sub>11</sub>H<sub>21</sub>)<sub>8</sub> forming the monolayer were preferentially oriented with a lying down orientation, with the

oriented molecules accounting for about half of the sample. Although a preferential orientation was found for homoleptic  $\text{TbPc}_2(\text{OC}_{11}\text{H}_{21})_8$ , the presence of anchoring groups on both Pcs probably prevented the assembling of the molecules in a single orientation during the grafting process. We also evidenced that the lying down orientation, promoting an electronic depletion on  $\text{TbPc}_2$  molecules, was partially responsible for the magnetic bistability enhancement.<sup>12</sup> Thus, our interest is to address the spontaneous organization of  $\text{TbPc}_2$  molecules on silicon surface towards a preferable induced lying down orientation. In order to do that, we designed a  $\text{TbPc}_2$  selectively functionalized with the anchoring groups on one Pc, namely a heteroleptic  $\text{TbPc}_2$  (Figure 7.3).

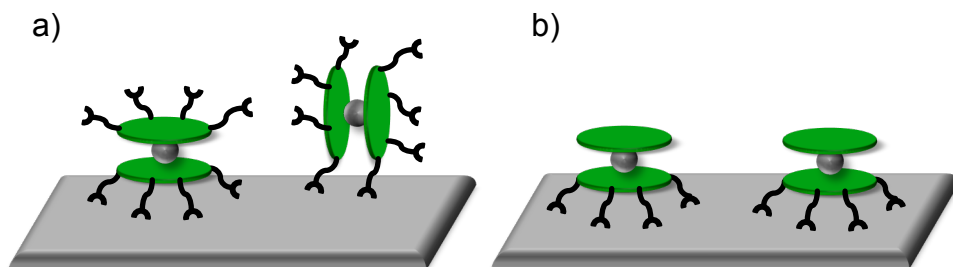


**Figure 7.3** a) Schematic molecules orientation obtained for homoleptic  $\text{TbPc}_2(\text{OC}_{11}\text{H}_{21})_8$ , b) predicted orientation for heteroleptic functionalized  $\text{TbPc}_2$ .

Unlike what happened in the homoleptic case, the presence of terminal double bonds functionalized alkyl chains on only one Pc would promote the lying down orientation in the grafting process.

### 7.2.1 Synthesis of $\text{TbPc}_2$ for Oriented Grafting on Silicon

The first heteroleptic  $\text{TbPc}_2$  we designed is reported in Figure 7.4: it was formed by a "naked" Pc and a tetrafunctionalized Pc with terminal double bonds for the anchoring on silicon surface via hydrosilylation reaction.

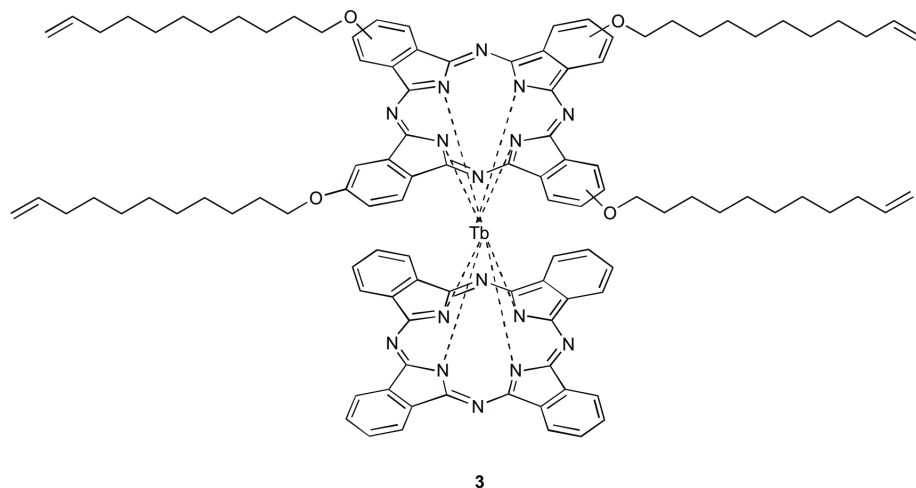
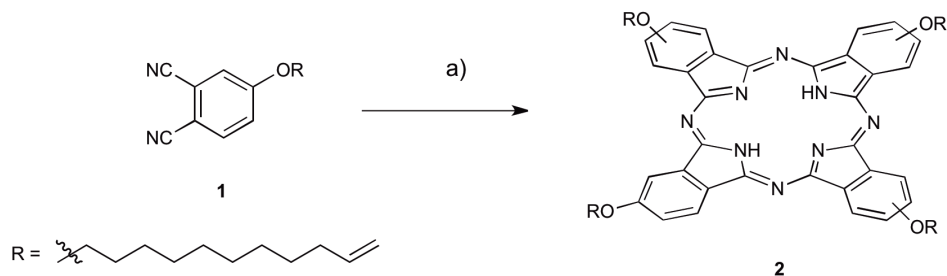


**Figure 7.4** Molecular structure of the first heteroleptic TbPc<sub>2</sub> designed.

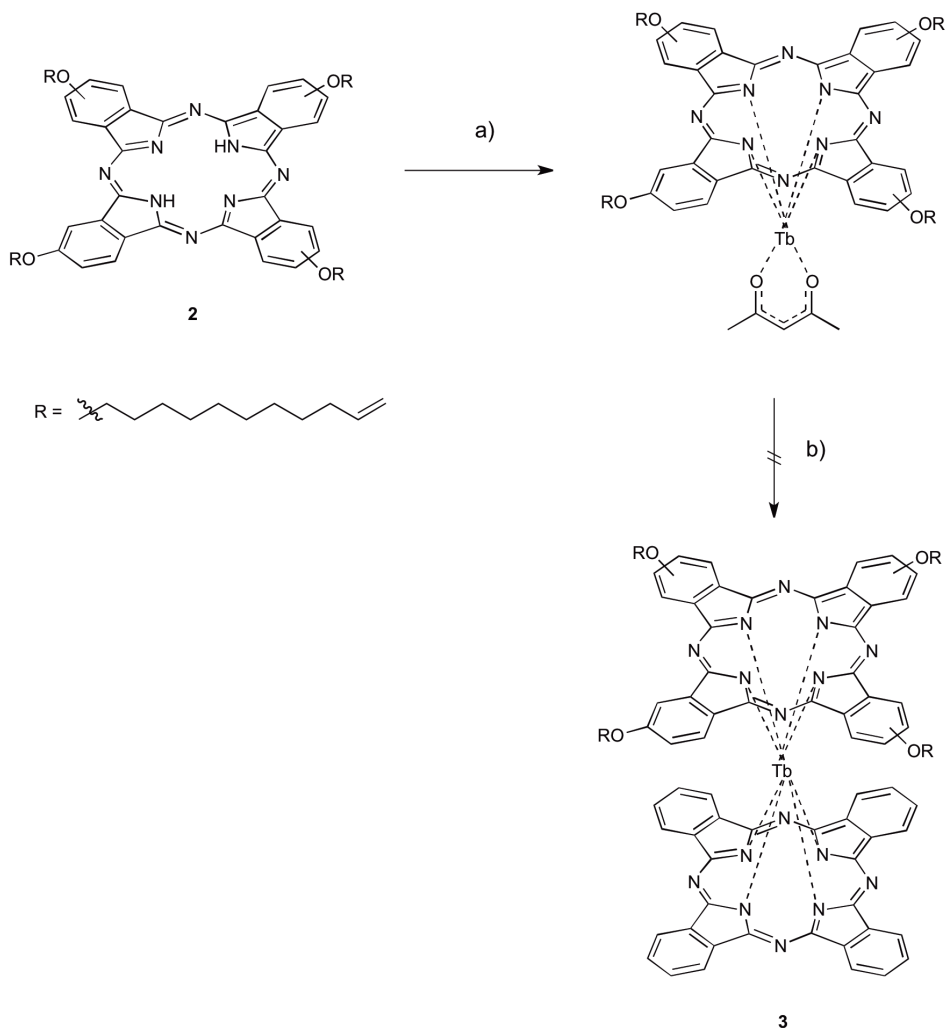
For the synthesis of **3** we decided to employ the third method presented in the previous paragraph, involving the formation of the intermediate mononuclear half sandwich complex on the functionalized Pc, followed by cyclic tetramerization of the phthalonitrile to form the second naked Pc. Thus the synthesis of **1** required the preparation of the tetrakisalkenyloxy substituted phthalocyanine **2**, that was obtained by reacting 4-( $\omega$ -undecenyloxy)-phthalonitrile **1** with DBU in 1-pentanol at 140°C (Scheme 7.1) from a modified reported procedure.<sup>13</sup>



**Scheme 7.1** Synthesis of **2**: a) DBU, 1-pentanol, 140°C, 12 h, 58%.

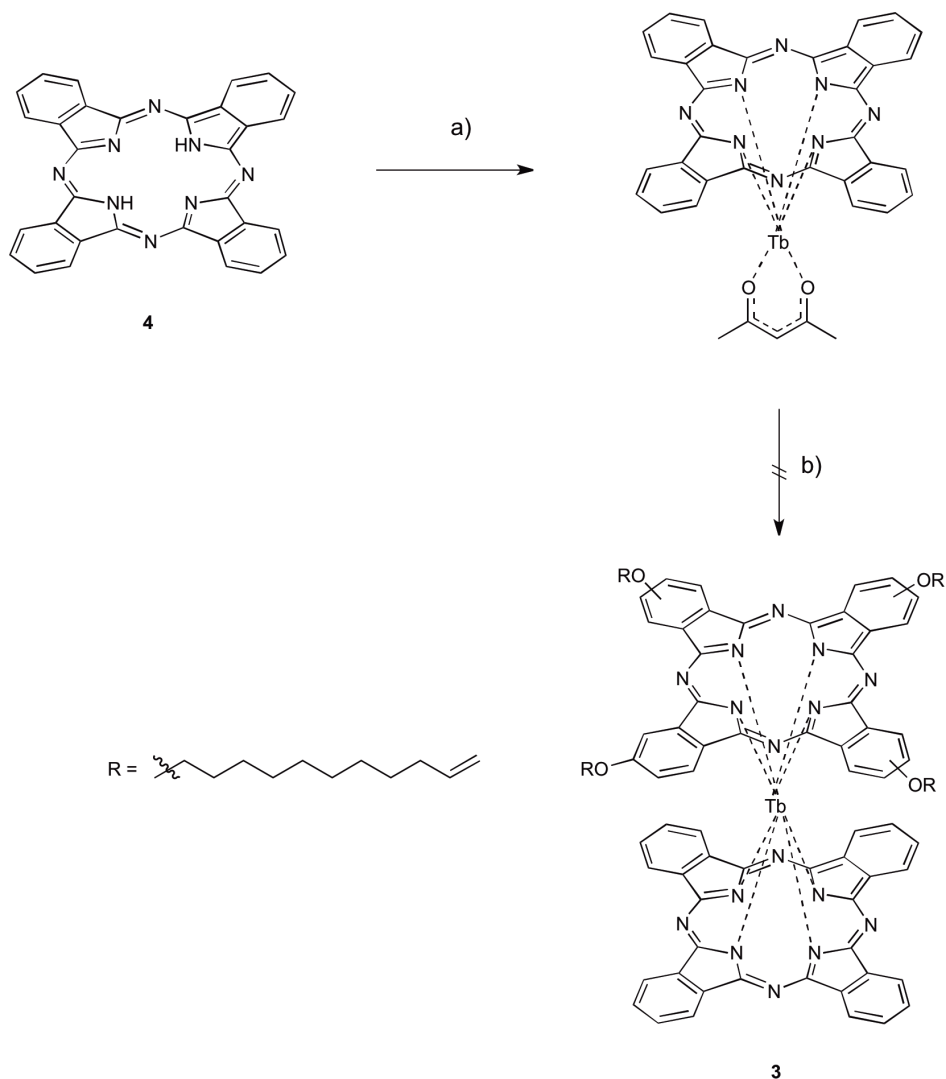
The target Pc **2** was obtained as a mixture of constitutional isomers after chromatographic purification in 58% yield. The identity of the compound was confirmed by MALDI-TOF and <sup>1</sup>H NMR. Phthalocyanine **2** was then reacted with terbium acetylacetonate in stoichiometric ratio and DBU, in 1-chloronaphthalene at 170°C to form the half sandwich complex (Scheme 7.2).

The formation of the half sandwich complex was monitored by UV/Vis spectroscopy, which showed a decrease in the intensity of the two distinctive bands metal-free Pc derivatives and the growth of a new band in-between them.<sup>14</sup> After the removal of the solvent, the half sandwich was reacted, without any further purification, with phthalonitrile in *o*-DCB/1-pentanol at 160°C in presence of DBU as a basic catalyst.



**Scheme 7.2** Synthesis of **3**: a)  $[Tb(acac)]_3 \cdot nH_2O$ , DBU, 1-chloronaphthalene, 170°C, 1.5 h; b) phthalonitrile, DBU, *o*-DCB/1-pentanol, 160°C, 12 h.

Unfortunately we did not observe the formation of the target molecule **3**. We then decided to test the complementary synthetic pathway (Scheme 7.3), starting from the unsubstituted Pc **4** to form the half sandwich complex and promoting the cyclic tetramerization of 4-( $\omega$ -undecenyloxy)phthalonitrile **1** on it.



**Scheme 7.3** Alternative synthetic pathway for **3**: a)  $[Tb(acac)]nH_2O$ , DBU, 1-chloronaphthalene, 170°C, 1.5 h; b) **1**, DBU, *o*-DCB/1-pentanol, 160°C, 12 h.





**PcLi<sub>2</sub> 4** was then reacted with terbium acetylacetonate to form the half sandwich complex in 1-chloronaphthalene at 170°C. The crude was cooled down, functionalized **PcLi<sub>2</sub> 2** was added and the mixture was heated up to 210°C. For the first time we were able observe the formation of the target complex **3**, even though as inseparable mixture with several byproducts. We also tried again to invert the orders of the reagents, forming the half sandwich complex on functionalized **PcLi<sub>2</sub> 2** and then adding the **PcLi<sub>2</sub> 4**, but we didn't observe any improvements in formation of **3**.

Simultaneously we were also investigating a parallel route involving difunctionalized phthalonitriles: the idea was to promote the formation of a single product instead of a mixture of isomers. In fact, as already mentioned, the use of monofunctionalized phthalonitriles always leads to the formation of a mixture of constitutional isomers of Pc, and consequently TbPc<sub>2</sub>. Instead, by employing difunctionalized phthalonitriles a single compound is obtained, furthermore with a higher degree a simmetry (Figure 7.5).

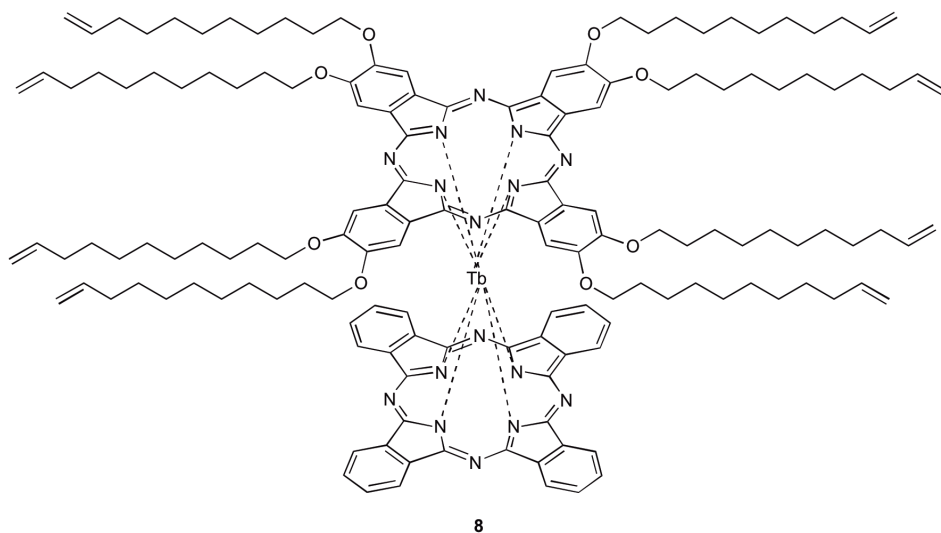
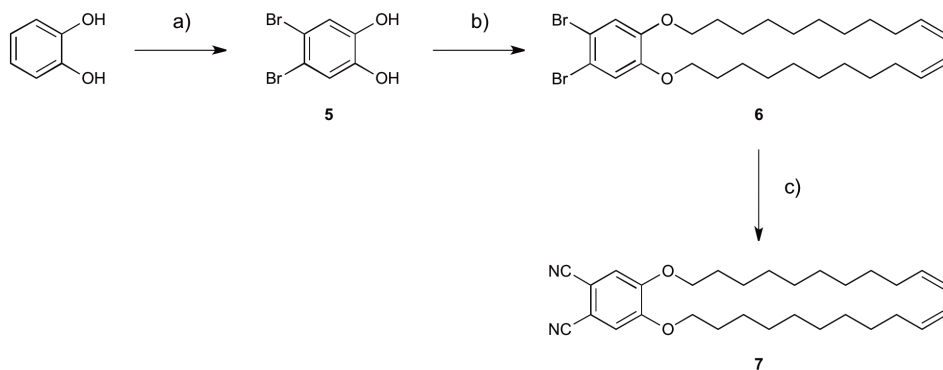


**Figure 7.5** Heteroleptic TbPc<sub>2</sub> **8** designed starting from a difunctionalized phthalonitrile derivative.

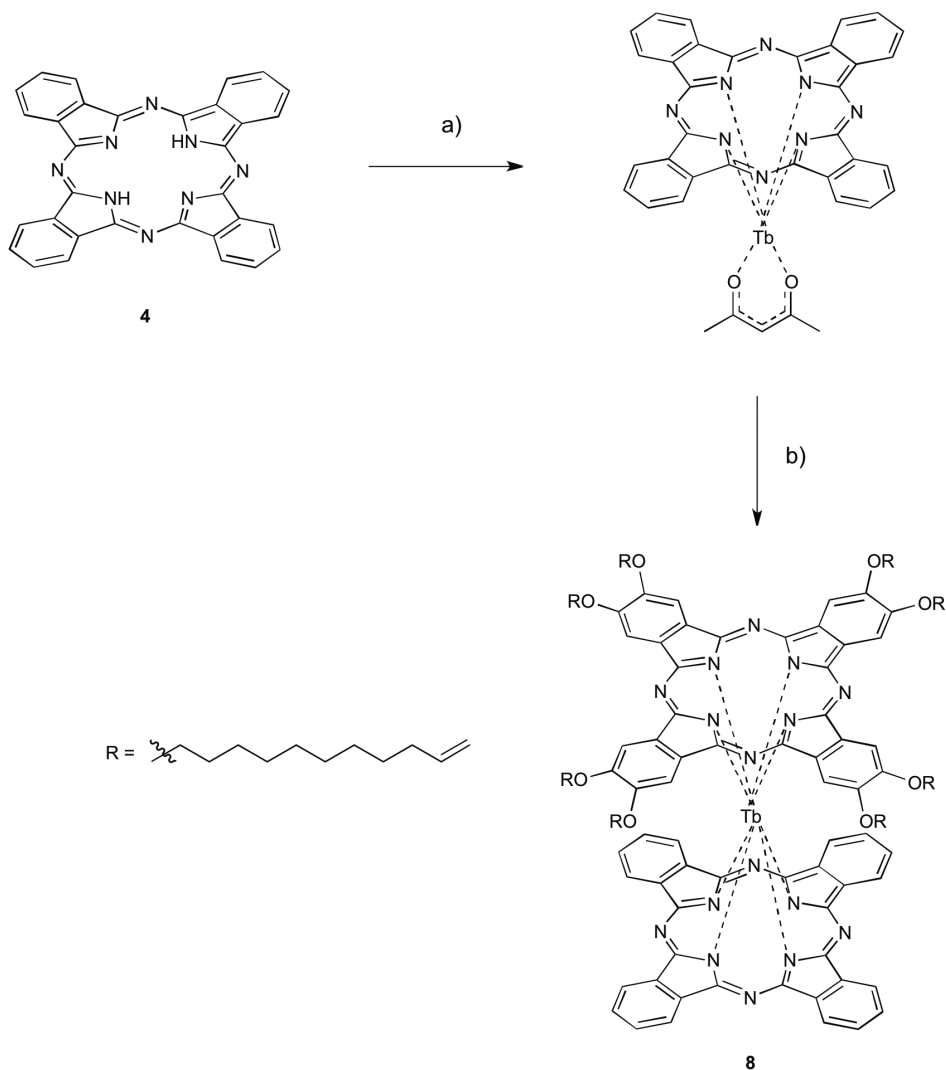
For the synthesis of **8** we required the corresponding difunctionalized phthalonitrile **7**, that was prepared in three synthetic steps with overall yield of 55%, starting from commercially available catechol (Scheme 7.5).



**Scheme 7.5** Synthesis of 7: a)  $Br_2$ ,  $CHCl_3$ , RT, 12 h, 83%; b) 11-bromo-1-undecene,  $K_2CO_3$ , EtOH, reflux, 6 h, 80%; c)  $Zn(CN)_2$ ,  $Pd(PPh_3)_4$ , DMF,  $120^\circ C$ , 4 h, 83%.

Dibromocatechol, synthesized following a reported procedure,<sup>16</sup> was reacted with 11-bromo-1-undecene in refluxing ethanol in presence of potassium carbonate to obtain compound 6 in 80% yield. The corresponding phthalonitrile 7 was prepared by a tandem zinc-palladium catalyzed cyanation of 6.<sup>17</sup> Compound 6 was reacted with zinc cyanide in DMF at  $120^\circ C$ , in presence of palladium tetrakis as catalyst. Target 3,4-bis( $\omega$ -undecenyloxy)phthalonitrile 7 was obtained in 83% yield. Compared to the classical Rosenmund-von Braun reaction, that requires temperature of around  $150^\circ C$  and a great excess of cyanide, this method allows preparation of target phthalonitriles in higher yield at lower temperatures, and with only almost stoichiometric amount of zinc cyanide. Furthermore the formation of copper phthalocyanine as undesired byproduct is prevented.

At this point we performed the half sandwich complex formation on the unsubstituted Pc 4, followed by cyclic tetramerization of 7.



**Scheme 7.6** Synthesis of **8**: a)  $[Tb(acac)]_3 \cdot nH_2O$ , DBU, *o*-dichlorobenzene, 170°C, 1.5 h; b) **7**, *o*-dichlorobenzene / 1-pentanol, 170°C, 12h, 11% (over two steps).

We obtained the desired neutral  $TbPc_2$  **8**, in mixture with its corresponding reduced protonated complex  $[TbPc_2]H$  and the octafunctionalized Pc formed from **7**. 2,3-Dichloro-5,6-dicyano-1,4-benzoquinone (DDQ) was added to the crude to fully oxidize the reduced  $[TbPc_2]H$  complex into the free-radical neutral form **8**: however intermolecular stacking of **8** with side products made the purification very complicated. Nevertheless purification of the crude with

several chromatographic columns afforded target molecule **5** in low yield (11%), not enough to synthesize sufficient material for magnetic measurements.

In order to reduce intermolecular interactions, and consequently to simplify the purification step, we decreased the length of alkyl chains, synthesizing the corresponding heteroleptic TbPc<sub>2</sub> bearing eight C7 alkyl chains (Figure 7.6).

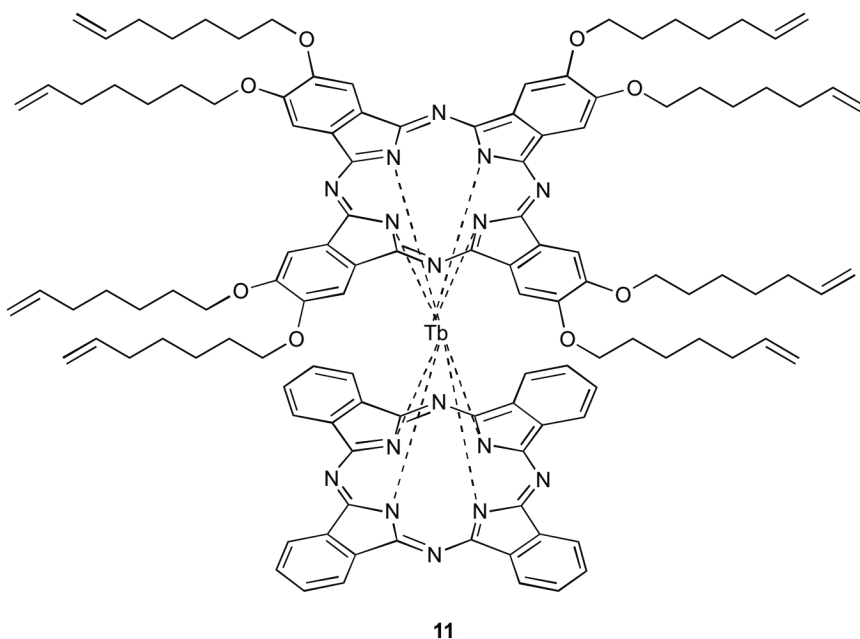
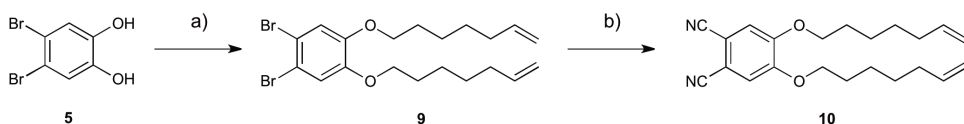


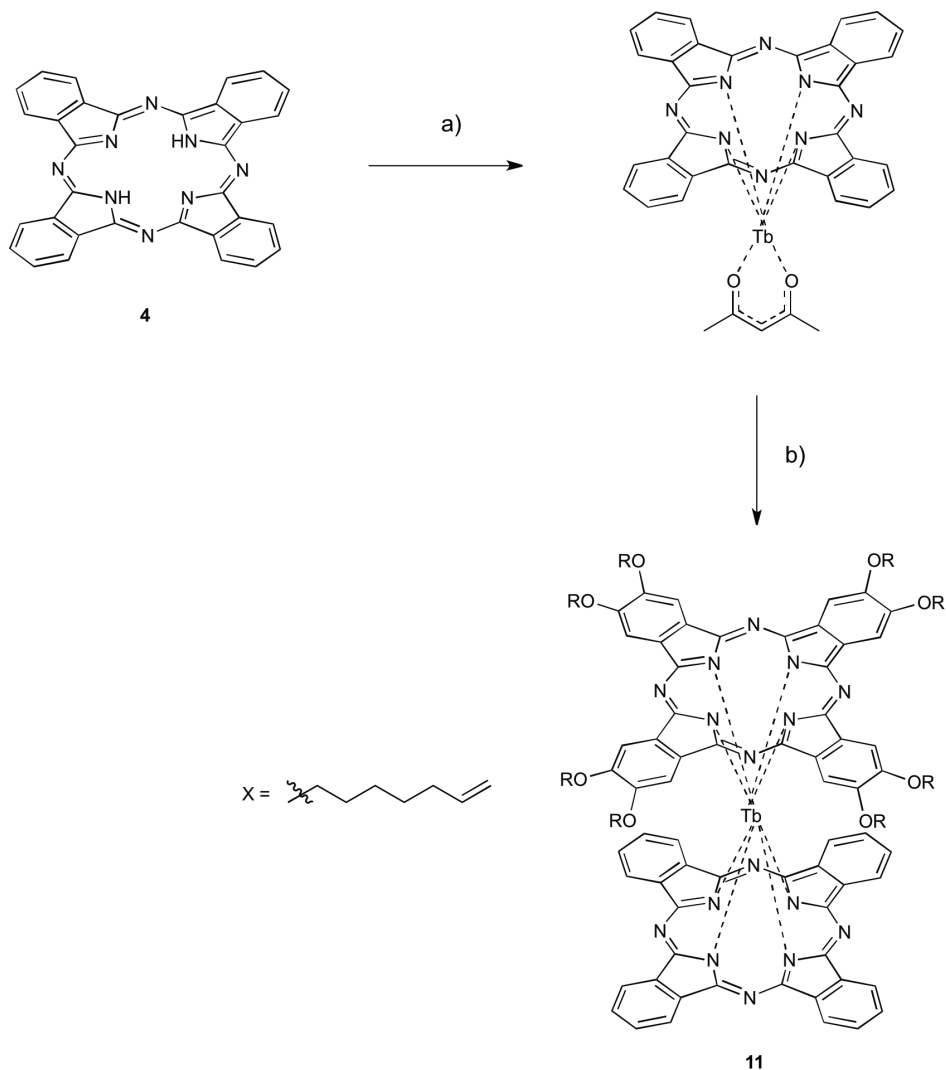
**Figure 7.6** Heteroleptic TbPc<sub>2</sub> **11** with C7 alkyl chains.

Following an analogous synthetic pathway to the previous one, we prepared 3,4-di( $\omega$ -heptenyloxy)phthalonitrile **10** in two steps starting from dibromocatechol with 66% overall yield (Scheme 7.7). Dibromocatechol was reacted with 7-bromo-1-heptene in refluxing ethanol in presence of potassium carbonate to obtain compound **9** in 88% yield.



**Scheme 7.7** Synthesis of **10**: a) 7-bromo-1-heptene, K<sub>2</sub>CO<sub>3</sub>, EtOH, reflux, 6 h, 88%; b) Zn(CN)<sub>2</sub>, Pd(PPh<sub>3</sub>)<sub>4</sub>, DMF, 120°C, 4 h, 75%.

Cyanation of **9** with zinc cyanide in presence of palladium tetrakis as catalyst resulted in formation of **10**, isolated in 75% yield after chromatographic purification. We then performed the half sandwich complex formation on the unsubstituted Pc, followed by cyclic tetramerization of **10**.



**Scheme 7.8** Synthesis of **11**: a)  $[Tb(acac)]nH_2O$ , *o*-dichlorobenzene, DBU,  $170^\circ C$ , 1.5 h; b) **10**, *o*-dichlorobenzene /1-pentanol,  $170^\circ C$ , 12 h, 26% (over two steps).

Also in this case the crude of the reaction contained a mixture of the desired neutral  $TbPc_2$  **11**, its corresponding reduced complex and the

octafunctionalized Pc formed from **10** during the tetramerization reaction. The treatment of the mixture with DDQ afforded the fully oxidation of [TbPc<sub>2</sub>]H complex into the free-radical neutral form **11**: further purification by flash chromatography yielded the target TbPc<sub>2</sub> **11** in 26% yield. The purification step turned out to be much more feasible. Compound **11** was characterized by MALDI-TOF and UV-Vis.

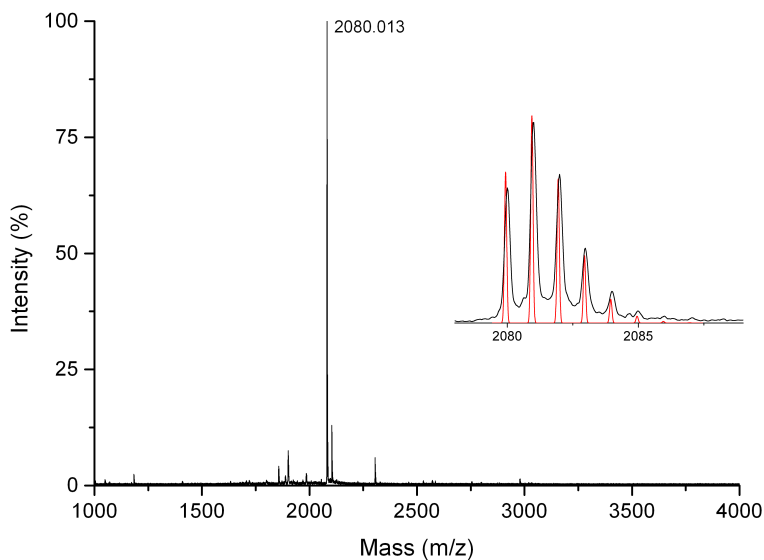


**Figure 7.7** High-resolution MALDI-TOF spectrum of **11**, with experimental (black lines) versus theoretical (black) isotopic distribution pattern in the inset.

MALDI-TOF spectrum showed the molecular peak at 2080.013 m/z, whose isotopic distribution matches the calculated one for the molecular ion of **11**. At higher m/z we found the smaller peak corresponding to the adduct with sodium, while at lower m/z the peaks due to partial MALDI-promoted fragmentations of **11** are observable.

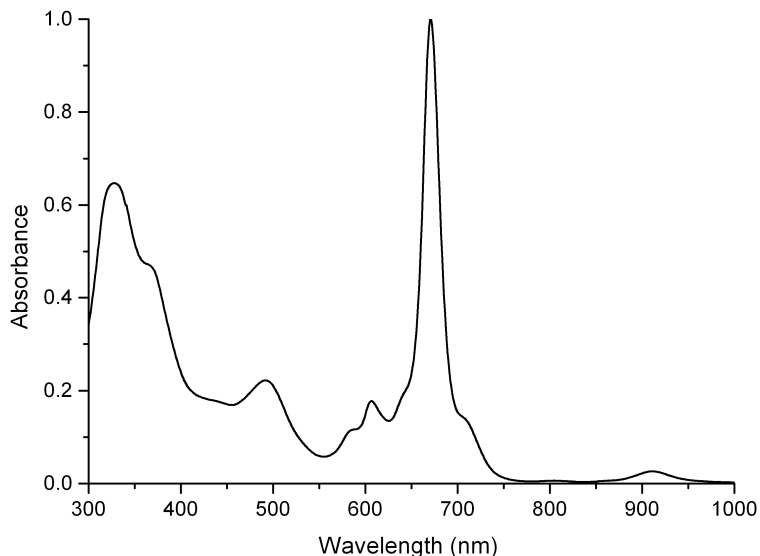


**Figure 7.8** UV-Vis absorption spectrum of **11** in chloroform.

UV-Vis spectrum of **11** confirmed the neutral  $\pi$  radical form of the molecule: the spectrum exhibits the characteristic absorption bands of double-decker phthalocyaninato complexes (see Paragraph 7.1.1).

Design and synthesis of TbPc<sub>2</sub> demand remarkable efforts from the synthetic point of view: as presented in this work, the outcome of TbPc<sub>2</sub> formation reactions can be very unpredictable. In our case the use of starting difunctionalized phthalonitriles promoted the formation of heteroleptic double deckers, while no formation of target molecules was observed using monofunctionalized phthalonitriles. We also found that reducing the length of the peripheral alkyl chains, we were able to considerably simplify the purification step, achieving higher yields.

## 7.2.2 Magnetic Characterization of Bulk

Before proceeding with the grafting process, we measured the bulk magnetic properties to ensure the SMM behavior of the TbPc<sub>2</sub> **11** was preserved after the functionalization. Magnetic characterization, performed with standard ac and dc magnetometric techniques clearly indicated the SMM behaviour of the

complex in its bulk phase. The magnetization versus field measurements, performed at several temperatures and scanning the field between + 30 and - 30 kOe at 50 kOe s<sup>-1</sup>, evidenced the opening of a hysteresis below 15 K with the typical butterfly shape induced by the enhancement of quantum tunnelling in zero applied field (Figure 7.9 right).<sup>18</sup> Moreover the comparison with the corresponding homoleptic **TbPc<sub>2</sub>(OC<sub>11</sub>H<sub>21</sub>)<sub>8</sub>** revealed an equivalent saturation magnetization value.

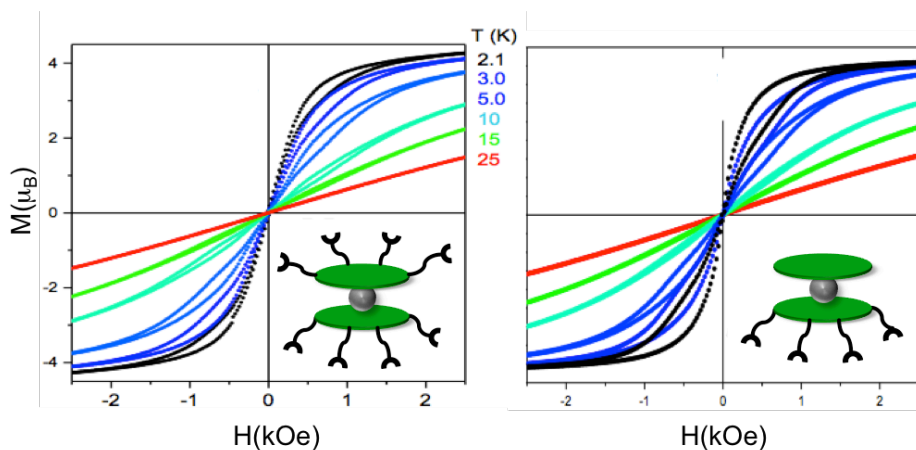


**Figure 7.9** Magnetization curves as a function of the temperature recorded at a field sweeping rate of 50 Oes<sup>-1</sup> for homoleptic **TbPc<sub>2</sub>(OC<sub>11</sub>H<sub>21</sub>)<sub>8</sub>** (left) and heteroleptic **11** (right).

### 7.2.3 Covalent Grafting on Silicon

Compound **11** was anchored on a H-terminated Si (100) surface via thermal hydrosilylation of the double bonds according to the published literature,<sup>19</sup> following the same experimental procedure reported in Chapter 6. The hydrosilylation reaction led to the formation of a robust Si-C bond and it occurred by placing the alkene-functionalized molecules in a 10<sup>-3</sup> M mesitylene solution at 200 °C in the presence of a freshly etched H-terminated Si(100). After grafting, several cycles of cleaning (including the sonication of the sample in several solvents) were performed in order to guarantee the removal of all the physisorbed materials leaving on the surface only the monolayer of grafted molecules. The silicon-anchored complex, **11@Si** hereafter, was characterized by XPS in order to verify the chemical integrity of the system.



Table 7.1 reports a semiquantitative estimation of the element contents on surface. Even considering the experimental error of XPS and the presence of adventitious carbon contamination in this ex situ prepared sample, the presence of Tb 3d<sub>3/2</sub> and N 1s signals (not present on the starting Si(100) surface) proved the deposition of the system.

Reference lines	Atomic Percentage (%)	
	11@Si	theoretical
Tb 3d <sub>3/2</sub>	0.6	0.7
N 1s	6.2	11.7
C 1s	93.2	87.6
N/Tb	9.6	16

**Table 7.1** XPS atomic composition of a monolayer 11@Si and the theoretical values for 11.

## 7.2.4 X-Ray Natural Linear Dichroism (XNLD)

X-ray Absorption Spectroscopy (XAS) experiment measures the variation of the X-ray absorption coefficient close to a specific electronic transition starting from a core level (absorption edge), thereby achieving element selectivity. When the core electron is a 1s electron, the edge is called a K-edge, when it is a 2p electron one measures L<sub>2,3</sub> edges and when it is a 3d electron one observes M<sub>4,5</sub> edges. For light elements such as carbon, nitrogen or oxygen the most common measurements are at the K-edges, for 3d transition elements at the K and L<sub>2,3</sub> edges, and for 4f and 5f elements at the L<sub>2,3</sub> and M<sub>4,5</sub> edges. The final level can be an empty level above the Fermi energy for a solid or an empty atomic or molecular level for a finite system.<sup>20</sup>

In a XNLD X-ray natural linear dichroism (XNLD) experiment, the difference between the cross section of vertically and horizontally linearly polarized light,  $\sigma^V - \sigma^H$ , is measured. This allows to evaluate the anisotropy of the charge distribution around the sampled element, providing information about the orientation of the molecules. The presence of a relevant dichroic signal evidences that the molecules have a preferential orientation in the film. Figure 7.10 reports XNLD spectra of TbPc<sub>2</sub> molecules deposited via ultrahigh vacuum

technique as thick film on Al foil and thin film on Au (111).<sup>2a</sup> By comparison between the XNLD spectrum of the thick film with the one from thin film on Au it's clear that the TbPc<sub>2</sub> molecules orientation is different. In fact the dichroic signal of the XNLD spectra, carried out in the same conditions, have opposite sign and the intensity is twice larger than that obtained for the evaporated thick film.

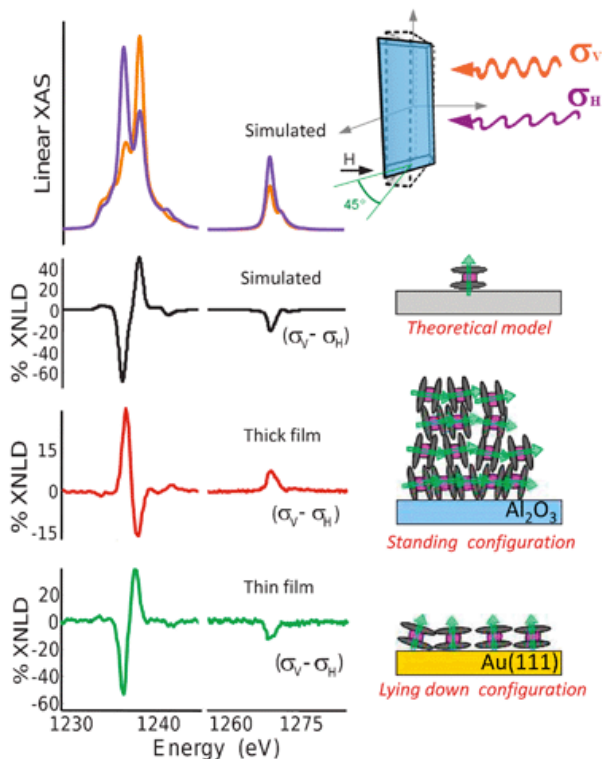


**Figure 7.10** XNLD spectra measured on thick-film and thin-film samples of TbPc<sub>2</sub>, and theoretical spectra calculated assuming that the molecules are lying down on the substrate. The arrangement of the TbPc<sub>2</sub> molecules on the substrate is schematized on the right.

Assuming that the TbPc<sub>2</sub> molecules lie down on the surface with their pseudo-tetragonal,  $z$ , axis parallel to the normal of the substrate, the intensity of the XNLD signal can be written as  $\sigma^V - \sigma^H = 1/2 (\sigma^\perp - \sigma^\parallel)$ , with  $\sigma^\parallel$  and  $\sigma^\perp$  defined as the theoretical cross section measured with the polarization vector parallel and perpendicular to the  $z$  molecular axis. In the case of molecules standing on the surface with the  $z$  axes randomly distributed in the plane of the surface the

relation  $\sigma^V - \sigma^H = -1/4 (\sigma^\perp - \sigma^\parallel)$ , holds.<sup>2a</sup> Having observed a halved and reversed intensity of the linear dichroic contribution in the thick film we can deduce that the molecules are in the standing orientation, while they are lying down in the thin one. These ordering effects are not unusual when flat molecules like phthalocyanines or porphyrins are evaporated, because the strong interactions with the substrate, as well as within the molecules, can affect the orientation and packing of the molecular deposit. In particular in Metal-Pc systems the first layers grow with the molecule in the lying position on noble metal surfaces because of strong molecule-surface interactions, while the molecules adopt a standing orientation in the case of rough surfaces and metal-oxide surfaces where molecule-molecule interactions are dominant.<sup>21</sup>

#### 7.2.4 X-ray Absorption Characterization of the **11@Si** Monolayer

Circular and linear polarization-dependent X-ray absorption experiments were carried out on the **11@Si** monolayer at the DEIMOS beamline, located at Synchrotron SOLEIL, in order to evaluate with the highest level of accuracy the magnetic and structural properties of the assembled nanostructure. At first X-ray Magnetic Circular Dichroism (XMCD) was measured for the  $M_{4,5}$  edges. By employing this technique it is possible to obtain highly resolved XMCD-detected magnetization curves as a function of the fast sweeping external field. Figure 7.11 reports the variation of the XMCD contribution at the  $M_5$  edge, normalized to the saturation value, as a function of the applied magnetic field between -30 and +30 kOe at two different temperatures. The characteristic butterfly-shaped hysteresis cycle confirmed the magnetic bistability of **11@Si** monolayer. Comparison with the bulk phase revealed a significantly larger opening of the hysteresis as already observed with the **TbPc<sub>2</sub>(OC<sub>11</sub>H<sub>21</sub>)<sub>8</sub>@Si** system in the previous Chapter, although a less relevant quantum tunneling of the magnetization in zero field was observed.

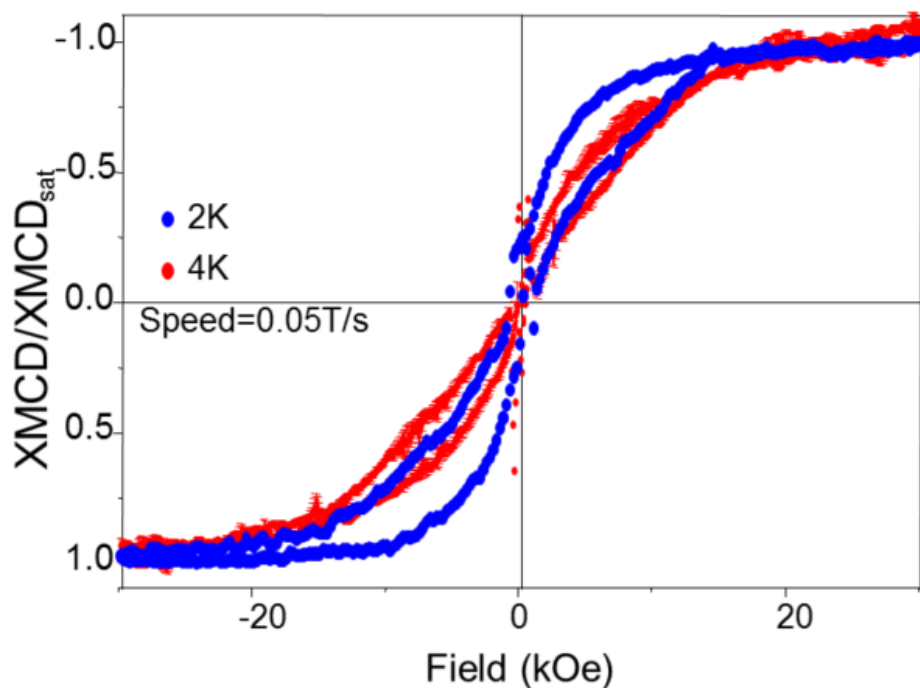


**Figure 7.11** XMCD-detected magnetization curves for **11@Si** measured at two different temperatures and  $500 \text{ Oe s}^{-1}$  scan speed.

We furthermore investigated the **11@Si** monolayer by employing XNLD: the sample was set so that the normal to the surface  $n$  and the X-ray propagation vector  $k$  lie in the horizontal plane with  $(n,k) = 60^\circ$ . The cross-sections with horizontal linear polarization ( $\sigma^H$ ) and with vertical linear polarization ( $\sigma^V$ ) was measured.

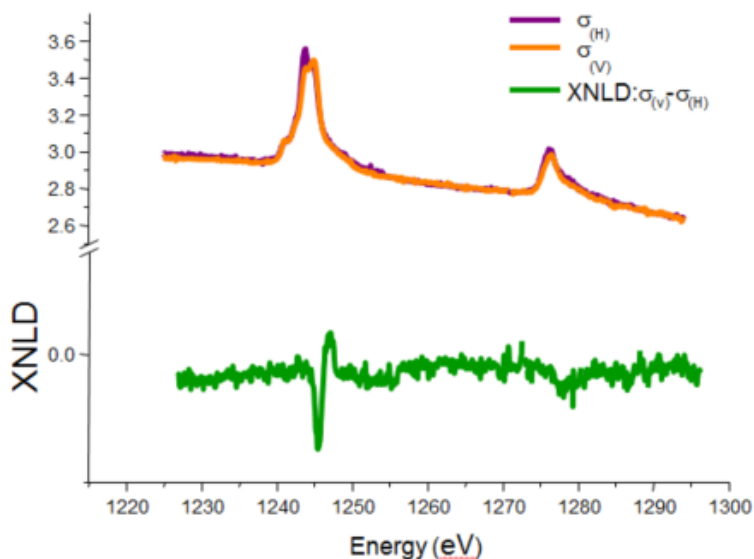


**Figure 7.12** XNLD spectra for **11@Si** measured at  $2.0 \pm 0.2$  K, 50 kOe, for  $(n,k) = 60^\circ$ . In the inset, the geometry of the two experiments are presented: in a XNLD experiment vertical ( $\sigma^V$ ) and horizontally ( $\sigma^H$ ) polarized light are used and the sample is rotated by an angle  $\theta$  between the normal to the surface and the X-ray light propagation direction, an external magnetic field is used only to enhance the detection capabilities.<sup>1</sup>

Comparison with **TbPc<sub>2</sub>(OC<sub>11</sub>H<sub>21</sub>)<sub>8</sub>@Si** and other experimental and theoretical reported works,<sup>2</sup> showed that the molecules forming the monolayer were preferentially oriented with a lying down orientations. However quantitative analysis of the results indicated that we achieved only a partial alignment of the molecules respect to the surface.

### 7.3 Conclusions

The symmetric heteroleptic octafunctionalized **TbPc<sub>2</sub> 11** with terminal double bond has been successfully functionalized and characterized as SMM. Complex **11** has been covalently grafted to silicon to form a chemically and physically robust monolayer **11@Si**. The chemical grafting has led to a significant enhancement of the magnetic bistability compare to the bulk phase, however the fully orientation of the **TbPc<sub>2</sub>** molecules has not been observed. With respect to the previous case (Chapter 6), no significant improvement of the desired lying down orientation has been observed. A possible explanation is that only a part of the lateral alkenes reacted with the silicon surface, allowing the standing

orientation (Figure 7.13). This alignment might be favored by lateral  $\pi$  stacking interactions among the phtahlocyanines rings.

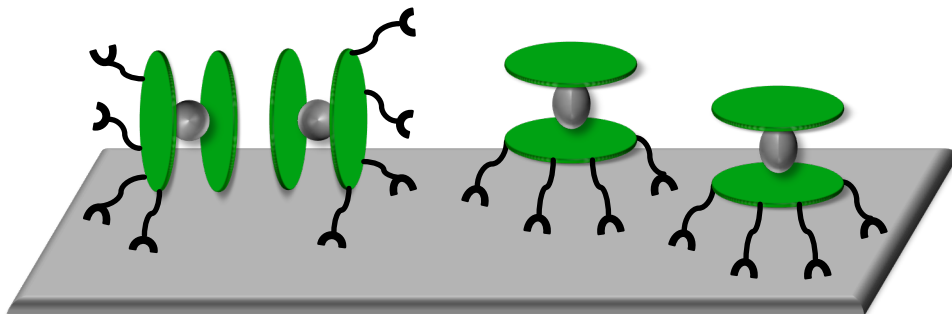


**Figure 7.13** Schematized partial orientation of  $11@Si$  monolayer.

Further investigations will be conducted by varying experimental conditions on the hydrosilylation reaction in order to address the system towards a complete lying down orientation.

## 7.4 Acknowledgments

Special thanks to Dr. Gianluca Paredi from the interdepartmental Centre SITEIA.PARMA, University of Parma, for mass spectrometry measurements. Thanks to Prof. Guido Condorelli and Cristina Tudisco, University of Catania, for the grafting on silicon and XPS analyses. Thanks to Prof. Roberta Sessoli and Dr. Matteo Mannini from department of Chemistry, University of Firenze, for magnetic measurements.

## 7.5 Experimental Section

**1**<sup>12</sup> and **4**<sup>22</sup> were synthesized following reported procedures. For the bulk magnetic characterization, monolayer preparation, XPS and XAS measurements see Experimental Section in Chapter 6.

### Tetra-4-( $\omega$ -undecenyloxy)phthalocyanine (**2**)

To a stirred solution of 4-( $\omega$ -undecenyloxy)phthalonitrile **1** (300 mg, 1.01 mmol) in 1-pentanol a catalytic amount of DBU was added. The resulting solution was stirred overnight at 140°C under N<sub>2</sub>. After cooling, methanol was added to the residue until a precipitate formed. The green finely dispersed mixture was filtered off and purified by flash chromatography (dichlorometane as eluent) to give **2** as a green solid (174 mg, 0.147 mmol, 58%).

<sup>1</sup>H NMR (CDCl<sub>3</sub>, 300 MHz):  $\delta$  = 6.91-6.72 (m, 12H, ArH), 5.95 (m, 4H, CH=CH<sub>2</sub>), 5.10 (m, 8H, CH=CH<sub>2</sub>), 3.98 (bs, 8H, OCH<sub>2</sub>), 2.22 (m, 8H, CH<sub>2</sub>CH=CH<sub>2</sub>), 2.01 (bs, 8H, OCH<sub>2</sub>CH<sub>2</sub>), 1.71-1.54 (m, 48H, -CH<sub>2</sub>-);

MALDI TOF: calculated for C<sub>76</sub>H<sub>98</sub>N<sub>8</sub>O<sub>4</sub> [M]<sup>+</sup> m/z: 1186.77, found m/z= 1186.79.

### Synthesis of PcLi<sub>2</sub>**2**

Under an argon atmosphere, Pc **2** (65 mg, 0.055 mmol) was added to a solution of Li (0.84 mg, 0.121 mmol) in ethanol absolute. A green color appeared, and when the mixture was warmed, the color changing to deep blue. The mixture was stirred at 80°C for 2 h. After cooling, solvent was evaporated and the blue residue was extracted with acetone, previously dried over sodium sulfate, to remove lithium compounds. Evaporation under reduced pressure and desiccation under an argon atmosphere left PcLi<sub>2</sub> **2** as a crystalline purple powder (41.6 mg, 0.035 mmol, 63%). The compound is unstable and it was used without characterizations and further purification in the next step.

### Synthesis of PcLi<sub>2</sub>**4**

To a solution of Li (1.19 mg, 0.172 mmol) in ethanol absolute, Pc **4** (40.0 mg, 0.078 mmol) was added under an argon atmosphere. A green color appeared, and when the mixture was warmed, the color changing to deep blue. The mixture was stirred at 80°C for 2 h. After cooling, solvent was evaporated and the blue residue was extracted with acetone, previously dried over sodium sulfate, to remove lithium compounds. Evaporation under reduced pressure and desiccation under an argon atmosphere left PcLi<sub>2</sub> **4** as a crystalline purple

powder (24.2 mg, 0.046 mmol, 59%). The compound is unstable and it was used without characterizations and further purification in the next step.

### Synthesis of 3

**PcLi<sub>2</sub> 4** (24 mg, 0.046 mmol) was dissolved in 1-chloronaphthalene and [Tb(acac)]<sub>3</sub>nH<sub>2</sub>O (25.7 mg, 0.055 mmol) was added. The reaction mixture was stirred at 170°C for 1.5 h. The resulting solution was cooled to room temperature, **PcLi<sub>2</sub> 2** (55.1 mg, 0.046 mmol) was added and the mixture was stirred overnight at 210°C. The dark-green solution was cooled to room temperature and the solvent removed under reduced pressure. Purification by flash chromatography of the crude resulted in a mixture of inseparable products containing **3**.

### 4,5-dibromocatechol (**5**)

To a flask containing catechol (2.0 g, 18.2 mmol) in CHCl<sub>3</sub>, a solution of bromine (1.87 mL, 36.3 mmol) in CHCl<sub>3</sub> was added over 1 h at 0°C. The resulting solution was stirred overnight at room temperature. The dibromocatechol **6** was isolated by filtration as an off-white solid (4.04 g, 15.1 mmol, 83% yield) without any further purification.

<sup>1</sup>H NMR (DMSO-d<sub>6</sub>, 400 MHz): δ (ppm) = δ 9.67 (s, 2H, ArOH), 7.03 (s, 2H, ArH).

ESI-MS: m/z 264.8 [M-H]<sup>-</sup>.

### 4,5-bis(ω-undecenyloxy)-1,2-dibromobenzene (**6**)

To a stirred solution of **5** (0.750 g, 2.80 mmol) in ethanol, K<sub>2</sub>CO<sub>3</sub> (2.1 g, 15.2 mmol) and 11-bromo-1-undecene (1.41 mL, 6.44 mmol) were added. The reaction was heated to reflux for 6 h. After cooling, the reaction mixture was concentrated under reduced pressure, and then diluted with ethyl acetate and H<sub>2</sub>O. The layers were separated and the aqueous layer was extracted with ethyl acetate. The combined organic layers were then dried over Na<sub>2</sub>SO<sub>4</sub>. Evaporation under reduced pressure afforded the crude product, which was further purified by flash chromatography (hexane:dichloromethane 7:3) to give **6** (1.28 g, 2.24 mmol, 80%) as a colorless oil.

<sup>1</sup>H NMR (CDCl<sub>3</sub>, 300 MHz): δ = 7.08 (s, 2H, ArH), 5.83 (m, 2H, CH=CH<sub>2</sub>), 4.99 (m, 4H, CH=CH<sub>2</sub>), 3.95 (t, 4H, J=6.6 Hz, OCH<sub>2</sub>), 2.07 (m, 4H, CH<sub>2</sub>CH=CH<sub>2</sub>), 1.82 (m, 2H, OCH<sub>2</sub>CH<sub>2</sub>), 1.48-1.32 (m, 24H, -CH<sub>2</sub>-); <sup>13</sup>C NMR (CDCl<sub>3</sub>, 100 MHz): δ (ppm) = 148.9, 139.1, 117.8, 114.5, 114.0, 69.4, 33.6, 29.3, 29.2, 29.1, 29.0, 28.9, 28.8, 25.7.

ESI-MS: m/z 595.2 [M+Na]<sup>+</sup>, 611.2 [M+K]<sup>+</sup>.



**4,5-bis( $\omega$ -undecenyloxy)phthalonitrile (7)**

To a solution of **6** (1.12 g, 1.96 mmol) in dry DMF, tetrakis(triphenylphosphine)-palladium(0) (0.227 g, 0.196 mmol) was added, followed by Zn(CN)<sub>2</sub> (0.277 g, 2.36 mmol). The resulting solution was stirred for 4 h at 120°C. After cooling, ammonia (37%, 20 mL) was added and the resulting precipitate was filtered off, washed with water and purified by flash chromatography (hexane:ethyl acetate 9:1) to give **7** (0.757 g, 1.63 mmol, 83% yield) as a white solid.

<sup>1</sup>H NMR (CDCl<sub>3</sub>, 300 MHz):  $\delta$  = 7.21 (s, 2H, ArH), 5.82 (m, 2H, CH=CH<sub>2</sub>), 4.97 (m, 4H, CH=CH<sub>2</sub>), 4.06 (t, 4H, *J*=6.3 Hz, OCH<sub>2</sub>), 2.70 (m, 4H, CH<sub>2</sub>CH=CH<sub>2</sub>), 1.86 (m, 2H, OCH<sub>2</sub>CH<sub>2</sub>), 1.48-1.26 (m, 24H, -CH<sub>2</sub>-); <sup>13</sup>C NMR (CDCl<sub>3</sub>, 100 MHz):  $\delta$  (ppm) = 152.5, 139.1, 116.0, 115.8, 114.2, 108.4, 69.7, 33.8, 29.5, 29.4, 29.2, 29.1, 28.9, 28.7, 25.8.

ESI-MS: *m/z* 487.4 [M+Na]<sup>+</sup>, 503.4 [M+K]<sup>+</sup>.

**4,5-bis( $\omega$ -heptenyloxy)-1,2-dibromobenzene (9)**

To a stirred solution of **5** (0.700 g, 2.61 mmol) in ethanol, K<sub>2</sub>CO<sub>3</sub> (2.1 g, 15.2 mmol) and 7-bromo-1-heptene (0.883 mL, 5.79 mmol) were added. The reaction was heated to reflux for 6 h. After cooling, the reaction mixture was concentrated under reduced pressure, and then diluted with ethyl acetate and H<sub>2</sub>O. The layers were separated and the aqueous layer was extracted with ethyl acetate. The combined organic layers were then dried over Na<sub>2</sub>SO<sub>4</sub>. Evaporation under reduced pressure afforded the crude product, which was further purified by flash chromatography (hexane:dichloromethane 7:3) to give **9** (1.06 g, 2.30 mmol, 88%) as a colorless oil.

<sup>1</sup>H NMR (CDCl<sub>3</sub>, 300 MHz):  $\delta$  = 7.08 (s, 2H, ArH), 5.82 (m, 2H, CH=CH<sub>2</sub>), 5.01 (m, 4H, CH=CH<sub>2</sub>), 3.96 (t, 4H, *J*=6.6 Hz, OCH<sub>2</sub>), 2.10 (m, 4H, CH<sub>2</sub>CH=CH<sub>2</sub>), 1.82 (m, 2H, OCH<sub>2</sub>CH<sub>2</sub>), 1.48 (m, 8H, -CH<sub>2</sub>-); <sup>13</sup>C NMR (CDCl<sub>3</sub>, 100 MHz):  $\delta$  (ppm) = 149.0, 138.7, 118.0, 114.7, 114.5, 69.5, 33.7, 28.9, 28.6, 25.4.

ESI-MS: *m/z* 483.1 [M+Na]<sup>+</sup>, 499.1 [M+K]<sup>+</sup>.

**4,5-bis( $\omega$ -heptenyloxy)phthalonitrile (10)**

To a stirred solution of **9** (0.708 g, 1.53 mmol) in dry DMF, tetrakis(triphenylphosphine)palladium(0) (0.177 g, 0.153 mmol) and Zn(CN)<sub>2</sub> (0.216 g, 1.84 mmol) were added. The resulting solution was stirred for 4 h at 120°C. After cooling, ammonia (37%, 20 mL) was added and the resulting precipitate was filtered off, washed with water and purified by flash chromatography (hexane:ethyl acetate 9:1) to give **10** (0.404 g, 1.15 mmol, 75%) as a white solid.

<sup>1</sup>H NMR (CDCl<sub>3</sub>, 300 MHz):  $\delta$  = 7.13 (s, 2H, ArH), 5.81 (m, 2H, CH=CH<sub>2</sub>), 4.99 (m, 4H, CH=CH<sub>2</sub>), 4.06 (t, 4H, *J*=6.5 Hz, OCH<sub>2</sub>), 2.11 (m, 4H, CH<sub>2</sub>CH=CH<sub>2</sub>), 1.88

(m, 2H, OCH<sub>2</sub>CH<sub>2</sub>), 1.51-1.44 (m, 8H, -CH<sub>2</sub>-); <sup>13</sup>C NMR (CDCl<sub>3</sub>, 100 MHz): δ (ppm) = 152.2, 138.4, 115.8, 115.6, 114.5, 108.2, 69.4, 33.4, 28.4, 28.2, 25.1.

ESI-MS: m/z 375.2 [M+Na]<sup>+</sup>, 391.3 [M+K]<sup>+</sup>.

### Heteroleptic TbPcPc(OC<sub>11</sub>H<sub>21</sub>)<sub>8</sub> (8)

Phthalocyanine **4** (52.0 mg, 0.101 mmol) was suspended in *o*-DCB and [Tb(acac)]<sub>3</sub>*n*H<sub>2</sub>O (46.1 mg, 0.101 mmol) was added, followed by DBU (19.9 μL, 0.131 mmol). The reaction mixture was heated at 170°C for 1.5 h. The resulting dark-blue solution was cooled to room temperature and the solvent removed under reduced pressure. The residue was washed with hexane to give the corresponding intermediate [Tb(acac)(Pc)], which was then reacted with **7** (204.3 mg, 0.440 mmol) and DBU (19.9 μL, 0.131 mmol) in a mixture *o*-DCB/1-pentanol (1:1). The resulting solution was heated at 170°C and stirred overnight. The dark-green solution was cooled to room temperature and the solvent removed under reduced pressure. The residue was dissolved in CHCl<sub>3</sub>, 2,3-dichloro-5,6-dicyano-1,4-benzoquinone (DDQ, 55.0 mg, 0.242 mmol) was added, and the reaction was stirred at room temperature for 1.5 h.. The solvent was removed under reduced pressure and the solid was purified by flash chromatography (chloroform as eluent) to give **8** as a green solid (28.1 mg, 0.011 mmol, 11%).

MALDI-TOF: calculated for C<sub>152</sub>H<sub>192</sub>N<sub>16</sub>O<sub>8</sub>Tb [M]<sup>+</sup> m/z: 2528.436, found m/z = 2528.488.

UV-Vis: λ<sub>max</sub> (CHCl<sub>3</sub>) 911, 701, 669, 607, 335 nm.

### Heteroleptic TbPcPc(OC<sub>7</sub>H<sub>13</sub>)<sub>8</sub> (11)

To a stirred solution of the metal free phthalocyanine **4** (70.0 mg, 0.136 mmol) in *o*-DCB, [Tb(acac)]<sub>3</sub>*n*H<sub>2</sub>O (74.5 mg, 0.163 mmol) was added followed by DBU (25.2 μL, 0.176 mmol). The solution was heated at 170°C for 1.5 h. The resulting dark-blue solution was cooled to room temperature and the solvent removed under reduced pressure. The residue was washed with hexane to give the corresponding intermediate [Tb(acac)(Pc)], which was then reacted with **10** (210.8 mg, 0.599 mmol) and DBU (25.2 μL, 0.176 mmol) in a mixture *o*-DCB/1-pentanol (1:1). The resulting solution was heated at 170°C and stirred overnight. The dark-green solution was cooled to room temperature and the solvent removed under reduced pressure. The residue was dissolved in CHCl<sub>3</sub>, 2,3-dichloro-5,6-dicyano-1,4-benzoquinone (DDQ, 74.1 mg, 0.326 mmol) was added, and the reaction was stirred at room temperature for 1.5 h. The solvent was removed under reduced pressure and the solid was purified by flash

chromatography (chloroform as eluent) to give **11** as a green solid (70.1 mg, 0.035 mmol, 26%).

**MALDI-TOF:** calculated for  $C_{120}H_{128}N_{16}O_8Tb$   $[M]^+$  m/z: 2079.935, found m/z= 2080.013.

**UV-Vis:**  $\lambda_{max}$  ( $CHCl_3$ ) 911, 671, 606, 491, 328 nm.

## 7.6 References

- <sup>1</sup> A. Cornia, M. Mannini, P. Saintavit, R. Sessoli, *Chem. Soc. Rev.* **2011**, *40*, 3076–3091.
- <sup>2</sup> a) L. Margheriti, D. Chiappe, M. Mannini, P.-E. Car, Ph. Saintavit, M.-A. Arrio, F. B. de Mongeot, J. C. Cezar, F. M. Piras, A. Magnani, E. Otero, A. Caneschi and R. Sessoli, *Adv. Mater.* **2010**, *22*, 5488–5493; b) S. Stepanow, J. Honolka, P. Gambardella, L. Vitali, N. Abdurakhmanova, T.-C. Tseng, S. Rauschenbach, S. L. Tait, V. Sessi, S. Klyatskaya, M. Ruben, K. Kern, *J. Am. Chem. Soc.* **2010**, *132*, 11900–11901.
- <sup>3</sup> I. S. Kirin, P. N. Moskalev, Y. A. Makashev, *Russ. J. Inorg. Chem.* **1965**, 1065–1066.
- <sup>4</sup> J. A. de Saja, M. L. Rodriguez-Mendez, *Adv. Colloid Interface Sci.* **2005**, *116*, 1–11.
- <sup>5</sup> Y. Chen, W. Su, M. Bai, J. Jiang, X. Li, Y. Liu, L. Wang, S. Wang, *J. Am. Chem. Soc.* **2005**, *127*, 15700–15701.
- <sup>6</sup> C. Piechocki, J. Simon, J.-J. André, D. Guillon, P. Petit, A. Skoulios, P. Weber, *Chem. Phys. Lett.* **1985**, *122*, 124–128.
- <sup>7</sup> N. Ishikawa, M. Sugita, T. Ishikawa, S. Koshihara, Y. Kaizu, *J. Am. Chem. Soc.* **2003**, *125*, 8694–8695.
- <sup>8</sup> A. De Cian, M. Moussavi, J. Fischer, R. Weiss *Inorg. Chem.* **1985**, *24*, 3162–3167.
- <sup>9</sup> N. Ishikawa, M. Sugita, T. Okubo, N. Tanaka, T. Iino, Y. Kaizu, *Inorg. Chem.* **2003**, *42*, 2440–2446.
- <sup>10</sup> J. Jiang, D. K. P. Ng, *Acc. Chem. Res.* **2009**, *42*, 79–88.
- <sup>11</sup> A. Iwase, C. Harnood, Y. Kameda, *J. Alloys Compd.* **1993**, *192*, 280–283.

- <sup>12</sup> M. Mannini, F. Bertani, C. Tudisco, L. Malavolti, L. Poggini, K. Misztal, D. Menozzi, A. Motta, E. Otero, P. Ohresser, P. Saintavit, G. G. Condorelli, E. Dalcanale, R. Sessoli, *Nat. Commun.* **2014**, *5*, article number: 4582.
- <sup>13</sup> B. Görlach, C. Hellriegel, S. Steinbrecher, H. Yüksel, K. Albert, E. Plies, M. Hanack, *J. Mater. Chem.* **2001**, *11*, 3317–3325.
- <sup>14</sup> C. R. Ganivet, B. Ballesteros, G. de la Torre, J. M. Clemente-Juan, E. Coronado, T. Torres, *Chem. Eur. J.* **2013**, *19*, 1457–1465.
- <sup>15</sup> S. Kyatskaya, J. R. G. Mascarós, L. Bogani, F. Hennrich, M. Kappes, W. Wernsdorfer, M. Ruben, *J. Am. Chem. Soc.* **2009**, *131*, 15143–15151.
- <sup>16</sup> M. J. Fleming, H. A. McManus, A. Rudolph, W. H. Chan, J. Ruiz, C. Dockendorff, M. Lautens, *Chem. Eur. J.* **2008**, *14*, 2112–2124.
- <sup>17</sup> M. Gonidec, R. Biagi, V. Corradini, F. Moro, V. De Renzi, U. del Pennino, D. Summa, L. Muccioli, C. Zannoni, D. B. Amabilino, J. Veciana *J. Am. Chem. Soc.* **2011**, *133*, 6603–6612.
- <sup>18</sup> N. Ishikawa, *Polyhedron* **2007**, *26*, 2147–2153.
- <sup>19</sup> J. M. Buriak, *Chem. Rev.* **2002**, *102*, 1271–1308.
- <sup>20</sup> J. Stöhr, H. A. Padmore, S. Anders, T. Stammler, *Surf. Rev. Lett* **1998**, *5*, 1297–1308.
- <sup>21</sup> a) H. Peisert, T. Schwieger, J. M. Auerhammer, M. Knupfer, M. S. Golden, J. Fink, P. R. Bressler, M. Mast, *J. Appl. Phys.* **2001**, *90*, 466–469; b) I. Biaswas, H. Peisert, M. Nagel, M. B. Casu, S. Schuppler, P. Nagel, E. Pellegrini, T. Chassé, *J. Chem. Phys.* **2007**, *126*, 174704; D. C. Qi, D. J. T. Sun, X. Y. Gao, L. Wang, S. Chen, K. P. Loh, A. T. S. Wee, *Langmuir* **2010**, *26*, 165–172.
- <sup>22</sup> C. Ma, K. Ye, S. Yu, G. Du, Y. Zhao, F. Cong, Y. Chang, W. Jiang, C. Cheng, Z. Fan, H. Yu, W. Li, *Dyes and Pigments* **2007**, *74*, 141–147.

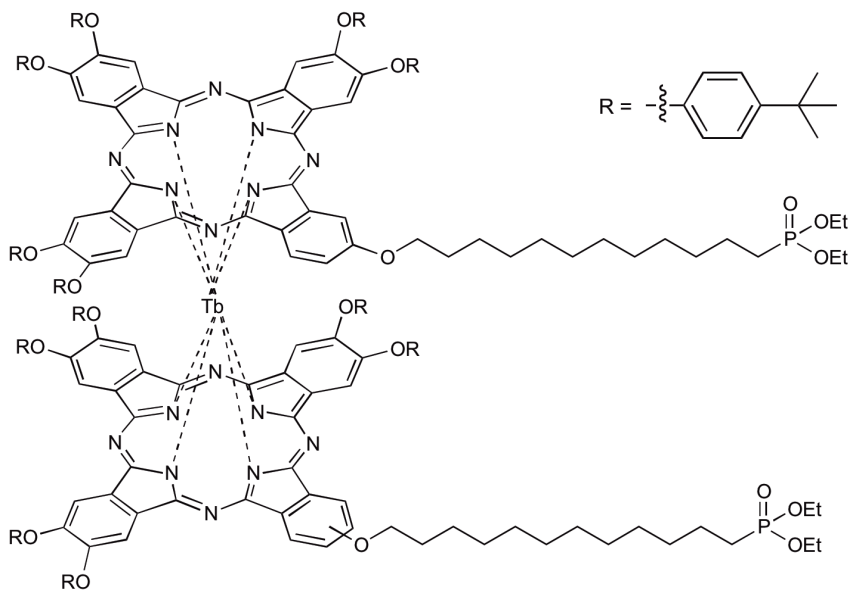
# Chapter 8

Synthesis and Magnetic  
Properties of Novel  
Functionalized TbPc<sub>2</sub>

## 8.1 Introduction

In Chapters 6 and 7 we described the importance of assembling and integrate SMMs into functional devices without compromising their properties.<sup>1</sup> In this context, the synthesis of functionalized TbPc<sub>2</sub> with appropriate anchoring groups to graft on surfaces is highly desirable. The integration of SMMs in real devices also requires the development of new SMMs with improved magnetic properties. The effort to synthesize new SMMs with larger anisotropy barriers and more prominent hysteresis already led to the discovery of several new SMMs. Nevertheless the blocking temperature  $T_B$  is still a limiting factor, as the working temperature of SMMs reported to date remains below few kelvins, far from operating conditions of real devices. Thus synthesis of SMMs with improved magnetic properties and higher  $T_B$  values is a challenge for researchers in this area.

In this Chapter we present the synthesis and the magnetic characterization of four novel functionalized TbPc<sub>2</sub> complexes (Figure 8.1).



Phosphonate TbPc<sub>2</sub> 7

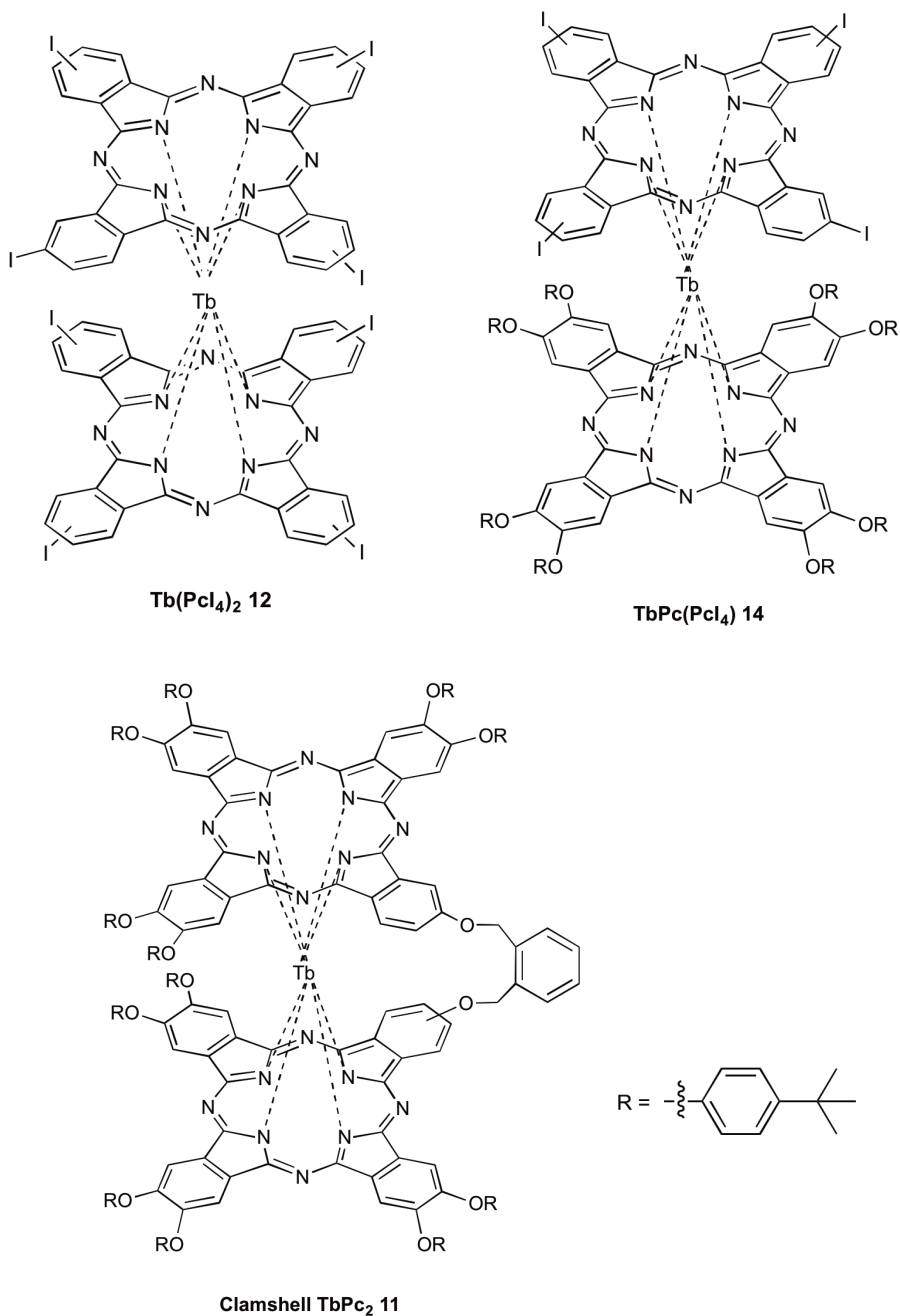


**Figure 8.1** Molecular structures of the four functionalized TbPc<sub>2</sub> synthesized.



### 8.1.1 Phosphonate TbPc<sub>2</sub>

The discovery of giant magnetoresistance effect (GMR) by Grünberg<sup>2</sup> and Fert,<sup>3</sup> awarded the Nobel prize in 2007, is considered the birth of the spintronics. GMR is the change of the electrical resistance of a magnetic device when an external magnetic field is applied and it is essentially associated to a change in the magnetic state of the device itself. The revolutionary scientific message revealed by GMR was that the electronic spin, as well as the electronic charge, can be used to carry information in electronic applications.<sup>4</sup> Spintronic systems exploit the fact that the electron current is composed of two types of electrons, "spin-up" and "spin-down" electrons, which form two largely independent spin currents and interact differently with magnetic materials. Information encoded in spins persists when the device is switched off, it can be manipulated without using magnetic fields and it can be written using low energies, to cite just a few advantages of this approach.<sup>5</sup> The contemporary exploitation of electronic and spin degrees of freedom was a particularly promising field both at fundamental and applied levels, and spintronics rapidly moved out of the academic laboratory to industrial mass production of spintronics-based devices. Studies on generation, manipulation and detection of spin-polarized electrical current made possible entirely new classes of spin-based sensor, memory and logic devices.<sup>6</sup> A new field of "molecular spintronics" emerged, combining the ideas and the advantages of spintronics and molecular electronics.<sup>4</sup> The key point is the creation of molecular devices using one or a few magnetic molecules. In this context, SMMs have attracted growing interest as active elements in organic spintronic devices, thanks to the intriguing properties of magnetic bistability at the molecular level showed at cryogenic temperatures. A molecular spintronic device generally consists of a semiconductor organic film located between two ferromagnetic electrodes, acting as a spin injector and a spin analyser, while the organic film can act as tunnelling barrier or as spin carrier.<sup>7</sup>

In 2011 Urdampilleta and co-workers reported<sup>8</sup> the preparation of a supramolecular spin valve device in which single-walled carbon nanotube contacted electrodes was laterally coupled through van der Waals interactions to a pyrene functionalized TbPc<sub>2</sub> complex (Figure 8.2). The TbPc<sub>2</sub> molecules laterally coupled to the electrically contacted SWCNT influenced the current passing through the SWCNT, thus permitting the readout of the molecular magnetic state by standard conductance measurements. The localized magnetic moments led to a magnetic field dependence of the electrical transport through the single-walled carbon nanotube. On reversing the magnetic field, the device exhibited magnetoresistance ratios up to 300% at temperatures less than 1 K.

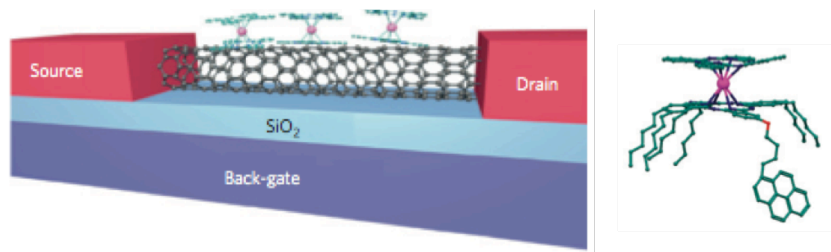


**Figure 8.2** Scheme of the supramolecular spin-valve architecture (left) and molecular representation of the TbPc<sub>2</sub> molecule.

This recent result opened a pathway towards the design of operable molecular spintronic devices projecting the implementation of new electrical functionalities, high integration depth and an alternative fabrication scheme to cost-intensive lithographic technologies.

Following a similar approach, in this Chapter we present the design and the synthesis of a phosphonate functionalized TbPc<sub>2</sub> **7** for the covalent grafting on pseudo-cubic perovskite manganite La<sub>2/3</sub>Sr<sub>1/3</sub>MnO<sub>3</sub> (LSMO), one of the most commonly used ferromagnetic substrates for molecular spintronics. This is a particularly attractive surface, as it's been shown that at low temperatures the conduction in LSMO exhibits a very high spin polarization approaching 100%, whereas the figure for elemental ferromagnets is <40%. Moreover, since LSMO is an oxide, it is stable in air.<sup>9</sup> Although magnetic behavior of TbPc<sub>2</sub> thin films sublimated on LSMO have been already investigated,<sup>10</sup> the covalent grafting of TbPc<sub>2</sub> on this surface is unexplored.

### 8.1.2 Clamshell TbPc<sub>2</sub>

Design of new efficient SMMs requests a deep understanding of the relationship between structures and properties. If it has been already demonstrated that the use of lanthanide-containing complexes allows to achieve a much larger spin reversal barriers, on account of the large single-ion magnetic anisotropy delivered by an appropriate configuration of 4*f* electrons,<sup>11</sup> the influence of many other factors is still under investigation. For instance the role of the metal ion is crucial: each lanthanide is characterized by *S* values that induce different magnetic properties to the LnPc<sub>2</sub>.<sup>12</sup> The redox state also affects the magnetic behavior of the LnPc<sub>2</sub>: in fact these complexes exist in three different forms, based on the oxidation state of the Pc rings (see Chapter 5), and

the LnPc<sub>2</sub> molecules can be either oxidized or reduced via single or double electrons reversible oxidation/reduction by reaction of mild oxidizing reagents or via electrochemistry. The redox process allows changes in electronic structure that affect the molecular structure of the sandwich unit,<sup>13</sup> and the impact on the resulting magnetic properties of making such modifications can be substantial.<sup>14</sup> We are interested in evaluate how the geometry of the complex affects the resulting magnetic properties. LnPc<sub>2</sub> molecules geometry is mainly affected by both the Ln radius<sup>15</sup> and the nature of the peripheral substituents.<sup>16</sup> Regarding this latter aspect, Zefirov and co-workers in 2012 reported the synthesis of a particular class of clamshell type phtahlocyanine complexes.<sup>17</sup> They studied the impact of an intramolecular flexible spacer group on the resulting spectroscopic and electrochemical properties of the LnPc<sub>2</sub>. They found that the introduction of the spacer group influenced the relative arrangement of macrocycles, and consequently their electronic structure and stability. In particular theoretical calculations evidenced the structural distortion caused by the linking group (Figure 8.3): whereas the distance between the upper and lower planes composed of the four isoindole nitrogen atoms (N<sub>iso</sub>) was almost unaffected, the bend angle decreased from 13.57° to 3.94° due to the presence of the spacer group. Remarkable changes were also observable for skew angle, which experienced a deviation from the theoretical 45° value, decreasing to 37°.

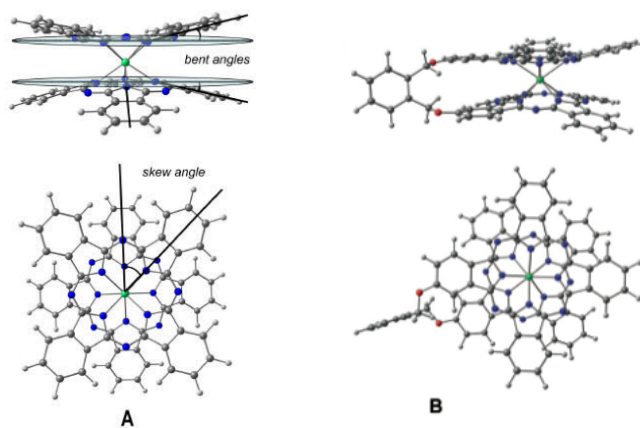


**Figure 8.3** View of the DFT optimized molecular structures of compounds: (A) LnPc<sub>2</sub>; (B) clamshell LnPc<sub>2</sub>. Side views are shown at the upper part, and top views at the lower part.

Our goal is to understand if such geometrical structural deviation could also promote an improvement of the magnetic properties in a LnPc<sub>2</sub>. In order to do

that, we designed the clamshell TbPc<sub>2</sub> **11** (see Figure 8.1). In fact it is well known that terbium displays the best magnetic performance for LnPc<sub>2</sub> complexes, thanks to the large energy gap between the states (e.g., first excited state of TbPc<sub>2</sub> is roughly 400 cm<sup>-1</sup> above the ground state).<sup>18</sup>

### **8.1.3 Iodinated TbPc<sub>2</sub>**

Grafting on surfaces requires the development of synthetic protocols in order to prepare LnPc<sub>2</sub> molecules derivatized with appropriate linkers. In this context a distinct advantage of the phthalocyanine-based SMMs is that a wide range of substituents may be theoretically introduced at the peripheral positions of the phthalocyanine macrocycles without significantly interfering with the metal binding properties of the ligands and the magnetic properties. Such functionalization is typically performed by employing De Cian synthesis starting from functionalized phthalonitriles.<sup>19</sup> Nevertheless, the harsh reaction conditions requested for the LnPc<sub>2</sub> formation exclude the use of the common functional groups. In fact, among the functionalized LnPc<sub>2</sub> complexes synthesized to date, the only functional groups found to survive the complex formation are ethers<sup>20</sup>, thioesters<sup>21</sup> and phthalimide.<sup>22</sup> We experienced in our research activities the incompatibility of several groups such as esters, amides and carbamates. The problem is overcome by performing the functionalization with the grafting groups after the LnPc<sub>2</sub> formation. Therefore effective post functionalization methods are in demand for LnPc<sub>2</sub> synthesis.

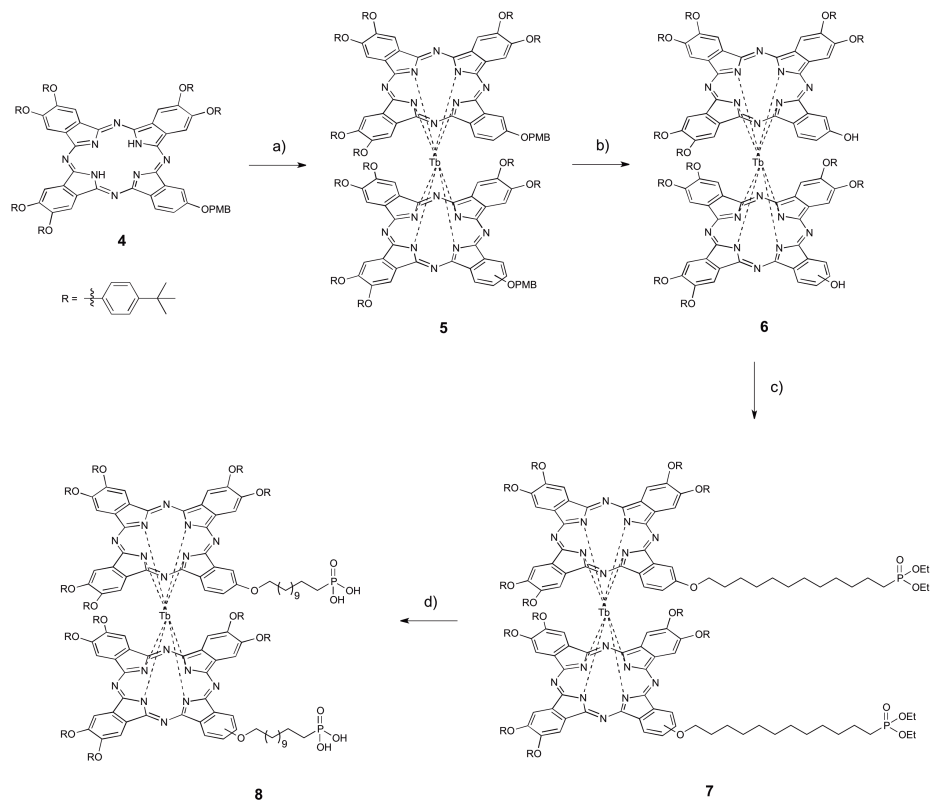
In this Chapter we present the novel preparation of iodinated TbPc<sub>2</sub>: the presence of aryl iodine atoms allows the further functionalization via Sonogashira reaction, one of the most important and widely used sp<sup>2</sup>-sp carbon-carbon bond formation reactions in organic synthesis.<sup>23</sup>

## **8.2 Results and Discussion**

### **8.2.1 Synthesis of Phosphonate TbPc<sub>2</sub>**

In order to promote the covalent grafting on LSMO, a TbPc<sub>2</sub> functionalized with phosphonic acid groups was designed (Scheme 8.1). Tatay and co-workers<sup>24</sup> reported in 2012 the self-assembling monolayer formation on LSMO via aklylphosphonic acid groups without affecting the electrode spin

polarization properties of the substrate. Synthesis of such functionalized TbPc<sub>2</sub> requested a demanding synthetic effort, as many pathways turned out to be unfeasible.

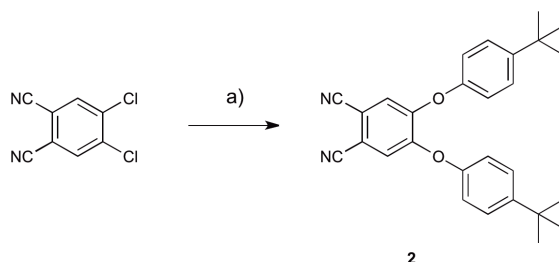


**Scheme 8.1** Synthesis of **8**: a) [Tb(acac)]<sub>n</sub>H<sub>2</sub>O, MeOLi, 1-octanol, 195°C, 1.5 h, 35%; b) trifluoroacetic acid, DCM, r.t, 2 h, quantitative; c) **1**, K<sub>2</sub>CO<sub>3</sub>, DMF, 90°C, 12 h, 48%; d) HCl 37%, 95°C under microwave irradiation (300 W), 1.5 h, yield not determinable.

Synthesis of **8** started from the asymmetric hydroxyl-protected Pc **4**. Synthesis and mostly purification of asymmetric Pcs is a long-standing challenge for synthetic chemists: however, partially inspired by a work published in 2011,<sup>25</sup> we developed a very useful protocol to synthesize A<sub>3</sub>B type hydroxyl-functionalized and the corresponding TbPc<sub>2</sub> bearing two hydroxyl groups suitable for further functionalization. The hydroxyl group, protected with the *p*-methoxybenzyl group (PMB), is stable under the harsh reaction conditions of the TbPc<sub>2</sub> formation: moreover it's easily removed by TFA under mild conditions. We also found that using *p*-tert-butylphenoxy groups on the Pcs

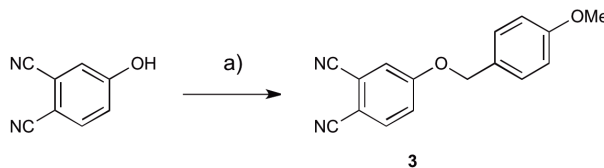
we were able to simplify the purification steps involving Pc and TbPc<sub>2</sub>. The bulky groups increase the solubility of the Pc and at the same time reduce their tendency to aggregate.

Functionalized phthalonitrile **2** was synthesized following a reported procedure,<sup>26</sup> starting from 4,5-dichlorophthalonitrile via a nucleophilic aromatic substitution with 4-*tert*-butylphenol, in DMSO in presence of potassium carbonate. At this point we performed the statistical Linstead cyclization on the monomers **3** and **4** in presence of lithium in refluxing 1-pentanol:



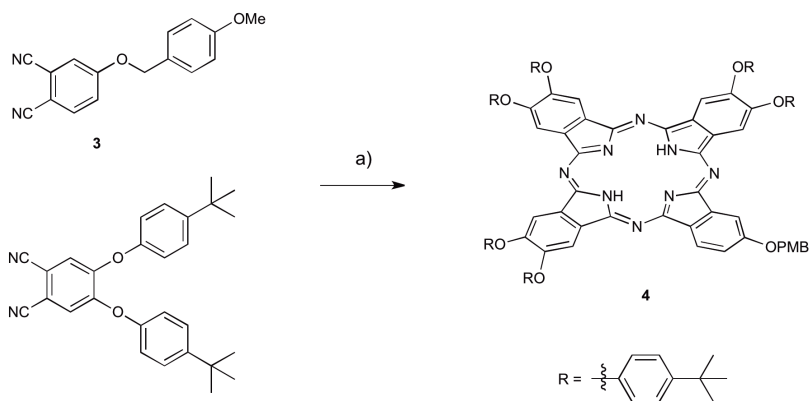
**Scheme 8.2** Synthesis of **2**: 4-*tert*-butylphenol, K<sub>2</sub>CO<sub>3</sub>, DMSO, 90°C, 2 h, 81%.

Hydroxyl-protected phthalonitrile **4** was prepared by reacting 4-hydroxyphthalonitrile with 4-methoxybenzyl chloride, in DMF in presence of sodium hydride (Scheme 8.3).



**Scheme 8.3** Synthesis of **3**: 4-methoxybenzyl chloride, NaH, DMF, 65°C, 4 h, 86%.

We found that, due to the lower reactivity of **3** the best stoichiometric ratio for the statistical condensation of **4** and **3** was 2:1 (Scheme 8.4).



**Scheme 8.4** Synthesis of **4**: Lithium, 1-pentanol, reflux, 3 h, 17%.

Purification by flash chromatography afforded the target A<sub>3</sub>B Pc **4** in 17% yield. The product was characterized by MALDI-TOF and <sup>1</sup>H NMR.

TbPc<sub>2</sub> formation was performed by heating Pc **4** in refluxing 1-octanol in presence of lithium methoxide (see Scheme 8.1). The use of lithium methoxide as a basic catalyst, instead of the more common DBU, allowed to obtain the target compound in higher yield. The advantage might derive from the noncoordinating nature of the lithium methoxide: the tendency of DBU to form coordinating bonds with the lanthanide ion of the intermediate half-sandwich mono(phthalocyanine) compound should create steric hindrance at the metal centre that prevents further complexation.<sup>27</sup> TbPc<sub>2</sub> **5** with two hydroxyl groups protected was obtained after purification in 16% yield and characterized by MALDI-TOF. At this point we performed the removal of the protecting groups with TFA in DCM at room temperature. We obtained compound **6** in quantitative yield, and we proceeded to the next synthetic step without any further purification. The introduction of the phosphonate groups was realized by attaching via nucleophilic substitution the diethyl 12-bromododecylphosphonate linker **1** (see Experimental section for the synthesis) to TbPc<sub>2</sub> **6**, in DMF at 90°C in presence of potassium carbonate. Compound **7** was obtained after purification by flash chromatography in 48% yield. Identity of the compound was confirmed by MALDI-TOF and <sup>31</sup>P NMR.

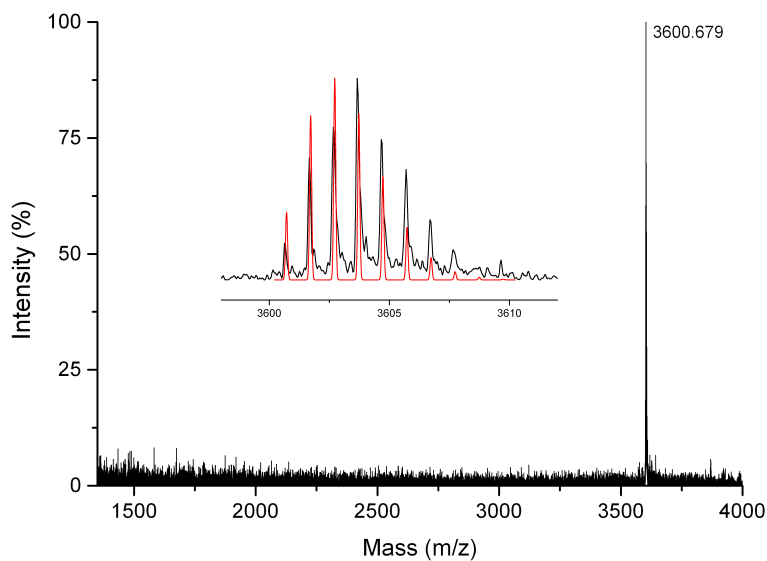


**Figure 8.4** High-resolution MALDI-TOF spectrum of phosphonate TbPc<sub>2</sub> **7**, with experimental (black lines) versus theoretical (black) isotopic distribution pattern in the inset.

MALDI-TOF spectrum showed the molecular peak at 3600.679 m/z, whose isotopic distribution matches the calculated one for the molecular ion of **7**. <sup>31</sup>P-NMR spectrum (Figure 8.5) showed a peak centered at 31.47 ppm, slightly up-field shifted with respect to the linker **1**. The presence of the paramagnetic Tb (III) does not affect the <sup>31</sup>P spectrum since the P atoms are far away from the metal.



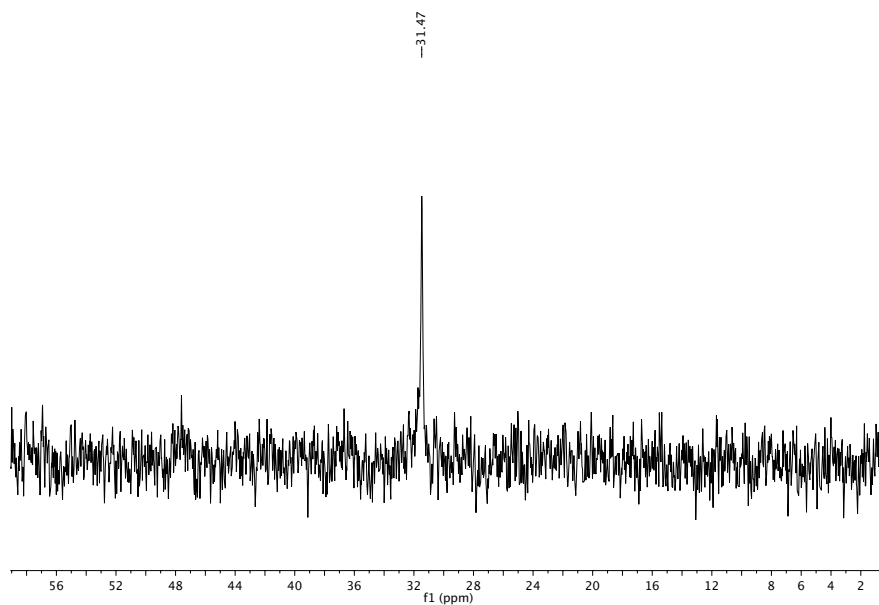
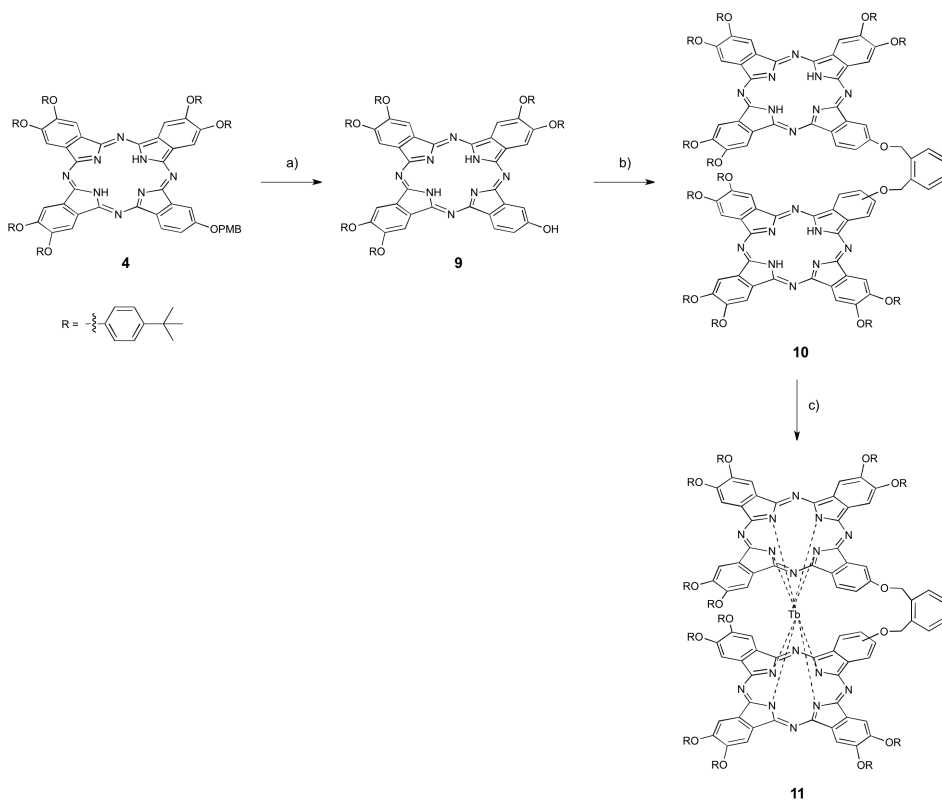


**Figure 8.5**  $^{31}\text{P}$  NMR of **7** in  $\text{CDCl}_3$ .

Every attempt we made to hydrolyze phosphonate groups on **7** failed, resulting in an inseparable mixture of **8** and products of partial hydrolysis. Thus we decided to employ directly complex **7** for the grafting on LSMO, as the use of phosphonate alkyl esters has already been reported for the surface modification of metal oxides in non aqueous media.<sup>28</sup>

8.2.2 Synthesis of Clamshell TbPc<sub>2</sub>

Clamshell TbPc<sub>2</sub> **11** was synthesized starting from the asymmetric A<sub>3</sub>B Pc **4** (Scheme 8.5).



**Scheme 8.5** Synthesis of **11**: a) trifluoroacetic acid, DCM, RT, 88%, 1 h; b) 1,2-bis(bromomethyl)benzene, NaH, DMF, 50°C, 12 h, 54%; c) [Tb(acac)]nH<sub>2</sub>O, MeOLi, 1-octanol, reflux, 2 h, 56%.

The removal of the hydroxyl protecting group PMB was accomplished with TFA in dichloromethane at room temperature. The reaction was completed in 1 h, and after flash chromatographic purification pure Pc **9** was isolated. Bisnuclear phthalocyanine **10** was obtained by reacting **9** with 1,2-bis(bromomethyl)benzene, using the stoichiometric ratio 0.5:1. The reaction was carried out in DMF in the presence of NaH at 50°C. Compound **10** was isolated after chromatographic purification in 54% yield. The identity of bisnuclear phthalocyanine **10** was confirmed by MALDI-TOF analysis.

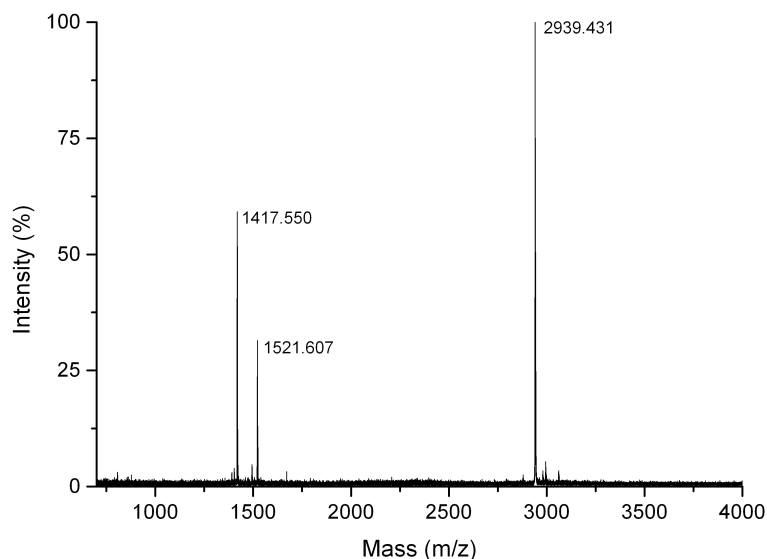


**Figure 8.6** High-resolution MALDI-TOF spectrum of bisnuclear Pc **10**.

The MALDI-TOF spectrum of binuclear phthalocyanine **10** contained, in addition to molecular ion peak at 2939.431 m/z, also signals of fragment ions formed upon cleavage of CH<sub>2</sub>-OPc bonds (Figure 8.6).<sup>29</sup> The amount of fragmentation depends on the laser power. At this point we performed the complexation reaction on **10** with terbium acetylacetonate and lithium methoxide in 1-octanol at 195°C. Purification by flash chromatography afforded clamshell TbPc<sub>2</sub> **11** in 55% yield.

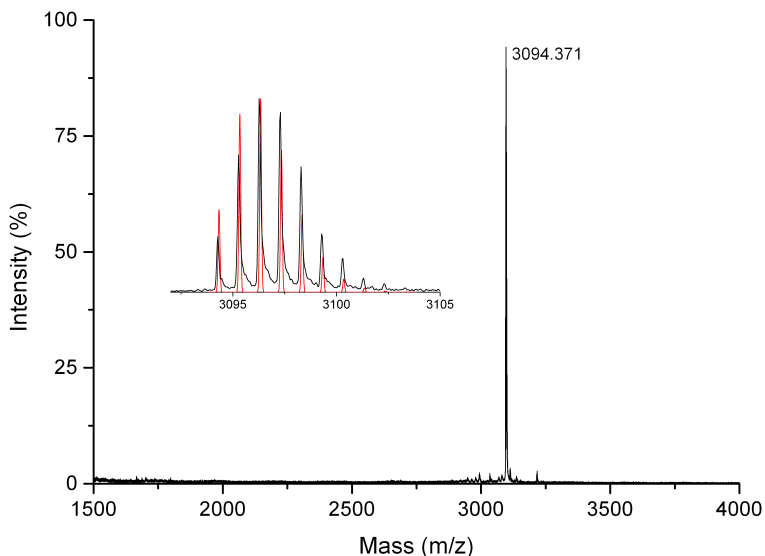


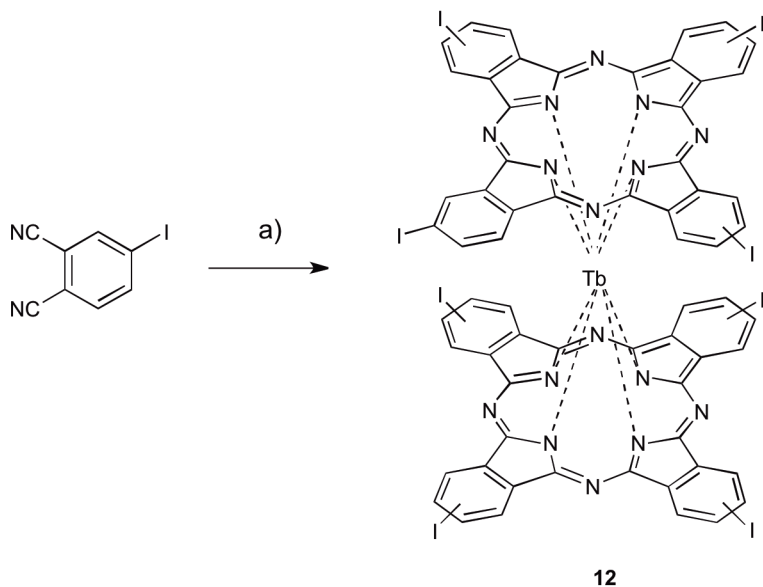
**Figure 8.7** High-resolution MALDI-TOF spectrum of clamshell TbPc<sub>2</sub> **11**, with experimental (black lines) versus theoretical (black) isotopic distribution pattern in the inset.

MALDI-TOF spectrum (Figure 8.7) revealed the molecular peak at 3094.371 m/z that corresponds well in position and isotopic distribution to the calculated ones for the molecular ion of **11**. Unlike bisnuclear phthalocyanine **10**, as a result of the terbium coordination with both Pcs, no fragmentation of benzyl bonds was observed. Moreover investigation with MALDI-TOF at higher m/z values excluded the formation of high molecular weight oligophthalocyanine complexes.

Note that compound **11** was isolated as an inseparable mixture of two regioisomers, which differ in spacer connection topology: isomer *a*, substituted at positions 2 and 2', and isomer *b*, linked at positions 2 and 3' of the phthalocyanine ligands (Figure 8.1).

### 8.2.3 Synthesis of Iodinated TbPc<sub>2</sub>

Homoleptic Tb(PcI<sub>4</sub>)<sub>2</sub> **12** was synthesized performing the De Cian synthesis starting from 4-iodophthalonitrile, a commercially available reagent, with terbium acetylacetonate in refluxing 1-hexanol in presence of DBU as basic catalyst (Scheme 8.6).



**Scheme 8.6** Synthesis of **12**:  $[Tb(acac)]_nH_2O$ , DBU, 1-hexanol, reflux, 2 h, 42%.

The crude contained a mixture of the desired neutral  $TbPc_2$  **12** and its corresponding reduced complex  $[TbPc_2]H$ . The treatment of the mixture with DDQ afforded the fully oxidation of the reduced form into the free-radical neutral complex. Homoleptic  $Tb(PcI_4)_2$  **12** was isolated after purification by flash chromatography in 42% yield and characterized by UV-VIS and MALDI-TOF (Figure 8.8).

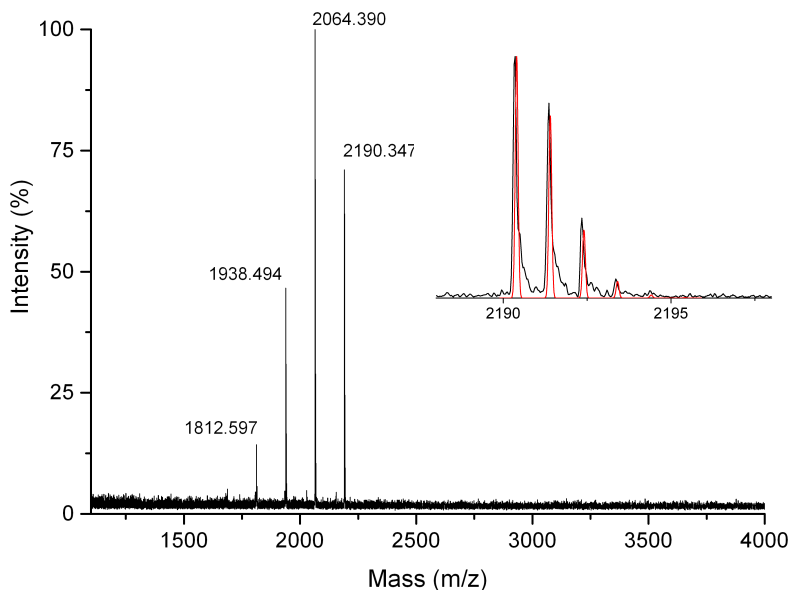


**Figure 8.8** High-resolution MALDI-TOF spectrum of **12**, with experimental (black lines) versus theoretical (black) isotopic distribution pattern in the inset.

MALDI-TOF spectrum revealed the molecular peak at 2190.347 m/z that corresponds well in position and isotopic distribution to the calculated ones for the molecular ion of **Tb(PcI<sub>4</sub>)<sub>2</sub>**. We also observed an unreported fragmentation pattern for this kind of compound: in fact we found three additional peaks at lower m/z values, relative to losses of one, two, three iodine atoms and simultaneous capture of the same equivalents of hydrogen atoms. The net result is an atomic exchange between iodine and hydrogen atoms in the molecular structure, caused by the laser of the instrument. Indeed, the amount of fragmentation depends on the laser power. Figure 8.9 shows MALDI-TOF spectrum of **12** at higher power: peaks due to losses up to six iodine atoms are observable.

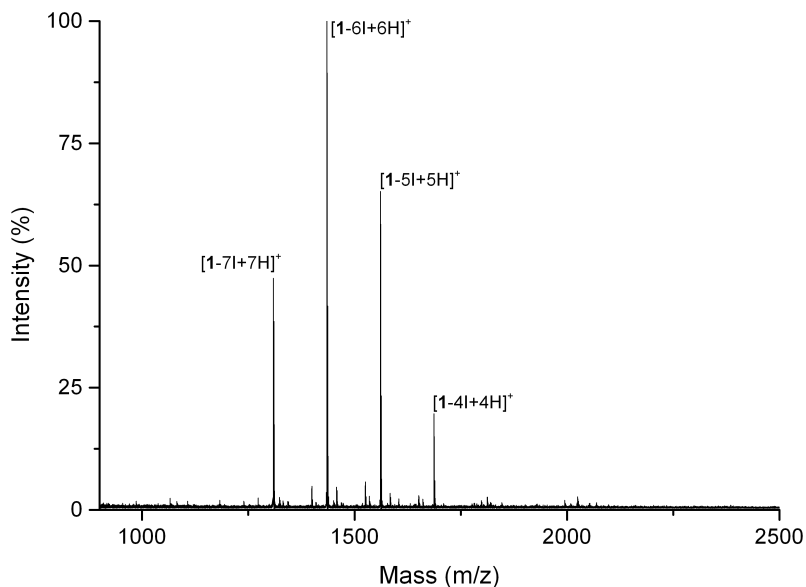


**Figure 8.9** High-resolution MALDI-TOF recorded at stronger laser power: peaks due to further fragmentations of **12** are visible.

Moreover  $^1\text{H}$  NMR experiments (Figure 8.10) confirmed the identity of the complex: the experimentally observed dipolar shifts for  $\alpha$ -protons (-96.5 ppm,  $\text{H}_\alpha$ ) and  $\beta$ -protons (-46.9 ppm) of the phthalocyanine cores were sufficiently resolved in  $\text{CDCl}_3$ , slightly up-field shifted with respect to the unsubstituted homoleptic  $\text{TbPc}_2$  (-85.4 ppm for  $\text{H}_\alpha$  - 40.6 ppm for  $\text{H}_\beta$ ).<sup>12</sup>

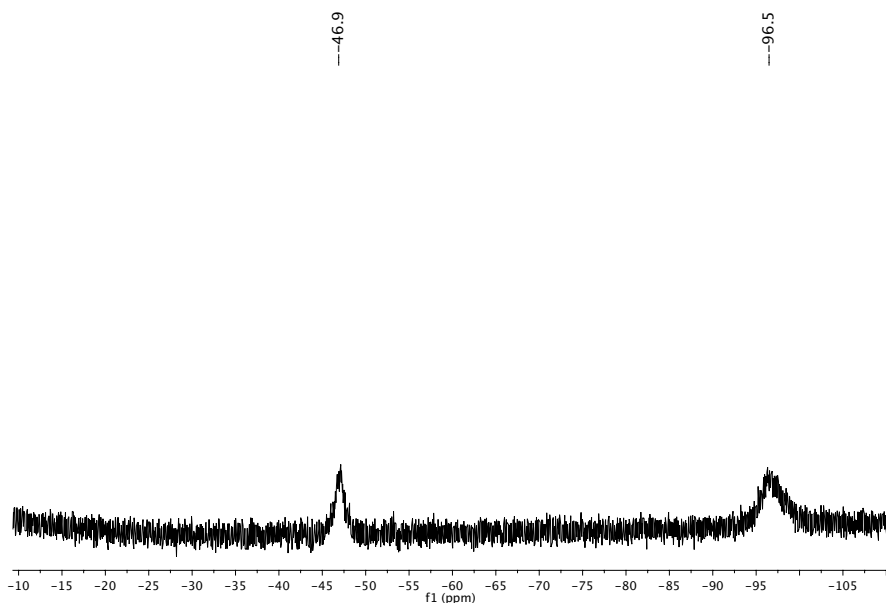
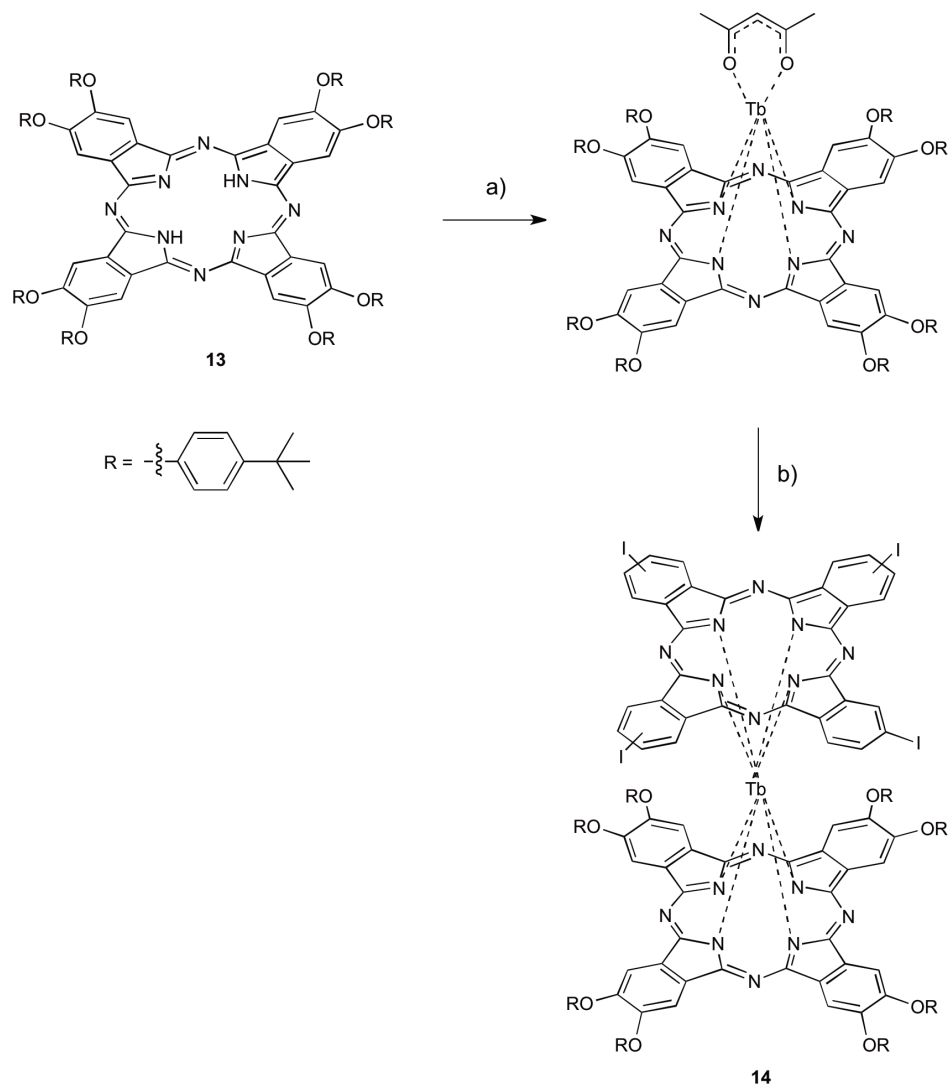


**Figure 8.10** <sup>1</sup>H NMR spectrum of **Tb(PcI<sub>4</sub>)<sub>2</sub> 12** recorded in CDCl<sub>3</sub> showing the chemical shifts for the H<sub>α</sub> and H<sub>β</sub> protons of the phthalocyanine rings.

The corresponding heteroleptic **TbPc(PcI<sub>4</sub>) 14** was synthesized via intermediate mononuclear lanthanide (III) Pc complex formation, starting from the free-base symmetric phthalocyanine **13**<sup>26</sup> (see Experimental section), followed by cyclic tetramerization of the 4-iodophthalonitrile around the terbium (III) center of the preformed monophthalocyaninate. Pc **13** was reacted with terbium acetylacetonate in in *o*-DCB at 170°C in presence of DBU (Scheme 8.7).





**Scheme 8.7** Synthesis of **14**: a)  $[Tb(acac)]nH_2O$ , *o*-dichlorobenzene, DBU,  $170^\circ C$ , 1.5 h; b) 4-iodophthalonitrile, *o*-dichlorobenzene/1-pentanol,  $160^\circ C$ , 4 h, 28% (over two steps).

The formation of the half sandwich complex was monitored by UV/Vis spectroscopy, which showed a decrease in the intensity of the two distinctive bands metal-free Pc derivatives and the growth of a new band in-between them. After the removal of the solvent, the half sandwich complex was reacted, without any further purification, with 4-iodophthalonitrile in *o*-DCB/1-pentanol at  $160^\circ C$  in presence of DBU. The cyclic tetramerization of the

phthalonitrile around the terbium(III) center of the preformed complex led to the heteroleptic **TbPc(PcI<sub>4</sub>) 14** formation. The crude was treated with DDQ in order to promote the oxidation of the reduced protonated complex, [Tb<sup>III</sup>(Pc)<sub>2</sub>H] (blue) to the free radical neutral form [Tb<sup>III</sup>(Pc)<sub>2</sub>] (green). After chromatographic purification **14** was isolated in 28% yield. The compound was characterized by MALDI-TOF (Figure 8.11) and UV-Vis.

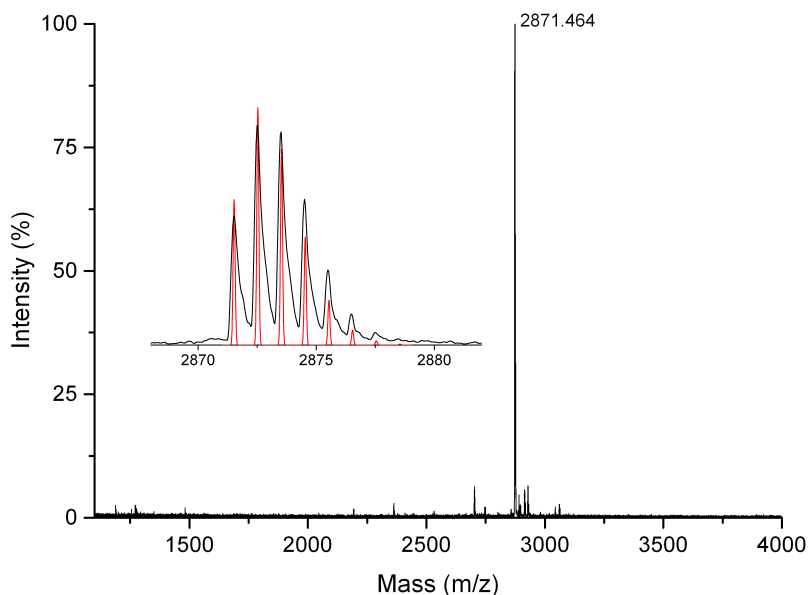


**Figure 8.11** High-resolution MALDI-TOF spectrum of **14**, with experimental (black lines) versus theoretical (black) isotopic distribution pattern in the inset.

MALDI-TOF spectrum revealed a unique peak centered at 2871.464 corresponding well in position and isotopic distribution to the calculated ones for the molecular ion of **TbPc(PcI<sub>4</sub>) 14**. Peak due to the single-atom loss of iodine is observable at lower  $m/z$  values: also in this case fragmentation is laser power-dependent (spectrum not shown).

## 8.2.4 Magnetic Characterization

Magnetic characterizations with standard dc magnetometric techniques were performed on the four functionalized TbPc<sub>2</sub> complexes in order to verify their SMM behaviors (Figure 8.12).

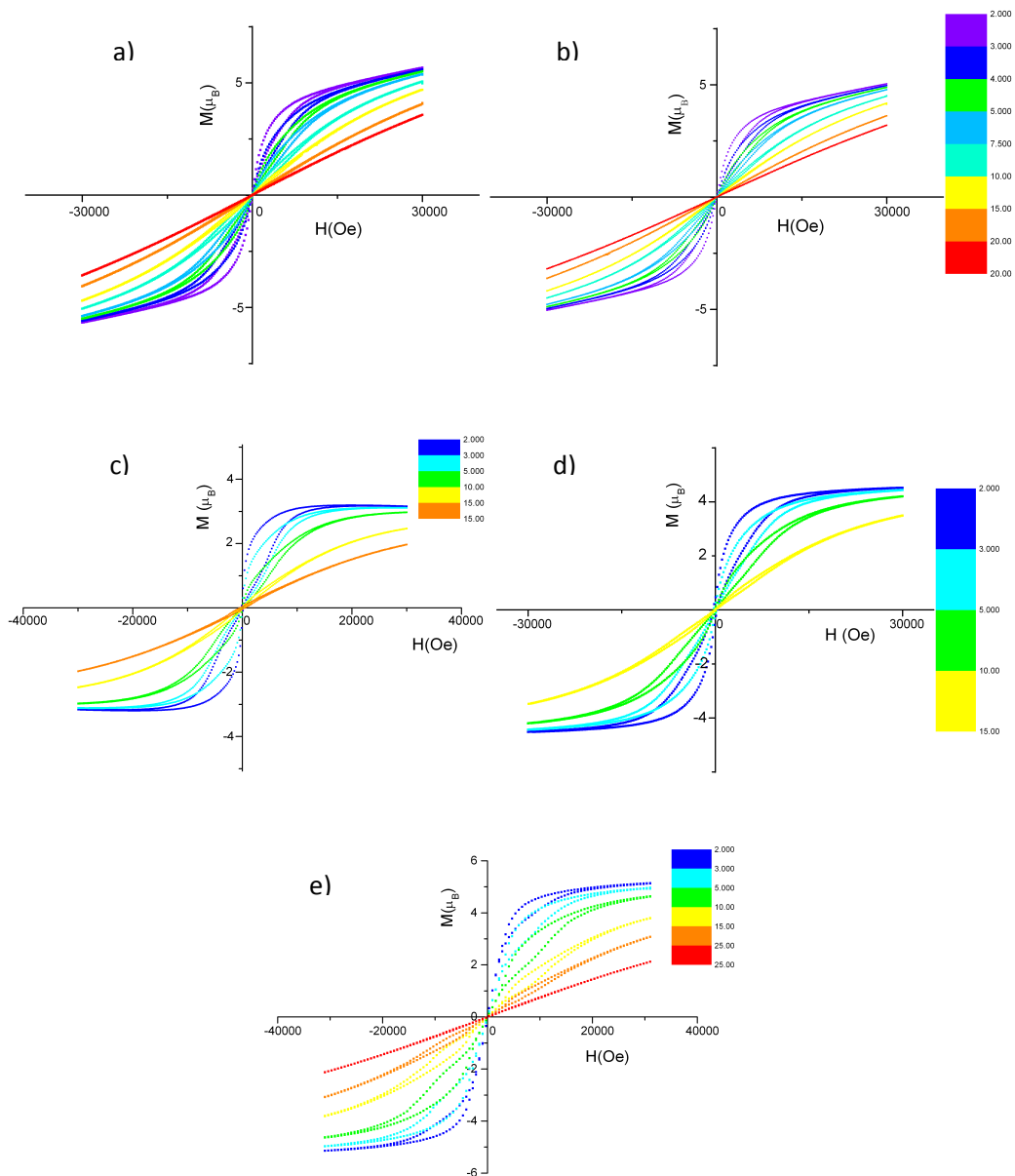


**Figure 8.12** Temperature dependence of the hysteresis loop recorded on a)  $Tb(PcI_4)_2$  12, b)  $TbPc(PcI_4)$  14, c) clamshell  $TbPc_2$  11, d) diethyl bisphosphonate  $Tb(Pc)_2$  7 and e) homoleptic unsubstituted  $TbPc_2$  at a field sweeping rate of  $50 \text{ Oe s}^{-1}$ .

Magnetization versus field measurements performed at several temperatures and scanning the field between 30 and - 30 kOe at 50 Oe s<sup>-1</sup> evidenced for all of the compounds an opening of the hysteresis with the typical butterfly shape induced by the enhancement of quantum tunnelling in zero applied field, confirming their SMM. Nevertheless, by comparison with the homoleptic unsubstituted TbPc<sub>2</sub> complex (Figure 8.12e),<sup>30</sup> we noticed that none of the synthesized compounds showed the hysteresis opening at temperature as high as the unfunctionalized TbPc<sub>2</sub> (25 K). However the saturation magnetization values appeared comparable with the one observed for unsubstituted homoleptic TbPc<sub>2</sub>.

Ac measurements were performed in order to determine energy barrier ( $U_{eff}$ ) and relaxation time ( $\tau_0$ ): ac susceptibility  $\chi''(T)$  was measured for frequencies from 0.5 Hz up to 10 kHz in a temperature range 5–60 K under a static applied field of 5 kOe. The  $\chi''$  versus frequency curves were analyzed by using the Debye model and the relaxation times  $\tau$  extracted from ac data. By fitting this data with the Arrhenius law we can extract  $\tau_0$  and  $U_{eff}$  values (Eq. 8.1):<sup>31</sup>

$$\ln\tau = \ln\tau_0 + \frac{U_{eff}}{k_B T} \quad \text{Eq. 8.1}$$

Magnetic data resulted by the fitting procedure for the functionalized TbPc<sub>2</sub> complexes are summarized in Table 8.1.

	$\tau_0$ (s)	$U_{eff}$ (K)
TbPc <sub>2</sub> (31)	(1.50 ± 0.1)*10 <sup>-12</sup>	856 ± 20
Phosphonate Tb(Pc) <sub>2</sub> (7)	(2.57 ± 2.09)*10 <sup>-12</sup>	834 ± 37
Clamshell TbPc <sub>2</sub> (11)	(5.66 ± 2.97)*10 <sup>-12</sup>	789 ± 22
Tb(PcI <sub>4</sub> ) <sub>2</sub> (12)	(1.71 ± 0.61)*10 <sup>-12</sup>	917 ± 18
TbPc(PcI <sub>4</sub> ) (14)	(8.49 ± 6.71)*10 <sup>-13</sup>	947 ± 37

**Table 8.1** Magnetic parameters extracted from ac susceptibility data under a static applied field of 5 kOe for the four functionalized TbPc<sub>2</sub> complexes and the homoleptic unfunctionalized TbPc<sub>2</sub>.

Although these values are affected by high experimental error, the comparison with the magnetic data for the unsubstituted amorphous TbPc<sub>2</sub><sup>31</sup> confirmed the

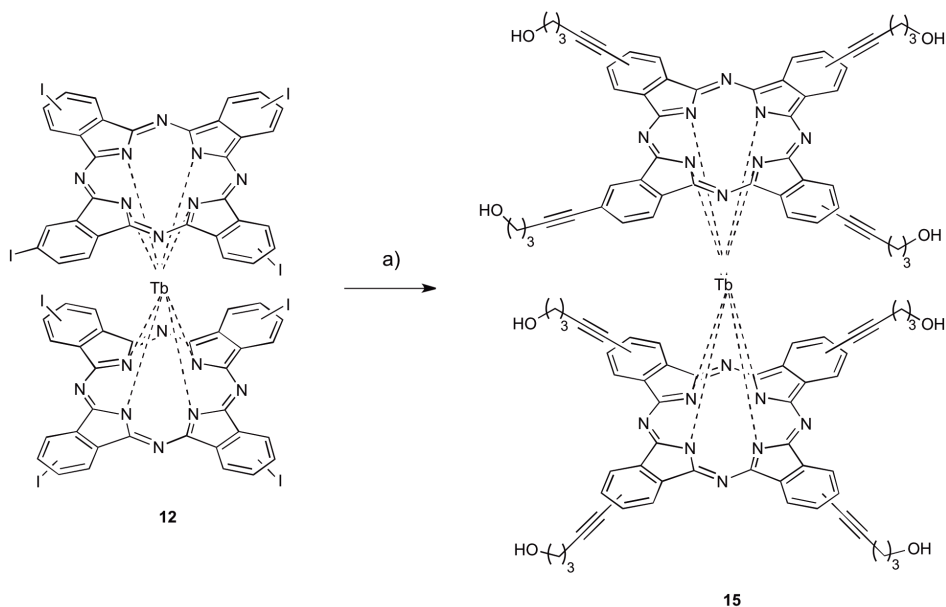
retention of the SMM behavior after the peripheral functionalization. The obtained results can be summarized as follows:

- Phosphonate TbPc<sub>2</sub> **7**: SMM behavior of **7** was confirmed by ac and dc measurements. This will allow us to further proceed with the covalent grafting on LSMO surface (currently under investigation).
- Clamshell TbPc<sub>2</sub> **11**: although the SMM behavior was retained, from the analysis of magnetic data (Table 8.1) we must conclude that the covalent connection through a flexible linker between the two Pcs of a TbPc<sub>2</sub> did not lead to any improvements in its magnetic properties.
- Iodinated TbPc<sub>2</sub> **12** and **14**: the SMM behavior was confirmed for both homoleptic and heteroleptic TbPc<sub>2</sub> complexes, with comparable  $U_{eff}$  and  $\tau_0$  with respect to the unsubstituted homoleptic amorphous TbPc<sub>2</sub>. The presence of aryl iodine atoms made them suitable for the further functionalization via Sonogashira reaction.

### 8.2.5 Sonogashira@TbPc<sub>2</sub>

The coupling of aryl or vinyl halides with terminal acetylenes catalyzed by palladium and other transition metals, commonly termed as Sonogashira cross-coupling reaction, is one of the most important and widely used sp<sup>2</sup>-sp carbon-carbon bond formation reactions in organic synthesis, frequently employed in the synthesis of natural products, biologically active molecules, heterocycles, molecular electronics, dendrimers and conjugated polymers or nanostructures.<sup>23</sup>

In order to verify the feasibility of Sonogashira reaction on iodinated TbPc<sub>2</sub>, we reacted **Tb(PcI<sub>4</sub>)<sub>2</sub>** with 4-pentyn-1-ol as alkynyl substrate at room temperature in a mixture 1:1 of TEA and THF, in presence of CuI and Pd(PPh<sub>3</sub>)<sub>4</sub> as active catalyst (Scheme 8.8).



**Scheme 8.8** Synthesis of **15**: a) 4-pentyn-1-ol,  $\text{Pd}(\text{PPh}_3)_4$ ,  $\text{CuI}$ , TEA, THF/TEA, r.t., 48 h, 40%.

The reaction was monitored with MALDI-TOF spectra acquisition: after 48 hours most of the starting **12** was converted to the octasubstituted target molecule **15**. Purification with flash chromatography column, followed by preparative TLC, afforded the isolation of **15** with 40% yield, a remarkable result for an octafunctionalization reaction. We directly isolated the neutral complex  $\text{TbPc}_2$ , without treatment with DDQ: in fact in this case the crude of the reaction only contained the neutral complex, and not its corresponding reduced complex  $[\text{TbPc}_2]\text{H}$ . However when we registered the UV-Vis spectrum in DMSO, the only solvent where **15** was sparingly soluble, we only observed the blue anionic form (Figure 8.13).

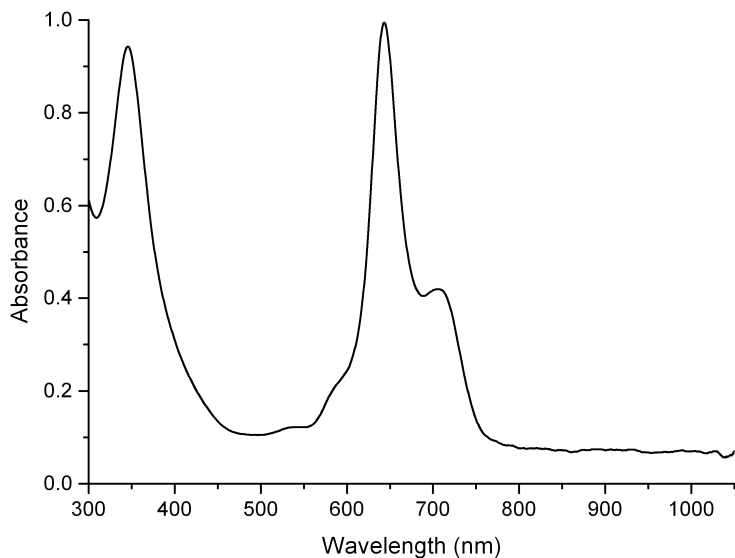


*Figure 8.13* UV-Vis absorption spectrum for **15** in DMSO.

The UV-Vis spectrum shows all the characteristic changes associated with the single-electron reduction of a TbPc<sub>2</sub>.<sup>32</sup> The reduced complex formation was most likely related to the solvent: indeed by adding DDQ directly into the UV cuvette we were able to promote the single-electron oxidation to restore the green neutral form (spectrum not shown).

The identity of **15** was confirmed from the MALDI-TOF spectrum (Figure 8.14).

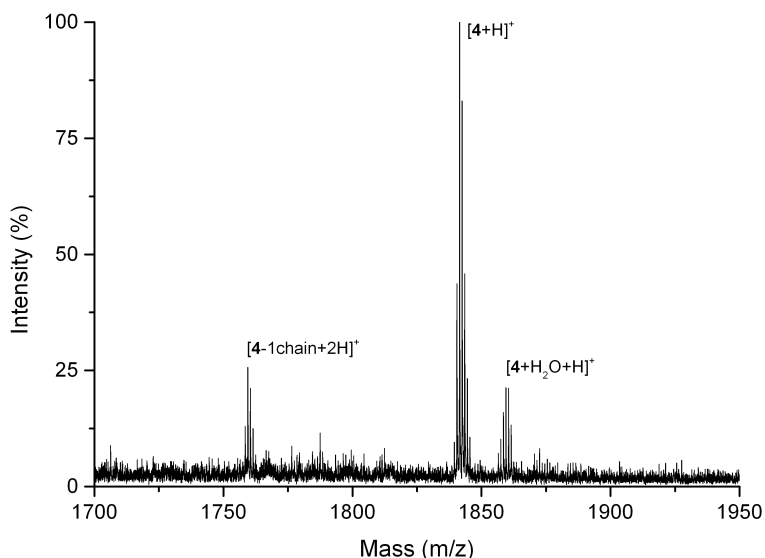


**Figure 8.14** High-resolution MALDI-TOF spectrum of **15**.

MALDI-TOF recorded in positive mode revealed a peak centred at 1840.488 corresponding well in position and isotopic distribution to the calculated ones for the molecular ion  $[15+H]^+$ . In fact the presence of the OH groups promoted the protonation of **15**. Fragmentation of one peripheral chain, substituted by a hydrogen atom, led to the formation of peak at 1758.431. It's noteworthy that this peak couldn't be due to the incomplete functionalization of **1**: in that case we would also observe the peak centred at 1884.572 due to the unfragmented TbPc<sub>2</sub> still bearing one iodine group. The peak observable at higher values of  $m/z$  (1858.510) is the protonated adduct with a molecule of water  $[15+H_2O+H]^+$ .

Although in literature Sonogashira reaction has been already exploited for phthalocyanines functionalization,<sup>33</sup> here we reported the first example of Sonogashira reaction performed on LnPc<sub>2</sub>. Even though these are preliminary tests, the novelty and the scientific impact of the reaction is clear. Different substrates will be further tested: the fine tuning of this methodology will allow the development of a new protocol for realize functionalized LnPc<sub>2</sub> to be integrated in the realization of SMMs-based devices.



### 8.3 Conclusions

In summary, four novel functionalized TbPc<sub>2</sub> complexes have been synthesized and the retain of their SMM behaviors has been proved by magnetic measurements.

- Phosphonate TbPc<sub>2</sub> **7** has been synthesized in three synthetic steps from Pc **4** in 17% overall yield. The presence of the phosphonate groups will allow the covalent grafting on LSMO surface.

- Clamshell TbPc<sub>2</sub> **11** has been successfully synthesized in three synthetic steps from the asymmetric Pc **4** in 27% overall yield. The magnetic characterization confirmed showed no improvements in blocking temperature  $T_b$  nor in the energy barrier  $U_{eff}$  in comparison with the unsubstituted homoleptic TbPc<sub>2</sub>. Thus we conclude that the impact on the resulting magnetic properties of the covalent connection through a flexible linker between the two Pcs of a TbPc<sub>2</sub> is ineffective.

- Iodinated TbPc<sub>2</sub> **12** and **14** have been synthesized in 42% and 28% yield respectively. The presence of aryl iodine atoms on the molecular structure has allowed us to successfully perform Sonogashira reaction on **Tb(PcI<sub>4</sub>)<sub>2</sub> 12**. This new synthetic protocol can be fruitfully exploited by using various substrates, thus obtaining differently functionalized TbPc<sub>2</sub> compounds.

### 8.4 Acknowledgments

Special thanks to Dr. Gianluca Paredi from the interdepartmental Centre SITEIA.PARMA, University of Parma, for mass spectrometry measurements. Thanks to Prof. Roberta Sessoli, Dr. Matteo Mannini and Dr. Nicola Cristiani from department of Chemistry, University of Firenze, for magnetic measurements.

## 8.5 Experimental Section

### Diethyl 12-bromododecylphosphonate (1)

A mixture of 1,12-dibromododecane (2 g, 6.10 mmol) and triethylphosphite (0.351 mL, 2.02 mmol) was stirred at 220°C under microwave irradiation for 5 minutes. The resulting solution was purified by flash chromatography (ethyl acetate:hexane 7:3) to give **1** (0.7 g, 1.82 mmol, 90%) as a colorless oil.

<sup>1</sup>H NMR (CDCl<sub>3</sub>, 400 MHz): δ (ppm) = 4.08 (q, 4H, *J*=6.1 Hz, OCH<sub>2</sub>CH<sub>3</sub>), 3.39 (t, 2H, *J*=6.7 Hz, BrCH<sub>2</sub>CH<sub>2</sub>), 1.83 (q, 2H, *J*=6.9 Hz, BrCH<sub>2</sub>CH<sub>2</sub>), 1.70 (m, 2H, CH<sub>2</sub>P=O), 1.57 (m, 2H, BrCH<sub>2</sub>CH<sub>2</sub>CH<sub>2</sub>), 1.42-1.25 (m, 22H, -CH<sub>2</sub>- and OCH<sub>2</sub>CH<sub>3</sub>); <sup>31</sup>P{<sup>1</sup>H}NMR (CDCl<sub>3</sub>, 161.9 MHz): δ (ppm) = 32.7 (s, P=O).

ESI-MS: *m/z* 385.2 [M+H]<sup>+</sup>, 407.4 [M+Na]<sup>+</sup>, 425.1 [M+K]<sup>+</sup>.

### 4,5-Bis((4-*tert*-butylphenyl)oxy)phthalonitrile (2)

To a solution of 4,5-dichlorophthalonitrile (1 g, 5.07 mmol) in DMSO, 4-*tert*-butylphenol (1.68 g, 11.2 mmol) was added. The reaction mixture was heated to 90°C and K<sub>2</sub>CO<sub>3</sub> (6 X 1.03 g every 5 min, 44.8 mmol total) was added. The mixture was stirred at 90°C for 2 h. After cooling, the reaction was quenched by addition of HCl 1 N and the yellow precipitate was filtered, washed with water, and dried. Recrystallization from methanol afforded the pure product **2** as a white solid (1.74 g, 4.11 mmol, 81%).

<sup>1</sup>H NMR (CDCl<sub>3</sub>, 400 MHz): δ (ppm) = 7.49 (d, 4H, *J*=8.8 Hz, <sup>t</sup>Bu-ArH<sub>m</sub>), 7.16 (s, 2H, ArH), 7.04 (d, 4H, *J*=8.8 Hz, <sup>t</sup>Bu-ArH<sub>o</sub>), 1.38 (s, 18H, ArCCH<sub>3</sub>).

ESI-MS: *m/z* 447.3 [M+Na]<sup>+</sup>, 463.2 [M+K]<sup>+</sup>.

### 4-((4-Methoxybenzyl)oxy)phthalonitrile (3)

To a solution of 4-hydroxyphthalonitrile (0.5 g, 3.47 mmol) in DMF, NaH (0.208 g, 8.67 mmol) and 4-methoxybenzyl chloride (0.565 mL, 4.16 mmol) were added. The reaction mixture was stirred at 65°C for 4 h. After cooling, solvent was evaporated under reduced pressure and the crude was extracted with ethyl acetate and washed with H<sub>2</sub>O. The organic layer was dried over Na<sub>2</sub>SO<sub>4</sub>. Evaporation under reduced pressure afforded the crude product, which was further purified by flash chromatography (dichloromethane:hexane 8:2) to give **3** (0.8 g, 2.98 mmol, 86%) as a white solid.

<sup>1</sup>H NMR (CDCl<sub>3</sub>, 400 MHz): δ (ppm) = 7.70 (d, 1H, *J*=8.8 Hz, ArH), 7.34-7.32 (m, 3H, ArH and ArOCH<sub>2</sub>ArH<sub>o</sub>), 7.25 (dd, 1H, *J*=8.8, 2.6 Hz, ArH), 6.94 (d, 2H, *J*=8.7 Hz, ArOCH<sub>2</sub>ArH<sub>m</sub>), 5.09 (s, 2H, ArOCH<sub>2</sub>Ar), 3.83 (s, 3H, ArOCH<sub>3</sub>).

ESI-MS: *m/z* 287.2 [M+Na]<sup>+</sup>, 302.9 [M+K]<sup>+</sup>.

**A<sub>3</sub>B Phthalocyanine (4)**

Lithium (31.6 mg, 4.55 mmol) was suspended in 1-pentanol and the mixture was heated to 100°C until complete dissolution of the metal. The resulting solution was cooled down, **3** (100 mg, 0.379 mmol) and **2** (321.7 mg, 0.758 mmol) were added and the reaction mixture was stirred at 140°C for 3 h. Solvent was evaporated and green residue purified by flash chromatography (gradient from hexane:dichloromethane 1:1 to 3:7) to isolate A<sub>3</sub>B phthalocyanine **4** as a green solid (66 mg, 0.043 mmol, 17%).

<sup>1</sup>H NMR (CDCl<sub>3</sub>, 400 MHz): δ (ppm) = 8.52-7.06 (m, 37H, ArH), 4.05 (s, 2H, ArOCH<sub>3</sub>), 1.37 (s, 54H, ArCCH<sub>3</sub>).

**MALDI TOF:** calculated for C<sub>98</sub>H<sub>88</sub>N<sub>8</sub>O<sub>8</sub> [M]<sup>+</sup> m/z: 1538.751, found m/z= 1538.792.

**Tb[Pc(O-PMB)]<sub>2</sub> (5)**

To a stirred solution of **4** (127 mg, 0.082 mmol) in 1-octanol, [Tb(acac)]*n*H<sub>2</sub>O (22.6 mg, 0.049 mmol) and MeOLi (31.4 mg, 0.825 mmol) were added. The resulting mixture was stirred at 195°C for 1.5 h. The dark-green solution was cooled to room temperature and the solvent removed under reduced pressure. The residue was dissolved in CHCl<sub>3</sub>, 2,3-dichloro-5,6-dicyano-1,4-benzoquinone (DDQ, 44.7 mg, 0.197 mmol) was added, and the reaction was stirred at room temperature for 1.5 h. The solvent was removed under reduced pressure and the solid was purified by flash chromatography (dichloromethane:hexane 6:4) to give **5** as a green solid (46 mg, 0.014 mmol, 35%).

**MALDI TOF:** calculated for C<sub>200</sub>H<sub>192</sub>N<sub>16</sub>O<sub>16</sub>Tb [M]<sup>+</sup> m/z: 3232.396, found m/z= 3232.352.

**Tb[Pc(OH)]<sub>2</sub> (6)**

Trifluoroacetic acid (3 mL) was added to a solution of **5** (46.4 mg, 0.014 mmol) in dichloromethane. The reaction mixture was stirred at room temperature for 2 h. The solvent was evaporated to yield **6** (43 mg, 0.014 mmol, quantitative), that was used without any further purification for the next step.

**MALDI TOF:** calculated for C<sub>184</sub>H<sub>176</sub>N<sub>16</sub>O<sub>14</sub>Tb [M]<sup>+</sup> m/z: 2992.281, found m/z= 2992.250.

**Diethyl bisphosphonate Tb(Pc)<sub>2</sub> (7)**

To a solution of **6** (34.8 mg, 0.012 mmol) in DMF, **1** (18.4 mg, 0.048 mmol) and K<sub>2</sub>CO<sub>3</sub> (16.6 mg, 0.12 mmol) were added. The reaction mixture was stirred overnight at 90°C. The solvent was removed under reduced pressure and the

crude was purified by flash chromatography (chloroform as eluant) to give **7** as a green solid (21 mg, 0.005 mmol, 48%).

<sup>31</sup>P{<sup>1</sup>H}NMR (CDCl<sub>3</sub>, 161.9 MHz): δ (ppm) = 31.5 (s, P=O).

**MALDI TOF:** calculated for C<sub>216</sub>H<sub>242</sub>N<sub>16</sub>O<sub>20</sub>P<sub>2</sub>Tb [M]<sup>+</sup> m/z: 3600.714, found m/z= 3600.679.

### **Bisphosphonate Tb(Pc)<sub>2</sub> (8)**

A suspension of **7** (20.7 mg, 0.005 mmol) in HCl 37% (1 mL) was stirred at 95°C under microwave irradiation for 1.5 h. The green precipitate was filtered off and washed with water. Purification by flash chromatography of the crude resulted in an inseparable mixture of **8** and products of partial hydrolysis.

### **Phthalocyanine free OH (9)**

To a solution of phthalocyanine **4** (150 mg, 0.097 mmol) in dichloromethane, 1 mL of TFA was added and the mixture reaction was stirred at room temperature. The solvent was removed and the crude was purified by flash chromatography (chloroform as eluant) to afford **9** as a green solid (122 mg, 0.086 mmol, 88%).

**UV-Vis:** λ<sub>max</sub> (CHCl<sub>3</sub>) 703, 670, 648, 612, 345 nm.

**MALDI-TOF:** calculated for C<sub>92</sub>H<sub>90</sub>N<sub>8</sub>O<sub>7</sub> [M]<sup>+</sup> m/z: 1418.693, found m/z= 1418.676.

### **Bisnuclear phthalocyanine (10)**

To a solution of phthalocyanine **9** (80 mg, 0.056 mmol) dissolved in DMF, NaH (4.06 mg, 0.169 mmol) and 1,2-bis(bromomethyl)benzene<sup>34</sup> (7.38 mg, 0.028 mmol) were added. The reaction mixture was stirred overnight at 50°C. The solvent was removed and the green residue purified by flash chromatography (gradient from hexane:dichloromethane 5:5 to dichloromethane) to isolate compound **10** as a dark green powder (45 mg, 0.015 mmol, 54%)

**UV-Vis:** λ<sub>max</sub> (CHCl<sub>3</sub>) 700, 668, 641, 341 nm.

**MALDI-TOF:** calculated for C<sub>192</sub>H<sub>186</sub>N<sub>16</sub>O<sub>14</sub> [M]<sup>+</sup> m/z: 2939.433, found m/z= 2939.431.

### **Clamshell TbPc<sub>2</sub> (11)**

To a stirred solution of **10** (45 mg, 0.015 mmol) in 1-octanol, [Tb(acac)]<sub>n</sub>H<sub>2</sub>O (8.34 mg, 0.018 mmol) and MeOLi (3.47 mg, 0.091 mmol) were added. The reaction mixture was stirred at 195°C for 1.5 h. After cooling, the solvent was removed and the green residue was purified by flash chromatography to afford **11** as a dark green powder (26 mg, 0.008 mmol, 56%).

**MALDI-TOF:** calculated for  $C_{192}H_{182}N_{16}O_{14}Tb [M]^+$   $m/z$ : 3094.327, found  $m/z$ = 3094.371.

**UV-Vis:**  $\lambda_{max}$  ( $CHCl_3$ ) 917, 682, 616, 498, 364, 331 nm.

### Homoleptic $Tb(PcI_4)_2$ (**12**)

To a stirred solution of 4-iodophthalonitrile (100 mg, 0.394 mmol) in 1-hexanol,  $[Tb(acac)]_nH_2O$  (28.7 mg, 0.063 mmol) and DBU (59.6  $\mu L$ , 0.394 mmol) were added. The reaction mixture was stirred at 160°C for 4 h. The dark-green solution was cooled to room temperature and the solvent removed under reduced pressure. The residue was dissolved in  $CHCl_3$ , DDQ (22.3 mg, 0.098 mmol) was added, and the reaction was stirred at room temperature for 1.5 h. The solvent was evaporated and the solid was purified by flash chromatography (dichloromethane as eluent) to give **12** as a dark-green solid (45 mg, 0.021 mmol, 42%).

**MALDI-TOF:** calculated for  $C_{64}H_{24}I_8N_{16}Tb [M]^+$   $m/z$ : 2190.398, found  $m/z$  = 2190.347.

**UV-Vis:**  $\lambda_{max}$  ( $CHCl_3$ ) 915, 676, 610, 478, 357, 331 nm.

### 2,3,9,10,16,17,23,24-octa-(para-tert-butylphenoxy)-phthalocyanine (**13**)

A solution prepared dissolving 4,5-Bis((4-tert-butylphenyl)oxy)phthalonitrile (250 mg, 0.589 mmol) and DBU (89.3  $\mu L$ , 0.589 mmol) in 1-pentanol was stirred overnight at 140°C. After cooling, methanol was added and the green precipitate filtered off: further purification by flash chromatography yielded **13** as a green solid (130 mg, 0.077 mmol, 52%).

**$^1H$  NMR** ( $CDCl_3$ , 400 MHz):  $\delta$  (ppm) = 8.84 (s, 8, ArH), 7.40 (d, 16H,  $J=8.2$  Hz,  $^tBu-ArH_m$ ), 7.18 (d, 16H,  $J=8.1$  Hz,  $^tBu-ArH_o$ ), 1.35 (s, 72H,  $ArCCH_3$ ).

**MALDI-TOF:** calculated for  $C_{112}H_{114}N_8O_8 [M]^+$   $m/z$ : 1698.876, found  $m/z$  = 1698.892.

**UV-Vis:**  $\lambda_{max}$  ( $CHCl_3$ ) 705, 669, 608, 349 nm.

### Heteroleptic $TbPc(PcI_4)$ (**14**)

To a stirred solution of the metal free phthalocyanine **13** (245 mg, 0.144 mmol) in *o*-DCB,  $[Tb(acac)]_nH_2O$  (80 mg, 0.173 mmol) was added followed by DBU (28.4  $\mu L$ , 0.188 mmol). The solution was heated at 170°C for 1.5 h. The resulting dark-blue solution was cooled to room temperature and the solvent removed under reduced pressure. The residue was washed with hexane to give the corresponding intermediate  $[Tb(acac)(Pc)]$ , which was then reacted with 4-iodophthalonitrile (161.3 mg, 0.635 mmol) and DBU (28.4  $\mu L$ , 0.188 mmol) in a mixture *o*-DCB/1-pentanol (1:1). The resulting solution was stirred at 160°C for

3 h. The dark-green solution was cooled to room temperature and the solvent removed under reduced pressure. The residue was dissolved in CHCl<sub>3</sub>, DDQ (78.6 mg, 0.346 mmol) was added, and the reaction was stirred at room temperature for 1.5 h. The solvent was evaporated and the solid was purified by flash chromatography (dichloromethane:hexane 7:3) to give **14** as a green solid (111 mg, 0.039 mmol, 27%).

**MALDI-TOF:** calculated for C<sub>144</sub>H<sub>124</sub>I<sub>4</sub>N<sub>16</sub>O<sub>8</sub>Tb [M]<sup>+</sup> m/z: 2871.522, found m/z = 2871.464.

**UV-Vis:** λ<sub>max</sub> (CHCl<sub>3</sub>) 913, 679, 612, 358, 332 nm.

### **Tb[Pc(C<sub>5</sub>H<sub>6</sub>OH)]<sub>2</sub> (**15**)**

To a stirred solution of **12** (50 mg, 0.023 mmol) in THF/TEA (1:1), tetrakis(triphenylphosphine)-palladium(0) (0.53 mg, 2% mol) and copper iodide (1.13 mg, 0.006 mmol) were added. The resulting mixture was degassed 3 times with freeze pump thaw technique: 4-pentyn-1-ol (42.5 μL, 0.456 mmol) was added and the reaction mixture was stirred at room temperature. The formation of the target compound was monitored during the course of the reaction by MALDI-TOF. After 48 hours solvent was evaporated and the residue was purified by chromatography column followed by preparative TLC (DCM:MeOH 8:2). Compound **12** was isolated as dark green solid (17 mg, 0.009 mmol, 40%).

**MALDI-TOF:** calculated for C<sub>104</sub>H<sub>81</sub>N<sub>16</sub>O<sub>8</sub>Tb [M+H]<sup>+</sup> m/z: 1840.568, found m/z = 1840.488.

**UV-Vis:** λ<sub>max</sub> (DMSO) 706, 643, 345 nm.

### **Magnetic characterization of the bulk systems**

Quantum Design PPMS Vibrating Sample Magnetometer (VSM) set-up in the continuous measurement mode sweeping the magnetic field at 50 Oe·s<sup>-1</sup> was used to characterize the bulk samples, pressed in a pellet, between - 50 kOe and + 50 kOe. AC magnetic susceptibilities up to 10 kHz were measured with the same Quantum Design PPMS platform in zero and 5 kOe static fields. Quantum Design MPMS SQUID magnetometer was employed to extend the AC susceptibility measurements in the low frequency range (down to 0.1 Hz).

## 8.6 References

- <sup>1</sup> N. Domingo, E. Bellido, D. Ruiz-Molina, *Chem. Soc. Rev.* **2012**, *41*, 258–302.
- <sup>2</sup> P. Grünberg, R. Schreiber, Y. Pang, M. B. Brodsky, H. Sowers, *Phys. Rev. Lett.* **1986**, *57*, 2442-2445.
- <sup>3</sup> M. N. Baibich, J. M. Broto, A. Fert, F. Nguyen Van Dau, F. Petroff, P. Etienne, G. Creuzet, A. Friederich, J. Chazelas, *Phys. Rev. Lett.* **1988**, *61*, 2472-2475.
- <sup>4</sup> S. Sanvito, A. R. Rocha, *J. Comput. Theor. Nanosci.* **2006**, *3*, 624–642.
- <sup>5</sup> L. Bogani, W. Wernsdorfer, *Nature Mater.* **2008**, *7*, 179-186.
- <sup>6</sup> S. Parkin, X. Jiang, C. Kaiser, A. Panchula, K. Roche, M. Samant, *Proc. IEEE* **2003**, *91*, 661-680.
- <sup>7</sup> V. A. Dediu, L. E. Hueso, I. Bergenti, C. Taliani, *Nat. Mater.* **2009**, *8*, 707–716.
- <sup>8</sup> M. Urdampilleta, S. Klyatskaya, J.-P. Cleuziou, M. Ruben, W. Wernsdorfer, *Nature Mater.* **2011**, *10*, 502-506.
- <sup>9</sup> L. E. Hueso, J. M. Pruneda, V. Ferrari, G. Burnell, J.-P. Valdés-Herrera, B. D. Simons, P. B. Littlewood, E. Artacho, A. Fert, N. D. Mathur, *Nature* **2007**, *445*, 410-413.
- <sup>10</sup> L. Malavolti, L. Poggini, L. Margheriti, D. Chiappe, P. Graziosi, B. Cortigiani, V. Lanzilotto, F. Buatier de Mongeot, P. Ohresser, E. Otero, F. Choueikani, P. Sainctavit, I. Bergenti, V. A. Dediu, M. Mannini, R. Sessoli, *Chem. Commun.* **2013**, *49*, 11506-11508.
- <sup>11</sup> S. Demir, J. M. Zadrozny, M. Nippe, J. R. Long, *J. Am. Chem. Soc.* **2012**, *134*, 18546–18549.
- <sup>12</sup> N. Ishikawa, M. Sugita, T. Okubo, N. Tanaka, T. Iino, Y. Kaizu, *Inorganic Chemistry* **2003**, *42*, 2440-2446.

- <sup>13</sup> N. Ishikawa, Y. Mizuno, S. Takamatsu, T. Ishikawa, S. Koshihara, *Inorg. Chem.* **2008**, *47*, 10217-10219.
- <sup>14</sup> R. A. Layfield, *Organometallics* **2014**, *33*, 1084–1099.
- <sup>15</sup> N. Koike, H. Uekusa, Y. Ohashi, C. Harnood, F. Kitamura, T. Ohsaka, K. Tokuda, *Inorg. Chem.* **1996**, *35*, 5798-5804.
- <sup>16</sup> a) S. Kahlal, A. Mentec, A. Pondaven, M. L'Her, J.-Y. Saillard, *New J. Chem.* **2009**, *33*, 574–582; b) R. Wang, R. Li, Y. Bian, C.-F. Choi, D. K. P. Ng, J. Dou, D. Wang, P. Zhu, C. Ma, R. D. Hartnell, D. P. Arnold, J. Jiang, *Chem. Eur. J.* **2005**, *11*, 7351–7357.
- <sup>17</sup> V. E. Pushkarev, A. Y. Tolbin, F. E. Zhurkin, N. E. Borisova, S. A. Trashin, L. G. Tomilova, N. S. Zefirov, *Chem. Eur. J.* **2012**, *18*, 9046–9055.
- <sup>18</sup> N. Ishikawa, M. Sugita, T. Ishikawa, S. Koshihara, Y. Kaizu, *J. Phys. Chem. B* **2004**, *108*, 11265-11271.
- <sup>19</sup> A. De Cian, M. Moussavi, J. Fischer, R. Weiss, *Inorg. Chem.* **1985**, *24*, 3162-3167.
- <sup>20</sup> a) S. Kyatskaya, J. R. G. Mascarós, L. Bogani, F. Hennrich, M. Kappes, W. Wernsdorfer, M. Ruben, *J. Am. Chem. Soc.* **2009**, *131*, 15143–15151; b) M. Gonidec, R. Biagi, V. Corradini, F. Moro, V. De Renzi, U. del Pennino, D. Summa, L. Muccioli, C. Zannoni, D. B. Amabilino, J. Veciana *J. Am. Chem. Soc.* **2011**, *133*, 6603–6612; c) C. R. Ganivet, B. Ballesteros, G. de la Torre, J. M. Clemente-Juan, E. Coronado, T. Torres, *Chem. Eur. J.* **2013**, *19*, 1457-1465; d) M. Mannini, F. Bertani, C. Tudisco, L. Malavolti, L. Poggini, K. Misztal, D. Menozzi, A. Motta, E. Otero, P. Ohresser, P. Saintavitt, G. G. Condorelli, E. Dalcanale, R. Sessoli, *Nat. Commun.* **2014**, *5*, article number: 4582.
- <sup>21</sup> a) K. Ban, K. Nishizawa, K. Ohta, A. M. van de Craats, J. M. Warman, I. Yamamoto, H. Shirai, *J. Mater. Chem.* **2001**, *11*, 321-331; b) G. Lu, M. Bai, R. Li, X. Zhang, C. Ma, P.-C. Lo, D. K. P. Ng, J. Jiang, *Eur. J. Inorg. Chem.* **2006**, 3703–3709.



- <sup>22</sup> M. Gonidec, D. B. Amabilino, J. Veciana, *Dalton Trans.* **2012**, *41*, 13632-13639.
- <sup>23</sup> R. Chinchilla, C. Nájera, *Chem. Soc. Rev.* **2011**, *40*, 5084-5121.
- <sup>24</sup> S. Tatay, C. Barraud, M. Galbiati, P. Seneor, R. Mattana, K. Bouzehouane, C. Deranlot, E. Jacquet, A. Forment-Aliaga, P. Jegou, A. Fert, F. Petroff, *ACS Nano* **2012**, *6*, 8753-8757.
- <sup>25</sup> N. W. Polaske, H.-C. Lin, A. Tang, M. Mayukh, L. E. Oquendo, J. T. Green, E. L. Ratcli, N. R. Armstrong, S. S. Saavedra, D. V. McGrath, *Langmuir* **2011**, *27*, 14900-14909.
- <sup>26</sup> S. E. Maree, T. Nyokong, *J. Porphyrins Phthalocyanines* **2001**, *5*, 782-792.
- <sup>27</sup> V. E. Pushkarev, A. Y. Tolbin, N. E. Borisova, S. A. Trashin, L. G. Tomilova, *Eur. J. Inorg. Chem.* **2010**, 5254-5262.
- <sup>28</sup> C. Queffélec, M. Petit, P. Janvier, D. A. Knight, B. Bujoli, *Chem. Rev.* **2012**, *112*, 3777-3807
- <sup>29</sup> A. Y. Tolbin, V. E. Pushkarev, L. G. Tomilova, N. S. Zefirov, *Mendeleev Commun.* **2009**, *19*, 78-80.
- <sup>30</sup> L. Malavolti, M. Mannini, P. Car, G. Campo, F. Pineider, R. Sessoli, *J. Mater. Chem. C* **2013**, *1*, 2935-2942.
- <sup>31</sup> D. Gatteschi, R. Sessoli, J. Villain, *Molecular Nanomagnets* **2006**, Oxford University Press, Oxford.
- <sup>32</sup> M. Gonidec, E. S. Davies, J. McMaster, D. B. Amabilino, J. Veciana, *J. Am. Chem. Soc.* **2010**, *132*, 1756-1757:
- <sup>33</sup> a) E. M. Maya, P. Vazquez, T. Torres, *Chem. Eur. J.* **1999**, *5*, 2004-2013; b) A. J. Jiménez, F. Spänig, M. S. Rodríguez-Morgade, K. Ohkubo, S. Fukuzumi, D. M. Guldi, T. Torres, *Org. Lett.* **2007**, *9*, 2481-2484.
- <sup>34</sup> D. Kikuchi, S. Sakaguchi, Y. Ishii, *J. Org. Chem.* **1998**, *63*, 6023-6026.

# Chapter 9

## In Situ Metalation of Free Base Phthalocyanine Covalently Bonded to Silicon Surfaces<sup>\*</sup>

<sup>\*</sup> This chapter has been published in Beilstein Journal of Nanotechnology: F. Lupo, C. Tudisco, F. Bertani, E. Dalcanale, G. G. Condorelli, *Beilstein J. Nanotechnol.* **2014**, 5, 2222-2229.

## 9.1 Introduction

Free (Pc) and metallophthalocyanines (M-Pc) are molecules of great interest because of their versatile optical and electronic properties as well as their thermal stability.<sup>1</sup> These properties make them attractive molecular materials for applications in photovoltaic cells,<sup>2</sup> sensing devices,<sup>3</sup> catalysis,<sup>4</sup> cancer therapy<sup>5</sup> and molecular electronics.<sup>3a,6</sup> The most promising architecture for the exploitation of the potentialities of Pc and M-Pc is the organization of the molecules in a suitable and accessible way on a solid surface. Therefore, phthalocyanine thin films have been deposited by using different techniques including Langmuir-Blodgett deposition,<sup>7</sup> spincoating<sup>8</sup> and vapor deposition.<sup>8,9</sup> Well-organized monolayers and multilayers have been also obtained through self-assembly.<sup>10</sup> Among the various approaches adopted to organize phthalocyanines on surfaces, covalent grafting on H-terminated silicon through hydrosilylation reaction has the advantage to form robust and highly stable Si-C bonds. For this reason, a device based on silicon-grafted molecules possesses a much greater robustness and reliability compared to van der Waals films or Au-bonded layers, which makes these systems suited for application in aggressive environments.<sup>11</sup> In addition, the possible use of differently doped silicon substrates could influence the electronic properties of grafted Pc and M-Pc,<sup>3a</sup> and, in turn, the device properties. Furthermore, the overall chemical and physical properties of M-Pc can be easily tuned by varying the nature of the coordinated metal, thus making phthalocyanine-based systems suitable for a wide range of applications. In particular, transition metal Pc have attracted great interest for their optical and magnetic properties<sup>6b,12</sup> as well as for their potential catalytic<sup>4</sup> and sensing applications.<sup>3b</sup> Various metallophthalocyanines (Zn, Fe, Co, Cu, Sn) have been deposited as monolayers and multilayers on various surfaces<sup>10b,13</sup> and, in some cases, free base Pc have been metalated directly on the metal surface from vapor-deposited atoms.<sup>14</sup> However, no report of the direct metalation of covalently bonded Pc on inorganic surfaces has been reported, yet.

In this work we study the silicon grafting of the tetra-4-( $\omega$ -undecenyloxy)phthalocyanine (hereafter **1-Pc**) (Figure 9.1) and its interaction with a silicon surface. **1-Pc** was synthesized to allow for a silicon grafting by functionalization with four undecenyl chains each having a terminal double bond. Phthalocyanine covalent anchoring was performed through thermic hydrosilylation on flat Si(100) and on porous silicon (**Si-1-Pc** and **PSi-1-Pc**, respectively). The success of the anchoring strategy on both surfaces was demonstrated by the combination of X-ray photoelectron spectroscopy (XPS)

with control experiments performed adopting the commercially available 2,3,9,10,16,17,23,24-octakis(octyloxy)-29*H*,31*H*-phthalocyanine (hereafter **2-Pc**), which is not suited for silicon anchoring (Figure 9.1).

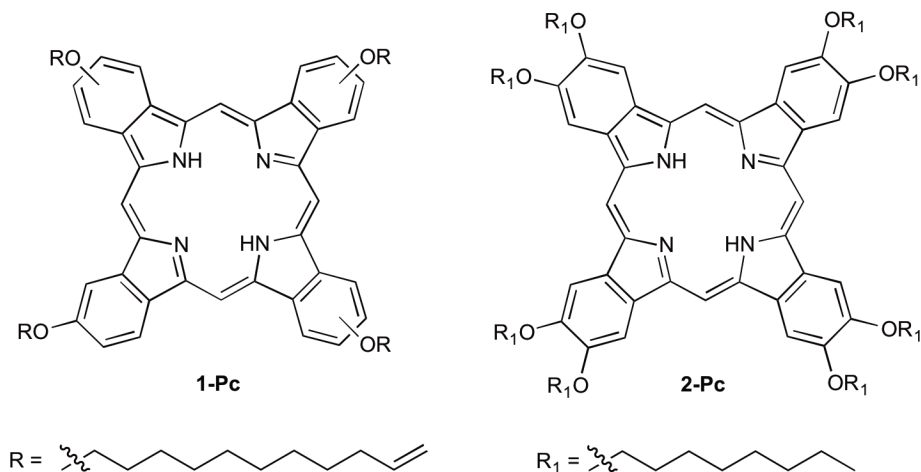


**Figure 9.1** Chemical structures of **1-Pc** and **2-Pc**.

**1-Pc** covalently bonded to silicon surface was in situ metalated with Co by using a solution of cobalt chloride. The direct formation of Co-Pc on flat and porous Si (**Si-Co-Pc** and **PSi-Co-Pc**, respectively) was monitored by XPS and FTIR. In particular, for phthalocyanines anchored on porous Si, transmission FTIR represents a suitable technique to monitor the M-Pc formation through the disappearance of the band at 3290 cm<sup>-1</sup>, corresponding to the pyrrolic -NH stretches.<sup>15</sup> Differences in the metalation efficiency between porous and flat silicon were evaluated by XPS and explained in terms of different surface interactions.

## 9.2 Results and Discussion

### 9.2.1 Synthesis of 1-Pc

Phthalocyanine **1-Pc** was prepared according to a slightly modified literature procedure<sup>16</sup> starting from the 4-(ω-undecenyl-oxy)phthalonitrile in refluxing 1-pentanol in presence of a catalytic amount of 1,8-diazabicyclo[5.4.0]undec-7-ene (DBU) as a basic catalyst. The target compound was isolated in 58% yield as a

dark-green powder after purification. **1-Pc** was successfully characterized by  $^1\text{H}$  NMR and MALDI-TOF mass spectrometry (see Experimental Section).

### 9.2.2 XPS Characterization of Si-bonded Phthalocyanine

Covalent anchoring of **1-Pc** on flat Si(100) and porous Si was performed through thermally activated hydrosilylation and the functionalized samples (**Si-1-Pc** and **PSi-1-Pc**, respectively) were characterized through XPS. In addition, further experiments were performed to demonstrate that the surface anchoring is not due to physisorption but it is due to the hydrosilylation reaction. Control samples were, therefore, prepared by treating flat and porous silicon surfaces with a phthalocyanine (**2-Pc**), in which no double bonds are present in the lateral chains, under the same experimental conditions adopted for **1-Pc** anchoring. Elemental compositions of **1-Pc** and **2-Pc** treated samples are reported in Table 9.1.

	<b>Si-1-Pc</b>	<b>Si-2-Pc</b>	<b>PSi-1-Pc</b>	<b>PSi-2-Pc</b>
C	36.6	11.8	56.5	30.5
N	2.4	0.5	4.6	0.6
Si	38.8	46.7	29.6	34.3
O	22.2	41.0	9.3	34.6

**Table 9.1** Atomic compositions (%) evaluated through XPS of **1-Pc** treated flat (**Si-1-Pc**) and porous (**PSi-1-Pc**) silicon samples. Analogous samples obtained from **2-Pc** treatment (**Si-2-Pc** and **PSi-2-Pc**) have been also reported as control experiments.

XPS data show that **Pc**-related signals (C 1s and N 1s) are higher for the **1-Pc** treated samples compared to the **2-Pc** treated samples. Since the C 1s signal is affected by the presence of ubiquitous adventitious carbon,<sup>17</sup> the success of **Pc** anchoring route can be evaluated from the N 1s signal, which is very low for **Si-2-Pc** and **PSi-2-Pc** samples while it is about 5 and 8 times higher for **1-Pc** treated surfaces. These data point to a surface-anchoring process determined by the hydrosilylation reaction of the double bonds while physisorption phenomena play a much less relevant role. The surface density of **1-Pc** on flat Si(100) was estimated from XPS data (Table 9.1).<sup>18</sup> The obtained value, ca.  $2 \times 10^{13}$  molecules/cm<sup>2</sup>, points to a molecular footprint of 5 nm<sup>2</sup> for each molecular

unit, which is intermediate between the cross-sectional areas expected for a configuration with the side chains vertical with respect to the phthalocyanine ring (ca. 1 nm<sup>2</sup>) and a configuration in which all four alkyl side chains are full extended in the same plane of the ring (ca. 9 nm<sup>2</sup>).

Useful information about the nature of the grafted layers was obtained from high-resolution spectra of the relevant photoemission bands. Figure 9.2 reports the C 1s photoelectron spectra of **Si-1-Pc** (a) and **PSi-1-Pc** (b). The observed bands do not show significant differences between flat and porous samples. For both samples, a careful deconvolution of the band envelope reveals three components: a main peak centered at 285.0 eV, due to both aliphatic and aromatic carbons;<sup>9</sup> a band at a binding energy (B.E.) of 286.5 eV due to the pyrrole carbons and to the shake-up related to benzene carbons, in tune with literature data;<sup>9</sup> and finally, a band at 288.3 eV (288.1 eV for **PSi-1-Pc**) due to the shake-up transition associated with the photoionization of pyrrole.<sup>9</sup>

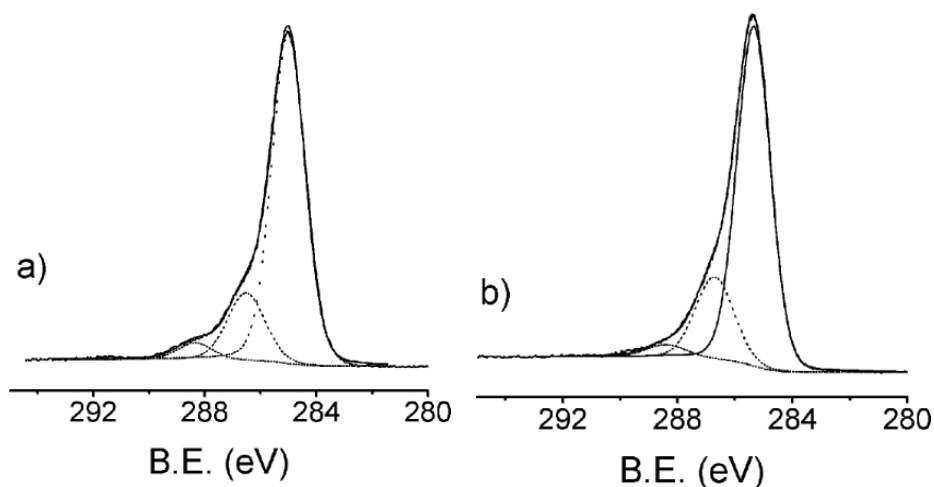


**Figure 9.2** C 1s XPS spectral region of a) **Si-1-Pc** and b) **PSi-1-Pc**.

The N 1s XPS spectral regions of **Si-1-Pc** and **PSi-1-Pc** are reported in Figure 9.3a and 9.3b, respectively. The spectrum collected from **Si-1-Pc** shows two bands, at B.E. values of 398.8 and 400.4 eV. The first signal is due to non-protonated pyrrolic nitrogen atoms and due to iminic bridges, whilst the high B.E. signal is due to protonated pyrrolic nitrogen atoms.<sup>19</sup> However the intensity ratio between the 398.8 and 400.6 eV bands is 2:3, which is significantly different from the value (3:1) expected for free-base phthalocyanines.<sup>19</sup> The increase of the high B.E signal can be explained as a consequence of the interaction with the silicon surface. The effects of various

surfaces on the shape of the N 1s band have been already observed and discussed for other metal phthalocyanine monolayers adsorbed on oxide semiconductors<sup>19</sup> and, recently, reported also for double-decker complexes on silicon.<sup>20</sup> In general, according to the mentioned studies, the interaction between the fraction of anchored phthalocyanine lying down close to the surface and the semiconductors surface itself, induce an electron depletion in the phthalocyanine ring and, in turn, a high energy shift (about 1.5 eV) from 398.8 to about 400.3 eV of the main N 1s component due to deprotonated nitrogen atoms.<sup>19a,19b,20</sup> Possible local interactions (i.e., H-bonds) between the phthalocyanine ring lying down close to the surface and the Si surface itself could contribute to a similarly high B.E. shift<sup>21</sup> and cannot be excluded. In any case, the surface-induced shift can explain the increase of the component at 400.4 eV and also the presence of a low shoulder at around 401.8 eV due to protonated nitrogen atoms.

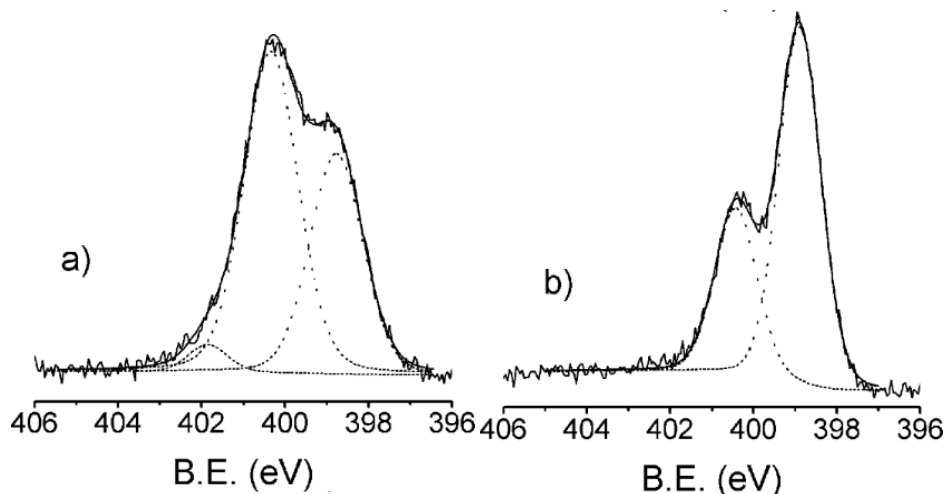
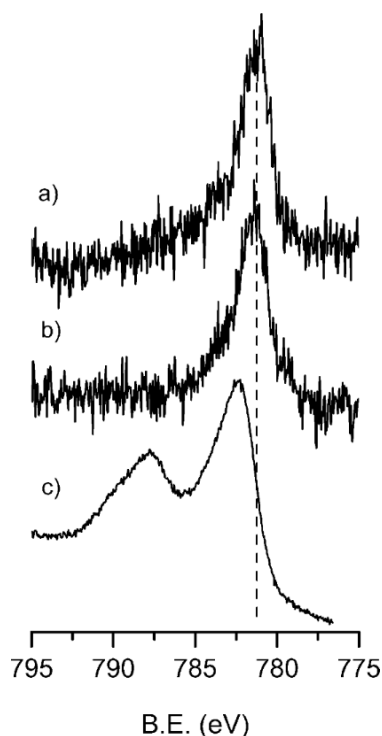


Figure 9.3 N 1s XPS spectral region of a) *Si-1-Pc* and b) *PSi-1-Pc*.

The N 1s XPS spectrum of **PSi-1-Pc** (Figure 9.3b) shows a different situation. The N 1s band consists of the same two components at 398.6 and 400.4 eV observed for **Si-1-Pc**, but in this case the component ratio is 2:1, which is closer to the value expected for free phthalocyanine, thus indicating that there are no strong interactions between the surface of P*Si* and the Pc molecules.

### 9.2.3 Metalation of SAM

The possibility to induce a direct metalation of the grafted Pc was explored for both **Si-1-Pc** and **PSi-1-Pc** samples. **1-Pc** that was covalently bonded to Si and PSi surfaces has been treated with a solution of  $\text{CoCl}_2$  in diglyme in the presence of triethylamine and then accurately sonicated to remove any physisorbed salt. XPS characterization of cobalt treated **Si-1-Pc** and **PSi-1-Pc** samples (**Si-Co-Pc** and **PSi-Co-Pc**, respectively) clearly showed the presence of Co, whilst no Cl could be detected (Cl content < 0.1% noise level). Similar bands centered at 781.2 eV are present in the spectra of both **Si-Co-Pc** and **PSi-Co-Pc** (Figure 9.4a and 9.4b). Although this band position is consistent with the presence of Co(II) atoms, the peak position and, in particular, the absence of the intense shake-up typical of Co(II) compounds such as  $\text{CoCl}_2$  (Figure 9.4c) indicate that Co signal is not due to physisorbed  $\text{CoCl}_2$ . The observed band shape and position are consistent with spectra reported for Co-phthalocyanine thin films.<sup>22</sup>



**Figure 9.4** Co  $2p_{3/2}$  XPS spectral region of a) **Si-Co-Pc** and b) **PSi-Co-Pc**. c) The Co  $2p_{3/2}$  region of  $\text{CoCl}_2$  powder has been added as reference.



In addition, complexation efficiency was estimated from the N/Co atomic ratio determined through XPS. Considering a theoretical N/Co ratio of 8 expected for 100% of complexation, N/Co ratios obtained for **Si-Co-Pc** and **PSi-Co-Pc** (28.6 and 10.7, respectively) indicate a percentage of metalation of 28% and 75%, respectively.

Further indication of Co complexation in the Pc-ring was obtained from the analysis of the N 1s spectra (Figure 9.5) after metalation.

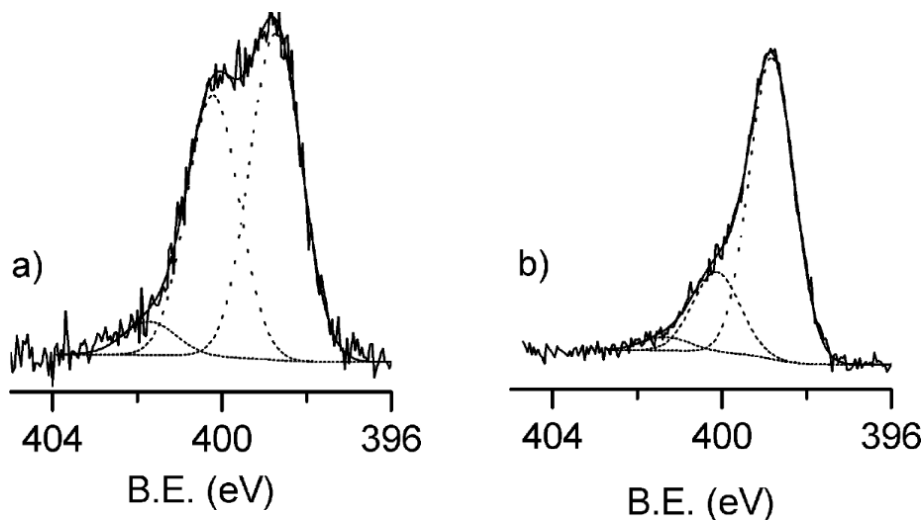
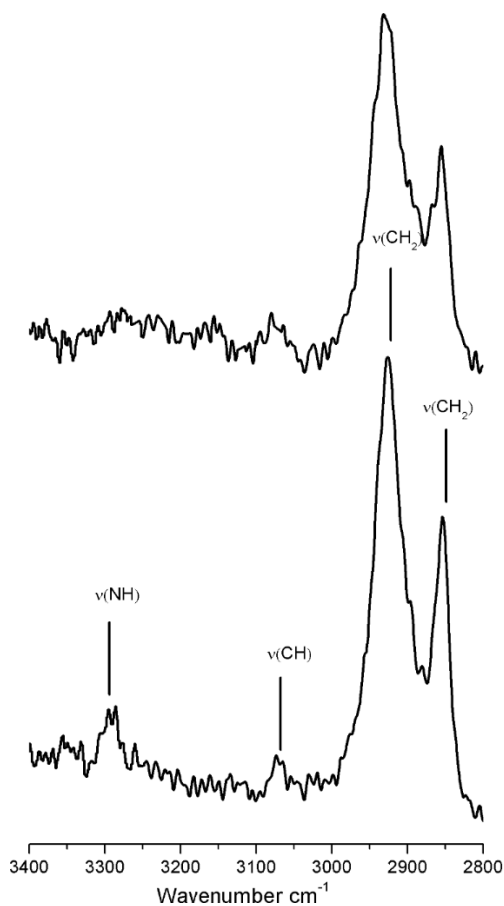


Figure 9.5 N 1s XPS spectral region of a) **Si-Co-Pc** and b) **PSi-Co-Pc**.

Clearly the presence of cobalt gives rise to a modification on the N 1s band shape compared to spectra before metalation (Figure 9.3). As expected, after metalation the intensity of the component at 400.4 eV due to -NH pyrrolic nitrogen atoms decreases compared to the low B.E. component at 398.8 eV since the metal coordination is associated to the deprotonation of pyrrolic nitrogen atoms to form N-Co.<sup>23</sup> In particular, for **PSi-Co-Pc**, for which the metalation efficiency is higher than that of **Si-Co-Pc**, the 400.4 eV signal becomes much lower and the spectrum becomes similar to the typical spectra of M-Pc in which a single band at low B.E. is present.<sup>23</sup> Note, in addition, that eventual interferences due to triethylamine physisorption on **PSi**, which would lead to the increase of the N 1s component around 400 eV, can be ruled out since the reverse trend was observed for **PSi-1-Pc**. Overall the metalation appears more efficient in the case of the porous silicon substrate compared to flat Si(100). This behavior is likely to be associated to the different surface interactions observed for **Si-1-Pc** and **PSi-1-Pc**. In the case of a flat substrate the proposed strong

surface interaction of the fraction of **1-Pc** lying down close the substrate prevents an efficient insertion of Co in the Pc ring, whilst in the case of porous samples, less strong surface interactions allow for a more efficient metalation. Further information about the grafting of **1-Pc** on porous silicon and about the in situ metalation could be obtained from transmission FTIR spectra by taking advantage of the high surface area of **PSi**. Figure 9.6 compares the FTIR region of 3400–2800  $\text{cm}^{-1}$  in which  $-\text{CH}_x$  and  $-\text{NH}$  stretches are present before and after the metalation. Typical bands present before the metalation are the strong  $\text{CH}_2$  stretches  $\nu_{\text{as}}(\text{CH}_2)$  at 2925  $\text{cm}^{-1}$  and  $\nu_{\text{sym}}(\text{CH}_2)$  at 2854  $\text{cm}^{-1}$ , the weak  $=\text{CH}$



**Figure 9.6** FTIR spectral region between 3400–2800  $\text{cm}^{-1}$  ( $\text{CH}_x$  stretching region) of **PSi-1-Pc** (below) and **PSi-Co-Pc** (above).

stretches  $\nu(=\text{CH})$  of the aromatic rings at 3070  $\text{cm}^{-1}$  and the characteristic  $-\text{NH}$  stretch of pyrrolic nitrogen atoms at about 3290  $\text{cm}^{-1}$ . After metalation,  $-\text{NH}$

stretch vibrations cannot longer be clearly detected, whilst the other bands are still observed. Since triethylamine is unable to deprotonate the phthalocyanine, the absence of N-H bonds is exclusively due to the Co complexation.<sup>15</sup>

### 9.3 Conclusions

The results presented here report on a grafting route to covalent anchor phthalocyanine on flat and porous silicon surfaces. The grafting route was validated by XPS characterization and control experiments that were performed by adopting a phthalocyanine inert towards hydrosilylation. XPS results also suggest that on flat substrates a relevant fraction of phthalocyanine interacts significantly with the silicon surface, thus inducing evident modifications of the N 1s band shape. On porous silicon, surface interactions are less relevant and the N 1s band shape is similar to the typical shape of free Pc.

In situ complexation of Co was achieved with phthalocyanine bonded to both flat and porous silicon surfaces. However, the metalation efficiency is higher in the case of porous samples. These differences were attributed to the different surface interactions observed for the two samples. If strong surface interactions are present, as in the case of flat silicon, metalation is less efficient, whilst if Pc does not interact significantly with the surface, as in the case of P*Si*, the efficiency of the metalation improves. Although further work is required to better clarify the nature of interaction between the silicon surface and the molecular system, these results represent a step forward in the understanding of the chemistry of phthalocyanine covalently bonded to inorganic surfaces.

### 9.4 Acknowledgments

The authors thank Ministero dell'Istruzione, dell'Università e della Ricerca (MIUR) for financial support through FIRB "RINAME Rete Integrata per la NAnoMEDicina" (RBAP114AMK). F. Lupo also thanks Università degli Studi di Catania for financial support.

## 9.5 Experimental Section

**1-Pc** was synthesized following the procedure described in Chapter 7. **2-Pc** was purchased from Aldrich chemicals.

### Preparation of Si-1-Pc and PSi-1-Pc

The anchoring of **1-Pc** on a single crystalline, Czochralski grown, p-type boron-doped, (100)-oriented silicon substrate was performed through a well established thermal hydrosilylation route.<sup>24</sup> Similarly to the procedure described in [38], Si(100) substrates were first cleaned with "piranha" solution (H<sub>2</sub>SO<sub>4</sub> (30%)/H<sub>2</sub>O<sub>2</sub> 70:30, v/v) at room temperature for 12 min, rinsed in double distilled water for 2 min, etched in 2% hydrofluoric acid for 90 s, washed with double distilled water for 20 s, accurately dried with pre-purified N<sub>2</sub>, and immediately placed in a three neck flask containing 10 mL of anhydrous mesitylene (Sigma-Aldrich) in which was dissolved 25 mg of **1-Pc** (2.1 mmol/L). The solution was then refluxed at 190°C for 2 h, under slow N<sub>2</sub> bubbling. After cooling to room temperature, the substrates were removed from the flask, rinsed, and repeatedly sonicated in dichloromethane, pentane, and toluene to remove any residual unreacted Pc.

Porous Si (PSi) was prepared by a metal-assisted chemical etching method.<sup>25</sup> A Czochralski grown, p-type boron-doped, Si(100) substrate was immersed in an aqueous solution of 0.14 M HF and 5×10<sup>-4</sup> M in AgNO<sub>3</sub> for 5 min, washed in water and then immersed for 1 min in a solution of HF (65%)/H<sub>2</sub>O<sub>2</sub> (25%)/H<sub>2</sub>O (10%), washed in water and then left for 1 h in a solution of HF (20%)/H<sub>2</sub>O (80%). At the end, the substrate was washed, dried and placed in a three-neck flask containing a solution of **1-Pc** in mesitylene (2.1 mmol/L) and treated as described for flat Si(100) grafting. In this case the reaction time was increased to 4 h.

Control experiments were performed by placing non-etched Si(100) or PSi substrates in a three-neck flask containing a **2-Pc** solution (2.1 mmol/L) in mesitylene and treated as described for Si(100) or PSi grafting.

### Preparation of Si-1-Pc and PSi-1-Pc

Metalation of the silicon-anchored Pc was obtained by wet chemistry. The freshly prepared **Si-1-Pc** and **PSi-1-Pc** were immersed in a flask containing a cobalt solution and then refluxed at 160°C for 8 h, under slow N<sub>2</sub> bubbling. The solution was prepared by dissolving 80 mg of CoCl<sub>2</sub> in 20 mL of anhydrous diglyme and 3 mL of TEA (triethylamine). The substrates were finally washed several times with diglyme and sonicated first in CH<sub>2</sub>Cl<sub>2</sub> and then in EtOH.

### Material Characterization

X-ray photoelectron spectra (XPS) were measured at a take-off angle of 45°, relative to the surface plane, with a PHI 5600 Multi Technique System (base pressure of the main chamber  $2 \times 10^{-10}$  Torr). The spectrometer is equipped with a dual Mg/Al standard X-ray source and a monochromatized Al source, a spherical capacitor analyzer (SCA) with a mean diameter of 279.4 mm. The samples were excited with monochromatized Al K $\alpha$  radiation. The XPS peak intensities were obtained after Shirley background removal. No relevant charging effect was observed. Freshly prepared samples were quickly transferred to the XPS main chamber. The XPS binding energy scale was calibrated by centering the C 1s peak (due to hydrocarbon moieties and adventitious carbon) at 285.0 eV.<sup>17b,26</sup>

Infrared attenuated total reflectance spectra of the monolayers were recorded by using a Jasco FT/IR-430 spectrometer (100 scans collected per spectrum, scan range 560–4000 cm<sup>-1</sup>, resolution 4 cm<sup>-1</sup>).

## 9.6 References

- <sup>1</sup> J. D. Baran, J. A. Larsson, *J. Phys. Chem. C* **2013**, *117*, 23887–23898.
- <sup>2</sup> M. G. Walter, A. B. Rudine, C. C. Wamser, *J. Porphyrins Phthalocyanines* **2010**, *14*, 759–792.
- <sup>3</sup> a) C. G. Claessens, U. Hahn, T. Torrest, *The Chemical Record* **2008**, *8*, 75–97; b) F. I. Bohrer, C. N. Colesniuc, J. Park, M. E. Ruidiaz, I. K. Schuller, A. C. Kummel, W. C. Trogler, *J. Am. Chem. Soc.* **2009**, *131*, 478–485.
- <sup>4</sup> A. B. Sorokin, *Chem. Rev.* **2013**, *113*, 8152–8191.
- <sup>5</sup> D. E. J. G. J. Dolmans, D. Fukumura, R. K. Jain, *Nat. Rev. Cancer* **2003**, *3*, 380–387.
- <sup>6</sup> a) G. I. Cárdenas-Jirón, P. Leon-Plata, D. Cortes-Arriagada, J. M. Seminario, *J. Phys. Chem. C* **2011**, *115*, 16052–16062; b) D. Klar, S. Klyatskaya, A. Candini, B. Krumme, K. Kummer, P. Ohresser, V. Corradini, V. de Renzi, R. Biagi, L. Joly, J. P. Kappler, U. del Pennino, M. Affronte, H. Wende, M. Ruben, *Beilstein J. Nanotechnol.* **2013**, *4*, 320–324.
- <sup>7</sup> S. Chen, Y. Liu, Y. Xu, Y. Sun, W. Qiu, X. Sun, D. Zhu, *Synth. Met.* **2006**, *156*, 1236–1240.
- <sup>8</sup> Z. Li, M. Lieberman, W. Hill, *Langmuir* **2001**, *17*, 4887–4894.
- <sup>9</sup> Y. Alfredsson, J. Åhlund, K. Nilson, L. Kjeldgaard, J. N. O’Shea, J. Theobald, Z. Bao, N. Mårtensson, A. Sandell, C. Puglia, H. Siegbahn, *Thin Solid Films* **2005**, *493*, 13–19.
- <sup>10</sup> a) V. Huc, F. Armand, J. P. Bourgoin, S. Palacin, *Langmuir* **2001**, *17*, 1928–1935; b) M. Trelka, C. Urban, C. Rogero, P. de Mendoza, E. Mateo-Marti, Y. Wang, I. Silanes, D. Écija, M. Alcamì, F. Yndurain, A. Arnau, F. Martín, A. M. Echavarren, J. A. Martín-Gago, J. M. Gallego, R. Otero, R. Miranda, *CrystEngComm* **2011**, *13*, 5591.

- <sup>11</sup> a) J. M. Buriak, *Chem. Rev.* **2002**, *102*, 1271–1308; b) E. Biavardi, C. Tudisco, F. Maffei, A. Motta, C. Massera, G. G. Condorelli, E. Dalcanale, *Proc. Natl. Acad. Sci. U. S. A.* **2012**, *109*, 2263–2268; c) E. Biavardi, S. Federici, C. Tudisco, D. Menozzi, C. Massera, A. Sottini, G. G. Condorelli, P. Bergese, E. Dalcanale, *Angew. Chem. Int. Ed.* **2014**, *53*, 9183–9188.
- <sup>12</sup> G. A. Kumar, J. Thomas, N. V. Unnikrishnan, V. P. N. Nampoori, C. P. G. Vallabhan, *J. Porphyrins Phthalocyanines* **2001**, *5*, 456–459.
- <sup>13</sup> L. Massimi, S. Lisi, D. Pacilè, C. Mariani, M. G. Betti, *Beilstein J. Nanotechnol.* **2014**, *5*, 308–312.
- <sup>14</sup> a) A. Sperl, J. Kröger, R. Berndt, *Angew. Chem. Int. Ed.* **2011**, *50*, 5294–5297; b) Y. Bai, F. Buchner, M. T. Wendahl, I. Kellner, A. Bayer, H.-P. Steinrück, H. Marbach, J. M. Gottfried, *J. Phys. Chem. C* **2008**, *112*, 6087–6092.
- <sup>15</sup> J. Leclaire, R. Dagiral, A. Pla-Quintana, A.-M. Caminade, J.-P. Majoral, *Eur. J. Inorg. Chem.* **2007**, 2890–2896.
- <sup>16</sup> B. Görlach, C. Hellriegel, S. Steinbrecher, H. Yüksel, K. Albert, E. Plies, M. Hanack, *J. Mater. Chem.* **2001**, *11*, 3317–3325.
- <sup>17</sup> a) R. Boukherroub, S. Morin, P. Sharpe, D. D. M. Wayner, P. Allongue, *Langmuir* **2000**, *16*, 7429–7434; b) P. Swift, *Surf. Interface Anal.* **1982**, *4*, 47–51.
- <sup>18</sup> a) A. S. Killampalli, P. F. Ma, J. R. Engstrom, *J. Am. Chem. Soc.* **2005**, *127*, 6300–6310; b) A. Dube, A. R. Chadeayne, M. Sharma, P. T. Wolczanski, J. R. Engstrom, *J. Am. Chem. Soc.* **2005**, *127*, 14299–14309; c) G. G. Condorelli, A. Motta, C. Bedoya, A. Di Mauro, G. Pellegrino, E. Smecca, *Inorg. Chim. Acta* **2007**, *360*, 170–178.
- <sup>19</sup> a) P. Palmgren, K. Nilson, S. Yu, F. Hennies, T. Angot, C. I. Nlebedim, J.-M. Layet, G. Le Lay, M. Göthelid, *J. Phys. Chem. C* **2008**, *112*, 5972–5977; b) S. Yu, S. Ahmadi, C. Sun, P. T. Z. Adibi, W. Chow, A. Pietzsch, M. Göthelid, *J. Chem. Phys.* **2012**, *136*, 154703; c) G. Mattioli, F. Filippone, P. Giannozzi, R. Caminiti, A. A. Bonapasta, *Chem. Mater.* **2009**, *21*, 4555–4567.

- <sup>20</sup> M. Mannini, F. Bertani, C. Tudisco, L. Malavolti, L. Poggini, K. Misztal, D. Menozzi, A. Motta, E. Otero, P. Ohresser, P. Saintavit, G. G. Condorelli, E. Dalcanale, R. Sessoli, *Nat. Commun.* **2014**, *5*, article number: 4582.
- <sup>21</sup> C. Tudisco, G. Trusso Sfrassetto, A. Pappalardo, A. Motta, G. A. Tomaselli, I. Fragalà, F. P. Ballistreri, G. G. Condorelli, *Eur. J. Inorg. Chem.* **2011**, 2124–2131.
- <sup>22</sup> a) F. Petraki, H. Peisert, J. Uihlein, U. Aygül, T. Chassé, *Beilstein J. Nanotechnol.* **2014**, *5*, 524–531; b) F. Petraki, H. Peisert, I. Biswas, T. Chassé, *J. Phys. Chem. C* **2010**, *114*, 17638–17643; c) J. Guo, H. Li, H. He, D. Chu, R. Chen, *J. Phys. Chem. C* **2011**, *115*, 8494–8502.
- <sup>23</sup> T. E. Shubina, H. Marbach, K. Flechtner, A. Kretschmann, N. Jux, F. Buchner, H.-P. Steinrück, T. Clark, J. M. Gottfried, *J. Am. Chem. Soc.* **2007**, *129*, 9476–9483.
- <sup>24</sup> a) G. G. Condorelli, A. Motta, M. Favazza, I. L. Fragala, M. Busi, E. Menozzi, E. Dalcanale, L. Cristofolini, *Langmuir* **2006**, *22*, 11126–11133; b) A. Gulino, F. Lupo, G. G. Condorelli, M. E. Fragalà, M. E. Amato, G. Scarlata, *J. Mater. Chem.* **2008**, *18*, 5011–5018.
- <sup>25</sup> C. Tudisco, P. Betti, A. Motta, R. Pinalli, L. Bombaci, E. Dalcanale, G. G. Condorelli, *Langmuir* **2012**, *28*, 1782–1789.
- <sup>26</sup> D. Briggs, G. Beamson, *Anal. Chem.* **1992**, *64*, 1729–1736.





# Appendix A

## Materials and Methods

## Materials

Unless stated otherwise, reactions were conducted in flame-dried glassware under an atmosphere of argon using anhydrous solvents (either freshly distilled or passed through activated alumina columns). All commercially obtained reagents were used as received unless otherwise specified.

Silica column chromatography was performed using silica gel 60 (Fluka 230-400 mesh ASTM), or silica gel 60 (MERCK 70-230 mesh).

## Methods

- **NMR Measurements**

<sup>1</sup>H NMR spectra were obtained using a Bruker AVANCE 300 (300 MHz) or a Bruker AVANCE 400 (400 MHz) spectrometer. All chemical shifts ( $\delta$ ) were reported in ppm relative to the proton resonances resulting from incomplete deuteration of the NMR solvents. <sup>31</sup>P NMR spectra were obtained using a Bruker AVANCE-400 (161.9 MHz) spectrometer. All chemical shifts ( $\delta$ ) were recorded in ppm relative to external 85% H<sub>3</sub>PO<sub>4</sub> at 0.00 ppm.

- **MS Measurements**

Electrospray ionization ESI-MS experiments were performed on a Waters ZMD spectrometer equipped with an electrospray interface. MALDI was performed on an AB SCIEX MALDI TOF-TOF 4800 Plus (matrix,  $\alpha$ -cyano-4-hydroxycinnamic acid).

- **UV-Vis Measurements**

UV-Vis spectra were collected using a Thermo Scientific Evolution 260 Bio spectrophotometer equipped with a Peltier water cooled cell changer device, using matched quartz cells of 1 cm path length.

## **Acknowledgments**

Il ringraziamento più grande è verso la mia famiglia e i miei genitori, i quali non mi hanno davvero mai fatto mancare nulla e mi supportano in ogni mia decisione.

Grazie a Enrico, che mi ha permesso di fare ricerca in un ambiente stimolante e gratificante, tranne quando ho dovuto scontare tutte le scommesse che ho perso sul Milan: ad ogni modo le rifarei tutte, una ad una!

Lasciare dopo 3 anni il Dalcanale group non è sicuramente facile: qui ho trovato persone fantastiche e stretto legami che non si esauriranno certo con la mia partenza. Marco, sei un pozzo di chimica, un inesauribile dispensatore di consigli, e soprattutto un grande amico. L'appuntamento ad agosto a Palombina con Dani è ormai più scontato della diagonale sbagliata di Bonera. Dani, lavorare in laboratorio con te è stato divertente oltre ogni modo. Secondo me, dopo aver condiviso laurea e dottorato nello stesso laboratorio con te, mi merito un posto da visiting researcher a Shanghai. Un enorme grazie a tutti i ragazzi e le ragazze con cui ho condiviso il mio percorso: la Roby, l'Eli, la Dany, i polski Kasjan e Kuba (che senza l'Italia ormai non sa più stare), Ale, il Bedo, la Vero, la Marti, Tahnee, Riccardo e Andreas: non avrei potuto desiderare compagni di laboratorio migliori di voi.

Un prego invece a tutti coloro che nel corso di questi anni sono continuamente entrati al 187 durante le loro pause per godersi 5 minuti di divertimento! Dai ragazzi del lab. 92 a quelli dell'intero Dipartimento di Chimica: abbiamo condiviso momenti davvero divertenti insieme, in dipartimento e al di fuori, che non scorderò mai. Tuttavia non vi perdonerò mai il fatto di lasciare la porta uscendo dal laboratorio facendoci crepare di freddo...

Thanks to Prof. Swager for the opportunity to join his group at Massachusetts Institute of Technology for 6 months, and special thanks to all the guys of the group for the great time we spent together. I won't forget the 25 cent wings Monday nights at Asgard, the volleyball tournament (go Intimidators!!!) and the support I received after Italy games during the world cup.

Enormous thanks to Chris, for everything he made for me in Boston, and to all the other guys of the crew: Rolf, Marius, Lara, David, Bene Api, Micha, Bernhard. We had great time together, I miss you all, though I'm sure that at

some point we will all meet up again back in Europe for an awesome reunion. Thanks to Georgios, Markus and Jonas for our awesome trip, best experience ever!

Grazie a tutti i miei amici, che siano di Parma, di Neviano o di Tortiano, siete la ragione di una vita. Tra le altre cose, non dimenticherò mai l'affetto di cui sono stato circondato prima di partire per Boston: sono molto fortunato ad avervi.

E un grazie a te Elena, perchè se dopo 3 anni sono di nuovo qui a ringraziarti, allora vuol dire che in tutto questo c'è stato tanto di te, di noi.

E' stata un'esperienza pazzesca, che mi ha dato tantissime opportunità di imparare, di maturare, di viaggiare, di conoscere nuove persone e soprattutto di conoscere me stesso. Grazie quindi a tutti voi che, consciamente o inconsciamente, mi avete lasciato qualcosa di voi che porterò con me in futuro.

Grazie a tutti!

Federico

## *The author*



Born: 12 December 1986, Parma, Italy

July 2005

**High School Diploma**  
Liceo Scientifico "G. Marconi"  
Parma, Italy

September 2008

**Bachelor in Chemistry**  
University of Parma, Italy  
Supervisor: Prof. A. Secchi

July 2010

**Master in Chemistry**  
University of Parma, Italy  
Supervisor: Prof. A. Secchi

November 2010 - November 2011

**Quality Control - R&D Chemist**  
Eulip S.p.A., Parma, Italy.

January 2012 - December 2014

**Doctoral Research**  
University of Parma, Italy  
Supervisor: Prof. E. Dalcanale

January 2014 - July 2014

**Research Exchange**  
Massachusetts Institute of Technology,  
Cambridge (USA). Supervisor: Prof. T. M.  
Swager

## Publications:

- 1) C. Tudisco, F. Bertani, M. T. Cambria, F. Sinatra, E. Fantechi, C. Innocenti, C. Sangregorio, E. Dalcanale, G. G. Condorelli, "Functionalization of PEGylated Fe<sub>3</sub>O<sub>4</sub> magnetic nanoparticles with tetrakisphosphate cavitand for biomedical application", *Nanoscale* **2013**, 5 (23), 11438.
- 2) M. Mannini, F. Bertani, C. Tudisco, L. Malavolti, L. Poggini, K. Misztal, D. Menozzi, A. Motta, E. Otero, P. Ohresser, P. Sainctavit, G. G. Condorelli, E. Dalcanale, R. Sessoli, "Magnetic behaviour of TbPc<sub>2</sub> single-molecule magnets chemically grafted on silicon surface", *Nature Communications* **2014**, 5, article number: 4582.
- 3) F. Lupo, C. Tudisco, F. Bertani, E. Dalcanale, G. G. Condorelli, "In situ metalation of free base phthalocyanine covalently bonded to silicon surfaces", *Beilstein J. Nanotechnol.* **2014**, 5, 2222.
- 4) C. Tudisco, M. T. Cambria, F. Bertani, F. Sinatra, A. Alba, S. Saccone, E. Fantechi, C. Innocenti, C. Sangregorio, E. Dalcanale, G. G. Condorelli, "Multifunctional magnetic nanoparticles for enhanced intracellular drug transport", *J. Mater. Chem. B* **2015**, **under revision**.

This Thesis reports the preparation of multifunctional materials, dealing with two different topics.

The first part concerns the design, synthesis and characterization of multifunctional hybrid magnetic nanoparticles (MNPs) that combine superparamagnetic properties with biocompatibility and biological activity. They are designed to load, carry and release *N*-methylated drugs, exploiting the outstanding molecular recognition properties of tetraphosphonate cavitands towards *N*-methylammonium salts. In the second generation, new functionalities have been introduced for fluorescence detection and tumor cell targeting.

The second part of the work deals with the synthesis of functionalized SMMs for grafting on surfaces. In particular, a peripherally decorated Tb<sup>III</sup>-bisphthalocyaninato SMM was synthesized and grafted on silicon wafer through the hydrosilylation protocol, leading to the formation of a robust covalently linked monolayer. The resulting Si-integrated SMM monolayer showed for the first time a surface enhancement of the magnetic bistability, rather than the commonly observed suppression of it.